ISBN 978-82-471-1131-4 (printed ver.)
ISBN 978-82-471-1130-7 (electronic ver.)
ISSN 1503-8181

NTNU
Norwegian University of
Science and Technology

Leif Idar Langelandsvik

Theses at NTNU, 2008:221

NTNU

Doctoral Thesis

NTNU
Norwegian University of
Science and Technology
Thesis for the degree of
philosophiae doctor
Faculty of Engineering Science and Technology
Department of Energy and Process Engineering

Doctoral Theses at NTNU, 2008:221

Leif Idar Langelandsvik

Modeling of natural gas transport and friction factor for large-scale pipelines

Laboratory experiments and analysis of operational data

NTNU
Norwegian University of
Science and Technology

Leif Idar Langelandsvik

Modeling of natural gas transport and friction factor for large-scale pipelines

Laboratory experiments and analysis of operational data

Thesis for the degree of philosophiae doctor

Trondheim, September 2008

Norwegian University of
Science and Technology
Faculty of Engineering Science and Technology
Department of Energy and Process Engineering

NTNU
Norwegian University of
Science and Technology

NTNU
Norwegian University of Science and Technology

Thesis for the degree of philosophiae doctor

Faculty of Engineering Science and Technology
Department of Energy and Process Engineering

ISBN 978-82-471-1131-4 (printed ver.)
ISBN 978-82-471-1130-7 (electronic ver.)
ISSN 1503-8181

Theses at NTNU, 2008:221

Printed by Tapir Uttrykk

Modeling of natural gas transport and friction factor for large-scale pipelines

Laboratory experiments and analysis of operational data

Leif Idar Langelandsvik, 2008

Abstract

The overall objective of this work was to improve the one-dimensional models used to simulate the transport of single-phase natural gas in Norway's large-diameter export pipelines. There was a particular focus on the simulator used by the state-owned company Gassco named Transient Gas Network (TGNet). This simulator was studied in order to uncover any weaknesses or inaccuracies and to predict the natural gas transport with better accuracy both in the daily operation and when long-term capacity calculations are made.

The conclusion was that the simulator in general resolves the physics well, provided that the input correlations such as viscosity correlation and friction factor correlation are accurate. The simulator was therefore found trustworthy to be used in the determination of the friction factor for operational data. No satisfactory correlations exist for the additional pressure loss in smooth curves, and like all other commercial simulators TGNet ends up modeling only a straight pipe. This is a weakness, but the magnitude of the associated error is unknown. The simulator also fails to predict the heat transfer for partly buried pipelines.

The sensitivity analysis performed on an artificial pipeline model as well as the uncertainty analysis for the full-scale experiments both indicated which parameters are most important in the simulations:

- Gas density calculations
- Ambient temperature (affecting the gas temperature)
- Flow rate measurements
- Inner diameter of pipeline

The fricton factor was analyzed both by means of laboratory experiments in the high Reynolds number facility Superpipe at Princeton University in US and by comprehensive analysis of real operational data at the largest Reynolds numbers ever covered.

The Superpipe measurements were made on a 5 inch inner diameter natural rough steel pipe, and covered both the smooth, transitionally rough and the fully rough region. Reynolds numbers from $150 \cdot 10^3$ to $20 \cdot 10^6$ were covered. Due to lack of studies on naturally rough surfaces in literature, these measurements yielded very interesting results. The transition zone was abrupt, but was neither a point transition nor an inflectional transition. The equivalent sand grain roughness was furthermore found to be 1.6 times the measured root mean square roughness, which is in contrast to the value of 3.0 to 5.0 that is commonly used.

Operational data were collected from two full-scale steel pipelines with an inner diameter of 40 and 42 inches respectively, covering Reynolds numbers from $10 \cdot 10^6$ to $45 \cdot 10^6$. The experiments showed friction factors signicantly lower than predicted by the Colebrook-White correlation and based on reported roughness measurements. It was also concluded that the pipelines are in the transition zone which is more abrupt than that of Colebrook-White.

Increased knowledge about the frictional pressure drop at large flow rates resulting from analysis of operational data has led to updated and increased capacity calculations in several pipelines. The increase is in the range 0.2-1.0%, and facilitates an improved utilization of the natural gas transport infrastructure on the Norwegian Continental Shelf.

This work includes three different papers, one presented at an international conference and two published in peer-reviewed international journals.

Acknowledgements

I am greatly indebted to everybody who has supported me in any way by encouragements, advice, interesting discussions and financial support. Without this support it would have been impossible to complete this PhD work in a 4-year period.

Without the clearly expressed support and encouraging words from my wife Rannveig, I had never started on this PhD. And the same support became not less important as I went along the road. Two of our three lovely kids have been born in this period, and periodically my focus has been too much on the research and too little on the children.

I am greatly indebted to those who have contributed financial support throughout these years. The Research Council of Norway contributed with PhD funding to the associated research project, but also Gassco AS and Polytec Research Foundation have contributed to my salary, travel, housing in Trondheim and research stay at Princeton University, US.

On the way fruitful discussions have revealed many good ideas and pushed me one step further. Many could be addressed, but particularly my Gassco "mentor" Willy Postvoll and the university supervisors at The Norwegian University of Science and Technology (NTNU), Adjunct Professor Jan M. Øverli and Professor Tor Ytrehus are to be mentioned. Their different but complementary approaches to the work have been important for the work in an academic area where the industrial application has been the driver and the underlying idea.

A decisive contribution to the work was also the experimental results and the ideas that I was able to obtain at Princeton University and the experimental facility Superpipe. Professor Alex Smits was most helpful from the very first moment I contacted him, and has since then responded swiftly to any inquiry and question I might have had. And everything was done most patiently. I learned so much, both on a professional and personal level, during the half year my family and I spent in New Jersey.

Contents

ABSTRACT III

ACKNOWLEDGEMENTS V

CONTENTS VII

LIST OF FIGURES IX

LIST OF TABLES XI

NOMENCLATURE XIII

CHAPTER 1 INTRODUCTION .... - 1 -
- 1.1 BACKGROUND .... - 1 -
- 1.2 OBJECTIVES .... - 4 -
- 1.3 OUTLINE .... - 4 -

CHAPTER 2 LITERATURE REVIEW AND SIMULATION MODEL .... - 7 -
- 2.1 PIPE FLOW HISTORY WITH LITERATURE REVIEW .... - 7 -
- 2.2 PIPELINE SIMULATORS, TGNET AS AN EXAMPLE .... - 16 -
- 2.3 DISCUSSION .... - 35 -

CHAPTER 3 SENSITIVITY ANALYSIS .... - 37 -
- 3.1 INTRODUCTION .... - 37 -
- 3.2 PIPELINE SETUP .... - 37 -
- 3.3 SENSITIVITY PARAMETERS .... - 39 -
- 3.4 RESULTS .... - 40 -
- 3.5 DISCUSSION .... - 50 -

CHAPTER 4 EXPERIMENTAL: VISCOSITY MEASUREMENTS .... - 59 -
- 4.1 INTRODUCTION .... - 59 -
- 4.2 MEASUREMENT RESULTS .... - 60 -
- 4.3 DISCUSSION .... - 62 -

CHAPTER 5 EXPERIMENTAL: ROUGHNESS MEASUREMENTS .... - 65 -
- 5.1 INTRODUCTION .... - 65 -
- 5.2 PIPES AND COATING .... - 65 -
- 5.3 SURFACE CONDITION .... - 66 -
- 5.4 METHODOLOGY .... - 68 -
- 5.5 ROUGHNESS RESULTS .... - 69 -
- 5.6 DETERMINATION OF SAND GRAIN EQUIVALENT ROUGHNESS .... - 72 -
- 5.7 APPLICATION TO A FULL-SCALE EXPORT PIPELINE .... - 73 -
- 5.8 DISCUSSION .... - 75 -

CHAPTER 6 EXPERIMENTAL: LABORATORY TESTS OF A NATURAL ROUGH PIPE .... - 77 -
- 6.1 INTRODUCTION .... - 77 -

6.2 SUPERPIPE FACILITY .... - 77 -
6.3 INSTALLATION OF NATURAL ROUGH STEEL PIPE .... - 78 -
6.4 PIPE SURFACE .... - 80 -
6.5 MEASUREMENT TECHNIQUE........ - 82 -
6.6 RESULTS .... - 83 -
6.7 UNCERTAINTY .... - 87 -
6.8 DISCUSSION .... - 89 -

CHAPTER 7 EXPERIMENTAL: OPERATIONAL DATA FROM FULL-SCALE PIPELINES ..... - 91 -
7.1 INTRODUCTION .... - 91 -
7.2 KÅRSTØ-BOKN PIPELINE LEG........ - 94 -
7.3 EUROPIPE 2, FULL LENGTH........ - 120 -
7.4 ZEEPIPE........ - 133 -
7.5 CALCULATIONS OF TRANSPORT CAPACITY........ - 141 -
7.6 DISCUSSION .... - 141 -

CHAPTER 8 CONCLUSIONS .... - 149 -

CHAPTER 9 RECOMMENDATIONS........ - 151 -

REFERENCES .... - 153 -

APPENDIX A MODEL DETAILS .... - 159 -
A.1 MOMENTUM BALANCE, 3D TO 1D........ - 159 -
A.2 ENERGY BALANCE, 3D TO 1D .... - 161 -

APPENDIX B PAPER, JOURNAL OF FLUID MECHANICS .... - 167 -

APPENDIX C PAPER, PIPELINE SIMULATION INTEREST GROUP .... - 187 -

APPENDIX D PAPER, INTERNATIONAL JOURNAL OF THERMOPHYSICS .... - 205 -

List of figures

Figure 1.1 Overview of the Norwegian natural gas transport system. - 3 -
Figure 2.1 Nikuradse's data series. - 8 -
Figure 2.2 Velocity profile. - 10 -
Figure 2.3 Colebrook-White equation plotted in a Moody diagram. - 12 -
Figure 2.4 GERG's formula with $k_S = 0.01$ mm. - 14 -
Figure 2.5 GERG's formula with $k_S = 5.0$ mm. - 14 -
Figure 2.6 Friction factor in a honed aluminium pipe from Superpipe. - 15 -
Figure 2.7 Numerical stencil in the box scheme. - 24 -
Figure 2.8 Outer film coefficient calculated by TGNet. - 29 -
Figure 2.9 Proposed interpolation for outer film coefficient. - 32 -
Figure 3.1 Sensitivity coefficients on flow rate. - 42 -
Figure 3.2 Sensitivity coefficients on flow rate. - 43 -
Figure 3.3 Sensitivity coefficients on outlet temperature. - 44 -
Figure 3.4 Sensitivity coefficients on outlet temperature. - 44 -
Figure 3.5 Sensitivity coefficients on tuned roughness. - 45 -
Figure 3.6 Sensitivity coefficients on tuned roughness. - 46 -
Figure 3.7 Sensitivity coefficients on tuned ambient temperature. - 47 -
Figure 3.8 Sensitivity of U_{INNER}, U_{WALL} and U_{OUTER} on U_{TOTAL}. - 48 -
Figure 3.9 Sensitivity of material conductivies and thicknesses on U_{WALL}. - 49 -
Figure 3.10 Sensitivity of sea velocity on U_{OUTER}. - 50 -
Figure 3.11 Colebrook-White friction factor for k = 3.8 micron, and the friction factor differentiated with regard to the Reynolds number holding k constant at 3.8 micron. - 55 -
Figure 3.12 Colebrook-White friction factor for k = 3.8 micron, and the friction factor differentiated with regard to roughness. - 57 -
Figure 4.1 Deviation for different prediction models and Sample 1. - 61 -
Figure 4.2 Deviation for different prediction models and Sample 2. - 61 -
Figure 4.3 Deviation for different prediction models and Sample 3. - 62 -
Figure 5.1 Cleaning pig in Europipe 2. - 67 -
Figure 5.2 Pipe cut-offs from Norpipe. - 67 -
Figure 5.3 Application of resin. - 68 -
Figure 5.4 Measured R_A for the Langeled pipes. - 69 -
Figure 5.5 Measured R_Q for the Langeled pipes. - 70 -
Figure 5.6 3D image, Pipe1A. - 70 -
Figure 5.7 3D image, Pipe6A. - 70 -
Figure 5.8 3D image, Pipe1C. - 71 -
Figure 5.9 3D image, Pipe6D. - 71 -
Figure 5.10 Measured roughness kurtosis in Langeled pipes. - 72 -
Figure 5.11 Viscous length scale and roughness Reynolds number. - 74 -
Figure 5.12 Viscous length scale and roughness Reynolds number. - 75 -
Figure 6.1 Sketch of Superpipe facility. - 78 -
Figure 6.2 Connection of two test pipes. - 79 -
Figure 6.3 Surface scan of natural rough steel pipe. - 80 -
Figure 6.4 Roughness probability density function. Solid line is probability density function and dotted line is a best fit of a Gausian distribution. - 81 -
Figure 6.5 Friction factor measurements. - 84 -
Figure 6.6 Velocity profile measurements for different Re numbers, inner scaling. - 85 -
Figure 6.7 Velocity profile measurements for two different Re numbers, absolute units. - 86 -
Figure 6.8 Hama roughness function. - 87 -
Figure 6.9 Pressure gradients. - 89 -
Figure 7.1 Analysis of operational data, sketch of approach. - 93 -
Figure 7.2 Elevation Profile, Kårstø-Bokn leg. - 94 -
Figure 7.3 Route of Europipe2 leg from Kårstø to Bokn. - 95 -
Figure 7.4 Interior of a Europipe2 spare pipe. - 95 -

Figure 7.5 Close-up of the Europipe2 surface. ... - 96 -
Figure 7.6 Illustrating the different pipe layers: steel, asphalt and concrete. ... - 96 -
Figure 7.7 Verification of signal transmission quality. ... - 99 -
Figure 7.8 Close-up of part of the signal transmission quality. ... - 99 -
Figure 7.9 Transient signals with step in flow rate. ... - 101 -
Figure 7.10 Transient signals with oscillating flow rate. ... - 102 -
Figure 7.11 Temperature variation throughout the year. ... - 104 -
Figure 7.12 Measured and UK Met modeled sea bed temperatures during pigging. ... - 105 -
Figure 7.13 Measured and simulated gas temperature at the pig’s current position. ... - 107 -
Figure 7.14 Measured and simulated gas pressure at the pig’s current position. ... - 108 -
Figure 7.15 Simulation Results Kårstø-Bokn compared with CW curves. ... - 109 -
Figure 7.16 Kårstø-Bokn results, comparing LGE-1 and LGE-3. ... - 111 -
Figure 7.17 Illustration of piecewise circle segment fit to pipeline data. ... - 112 -
Figure 7.18 Curvature distribution. ... - 113 -
Figure 7.19 Friction factor effect due to curvature. ... - 114 -
Figure 7.20 Burial depth Ep2. ... - 121 -
Figure 7.21 Simulated gas temperature versus kilometer position, Kårstø-Bokn. ... - 122 -
Figure 7.22 Simulated gas temperature versus kilometer position. ... - 123 -
Figure 7.23 Simulated gas temperature versus time after pig launch. ... - 123 -
Figure 7.24 Simulated friction factors with first configuration file compared with CW. ... - 127 -
Figure 7.25 Simulated friction factors with first configuration file compared with CW curves, larger Reynolds number range. ... - 128 -
Figure 7.26 Simulated friction factors with second configuration file compared with CW. ... - 128 -
Figure 7.27 Temperature deviation for the test points exposed(1.3, 2.0), $T_{measured}-T_{simulated}$. ... - 129 -
Figure 7.28 Temperature deviation for the test points partly(2.9, 4.0), $T_{measured}-T_{simulated}$. ... - 130 -
Figure 7.29 Elevation profile Zeepipe. ... - 134 -
Figure 7.30 Burial depth Zeepipe. ... - 134 -
Figure 7.31 Simulated friction factors Zeepipe compared with CW curves. ... - 138 -
Figure 7.32 $T_{measured}-T_{simulated}$ in Zeepipe. ... - 139 -
Figure 7.33 Temperature deviation versus season in Zeepipe. ... - 140 -
Figure 7.34 Simulated roughness versus season in Zeepipe. ... - 140 -
Figure 7.35 Simulated friction factor results Europipe 2 compared with CW curves. ... - 142 -
Figure 7.36 Europipe 2 pig after arrival in Dornum. ... - 143 -
Figure 7.37 Possible points of collapse with fully rough line for Europipe 2. ... - 145 -
Figure 7.38 Friction factor results compared with different versions of the GERG formula. ... - 146 -

List of tables

TABLE 2.1 CALCULATION OF U_{OUTER} IN TGNET. - 28 -
TABLE 2.2 DIFFERENT PARAMETERS IN NUSSELT FORMULA FOR FORCED CONVECTION. - 30 -
TABLE 3.1 PIPELINE PARAMETERS. - 38 -
TABLE 3.2 GAS COMPOSITION. - 38 -
TABLE 3.3 OTHER PARAMETERS. - 38 -
TABLE 3.4 OTHER CORRELATIONS. - 38 -
TABLE 3.5 OPERATING CONDITIONS AT BASE CASE. - 39 -
TABLE 3.6 IMMEDIATE EFFECTS IN FLOW RATE AND GAS OUTLET TEMPERATURE FROM CHANGING A SENSITIVITY PARAMETER. - 40 -
TABLE 3.7 NECESSARY ADJUSTMENT IN ROUGHNESS AND AMBIENT TEMPERATURE TO REVERT TO BASE CASE RESULTS. - 41 -
TABLE 3.8 MODIFIED PIPE DIAMETERS FOR HIGH FLOW RATE CASE. - 52 -
TABLE 3.9 MODIFIED PIPE DIAMETERS FOR LOW FLOW RATE CASE. - 52 -
TABLE 3.10 QUANTIFICATION OF DIFFERENT TERMS IN EQUATION. - 54 -
TABLE 3.11 QUANTIFICATION OF DIFFERENT TERMS IN EQ. 3.14. - 56 -
TABLE 4.1 LGE-3 COEFFICIENTS. - 62 -
TABLE 6.1 FRICTION FACTOR UNCERTAINTY CALCULATIONS. - 88 -
TABLE 7.1 GAS CHROMATOGRAPH UNCERTAINTY. - 98 -
TABLE 7.2 VERIFICATION OF SIGNAL TRANSMISSION. - 100 -
TABLE 7.3 SIMULATED ROUGHNESS WITH STEP IN FLOW RATE. - 101 -
TABLE 7.4 SIMULATED ROUGHNESS WITH OSCILLATING FLOW RATE. - 102 -
TABLE 7.5 DETAILS ABOUT STEADY-STATE PERIODS, KÅRSTØ-BOKN. - 110 -
TABLE 7.6 CURVATURE EFFECT ON CURVED PIPE FRICTION FACTOR. - 114 -
TABLE 7.7 FRICTION FACTOR UNCERTAINTY FOR KÅRSTØ-BOKN RESULTS. - 115 -
TABLE 7.8 FRICTION FACTOR UNCERTAINTY CONTRIBUTIONS IN KÅRSTØ-BOKN EXPERIMENTS. - 117 -
TABLE 7.9 DETAILS ABOUT THE DIFFERENT CONFIGURATION FILES THAT WERE TESTED FOR EUROPIPE 2. - 121 -
TABLE 7.10 DETAILS ABOUT THE STEADY-STATE PERIODS IN EUROPIPE 2. REPORTED RESULTS ARE FROM EXPOSED(1.3, 2.0). - 125 -
TABLE 7.11 FRICTION FACTOR UNCERTAINTY FOR KÅRSTØ-BOKN RESULTS. - 131 -
TABLE 7.12 DETAILS ABOUT THE STEADY-STATE PERIODS IN ZEEPIPE. - 136 -

Nomenclature

Latin symbols

A	pipe cross sectional area
A_0	annual amplitude of the surface soil
A_0	cross sectional area through which a force is applied (re. Young's modulus)
B	turbulent wall law additive constant
ΔB	Hama's additive roughness function
c_f	skin friction coefficient
c_p	specific heat capacity at constant pressure
c_v	specific heat capacity at constant volume
C	constant in Idelchik's weld loss formula
Cp_s	sea-water heat capacity
CW	Colebrook-White correlation
d	damping depth
dr	draught factor
dp/dx	pressure gradient
d_o	outer pipe diameter
D	inner pipe diameter
D_c	burial depth, to pipe centerline
D_h	thermal diffusivity
EFF	efficiency factor
e	specific inner energy
E	Young's modulus
f	friction factor
f_s	straight pipe friction factor
f_c	curved pipe friction factor
f_b	curved pipe friction factor
f_{weld}	friction due to welds
F	applied force
g	gravity
Gr	Grashof number
h	specific enthalpy
h_b	head loss in bend
h_i	inner wall film heat transfer coefficient
h_o	outer heat transfer film coefficient
h_w	total wall heat resistance
HSC	high spot count
k, k_s	Nikuradse's sand grain equivalent roughness
k_s	soil thermal conductivity
k_{rms}	root mean square roughness (equivalent to R_q)
k^+	roughness Reynolds number (roughness scaled by viscous length scale)
kp	kilometer position
K_c	geometrical constant
l_w	weld spacing

L	pipeline length
L_0	original length of the object (re. Young's modulus)
m	mass flux
$\dot{m}$	mass flow
M	molar mass
MSm^3/d	million standard cubic meters a day (15 degC)
n	number of wall layers
n	controls the transition region shape in AGA's formula
Nu	Nusselt number
Nu_n	Nusselt number natural convection
Nu_f	Nusselt number forced convection
p	pressure
P	pressure
$\overline{P}$	mean pressure
Pr	Prandtl number
Pr_w	Prandtl number using wall temperature
q	heat transfer
Q_{tot}	total heat transfer between surroundings and pipeline
r	inner pipe radius
r_{ii}	inner radius of the i'th wall layer
r_{oi}	outer radius of the i'th wall layer
R	radius of curvature
R	inner radius of pipe
R	universal gas constant
Ra	Rayleigh number
Re	Reynolds number
R_a	average absolute roughness
R_q	root mean square roughness (equivalent to k_{rms})
R_z	peak to valley roughness
R^+	radius of pipe scaled with viscous length scale
SG	specific gravity
t	time
T	bulk gas temperature
T_a	average soil temperature
T_{gas}	gas temperature
T_{env}	temperature of environment/surroundings
$T_{measured}$	measured gas temperature
$T_{simulated}$	simulated gas temperature
U	bulk velocity
U	cross sectional averaged and Reynolds averaged velocity
U	heat transfer coefficient
U_{inner}	heat transfer coefficient for the inner film resistance
U_{wall}	heat transfer coefficient for the wall resistance
U_{outer}	heat transfer coefficient for the outer film resistance
$U_{W,tot}$	total heat transfer coefficient from the surroundings to the gas
u	gas velocity in x-direction
u_s	sea-water velocity
u^+	axial velocity, inner variables
u^*	wall friction velocity
v	gas velocity in y-direction

V	velocity vector (three components)
w	gas velocity in z-direction
x	axial position in pipeline
x	normalized burial depth
y	y-direction in pipe cross-section
y^+	radial position, inner variables
y_0^+	thickness of the viscous sublayer in wall units
z	z-direction in pipe cross-section
z	compressibility factor

Greek symbols

α	inclination angle of pipeline
β	coefficient of thermal expansion
β	profile factor
δ	weld eight
κ	Von Karman constant
Φ	dissipation function
λ_{HSC}	typical wavelength between large roughness elements
μ	dynamic viscosity
ν	kinematic viscosity
ρ	density
ρ_s	sea-water density
σ_{ij}	stress
τ_w	wall shear stress

CHAPTER 1

Introduction

1.1 Background

Natural gas plays an important role in the energy supply of Europe and the world. Natural gas accounts for almost a quarter of world's energy consumption. Total world production in 2006 was 2,865 billion cubic meters, i.e. $2.9 \cdot 10^{12}$ MSm^3, of which Norway contributed 3.1% (www.bp.com). Natural gas is mainly transported by means of transmission pipelines, either onshore or offshore.

The Norwegian production is transported in seven large diameter subsea pipelines to the United Kingdom and continental Europe, covering around 15% of the European natural gas consumption. Reliable, safe and optimal operation of these pipelines is crucial for Norway as a natural gas provider, but is even more important for every single customer all over Europe. The transportation network is operated by the state-owned company Gassco, and includes platforms for mixing and routing (no production), pipelines, processing plants and receiving terminals. An overview is given in Figure 1.1.

The Norwegian export pipelines are between 500 and 800 km long. They have an inner diameter of around 1 m, with pressure transmitters, flow meters and quality measurements only at the inlet and at the outlet. To know the state of the gas between those two points one solely has to rely on computer models and simulators, which are very important in order to obtain optimal operation of the pipelines. The computer models are used for general monitoring of the gas transport, providing estimated arrival times for possibly unwanted quality disturbances and cleaning pigs, predictive simulations when the operational conditions change and for transport capacity calculations. The transport capacity is usually made available to the shippers of the gas many years in advance, and accurate calculations early in the lifetime of a pipeline are appreciated and valuable.

High accuracy in the transport capacity calculations is important to ensure optimal utilization of invested capital in the pipeline infrastructure. One wants the calculations to be as close to, but not larger than, the true capacity as possible. This will ensure optimal utilization of invested capital. As soon as a pipeline is built, the true capacity is determined by the diameter, length, available inlet compression and other physical parameters. It is the job of scientists to estimate this figure exactly, and the approach used by Gassco today is to use a capacity test, where the wall roughness is used to tune the model to match the flow conditions from a well-controlled steady-state period. Based on this roughness the friction factor is extrapolated along the appropriate Colebrook-White friction factor curve to find the hydraulic capacity. The validity of the Colebrook-White formula for different pipelines has been subject to discussion for decades, and the uncertainty of the capacity calculation grows with decreasing capacity test flow rates.

Preliminary investigations performed on real full-scale pipeline suggest that the Colebrook-White formula might lead to conservative capacity calculations in the range of 0.5 – 1.5%, which amounts to a potential annual increase in the gas export from the Norwegian Continental Shelf of USD 100-400 million. In that case the true friction factor characteristic has a steeper slope than predicted by Colebrook in this region. The Reynolds number in question is $20\text{-}40 \cdot 10^6$ with a friction factor value around $7.0 \cdot 10^{-3}$.

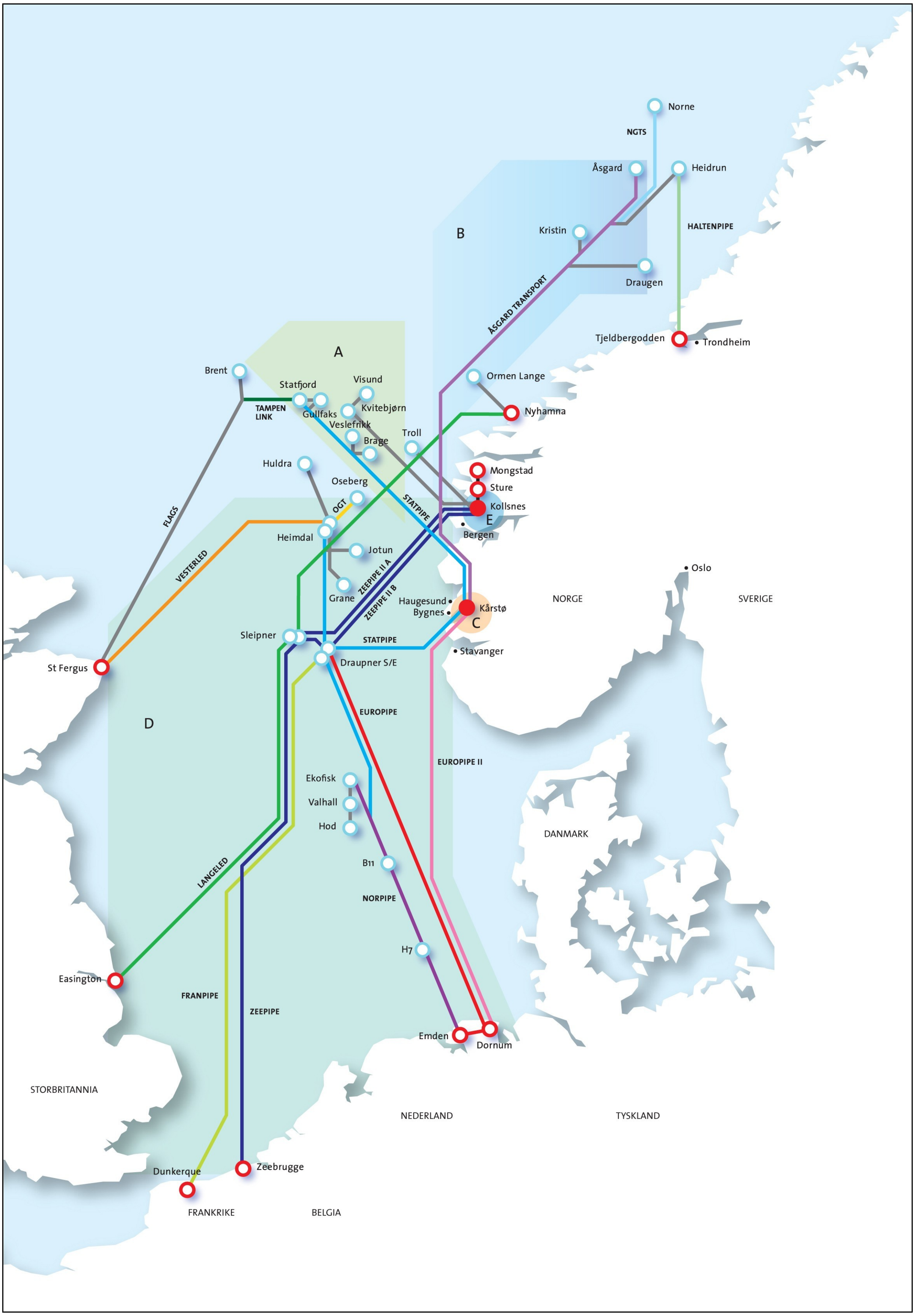

Figure 1.1 Overview of the Norwegian natural gas transport system.

1.2 Objectives

The overall objective of the work presented in this dissertation is to improve the one-dimensional models used to simulate the gas transport in Norway's large diameter pipelines.

It is also a major goal to calculate the transport capacity in the long subsea export pipelines with better accuracy, and through this be able to increase the calculated capacity and make it available to the shippers of gas.

This objective has been broken down to four sub-objectives.

- The first objective is to analyze how the one-dimensional models in general are derived, and pinpoint and quantify common simplifications and shortcomings that are frequently ignored. There is to be particular focus on the simulator used by Gassco, which is Transient Gas Network (TGNet) from Energy Solutions International.
- The second objective is to perform a sensitivity analysis and judge the importance of the different input parameters to the simulator, such as equation of state, calculated heat transfer, accurate pipeline diameter etc., and show which parameters have the largest effect on the calculated uncertainty in the simulations.
- The third objective is to increase the knowledge about how the physically measured surface roughness of a specific pipeline can be used to predict the friction factor. This implies refining the single sand-grain equivalent roughness introduced by Nikuradse.
- The fourth objective is to experimentally increase the knowledge about the friction factor behavior in large diameter pipelines at large Reynolds numbers and assess the validity of Colebrook-White at these conditions. The transitional behavior and determining the point of departure from the smooth line are particularly emphasized. Laboratory experiments and full-scale tests at realistic and relevant Reynolds numbers should be used.

1.3 Outline

CHAPTER 2 provides a review of some of the relevant literature for this work, and gives an overview of how TGNet works with focus on the equations and the numerics. This is also regarded to serve as an introduction to one-dimensional simulators in general. Weaknesses and shortcomings are pinpointed, and the importance of them is quantified and discussed to some extent.

In CHAPTER 3, a comprehensive sensitivity analysis of TGNet is provided. This means that all relevant input parameters are altered by a magnitude comparable with their uncertainty. The resulting effect on the simulation of one low flow rate case and one high flow rate case respectively is thus found.

CHAPTER 4 reports highly accurate dynamic viscosity measurements of three real natural gas samples. Relevant viscosity prediction models/correlations are compared with the measurements, and one correlation is recommended for further use.

CHAPTER 5 reports new three-dimensional roughness measurements of several pipes from the Langeled pipeline before they were installed. The measurements are analyzed and compared with other published roughness measurements. They are also used to predict a departure point from the smooth friction factor curve.

CHAPTER 6 summarizes friction factor measurements obtained from a natural rough steel pipe in the well reputed facility Superpipe at Princeton University, New Jersey. The measurements cover the smooth turbulent region, the transition region as well as the fully rough region, and they thus constitute important contributions to the discussion of how the roughness effects start to play a role and how the transition region is defined.

In CHAPTER 7 a comprehensive set of operational data from full-scale operational pipelines in the North Sea is presented and analyzed. TGNet is used to quantify and analyze the friction factor for different flow rates, and how it depends on the Reynolds number. Results from a 12 km long segment of a long transport pipeline as well as from several full length transport pipelines are reported.

CHAPTER 8 provides an interpretation and discussion of the obtained results, and concludes how they have been used and can be used to increase the insight in the one-dimensional modeling of natural gas transport at these conditions.

Papers prepared and published as part of the work are added as appendices together with details from the dissertation. Appendix A shows the detailed steps when the three-dimensional equation set is transformed to one-dimensional models suitable for implementation in a pipeline simulator.

Appendix B is *Flow in a commercial steel pipe*, which appeared in Journal of Fluid Mechanics, Vol. 595 (2007), pp. 323-339. Velocity profile and friction factor measurements from a commercial steel pipe in the Superpipe facility are reported.

Appendix C contains *An Evaluation of the Friction Factor Formula based on Operational Data*, which was presented at the Pipeline Simulation Interest Group (PSIG) meeting in 2005 in San Antonio, Texas.

Appendix D is the paper *Dynamic Viscosity Measurements of Three Natural Gas Samples – Comparison against Prediction Models*, presented in International Journal of Thermophysics in 2007, where viscosity measurements are reported.

CHAPTER 2

Literature Review and Simulation Model

This chapter gives an introduction to turbulent pipe flow, the equations describing it and also an overview of the historical development in the field. The first section focuses on the basics, the history and the friction factor. The following section describes the one-dimensional models and simulators used in natural gas pipe flow, with particularly focus on Transient Gas Network (TGNet).

2.1 Pipe flow history with literature review

Osborne Reynolds

Osborne Reynolds is credited the start of the modern fluid dynamics. In 1883 he documented turbulent flow in a pipe. The most popular similarity expression used in pipe flow also bears his name. The non-dimensionalized Reynolds number, which expresses the relation between inertial forces and viscous forces, is defined as $\mathrm{Re} = \frac{\rho U D}{\mu}$. Two different flow setups will exhibit the same characteristics as long as this number remains the same. This is in fact a very valuable result, and has not been questioned since the invention more than 120 years ago. Other dimensionless characterizing numbers have also been added and extensively used since then.

Flow equations

The fluid flow in a pipe is fully described by the three laws of conservation:

- Conservation of mass (continuity)
- Conservation of momentum (Newton's second law)
- Conservation of energy (first law of thermodynamics)

The three unknowns which must be obtained simultaneously from these three basic equations are the velocity, the thermodynamic pressure and the absolute temperature. These equations have been known for more than 100 years, but in their complete form they are impossible to solve analytically for a turbulent system. Theoretical efforts have been concentrated on finding solutions to parts of the flow, and/or for very simplified geometries. Computational efforts includes direct numerical simulations, which are limited to $\mathrm{Re} \sim 10^4$, and large eddy simulations, which require a turbulence model, for higher Reynolds numbers.

Nikuradse

One of the most extensive experimental tests of flow in pipes was performed by one of Prandtl's students, Nikuradse, in the 1930s. He measured the pressure drop and the velocity profile for water flow in pipes. The diameter of the test pipes ranged from 10 mm to 100 mm, and the experiments covered Reynolds numbers from $4\cdot10^3$ to $3\cdot10^6$. These experiments have become a landmark in the history of experimental fluid dynamics, still referenced and highly respected by experimentalists. Up to now, only a few experimentalists have reproduced data for such high Reynolds numbers. The experiments from smooth pipes are reported in Nikuradse (1932). At that time the Reynolds number dependent power law was the prevailing formula for describing the mean velocity profile. However, Nikuradse's experiments demonstrated the complete similarity described by the logarithmic law in the overlap region. In 1933, he performed tests in rough pipes, see Nikuradse (1933). Prior to the flow tests, the interior of the pipes were artificially roughened by gluing sand grains to the surface. They showed the three regions constituted by the friction factor, i.e. smooth and rough turbulent flow and the transitional region (Figure 2.1). However, Zagarola (1996) gives a list of 16 weaknesses in either the experiments or the report, underlining the fact that experimental techniques have progressed in the years that have passed. The great benefit of Nikuradse's measurements is that for many tests they covered the entire transition region from smooth to rough turbulent flow. Nikuradse found that the friction factor eventually becomes independent of the Reynolds number, and presented the formula for rough turbulent flow.

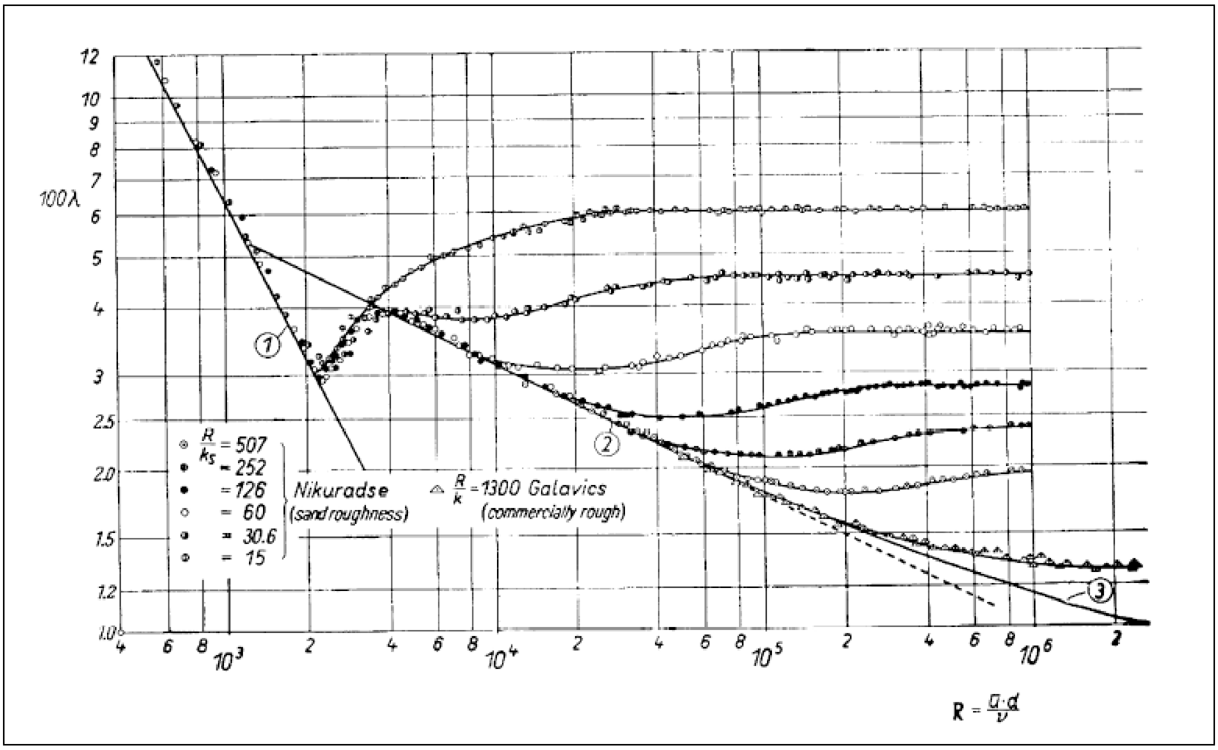

Figure 2.1 Nikuradse's data series.

Prandtl and von Karman

In order to describe turbulent flow in pipes, the velocity profile is very important. Great physical insight into this was given by Ludwig Prandtl and Theodore von Karman in 1933 and 1930 respectively. Prandtl suggested that close to the wall, the profile will only depend on wall shear stress, fluid properties and distance y from the wall (and not on freestream parameters). Moreover, Karman defines an outer region where he suggests that the flow pattern is independent of viscosity. The important parameters are wall shear stress, density, distance from wall and the radius of pipe. In 1938, Millikan (1938) suggested that at large enough Reynolds numbers an overlap region may exist where both inner and outer region properties are valid at the same time. The combination of these two layers yields the well known logarithmic overlap layer:

$$u^+ = \frac{1}{\kappa} \ln y^+ + B \qquad \textbf{Eq. 2.1}$$

where u^+ is the mean velocity divided by the wall friction velocity:

$$u^+ = \frac{u}{u^*} = \frac{u}{\sqrt{\frac{\tau_w}{\rho}}} \qquad \textbf{Eq. 2.2}$$

and y^+ is the wall normal distance divided by the viscous length scale:

$$y^+ = \frac{y}{\frac{\nu}{u^*}} \qquad \textbf{Eq. 2.3}$$

κ is the von Karman constant, for which 0.41 often is used, and B is an additive constant where 5.0 often is used.

The viscous length scale is taken as a length scale for the small scale turbulent motion close to the wall. It decreases with increasing Reynolds number, and the thickness of the viscous sublayer is usually given as around five times this scale.

It is common to subdivide the inner layer into a viscous sublayer, where the velocity is proportional to the wall distance, and a buffer layer which represents a transition to the overlap layer.

Figure 2.2 is a representation of the velocity profile from White (1991).

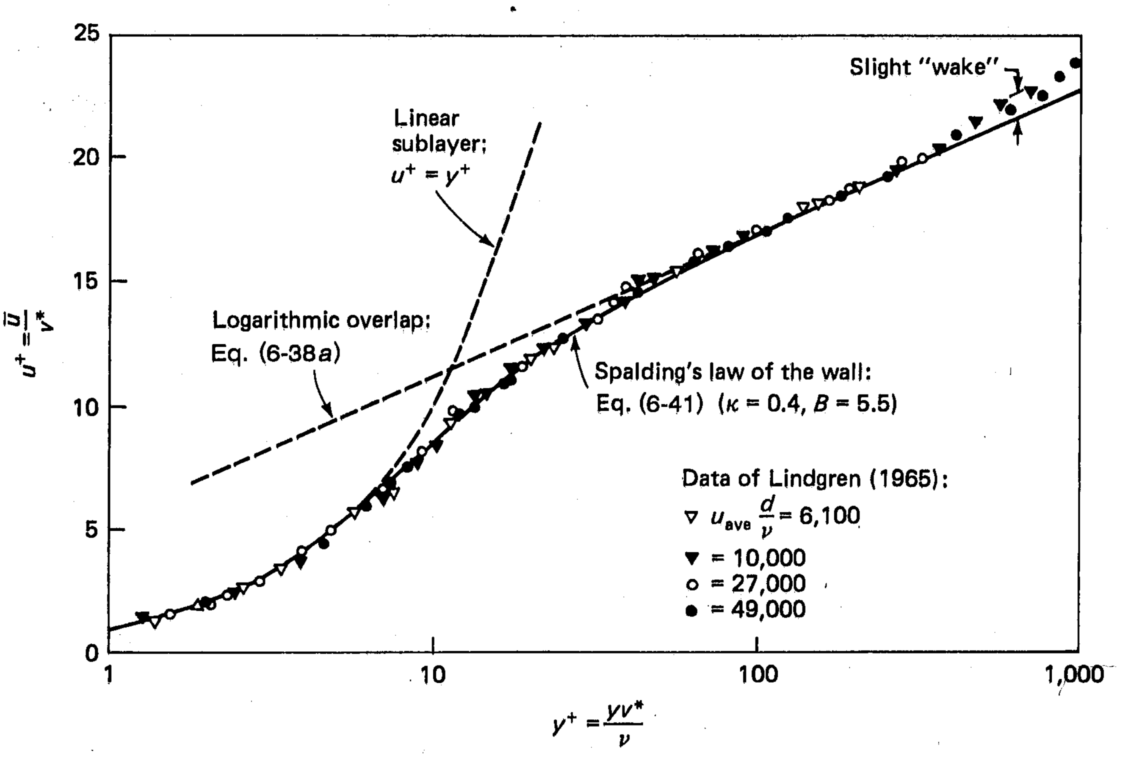

Figure 2.2 Velocity profile.

Hama

For a rough pipe, an overlap region can be found in the same manner as above. The defect law developed for the outer region is independent of roughness height, and since the reasoning behind the logarithmic law is based on the velocity gradient, von Karmans constant should be independent of the roughness height. Therefore, the roughness dependence is in the additive constant and the velocity profile in the overlap layer can be written as

$$u^+ = \frac{1}{\kappa} \ln y^+ + h(k^+) \qquad \textbf{Eq. 2.4}$$

which was reformulated by Hama (1954) by defining a roughness dependent velocity shift that applies to the smooth wall case:

$$u^+ = \frac{1}{\kappa} \ln y^+ + B - \Delta B \qquad \textbf{Eq. 2.5}$$

Hama (1954) also determined the ΔB for many different roughness types.

Friction factor

One of the key issues in a flow model is to find the wall shear stress, τ_w.

The friction factor (*f*) for a pipe, commonly denoted the Darcy friction factor, is defined as:

$$f = \frac{-\frac{dp}{dx}D}{\frac{1}{2}\rho U^2} \qquad \textbf{Eq. 2.6}$$

as opposed to the skin friction coefficient used in aerodynamics, which is defined as:

$$c_f = \frac{\tau_w}{\frac{1}{2}\rho U^2} \qquad \textbf{Eq. 2.7}$$

Many people make the quick combination $f = 4c_f$ without any further hesitation. This is however an approximation, which in most cases is reasonably satisfactory, but it neglects the fact that for a compressible fluid the pressure drop also accelerates the gas and not only balances the wall shear stress. This effect is discussed in Langelandsvik et al. (2008).

Prandtl proposed a friction factor relationship by integrating the logarithmic law across the cross section, which was based on the assumption that the law is valid for all Reynolds numbers. The constants in the law were slightly adjusted to fit the smooth pipe measurements of Nikuradse, and the resulting correlation became:

$$\frac{1}{\sqrt{f}} = -2\log\left(\frac{2.51}{\mathrm{Re}\sqrt{f}}\right) \qquad \textbf{Eq. 2.8}$$

In fully rough turbulent flow, Nikuradse found that the quadratic law of resistance, with the following formulation, fitted well:

$$f = \frac{1}{\left(1.74 + 2\log\frac{r}{k}\right)^2} \qquad \textbf{Eq. 2.9}$$

or equivalently:

$$\frac{1}{\sqrt{f}} = -2\log\left(\frac{k}{3.7D}\right) \qquad \textbf{Eq. 2.10}$$

Colebrook (1939) successfully combined the smooth region correlation and the rough region correlation and established a correlation that should be valid over the entire Reynolds number range, including the transition region. Since then this correlation has more or less been established as an industry standard and it is named the Colebrook-White correlation:

$$\frac{1}{\sqrt{f}} = -2\log\left(\frac{2.51}{\mathrm{Re}\sqrt{f}} + \frac{k}{3.7D}\right) \qquad \textbf{Eq. 2.11}$$

The correlation is plotted in a Moody-diagram in Figure 2.3 for a 1 m diameter pipeline and several sand grain roughness values.

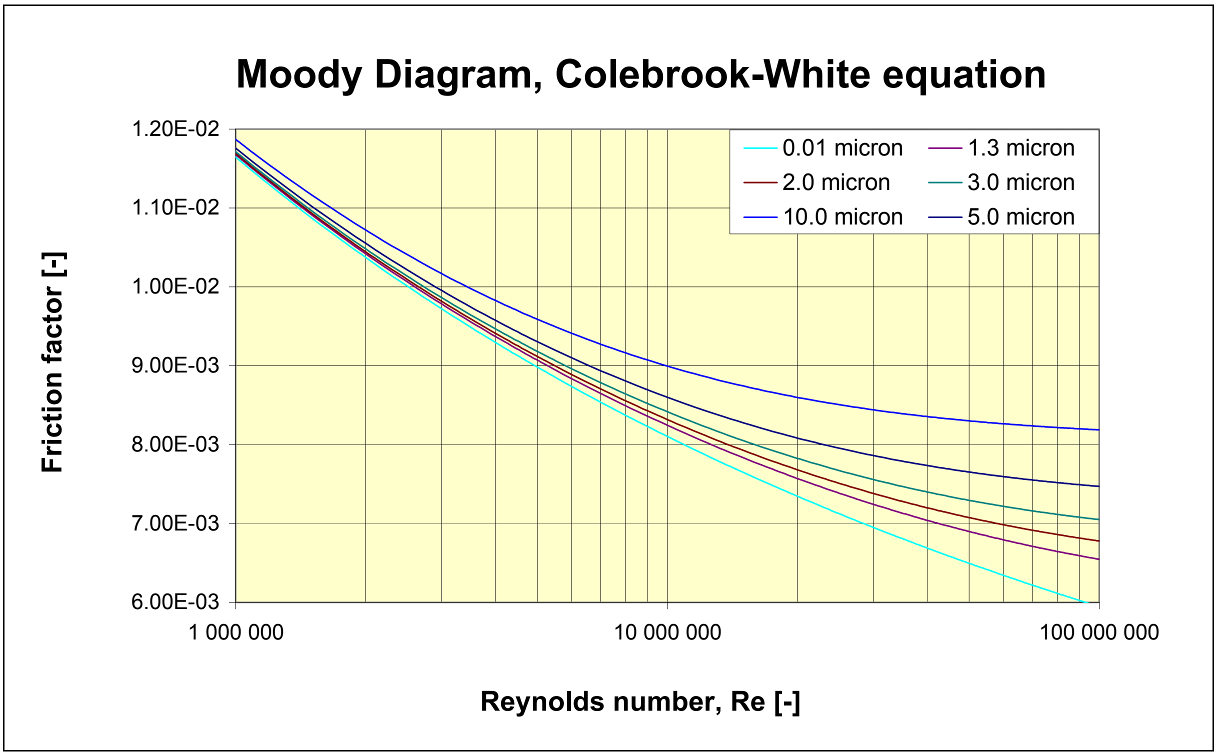

Figure 2.3 Colebrook-White equation plotted in a Moody diagram.

This formula did not reproduce the inflectional friction factor behavior that was found by Nikuradse. Instead Colebrook (1939) compares it with experimental results from commercial pipes, and concludes that pipelines with non-uniform roughness are better represented by this formula. Moody (1944) discusses the application of available friction factor data and the recent Colebrook-White formula having engineers designing pipes in mind. He plotted the Colebrook-White friction factor formula in a diagram, which today bears the name Moody-diagram.

Several aspects of the Colebrook-White formula have been subject to discussions among scientists and fluid engineers since the 1930s. The point of departure from the smooth roughness line, the transitional region behavior and the level of the fully rough line have all been discussed. No common understanding has been reached, which proves that pipeline surfaces are different, and one certainly needs more than Nikuradse's sand grain equivalent roughness, *k*, to describe the surface and the friction factor behavior satisfactorily.

The American Gas Association, AGA, presented two comprehensive reports analyzing the flow of natural gas in real pipelines in 1956, Smith et al. (1956), and in 1965, Uhl et al. (1965). One of their main conclusions was that friction factor shows a more abrupt transition from smooth to rough turbulent flow than the smooth and gentle transition predicted by Colebrook-White. They also found a higher friction factor for low Reynolds numbers than Prandtl's smooth line. This owes to extra pressure drop because of bends, curves, fittings etc.

Results from a joint research project involving four European natural gas transmission companies were presented in Gersten et al. (2000), and later also discussed in Piggott et al. (2002). The new proposed friction factor formula is partly based on the experimental results from AGA, and reads:

$$\frac{1}{\sqrt{f}} = -\frac{2}{n}\log\left[\left(\frac{1.499}{dr\,\mathrm{Re}\sqrt{f}}\right)^{0.942\cdot n\cdot dr} + \left(\frac{k}{3.7D}\right)^{n}\right] \qquad \textbf{Eq. 2.12}$$

where *dr* is the draught factor which accounts for additional pressure losses caused by secondary flows e.g. due to curvature. *n* is used to control the shape of the transition region. *n = 1* describes a transition similar to the gentle Colebrook-White transition, while *n = 10* implies a more abrupt transition, or a so-called point transition. The reader is not provided with any further advice about how the value of this parameter should be selected. For the fully rough regime, the formula coincides with Colebrook-White. In the smooth regime, provided *dr* equals 1.0, it coincides with the equation from Zagarola and Smits (1998), which is an updated version of Prandtl's smooth law.

The Superpipe experimental facility at Gas Dynamics Laboratory, Princeton University was built in 1994-1995 to facilitate further research on turbulent flow in pipes at high Reynolds numbers. Zagarola (1996) measured the pressure gradient and mean velocity profile in a presumable smooth pipe at Reynolds numbers ranging from 10^4 to 10^7. The results provided strong support for the existence of a logarithmic scaling region, given that the Karman number is large enough, and eventually he recommended a modified formula for the frictional resistance in smooth turbulent flow. The parameters in the Prandtl formula were adjusted slightly. In McKeon et al. (2005), the Superpipe measurements on the smooth pipe are repeated using a smaller pitot probe. Combined with the application of more accurate methods for correcting the pressure measurements this leads to a modified version of the friction formula in smooth pipes. Other constants in the log law formula were also recommended. The modified smooth friction factor correlation reads:

$$\frac{1}{\sqrt{f}} = 1.930\log\left(\mathrm{Re}_D\sqrt{f}\right) - 0.537 \qquad \textbf{Eq. 2.13}$$

This predicts a smooth pipe friction factor which is around 3% larger than the law of Prandtl for Reynolds numbers in the range $10\text{-}50\cdot 10^6$.

GERG's formula and McKeon's formula for smooth flow are compared with the traditional Colebrook-White curves in Figure 2.4 and Figure 2.5. Figure 2.4 plots the GERG friction factor with $k_S = 0.0$ μm, i.e. the GERG smooth friction factor. In this case both *n* and the draught factor, *dr*, move the friction factor curve upwards, causing larger friction, but do not change the shape of the curve. It is also seen that the GERG smooth curve, which should coincide with the curve proposed by Zagarola, but later modified by McKeon, gives a slightly larger friction factor than that of McKeon.

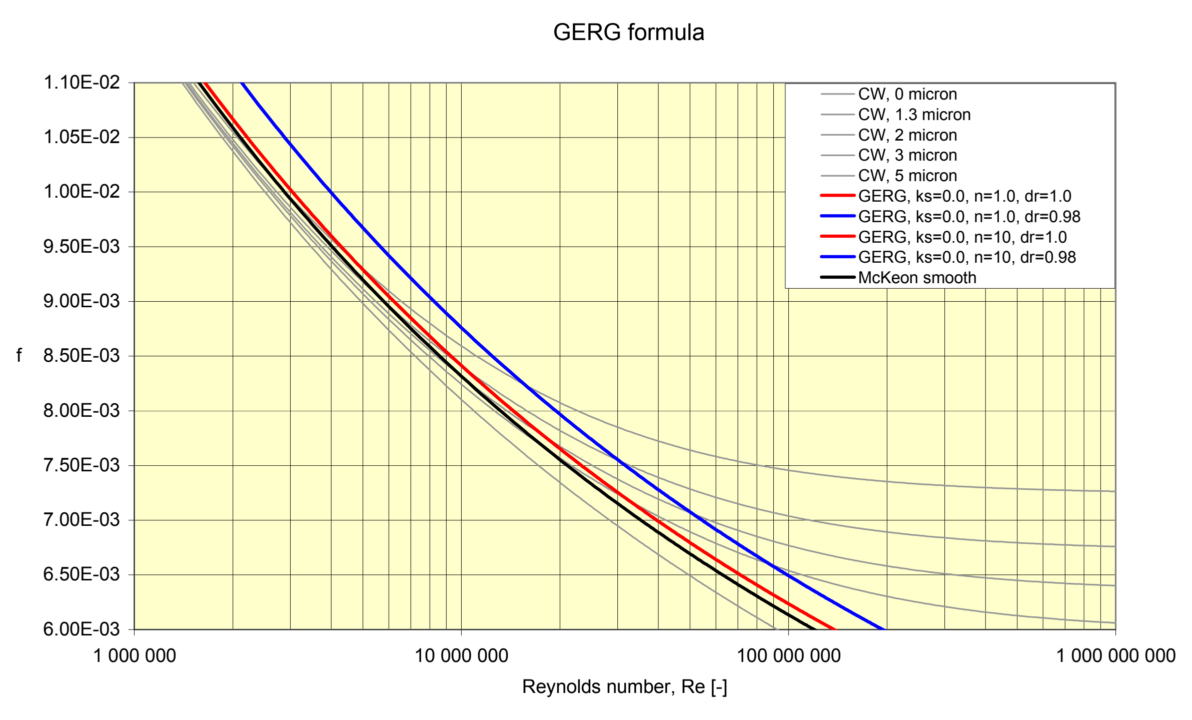

Figure 2.4 GERG's formula with k_s = 0.01 μm.

In Figure 2.5 the effect of *n* and *dr* is more evident, in that k_s = 5.0 μm is used. The *n* factor controls the abruptness, and the value 10 gives a very abrupt transition. The *dr* factor increases the friction, but the curves are shifted rightwards rather than upwards. The fully rough friction remains the same, but larger Reynolds number are required to reach its value.

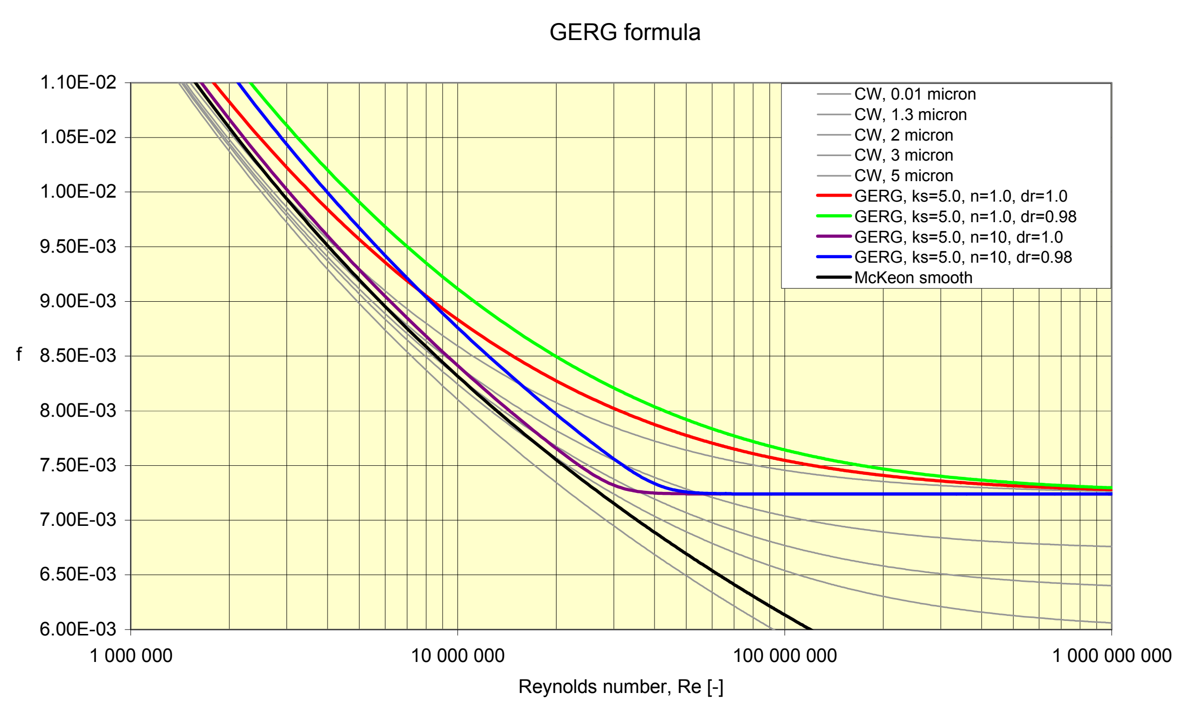

Figure 2.5 GERG's formula with k_s = 5.0 μm.

Experiments on a rough honed pipe with $k_{rms} = 2.5\ \mu m$ installed in Superpipe are reported in Shockling et al. (2006) and Shockling (2005). They found inflectional friction factor behavior, similar to Nikuradse (Figure 2.1) but not so pronounced. The data are plotted in Figure 2.6, and the contrast to the smooth transition predicted by Colebrook-White (Figure 2.3) is obvious.

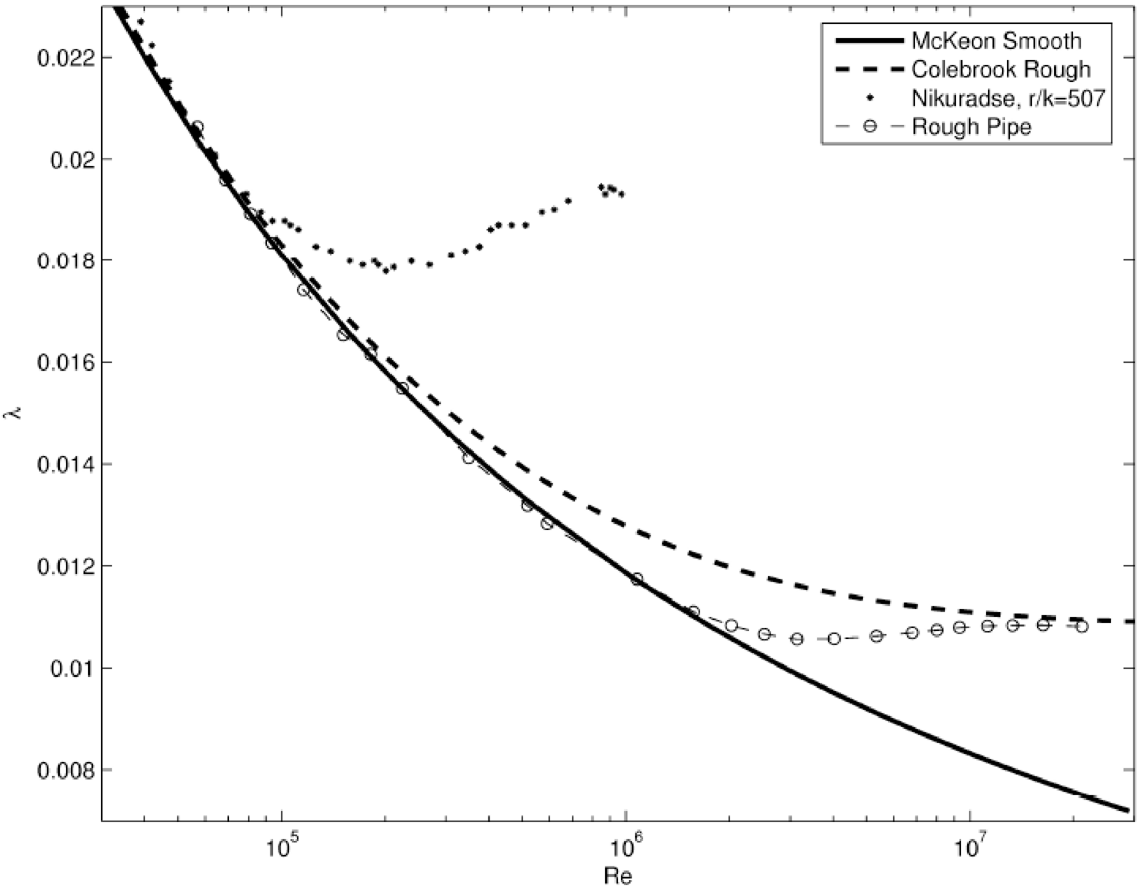

Figure 2.6 Friction factor in a honed aluminium pipe from Superpipe.

In the 1990s, Sletfjerding conducted pressure drop measurements of natural gas pipelines in a laboratory facility in Norway, see Sletfjerding (1999). A plain steel pipe and a coated steel pipe were used together with a number of pipes artificially roughened with glass beads glued to the surface as done by Nikuradse. The Reynolds number range covered was approximately $1\text{-}25\cdot10^6$, and the inner diameter of the pipe was 150 mm. It turned out that the Reynolds number range was too narrow to cover the complete transition from smooth to rough turbulent flow. For the coated pipe, which had the lowest roughness, smooth turbulent flow and the beginning of the transition region are covered. The transition resembles that described by Colebrook-White, i.e. not giving support to Nikuradse's inflectional behavior. The steel pipe has the second lowest roughness value, and data from the rough turbulent region are reported. As the Reynolds number decreases the curve does not follow Colebrook-White into the transition region. It seems to decrease slightly giving a weak support to an inflectional shape. The experiments do not reach Reynolds numbers low enough to describe the full transition region. The glass bead roughened pipes all show complete rough turbulent behavior under the test conditions, and are only used to analyze the relation between the physical roughness quantified in different ways and Nikuradses's sand grain equivalent roughness.

Roughness

As was pointed out in CHAPTER 1 one of the main unresolved issues in pipeline flow modeling is the link between the measured surface roughness, and the roughness factor used in the simulation models, the hydraulic roughness. As a step in an attempt to understand this relation, the roughness of coated pipelines has been measured by several parties.

Sletfjerding et al. (1998) and Sletfjerding (1999) reported flow tests on coated steel pipes. The pipes were honed steel pipes painted with a two-component epoxy coating. The reported root mean square roughness, R_q, was 1.32 μm for the coated surface and 3.65 μm for uncoated surface. R_z was 5.79 and 21.66 μm respectively and R_a was 1.02 and 2.36 μm.

Gersten & Papenfuss (1999) performed roughness measurements on samples both from an uncoated steel pipe and a coated steel pipe, both being real pipelines from Ruhrgas AG. Mean R_z for the uncoated pipeline was 64 μm while it was 24 μm for the coated pipeline. Mean R_a were 9.4 and 3.9 μm respectively. They did not report any figures for R_q.

Charron et al. (2005) report extensive roughness measurements on pipes. They use three different cut-off wavelengths, 0.8, 2.5 and 8.0 mm, to capture and identify both the short-wavelength roughness and the long-wavelength undulation. For the sand blasted steel pipe the measurements vary little with wavelength, and R_a is 1.2 μm and Rz is around 10 μm. With a solvent based coating applied as a thin film, R_a ranges from 2 to 5 μm and R_z from 13 to 30 μm. In general a longer wavelength gives larger roughness value, but the variation is large, indicating an irregular surface. With the coating applied as a thick film, the measured roughness decreases, yielding R_a from 1 to 3 μm and R_z in the range 5-15 μm. The root mean square roughnesses are not reported.

2.2 Pipeline simulators, TGNet as an example

In the analysis of the operational data from the pipeline system in the North Sea, the commercial one-dimensional pipeline simulator Transient Gas Network (TGNet) has been used. This section gives a description of the physics and numerics in this simulator. There is a range of pipeline simulators available from different vendors. Those suitable for simulating long transport pipelines are one-dimensional and do not differ very much from TGNet. Therefore this description may also serve as a generic introduction to gas pipeline simulators. Unless other reference is given, the information about the simulation tool Transient Gas Network has been collected from Pipeline Studio User's Guide (1999).

Furthermore, details about the transformation from three dimensional Navier Stokes equations to one-dimensional flow equations are given. Some of the most common derivations involve small approximations which will be pinpointed, and also quantified as far as possible. References to literature where the empirical correlations are obtained are also given.

The first section lists the basic equations. Reference is also made to Appendix A, where details about the derivation are discussed. The second section deals with how the heat transfer between the gas and the surroundings is modeled. Then a number of different auxiliary correlations and formulas such as viscosity correlation and friction factor are collected in a separate section. The fourth section describes how the set of equations are solved in a numerical scheme. The fifth section discusses some of the limitations and inaccuracies in this kind of models. It is particularly focused on the transformations of the equation set from 3D to 1D, and the heat transfer calculations.

2.2.1 Basic equations

The basic equations are derived from the three fundamental parts constituting the Navier Stokes equations, namely the mass balance, the momentum balance and the energy balance. The full set of Navier Stokes covers the three-dimensional situation. In making efficient pipeline simulators, it is very common to assume one-dimensional flow. The equations are hence integrated across the cross section. A full three-dimensional calculation is very computational intensive, and requires either empirical turbulence models or a Direct Numerical Simulation (DNS) approach. Either way the Reynolds number range is limited, particularly with DNS.

Mass balance

$$\frac{\partial \rho}{\partial t} + \frac{\partial}{\partial x}(\rho U) = 0 \qquad \textbf{Eq. 2.14}$$

Momentum balance

$$\rho \frac{\partial U}{\partial t} + \rho U \frac{\partial U}{\partial x} = -\frac{\partial p}{\partial x} + \rho g \sin \alpha - \frac{1}{2}\rho U^2 \frac{f}{D} \qquad \textbf{Eq. 2.15}$$

where f is the Darcy-Weissbach friction factor.

$$f = \frac{-\,{}^{dp}\!/_{dx}}{\frac{1}{2}\rho U^2} D \approx \frac{4\tau_W}{\frac{1}{2}\rho U^2} \qquad \textbf{Eq. 2.16}$$

Energy balance

$$\rho c_v \left(\frac{\partial T}{\partial t} + U \frac{\partial T}{\partial x} \right) = -T \left\{ \frac{\partial p}{\partial T} \right\}_\rho \frac{\partial U}{\partial x} + \rho \frac{f}{2D} U^3 - \frac{4U_{W,tot}}{D}\left(T_{gas} - T_{env}\right) \qquad \textbf{Eq. 2.17}$$

where $U_{W,tot}$ is the total heat transfer coefficient from the surroundings to the gas, and defined as:

$$U_{W,tot} = \frac{Q_{tot}}{\left(T_{gas} - T_{env}\right)A} \qquad \textbf{Eq. 2.18}$$

The first term on the right hand side includes the Joule Thompson effect. The second term is the dissipation term, which covers the breakdown of mechanical energy to thermal energy due to viscous forces in the fluid. The final term describes the heat transfer due to temperature differences between the gas and the medium surrounding the pipe.

2.2.2 Heat transfer

The heat transfer from the surroundings to the gas is calculated as a combination of three different steps:

- Heat transfer between the surroundings and the outer pipe wall using a film coefficient.
- Heat conduction through the pipe wall consisting of different wall layers using the thermal properties of the pipe walls.
- Heat transfer between the inner pipe wall and the fluid using a standard heat transfer correlation.

Outer film coefficient

The definition of the outer film coefficient depends on whether the pipeline is exposed to water or if it is buried in soil. If it is buried, two different correlations may be used depending on the burial depth.

Shallow burial

The outer heat transfer film coefficient, h_o [W/(m^{2}K)], for shallow burial is given by:

$$h_o = \frac{2k_s / d_o}{\ln\left(x + \sqrt{x^2 - 1}\right)} \qquad \textbf{Eq. 2.19}$$

D_c	Depth to pipe centerline	[meters]
d_o	Outside pipe diameter	[meters]
x	$2D_c/d_o$	[-]
k_s	Surroundings/soil thermal conductivity	[W/(mK)]

Deep burial

The outer heat transfer film coefficient, h_o [W/(m^{2}K)], for deep burial is given by:

$$h_o = \frac{2k_s / d_o}{\ln\left(4D_c / d_o\right)} \qquad \textbf{Eq. 2.20}$$

The TGNet user manual recommends the deep burial correlation be used for pipes buried to a depth of greater than or equal to twice the outside diameter of the pipeline.

The deep burial is a slight simplification of the shallow burial correlation as the -1 under the square root has been omitted. Consequently the shallow burial correlation converges to the deep burial correlation as the depth increases.

The formulas used by TGNet are the same as one obtains by using the conduction shape factor for a buried cylinder recommended in Incropera & DeWitt (1990). Incropera & DeWitt recommends the "deep" variant be used for depths greater than 1.5 times the pipe diameter.

Exposed to water

For a pipeline exposed to water, TGNet uses a correlation which gives the Nusselt-number as a function of the Reynolds number and the Prandtl number. The outer film coefficient, h_s [$W/(m^2K)$], may be obtained by a straightforward manipulation of the Nusselt number.

$$Nu = 0.26 \cdot \mathrm{Re}^{0.6} \cdot \mathrm{Pr}^{0.3} \qquad (\mathrm{Re} > 200) \qquad \textbf{Eq. 2.21}$$

Nu	Nusselt number ($h_s d_o/k_s$)	
Re	Reynolds number ($\rho_s u_s d_o/\mu_s$)	
Pr	Prandtl number ($Cp_s\mu/_s k_s$)	
k_s	Surrounding/sea-water thermal conductivity	[W/(mK)]
ρ_s	Surroundings/sea-water density	[kg/m^3]
u_s	Surroundings/sea-water velocity	[m/s]
μ_s	Surroundings/sea-water viscosity	[kg/ms]
Cp_s	Surroundings/sea-water heat capacity	[J/kgK]

This formula is almost the same as proposed by Zukauskas and Ziugzda (1985).

Inner film coefficient

As for the outer film coefficient with the pipe exposed to water, the inner film coefficient is obtained via the Nusselt-number:

$$Nu = 0.023 \cdot \mathrm{Re}^{0.8} \cdot \mathrm{Pr}^{0.4} \qquad (\text{turbulent flow}) \qquad \textbf{Eq. 2.22}$$

The given constants in the formula are default values. The user may change the multiplicative constant, the Reynolds number exponent and the Prandtl number exponent. Furthermore the user may also specify an additive constant.

The formula is the same as referred to by Mills (1995) for Re larger than $10 \cdot 10^3$.

Wall layers

The resistance of the wall is determined from the standard equation for heat conduction through a multi-layer cylinder.

$$h_w = \sum_{i=1}^{n} \frac{\ln\left(r_{oi} / r_{ii} \right)}{k_i} \qquad \textbf{Eq. 2.23}$$

where

h_w	Overall wall resistance	[$(W/m^2K/m)^{-1}$]
n	Number of wall layers	[-]
k_i	Thermal conductivity of the i'th wall layer	[$W/m^2K/m$]
r_{oi}	Outer radius of the i'th wall layer	[meters]

r_{ii}	Inner radius of the i'th wall layer	[meters]

Overall heat transfer

The overall heat transfer coefficient, U, is then calculated from the standard relationship

$$\frac{1}{U} = \frac{1}{h_i} + r_i \cdot h_w + \frac{r_i}{r_o \cdot h_o} \qquad \textbf{Eq. 2.24}$$

where

U	Overall heat transfer coefficient	$[\mathrm{W/m^2K}]$
h_i	Inner wall film transfer coefficient	$[\mathrm{W/m^2K}]$
h_w	Thermal resistance of the pipe wall	$[(\mathrm{W/m^2K/m})^{-1}]$
h_o	Outer wall film transfer coefficient	$[\mathrm{W/m^2K}]$
r	Inner radius of the pipe	[meters]
r_o	Outer radius of the pipe	[meters]

2.2.3 Additional

Friction factor correlation

TGNet uses the well-known Colebrook-White formula which reads

$$\frac{1}{\sqrt{f}} = -2\log\left(\frac{2.51}{\mathrm{Re}\sqrt{f}} + \frac{k}{3.71D}\right) \cdot EFF \qquad \textbf{Eq. 2.25}$$

The vendor of TGNet has included an additional efficiency factor, named *EFF*, which is meant to compensate for additional drag effects. The friction factor decreases if *EFF* is increased.

Heat capacity

According to the user manual for TGNet, the following correlation for isobaric heat capacity has been derived using data from Katz et al. (1959).

$$c_p = 1.432 \cdot 10^4 - 1.045 \cdot 10^4 \cdot SG + 3.255 \cdot T + 10.01 \cdot SG \cdot T + EXP \qquad \textbf{Eq. 2.26}$$

with:

$$EXT = \frac{15.69 \cdot 10^{-2} \cdot p^{1.106} \cdot e^{-6.203 \cdot T \cdot 10^{-3}}}{SG} \qquad \textbf{Eq. 2.27}$$

The correlation is claimed to be valid for natural gases with properties in the following ranges:
Specific gravity (SG):0.55-0.80
Temperature: 255-340 K
Pressure: 0-100 barg

The GPSA (2004) empirical correlation for the ratio of specific heats is used:

$$\frac{c_v}{c_p} = 1.0836 - 0.000115T + {(5.61 - 0.002T)}/{M}$$ **Eq. 2.28**

which is valid over the following ranges:

Temperature:	283-394 K
Molecular Weight (*M*):	15.0-100

The following definitions apply:

$$c_p = \left(\frac{\partial h}{\partial T}\right)_p$$ **Eq. 2.29**

$$c_v = \left(\frac{\partial e}{\partial T}\right)_V$$ **Eq. 2.30**

Equation of state

The equation of state bearing the names of Beneditct, Webb, Rubin and Starling, BWRS, from Starling (1973) is used by TGNet. This has the following form:

$$P = \rho RT + \left(B_0 RT - A_0 - \frac{C_0}{T^2} + \frac{D_0}{T^3} - \frac{E_0}{T^4}\right)\rho^2 + \left(bRT - a - \frac{d}{T}\right)\rho^3 + \alpha\left(a + \frac{d}{T}\right)\rho^6 + \frac{c\rho^3}{T^2}\left(1 + \gamma\rho^2\right)e^{-\gamma\rho^2}$$

Eq. 2.31

Starling (1973) gives the parameter values for different pure components together with mixing rules. TGNet uses a parameter set that is specifically tuned to match the North Sea natural gas properties.

Viscosity

TGNet uses the Lee-Gonzales-Eakin correlation, see Lee et al. (1966), which has the following form:

$$\mu = Ke^{\left(X\rho^y\right)}$$ **Eq. 2.32**

where:

$$K = \frac{(7.77 + 0.0063M)T^{1.5}}{122.4 + 12.9M + T}$$ **Eq. 2.33**

$$X = 2.57 + \frac{1914.5}{T} + 0.0095M$$ **Eq. 2.34**

$$Y = 1.11 + 0.04X$$ **Eq. 2.35**

M is molar mass
T is gas temperature
ρ is density

With this set of coefficients, the correlation is named LGE-1 in the next chapters.

2.2.4 Calculation/Numerics

Introduction

It is seen that the equations that describe one-dimensional flow in pipelines consist of three balances, the mass balance, the momentum balance and the energy balance. The resulting set of equations is a set of partial differential equations, with two independent variables, x and t. The equations have three dependent variables, which may vary a little due to certain preferences, but as stated here the dependent variables are density, mass flux and energy.

Partial differential equations (PDEs) are usually grouped into elliptic, hyperbolic and parabolic equations. The names are adopted from the description of ordinary second degree equations, due to the similarity in the calculation of one parameter. However, this classification also makes sense when one looks at the physical problems the different equations describe, and how their solutions may be obtained. The following information is collected from Borse (1997) and Kristoffersen (2005).

A. *Elliptic:* Poissons's equation is a typical textbook example. The solution at a certain point in time and space depends on and influences the solutions at every other point at the same time. Hence, it is necessary to use iterative techniques to solve these equations.
B. *Parabolic:* The diffusion or heat flow equation is a classical example and illustrates the point that the solution can be stepped forward in time. To solve for a certain x and t, one needs information at all x-values for the previous time step, t-1.
C. *Hyperbolic:* The wave equation illustrates the properties of hyperbolic PDEs. The information travels along characteristic lines in the space of solution, for example in the x-t space for the gas flow equations. Like the parabolic equations, the equations can be solved by stepping forward in time.

Calculation method

TGNet solves the set of partial differential equations by first discretizing the mass and momentum balance equations following a well-known box scheme (see for example Keller (1974)), and then solving the resulting difference equations. This scheme is employed for the one-dimensional gas flow equations by Luskin (1979), and a brief outline is given below. The unknowns in this outline are density and mass flux, whereas in TGNet it is rewritten to be solved for pressure and mass flux.

The entire pipeline consists of pipes as defined by the user. TGNet divides each pipe into segments of equal lengths. The segment endpoints are termed knots, and the number of knots is specified by the user.

The mass balance and momentum balance equations may be written on the following form for one single pipe segment:

$$\frac{\partial u}{\partial t} + A(x,u)\frac{\partial u}{\partial x} = F(x,t,u) \qquad \textbf{Eq. 2.36}$$

where

$$u = [\rho, m]^T$$

$$A(x,u) = L^{-1}\begin{bmatrix} 0 & 1 \\ \gamma^2 - v^2 & 2v \end{bmatrix}$$

$$F(x,t,\rho,m) = \left[0, \frac{-fm|m|}{2d\rho} - L^{-1}\rho g \sin\alpha\right]^T$$

v	is bulk gas velocity
m	is mass flux
γ	is speed of sound

The eigenvalues of *A* are bounded away from zero provided the gas velocity is lower than the speed of sound and therefore the local Jacobian is invertible. Furthermore, *A* has one negative and one positive eigenvalue. Hence, one needs to specify one boundary condition at each end. Often the mass flux at both ends is supplied.

The formulation can easily be augmented to include an arbitrary number of discrete pipe segments by redefining both *u, A* and *F* to include the same parameters for all the different pipe segments.

To avoid having to solve nonlinear algebraic problems, *A* and *F* are linearized about the solution at the *j*th time level when solving for the solution at the (*j+1*)th time level. When *A* and *F* in Eq. 2.36 are linearized around the solution for the previous time step, it takes the following form:

$$\frac{\partial U}{\partial t} + A(\check{U})\frac{\partial U}{\partial x} + \left[D_u A(\check{U}); \frac{\partial \check{U}}{\partial x}\right](U - \check{U}) = F(\check{U}) + D_u F(\check{U})(U - \check{U}) \qquad \textbf{Eq. 2.37}$$

where

$\check{U}$ is $U\left(x, t - \frac{\Delta t}{2}\right)$

The bracketed term in Eq. 2.37 defines an $n \times n$ matrix where the *(i,j)*th element is determined according to the following notation:

$$[D_u A(x,v); z]_{i,j} = \sum_{l=1}^{n} D_{j+1} A_{i,l}(x,v) z_l$$

D_u is a partial differential operator which differentiates with respect to the subscripted variable index.

The different terms in Eq. 2.37 may be described and/or interpreted as:

1. The time derivative of *U* at current time step.
2. The *A*-matrix at previous time step multiplied by the space derivative of *U* at current time step.
3. The derivative of the product of *A* and $\frac{\partial U}{\partial x}$ with respect to *U* at previous time step. This derivative is multiplied to the difference in *U* from previous to current time step.
4. *F* evaluated at previous time step.
5. The derivative of *F* with respect to *U* multiplied by the difference in *U* from previous to current time step.

Eq. 2.37 is evaluated at $(x_{i+1/2}, t_{j+1/2})$. At this point the expressions involving $\overset{\vee}{U}$ but not *U* are known. A complete set of difference equations are obtained if one inserts the following for *U* and its derivatives in *x* and *t*:

$$U(x_{i+1/2}, t_j) = \frac{1}{2}\left(U(x_{i+1}, t_j) + U(x_i, t_j)\right) \qquad \textbf{Eq. 2.38}$$

$$U(x_i, t_{j+1/2}) = \frac{1}{2}\left(U(x_i, t_{j+1}) + U(x_i, t_j)\right) \qquad \textbf{Eq. 2.39}$$

$$\frac{\partial U}{\partial t}(x_{i+1/2}, t_{j+1/2}) = \frac{1}{\Delta t}\left(U(x_{i+1/2}, t_{j+1}) - U(x_{i+1/2}, t_j)\right) \qquad \textbf{Eq. 2.40}$$

$$\frac{\partial U}{\partial x}(x_{i+1/2}, t_{j+1/2}) = \frac{1}{h}\left(U(x_{i+1}, t_{j+1/2}) - U(x_i, t_{j+1/2})\right) \qquad \textbf{Eq. 2.41}$$

$$\frac{\partial U}{\partial x}(x_{i+1}, t_j) = \frac{1}{h}\left(U(x_{i+1}, t_j) - U(x_i, t_j)\right) \qquad \textbf{Eq. 2.42}$$

For one computational box, the unknowns turn out to be (x_i, t_{j+1}) and (x_{i+1}, t_{j+1}) and they depend on the quantities (x_i, t_j) and (x_{i+1}, t_j) which are known from the previous time step. However, the solution of (x_i, t_{j+1}) also depends on the solution of (x_{i+1}, t_{j+1}) and vice versa. Hence the equations describing the solution at the different points along the pipe at time *t* are implicit, and have to be solved simultaneously. The numerical stencil is shown below.

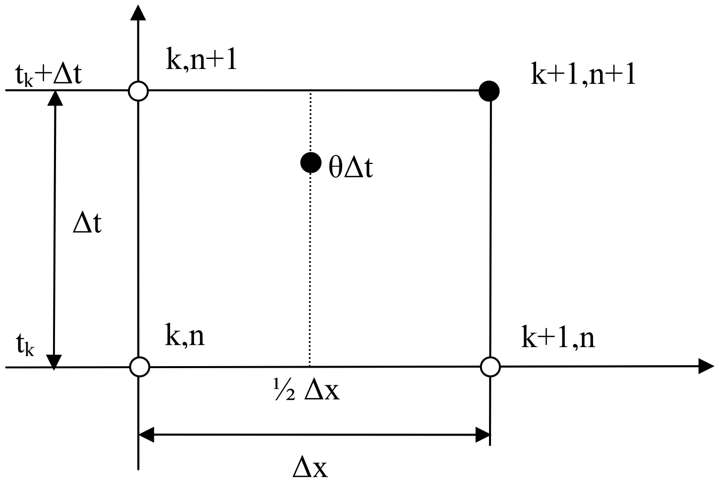

Figure 2.7 Numerical stencil in the box scheme.

The solution of this linearized set of equations yields the flows and pressures. At a given time step these hydraulic equations are solved first, using the temperatures from the previous time step. Then the energy balance equation is solved for the temperature with the updated densities and pressures. Since the temperature response is significantly slower than the hydraulic response, this is considered sufficient. Solving all three balance equations simultaneously would add significant complexity to the solution methodology, and possibly also the CPU-time needed on a computer. However, there is no theoretical evidence beyond this experience to support that this works satisfactorily (Holden (2005)).

The resulting equations are second order correct in space and first order correct in time.

Further details of the calculation scheme are given in Luskin (1979).

The calculation scheme employed by TGNet in a steady-state simulation is outlined as follows:

1. Guesses the starting conditions along the pipeline; density, mass flux, temperature and composition (if specified).
2. Sets up the set of equations for the pipes: This means populating the difference equations obtained from Eq. 2.37.
3. Sets up the equations for the equipments (valves, compressors, heaters etc.).
4. Sets up the equations for the nodes, i.e. the connection points between the pipes. This provides the boundary conditions for the solution of a pipe.
5. Solves the equations for pressure and mass flow.
6. Calculates the size of the next time step to be taken. Uses the CFL-condition.
7. Updates the density and gas velocity along the pipe. Uses the calculated pressure and mass flux for this time step and the specified equation of state.
8. Updates the friction factors.
9. Calculates the flow imbalance for each pipe. The steady-state is assumed to be found when this error is below a user specified convergence criterion.
10. Calculates the temperature profile for the current conditions.
11. Loop back to entry 2 until steady-state conditions are reached.

2.2.5 Discussion of limitations and inaccuracies

This section aims to give a list of weaknesses and inaccuracies in the one-dimensional set of equations used by TGNet. Some of the known limitations listed in the TGNet manual are given in the first subsection. Inaccuracies that originate in the transformation to one dimensional form are focused on in the next subsection. The inner and outer film coefficients are discussed in the subsequent sections.

Pipe expansion and heat conduction

Pipe expansion due to temperature and pressure are not modeled. The nominal pipe diameter supplied by the user is used irrespective of pressure and temperature. It is obvious that the pipe will expand as the pressure and/or temperature increases. This effect will be investigated in the sensitivity analysis in CHAPTER 3.

Heat conduction in the pipe wall along the flow direction is neglected. Large temperature variations along the pipe would cause heat conduction in the longitudinal direction, but this is not accounted for. Usually the longitudinal temperature gradient is very small, and hence only a small error is introduced by this simplification.

Transformation from 3D to 1D

The Navier Stokes equations are a three-dimensional set of equations. In order to get a set of equations that is manageable for simulation software, most simulators, including TGNet, uses a one-dimensional version that is obtained by averaging across the cross section. This averaging process is described in more detail in Appendix A. Some small approximations which are made are also discussed and quantified. The approximations mainly originate from the fact that the velocity profile is not flat. This requires a profile factor to be applied together with a number of the terms in Eq. 2.14 - Eq. 2.17. The profile factor approaches unity as the velocity profile gets flatter, which it inevitably does with increasing Reynolds numbers.

Heat transfer – inner film coefficient

The three-dimensional temperature profile is usually non-uniform in a cross section. In the immediate vicinity of the wall, the fluid elements need to be in thermal equilibrium with the wall. Hence the temperature of these fluid elements is equal to the inner wall temperature. Depending on whether heat flows from the gas to the wall or the other way, this temperature is higher/lower than the bulk temperature. The turbulent term in Eq. A-18 will also vanish close to the wall, due to the suppression of turbulent fluctuations. The heat transferred to or from the wall is only by conduction in the viscous sublayer.

The bulk temperature will differ from the real gas temperature close to the wall, and therefore a one-dimensional simulator like TGNet must allow a temperature jump between the gas and the wall surface. Many different correlations giving this temperature jump have been presented, and they are based on curve fitting of experimental results. Dimensional analysis has shown that the Nusselt number, the Reynolds number and the Prandtl number have to be involved. The constants used by TGNet (Eq. 2.22) are the same as in the Dittus-Boelter equation, whose origination was thoroughly discussed in Winterton (1998). The equation reads:

$$Nu = 0.023 \cdot \mathrm{Re}^{0.8}\,\mathrm{Pr}^{n} \qquad \textbf{Eq. 2.43}$$

where n = 0.4 is recommended in cases where heat is flowing from the pipe wall to the gas, and n = 0.3 is recommended for heat flow in the opposite direction.

According to Mills (1995) and Incropera et al. (1990), the formulas have been confirmed experimentally for the following conditions:

$$0.7 \le \mathrm{Pr} \le 160 \qquad \textbf{Eq. 2.44}$$

$$\mathrm{Re} \ge 10{,}000 \qquad \textbf{Eq. 2.45}$$

These equations may be used for small to moderate temperature differences between the gas and the wall.

Gnielinski (1976) developed another correlation for the Nusselt number, based on available experimental data, and this is more elaborate:

$$Nu = \frac{\frac{f}{8}(\mathrm{Re}-1000)\,\mathrm{Pr}}{1+12.7\sqrt{f/8}\left(\mathrm{Pr}^{2/3}-1\right)}\left(1+\left(\frac{D}{L}\right)^{2/3}\right)\left(\frac{\mathrm{Pr}}{\mathrm{Pr}_W}\right)^{0.11} \qquad \textbf{Eq. 2.46}$$

where the pipe length, L, has been introduced in addition to the Prandtl number using the wall temperature, Pr_W. It was proved to be a better approximation of experimental data than Eq. 2.43, but restricted to Reynolds numbers below 10^6.

It is seen that the formula used by TGNet is the Dittus-Boelter equation for gas heating. Heating of the gas from the surroundings will also be the case along most of the length of a pipeline, as the temperature falls below the ambient temperature due to the Joule Thompson effect. Depending on the inlet temperature of the gas, there will be a short section at the beginning where heat is flowing from the gas to the pipe wall.

Heat transfer – outer film coefficient

A pipeline may be either entirely buried in soil, exposed to water or eventually a combination of these two cases, i.e. partially buried and partially exposed to water. The determination of the outer film coefficient strongly depends on the situation present. In the buried part of the pipeline the heat transfer between the pipeline and the surroundings is by means of conduction. However, where the pipe is exposed to water, heat transfer by means of convection is the dominating phenomena.

Simulations in TGNet

As was described in Section 2.2.2 TGNets calculation of the outer film coefficient depends on whether the pipeline is buried or exposed to water. The exact calculation for the different situations was investigated by means of some simulations. A pipeline model with the following main features was built:

Inner diameter: 1.00 m
Wall thickness: 0.001 m
Ambient temperature: 5.0 degC
Flow rate: 52-53 MSm^3/d (the pressure drop was kept constant)
Ground conductivity: 2.0 W/(mK)
Sea-water velocity: 0.1 m/s

The wall thickness was chosen to be very low with a very high thermal conductivity to ensure minimal temperature gradient across the wall, even though this does not affect the calculation of the outer film coefficient. Hence, the contributors to the total heat transfer coefficient in Eq. 2.24 are the inner and outer film coefficients only. The temperature of the gas and the wall together with the total and outer heat transfer coefficient in the table below are obtained from the simulator.

Table 2.1 Calculation of U_{outer} in TGNet.

Burial Depth [m]	T_{gas} [degC]	T_{wall} [degC]	T_{amb} [degC]	U_{total} [W/(m^{2}K)]	U_{outer} [W/(m^{2}K)]
3.5	-2.76	-2.74	5.0	1.52	1.52
3.0	-2.63	-2.62	5.0	1.61	1.61
2.5	-2.46	-2.44	5.0	1.74	1.74
2.0	-2.18	-2.16	5.0	1.94	1.94
1.5	-1.54	-1.52	5.0	2.27	2.27
1.0	-0.6	-0.59	5.0	3.03	3.03
0.75	0.41	0.43	5.0	4.14	4.15
0.501	4.61	4.63	5.0	59.35	63.17
Exposed to water	4.71	4.73	5.0	79.05	85.05

Using the correlation for buried pipe, the calculation in TGNet fails for burial depth ≤ D/2. This means that one has to use the correlation for pipeline exposed to water for situations where parts of the cross section are exposed to sea-water, which also has been done in these simulations. For depths > D/2, the correlation in Eq. 2.19 was used. Using the exposed correlation is also possible for these cases, but it does not make any sense.

In Figure 2.8, the outer film coefficient calculated by TGNet is plotted against burial depth. It is seen that the coefficient is quite stable for burial depths > D, but that the increase is steep as the burial depth decreases to D/2. For burial depths less than D/2, which means that a part of the cross section is exposed to water, the calculated coefficient remains the same independent of the depth.

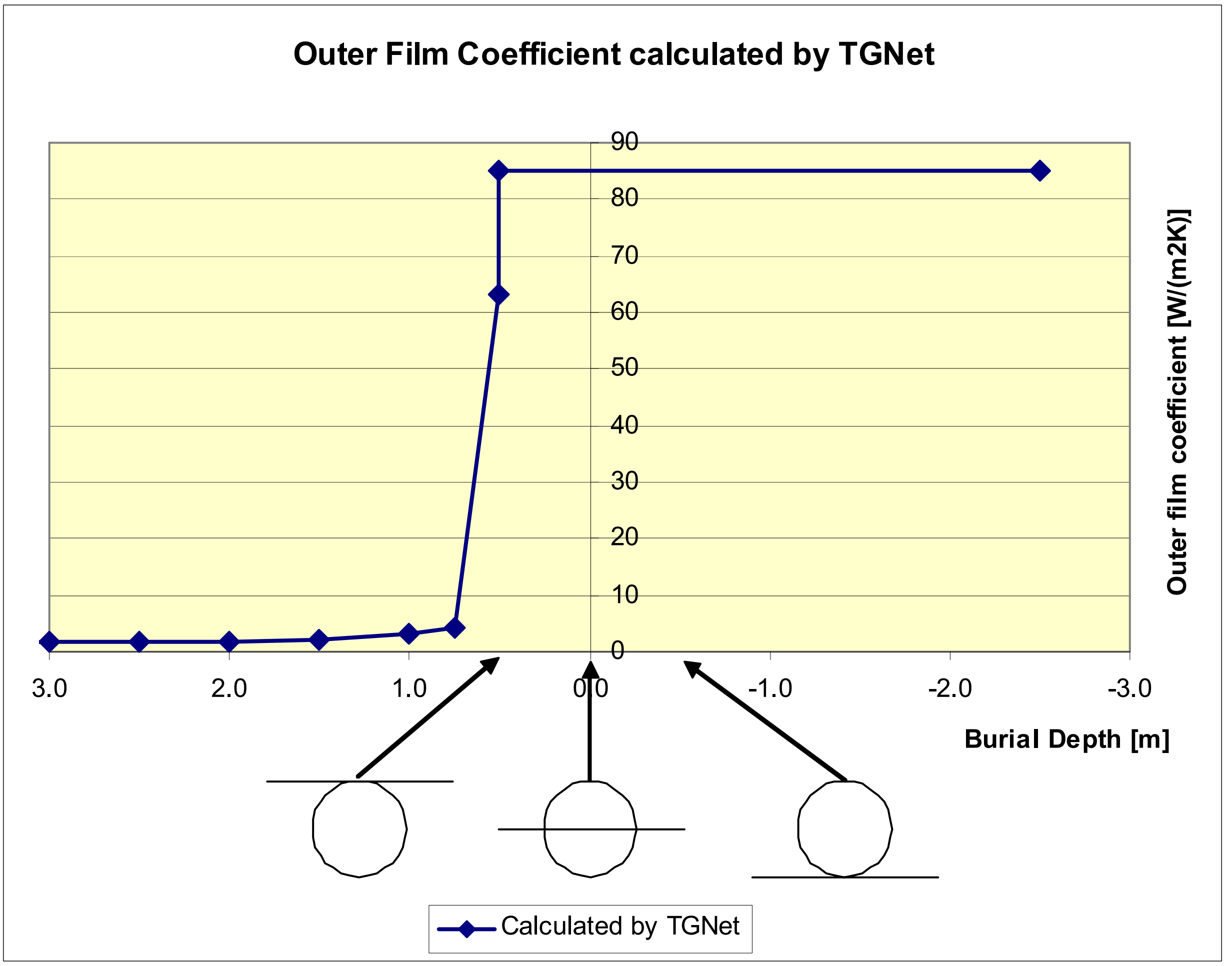

Figure 2.8 Outer film coefficient calculated by TGNet.

Buried pipeline

The outer film coefficient used by TGNet for a buried pipeline is the same as proposed in Incropera & DeWitt (1990) and also recommended by Gersten et al. (2001) (Eq. 2.19). Gersten recommends restricting the use of the formula to burial depths of H ≥ 0.75 D, which means a soil layer of 0.25 D covering the top of the pipeline.

The calculations are based on steady-state conditions. Normally there are seasonal variations that determine the water temperature at the sea bed. In the southern part of the North Sea and close to continental Europe, the temperatures will typically vary from 5 degC in winter time to 15 degC in summer time. More frequent changes for instance due to weather variations are of course superimposed to this mean. Depending on the burial depth, it is obvious that it takes some time for this temperature change to propagate down to the pipe. If one assumes that the temperature variation at the sea bed can be described by a sinusoidal function, the soil temperature at an arbitrary depth will also take a sinusoidal form. Hillel (1982) presented the following formula:

$$T(z,t) = T_a + A_0 e^{-z/d} \sin\left[\frac{2\pi(t-t_0)}{365} - \frac{z}{d} - \frac{\pi}{2}\right] \qquad \textbf{Eq. 2.47}$$

where T_a is the average soil temperature, A_0 is the annual amplitude of the surface soil temperature, t_0 is the time lag from an arbitrary starting date and d is the damping depth, defined as $d = (2D_h / \omega)^{1/2}$ with D_h as the thermal diffusivity.

Assuming a burial depth of 1.5 meters and a thermal diffusivity of $5 \cdot 10^{-7}$ m²/s, there will be a phase shift of 39 days, and the amplitude will also be decreased by 50%. TGNet does not take this time variant behavior into account, but is based on steady-state calculations.

Exposed and partially exposed pipeline

Heat transfer by means of convection may be split into forced convection and natural convection. Forced convection is due to imposed sea current and natural convection happens when the heated/cooled water close to the pipeline is exchanged by fresh water due to buoyancy effects.

Churchill and Chu (1975) correlated the average Nusselt number for natural convection as

$$Nu_n = 0.36 + \frac{0.518 Ra^{0.25}}{\left[1 + (0.559/\mathrm{Pr})^{9/16}\right]^{4/9}} \qquad 10^{-6} < Ra < 10^{9} \qquad \textbf{Eq. 2.48}$$

where Ra is the Rayleigh number, defined as:

$$Ra = \mathrm{Pr} \cdot Gr \qquad \textbf{Eq. 2.49}$$

and Gr is the Grashof number:

$$Gr = \frac{\beta \Delta T g D^3}{\nu} \qquad \textbf{Eq. 2.50}$$

β is the coefficient of thermal expansion for water and ν is the kinematic viscosity of water.

For forced convection, the interpretation of experimental results usually involves the general expression:

$$Nu_f = c\,\mathrm{Re}^m\,\mathrm{Pr}^n \qquad \textbf{Eq. 2.51}$$

Based on extensive experiments, Zukauskas and Ziugzda (1985) proposed the following parameters depending on Re_f:

Table 2.2 Different parameters in Nusselt formula for forced convection.

Re_f	C	M	N
$10^0 - 4 \cdot 10^1$	0.76	0.4	0.37
$4 \cdot 10^1 - 10^3$	0.52	0.5	0.37
$10^3 - 2 \cdot 10^5$	0.26	0.6	0.37
$2 \cdot 10^5 - 10^7$	0.023	0.8	0.4

The recommended values for *c*, *m* and *n* depend on the Reynolds number Re_f, of the surrounding fluid. Using a water velocity of 0.1 m/s, a diameter of 1.0 m and the dynamic viscosity 1.05 cP, which is valid for water at standard conditions, this gives $Re_f \sim 10^5$. At these conditions, the recommendations are $c = 0.26$, $m = 0.6$ and $n = 0.37$.

Churchill (2002) reports a general formula for combination of forced and natural convection of the form:

$$Nu_{comb} = \left(Nu_n^n + Nu_f^n\right)^{\frac{1}{n}} \qquad \textbf{Eq. 2.52}$$

Based on other work, he also recommends a value for *n* between 2 and 4, with a best proposal of 3.

The formula used by TGNet has the same structure as the one for forced convection. This means that TGNet ignores the natural convection term. Also the default values for the constants are exactly the same as recommended, except for the Prandtl exponent, where TGNet uses 0.3 as the default value.

With a water velocity of 0.1 m/s, Nu_f can be shown to be about 4 times larger than Nu_n. The forced convection will then be the dominating contribution to the convection, which also seems reasonable, taking into account the imposed water velocity. However, it is obvious that the error made by ignoring the natural convection will increase with decreasing water velocity. Eventually the forced convection will be zero at zero water velocity. TGNet fails when the water velocity is set to zero.

Gersten et al. (2001) suggest that the correlation for a buried pipeline is valid for burial depth ≥ 0.75 D and that the correlation for exposed pipe is valid for burial depth ≤ -1.5 D. Between these points, they suggest a simple linear interpolation, which is illustrated by the red line in Figure 2.9. It is obvious that TGNet calculates too high a film coefficient, i.e. too low heat flow resistance, in most of this region.

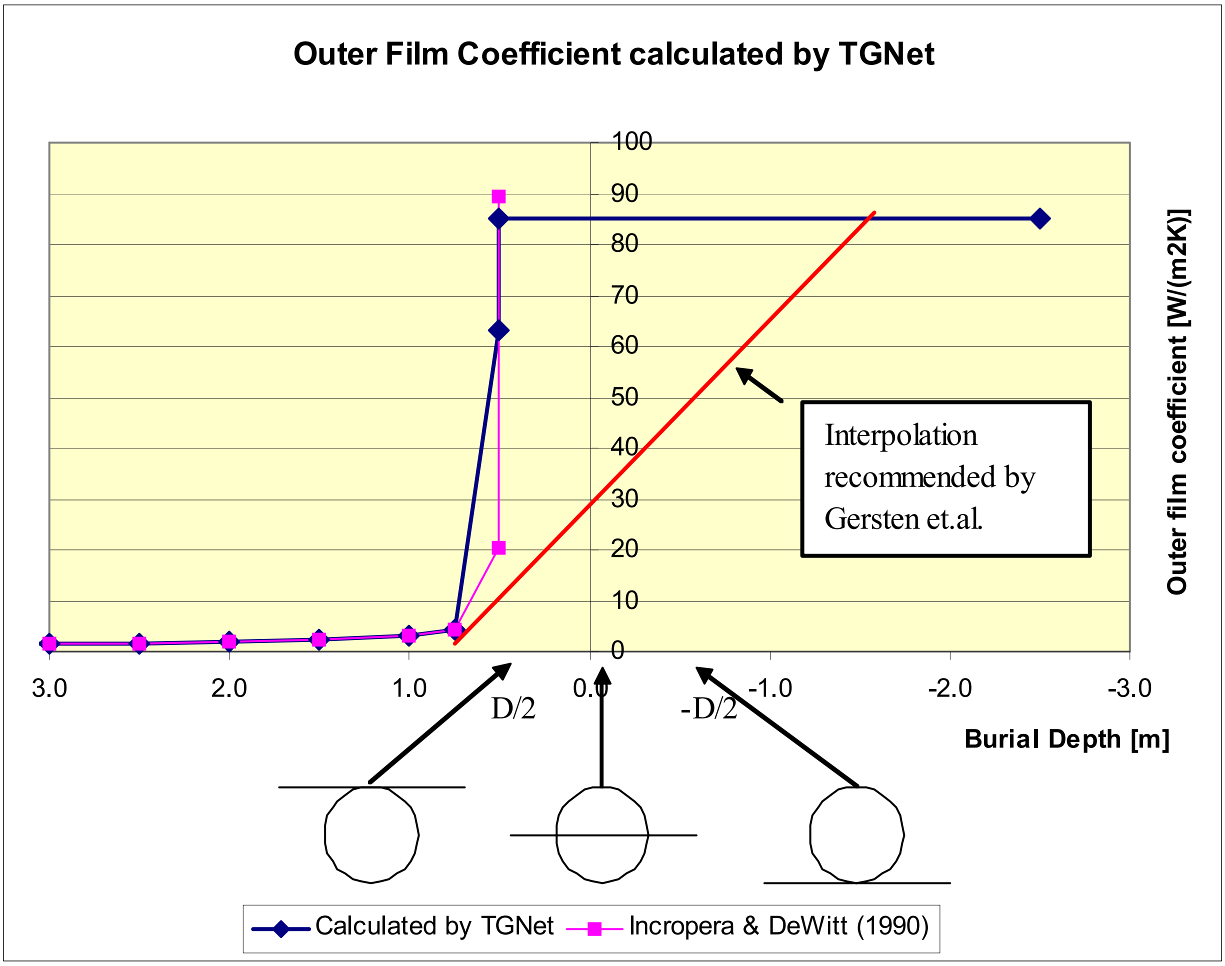

Figure 2.9 Proposed interpolation for outer film coefficient.

Additional losses

Normally one only models the pressure drops in pipelines due to friction, gravitation and acceleration. However, other effects causing pressure drop are also present in a real pipeline. Some examples are fittings such as valves, junctions and curves and welds.

Curves

It is apparent that bends and curves have to cause an extra pressure drop in addition to the pressure drop in a straight pipeline of the same length. The velocity profile is changed in that the velocity in the outer part of the bend increases while it decreases in the inner part. This causes cross-sectional pressure gradients and secondary flows leading to extra losses. In sharp bends separation of the flow might be seen at the inner wall.

Not much literature exists on the pressure loss in curved pipeline flow at relevantly large Reynolds numbers. Research groups seem to focus on laminar flow and bio applications, very sharp bends or low Reynolds number turbulent flow. For example Berger et al. (1983) is a review article giving a comprehensive overview of the status in curved pipe flow, but mainly focusing on laminar flow. Coffield et al. (1994) performed pressure loss tests for turbulent pipe flow in sharp bends for relatively large Reynolds numbers, reaching $Re = 2.5 \cdot 10^6$, which is about 5 times larger than covered by previous investigations. They developed pressure drop correlations, and compared them with six other available correlations. Their results show that all correlations differed a lot, leaving the absolute impression that this field needs further investigation.

The more traditional literature on the topic includes Ito (1959), Ito (1960) and Powle (1981).

Ito (1959) presents head loss measurements in pipes with a radius ratio ranging from 16.4 to 648. One of the main findings is the condition for when a curved pipe can be treated as a straight pipe:

$$\mathrm{Re}\left(r/R\right)^2 < 0.034 \qquad \textbf{Eq. 2.53}$$

He finds an empirical formula for the friction factor in curved pipes that fits the experimental results well for $300 > \mathrm{Re}(r/R)^2 > 0.034$:

$$f_c = 0.029\left(r/R\right)^2 + 0.304\,\mathrm{Re}^{-0.25} \qquad \textbf{Eq. 2.54}$$

The radius ratio was limited to 648 and the maximum Reynolds number was around $200 \cdot 10^3$. Nevertheless this seems to be one of the most extensive experiments that is covered in literature. With increasing radius of curvature, *R*, it is clear that the first term vanishes, and the friction factor depends only on Re. The last term is very similar to Blasius friction factor, Blasius having the constant 0.312 instead of 0.304. But by using the Blasius correlation for a straight pipe Ito (1959) found a valid reformulation of the formula above, to be valid for larger values of $\mathrm{Re}(r/R)^2$ (exceeding 6):

$$\frac{f_c}{f_s} = 1.00\left[\mathrm{Re}\left(\frac{r}{R}\right)^2\right]^{1/20} \qquad \textbf{Eq. 2.55}$$

Here the curved friction factor is expressed as a Reynolds number and geometry dependent factor multiplied by the straight pipe friction factor.

More recently in a review article Ito (1987) concluded that the older results by Ito are still valid based on recent experiments.

Powle (1981) starts with the frictional pressure drop in the momentum balance, which is defined as

$$\Delta p = f\frac{L}{D}\frac{\rho}{2}U^2 \qquad \textbf{Eq. 2.56}$$

He states that the head loss in a bend can be expressed as:

$$h_b = K_c\frac{U^2}{2g} + \frac{f_s L U^2}{4gr} \qquad \textbf{Eq. 2.57}$$

where f_s is the friction factor in a straight pipe of the same length, and K_c is a constant that depends on the geometrical parameters inner radius, radius of curvature and deflection angle. This gives the following expression for f_b, the friction factor in the bend:

$$f_b = \frac{2K_c}{L/r} + f_s \qquad \textbf{Eq. 2.58}$$

Powle (1981) also refers a formula for determining K_c. This was originally only valid for a radius ratio (radius of curvature divided by inner radius) range 1 to 25, but is shown to prove valid also for the experiments presented by Ito (1960), which has higher radius ratios.

A gas transmission line normally possesses very few bends, but has a number of very smooth curves. All of the research has however been concentrated on pipe bends of different angles, probably due to its industrial application.

While Ito proposes a friction factor correction factor which depends on the Reynolds number and geometry, Powle proposes a fixed increment in friction factor that is dependent on geometry but independent of the Reynolds number.

By assuming constant temperature and ignoring the acceleration term in the momentum balance, it is commonly known that the mass flow can be expressed as:

$$\dot{m} = \sqrt{\frac{M}{zRT}\left(p_1^2 - p_2^2\right)\frac{1}{f}\frac{D^5}{L}} \qquad \textbf{Eq. 2.59}$$

Following Ito, it is easily seen that a correction factor in f can be replaced by a correction factor in pipeline length, i.e. using an equivalent length of straight pipe to model the curved sections. But the correction factor is Re-dependent, and thus the pipeline length and simulation model cannot be held fixed across different operating conditions and flow rates. The same shortcoming is obvious with Powle's approach. A fixed increment in f, even though it is independent of the Reynolds number, causes a problem when the friction factor varies since it does not represent a fixed correction factor that can be transferred to L.

Crawford et al. (2007) state that the pressure drop in bends and curved pipes is due to a combination of frictional forces, secondary flows and separation. For curved pipes the frictional forces are predominant, whereas in sharper bends separation becomes more important. Based on experiments with three different radius curvatures and Reynolds numbers reaching $121 \cdot 10^3$, a pressure drop correlation for sharp bends is presented. The loss coefficient is significantly larger than that of Ito (1960) for sharp bends, and moderately larger for smoother bends $(R/r = 20)$. Crawford et al. conclude that for bends the straight pipe equivalent length depends on the Reynolds number.

Consequently based on available results from literature, it is not very likely to find a fixed equivalent pipeline length for a curved pipeline that can be used in the ordinary simulation software.

Weld beads

A gas pipeline is usually composed of pipe segments of 10-15 meters length. In the junctions a weld bead is found inside the pipeline. Also the pipe surface closest to the weld is uncoated, and therefore represents a higher roughness than the coated areas. Many pipelines are also formed by bending steel plates, and these pipelines have a longitudinal weld bead.

As these weld beads represent irregularities in the coated and smooth interior of the pipe, they cause extra pressure drops.

The crosswise joint welds are treated by Idelchik (1986), who quantifies the additional friction factor due to these welds:

$$f_{weld} = \frac{D}{l_w} C \left(\frac{\delta}{D} \right)^{3/2} \qquad \textbf{Eq. 2.60}$$

where l_w is the weld spacing and δ is the weld height. The constant C is a function of the weld spacing, and has a claimed value of 0.52 for a weld spacing of 10 m. The weld characteristics 2 mm height and 10 m spacing thus gives $f_{weld} = 4.65 \cdot 10^{-6}$, which only amounts to 0.05-0.1% of the friction factor. This is negligible in the friction factor plots.

Since the pressure drop contribution from welds is represented by an additional friction factor, it is difficult to model the effect with an equivalent length of pipe, as was discussed for curves above.

2.3 Discussion

Through this chapter different weaknesses of the one-dimensional pipeline simulators are described in general. Even though these weaknesses have not been quantified here, most of them can be deemed to be of minor importance. The only questionable effects are the outer film heat transfer for partly buried pipelines, which obviously can be improved, and the effect of slight curves for which there is insufficient analysis in the literature. The step in outer film heat transfer that is used in TGNet (Figure 2.8) can be of importance under certain conditions which are sensitive to this parameter.

CHAPTER 3

Sensitivity Analysis

3.1 Introduction

Many different parameters influence the results obtained by a pipeline simulator. The selected correlations, the numerics and possible inaccuracies in the model may cause the modeled values to deviate from the measured ones. The goal of the present analysis is to investigate the importance of the different parameters which were adjusted in simulations using the simulation tool Transient Gas Network (TGNet). The amount of adjustment was decided to be of the same order of magnitude as the assumed uncertainty of the various parameters.

In a pipeline simulator for a real gas transport line, it is common to make the wall roughness embrace both the physical roughness of the wall as well as (un)known model inaccuracies and uncertainties. With this in mind, it is especially interesting to see if the influence of the investigated parameters on the simulator is nonlinear. If the effect due to an inaccurate parameter can be compensated by adjusting the wall roughness by a fixed value valid for a range of flow rates and Reynolds numbers, the effect is called linear. If the necessary roughness compensation differs with the flow rate, static roughness compensation may make the tuned model suffer from inaccuracy when operational conditions change, which they normally do over time.

The free variables in the analysis were chosen to be the flow rate and the gas outlet temperature, whereas the inlet and outlet pressures were held constant.

The analysis is carried out in two steps. First, the pressure drop and other input parameters are held constant as the specific parameter of interest is changed. The resulting flow rate and gas outlet temperature is recorded and compared with the base case results. Second, the roughness and ambient temperature are adjusted until the base case flow rate and gas outlet temperature are obtained again. This represents the tuning that is necessary to compensate for a possible inaccurate parameter in a normal situation.

The results are presented and partly discussed in Section 3.4, but a more detailed discussion of some parameters can be found in Section 3.5.

3.2 Pipeline setup

A pipeline model describing a realistic pipeline similar to those found in the North Sea was built. The pipe is assumed to be fully exposed to sea-water along the entire length, and the following characteristics were used:

Table 3.1 Pipeline parameters.

Parameter		Value		
Pipeline length		500 km		
Number of pipes		10, equally sized 50 km		
Knot spacing		5 km		
Inner diameter		0.9664 m		
Outer diameter		1.0774		
Wall layers	Layer 1 (inner)	Steel	24 mm	7800 kg/m^3
		0.5 kJ/kgK	50 W/mK	
	Layer 2	Asphalt	7 mm	1300 kg/m^3
		1.9 kJ/kgK	0.74 W/mK	
	Layer 3	Concrete	80 mm	2500 kg/m^3
		0.65 kJ/kgK	2.9 W/mK	

The following gas composition was used:

Table 3.2 Gas composition.

Component	Mole%
Methane	92.0
Ethane	5.0
Propane	2.0
Iso Butane	0.5
Normal Butane	0.5

Other simulation parameters used were:

Table 3.3 Other parameters.

Parameter	Value
Roughness	3.8 μm
Inlet gas temperature	35 degC
Sea-water temperature	5 degC
Sea-water velocity	0.1 m/s

And the following correlations for friction factor, equation of state, viscosity and heat transfer:

Table 3.4 Other correlations.

Friction Factor	Colebrook-White
Equation of State	BWRS
Viscosity correlation	Lee-Gonzales-Eakin
Inner heat film	Eq. 2.22
Outer heat film	Eq. 2.21

Two base cases were chosen, one with a large pressure drop and one with a smaller pressure drop. The exact flow rate and gas outlet temperature with the nominal parameter values are shown in the table below, together with the Reynolds number range along the pipe.

Table 3.5 Operating conditions at base case.

	High flow rate	**Low flow rate**
Inlet pressure [barg]	140	120
Outlet pressure [barg]	90	110
Nominal flow rate [MSm^3/d]	47.453	20.584
Outlet gas temperature [degC]	4.03	4.93
Reynolds number	$33 - 41 \cdot 10^6$	$15 - 16 \cdot 10^6$

The Reynolds number increases along the pipeline due to increasing gas velocity.

3.3 Sensitivity parameters

The following input parameters for the simulation were manipulated in the sensitivity analysis:

- Beta(momentum)
  The acceleration term in the momentum balance was multiplied by a factor as high as 100. This is far more than the realistic uncertainty. It was set so large to see if there was any effect at all.
- Beta(dissipation)
  The friction dissipation term in the energy balance was multiplied by factor 1.2.
- Total heat transfer coefficient (U_{total})
  The total heat transfer coefficient (yielding the sum of inner film, wall and outer film resistance) was increased by 10% along the whole pipe, for the first half section of the pipe and eventually for the last half section of the pipe.
- Viscosity
  The viscosity was increased by 1% compared with the calculated value from the Lee-Gonzalez-Eakin correlation.
- Density
  The density was increased by 1% compared with the calculated value from the BWRS equation.
- Pipe length
  The length of the pipe was increased by 0.02%, i.e. 100 m.
- Ambient temperature
  The ambient temperature was increased by 0.5%, i.e from 5 degC (278.15 K) to 6.39 degC (279.54 K).
- Pipeline diameter (uncertainty)
  The inner diameter was increased by 0.1%[1] corresponding to the given uncertainty in inner diameter at the ends of each segment (see Offshore Standard 2000).
- Pipeline diameter (pressure expansion)
  The exact pipeline diameter was recalculated taking the pressure expansion of the steel into account. More detailed explanation and calculations are found in the discussions section, see Section 3.5.

All results are obtained from computer simulations using TGNet and a configuration file with the established pipeline parameters.

---

[1] The inner diameter is stated to be within ±0.16% of the nominal diameter at the section ends. As these are absolute limits, it is assumed that a 95% confidential interval yields about 0.1%.

Some of the parameter changes were made by simply manipulating the configuration file for the simulation, while other changes required manipulation of a TGNet source code file, and subsequent compilation of the system.

3.4 Results

Table 3.6 shows how the simulated flow rate and gas outlet temperature change when the specific sensitivity parameter in question is adjusted.

Table 3.7 shows the changes in roughness and ambient temperature, or tuning, that are necessary to revert to base case flow rate and temperature.

Table 3.6 Immediate effects in flow rate and gas outlet temperature from changing a sensitivity parameter.

	Factor [-]	High flow rate		Low flow rate	
		ΔFlow [MSm^3/d]	ΔTemp out [˚C]	ΔFlow [MSm^3/d]	ΔTemp out [˚C]
Base Case		0	0	0	0
Beta(momentum)	100	0	0	0	0
Beta(dissipation)	1.2	-0.018	+0.10	-0.001	+0.01
U_{total}, entire length	1.1	+0.013	+0.08	+0.004	+0.01
U_{total}, first half	1.1	+0.020	0	+0.004	0
U_{total}, last half	1.1	-0.008	+0.09	0.000	+0.01
Viscosity	1.01	-0.016	0	-0.010	0
Density	1.01	+0.235	+0.01	+0.102	0
Pipe length	1.0002	-0.005	0	-0.002	0
Pipeline diameter (uncertainty)	1.001	+0.123	0	+0.054	0
Pipeline diameter (pressure expansion)	[2]	0	0	0	0
Ambient temperature	1.005	-0.304	+1.41	-0.138	+1.39

---

[2] See Section 3.5.3.

Table 3.7 Necessary adjustment in roughness and ambient temperature to revert to base case results.

	Factor [-]	High flow rate		Low flow rate	
		Δroughness [micron]	Δambient temperature [˚C]	Δroughness [micron]	Δambient temperature [˚C]
Base Case					
Beta(momentum)	100	0	0	0	0
Beta(dissipation)	1.2	+0.025	-0.14	0	-0.01
U_{total}, entire length	1.1	+0.055	-0.08	+0.03	-0.01
U_{total}, first half	1.1	+0.04	0	+0.03	0
U_{total}, last half	1.1	+0.02	-0.08	+0.001	-0.01
Viscosity	1.01	-0.03	0	-0.065	0
Density	1.01	+0.46	-0.01	+0.66	0
Pipe length	1.0002	-0.01	0	-0.015	0
Pipeline diameter (uncertainty)	1.001	0.23	0	0.35	0
Pipeline diameter (pressure expansion)	[3]	0	0	0	0
Ambient temperature	1.005	-	-	-	-

Note that a tuning in roughness and ambient temperature to compensate for the change in ambient temperature was not performed, since it simply would have resulted in returning the ambient temperature back to its original value.

It is seen that all errors in flow rate and outlet temperature due to input parameter uncertainty are of the same order of magnitude, except for the effect of ambient temperature and density, which turn out to the far most important parameters. The flow rate is changed by -0.304 MSm^3/d and -0.138 MSm^3/d respectively if an error of 0.5% in ambient temperature is present. Uncertainty in inner diameter is also important.

It is also interesting to see that the diameter change due to pressure expansion has no effect at all.

The results are further analyzed in the subsequent sections.

3.4.1 Sensitivity coefficients, flow rate and gas outlet temperature

The parameter adjustments used in the preceeding section are realistic in that they are comparable to their expected uncertainty. In this section, the effect on flow rate and outlet temperature is scaled by the relative change in the input parameter, i.e. what is plotted is:

---

[3] See Section 3.5.3.

$$\frac{\Delta flow \Big/ flow}{\Delta parameter \Big/ parameter}$$

Eq. 3.1

and

$$\frac{\Delta outlet - temperature \Big/ outlet - temperature}{\Delta parameter \Big/ parameter}$$

Eq. 3.2

for each parameter. This is called the *sensitivity coefficient*, which is non-dimensional.

The sensitivity coefficient on flow rate is shown in Figure 3.1 and Figure 3.2, whereas Figure 3.3 and Figure 3.4 display the sensitivity coefficient on gas outlet temperature.

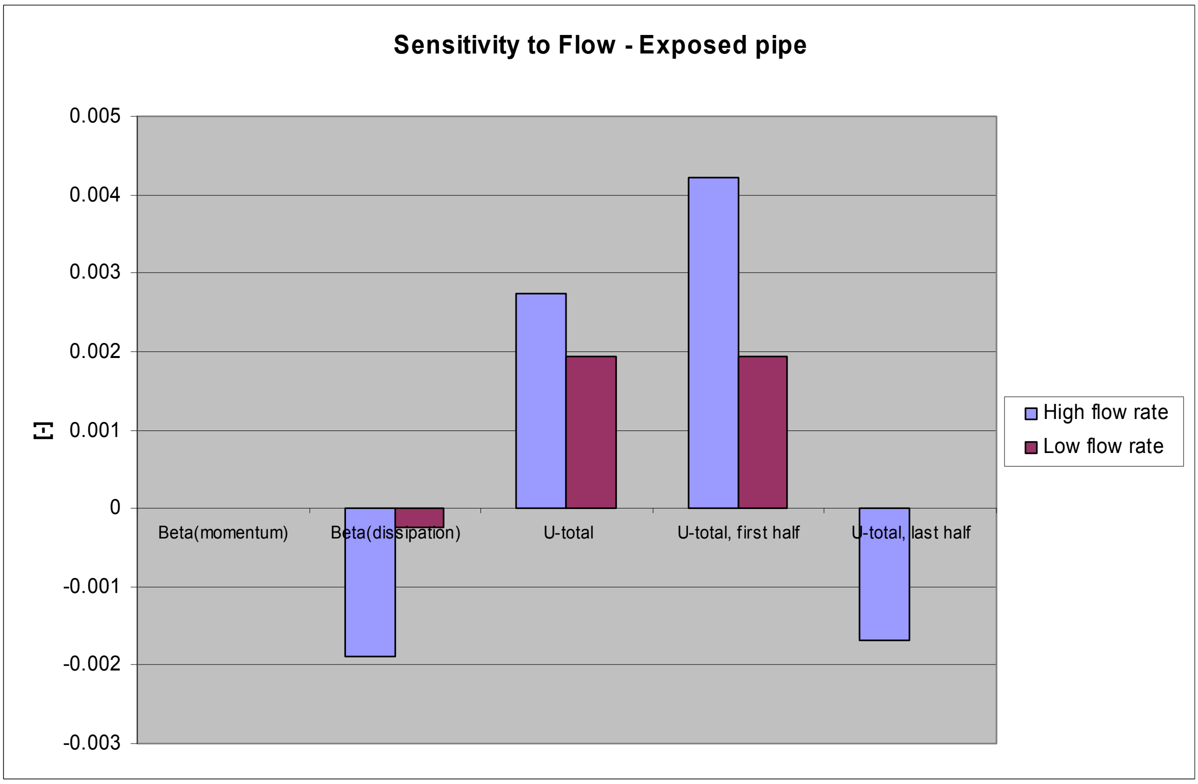

Figure 3.1 Sensitivity coefficients on flow rate.

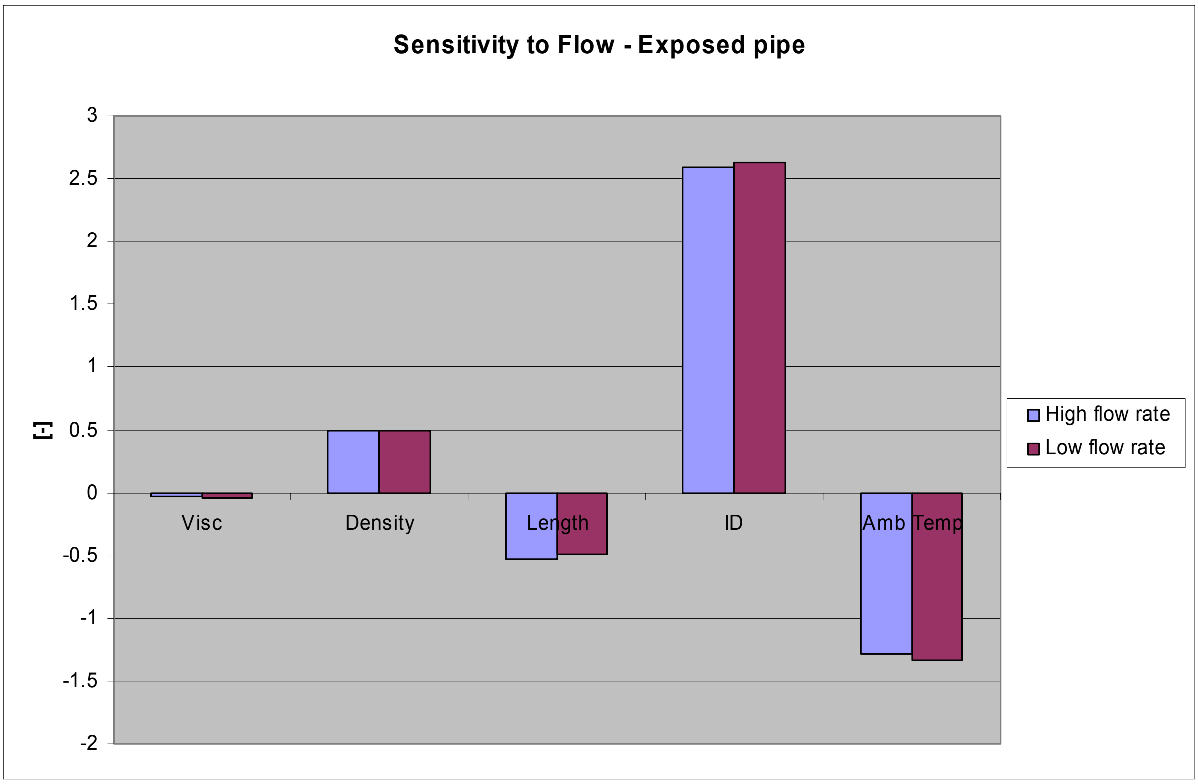

Figure 3.2 Sensitivity coefficients on flow rate.

The sensitivity coefficients for viscosity, density, length, inner diameter and ambient temperature range from 0.1 to 1.5. For the correction factors and heat transfer coefficients the sensitivity coefficients range from 0.001 to 0.005. But the expected uncertainty is also at least one order of magnitude larger for the latter ones.

The corresponding sensitivity coefficients on gas outlet temperature are shown in Figure 3.3 and Figure 3.4. From Figure 3.3 it is seen that the sensitivity coefficients for the high flow rate case are much larger than for the low flow rate case. The lower the flow rate gets, the slower the gas is cooled by the pressure drop, and hence less dependent on heat transfer from the surroundings to maintain a temperature close to the ambient sea temperature. We also see that a change in the heat transfer in the first half of the pipe does not affect the outlet temperature at all, which proves that a temperature measurement at the outlet gives very little information about the gas temperature in the first part of the pipeline.

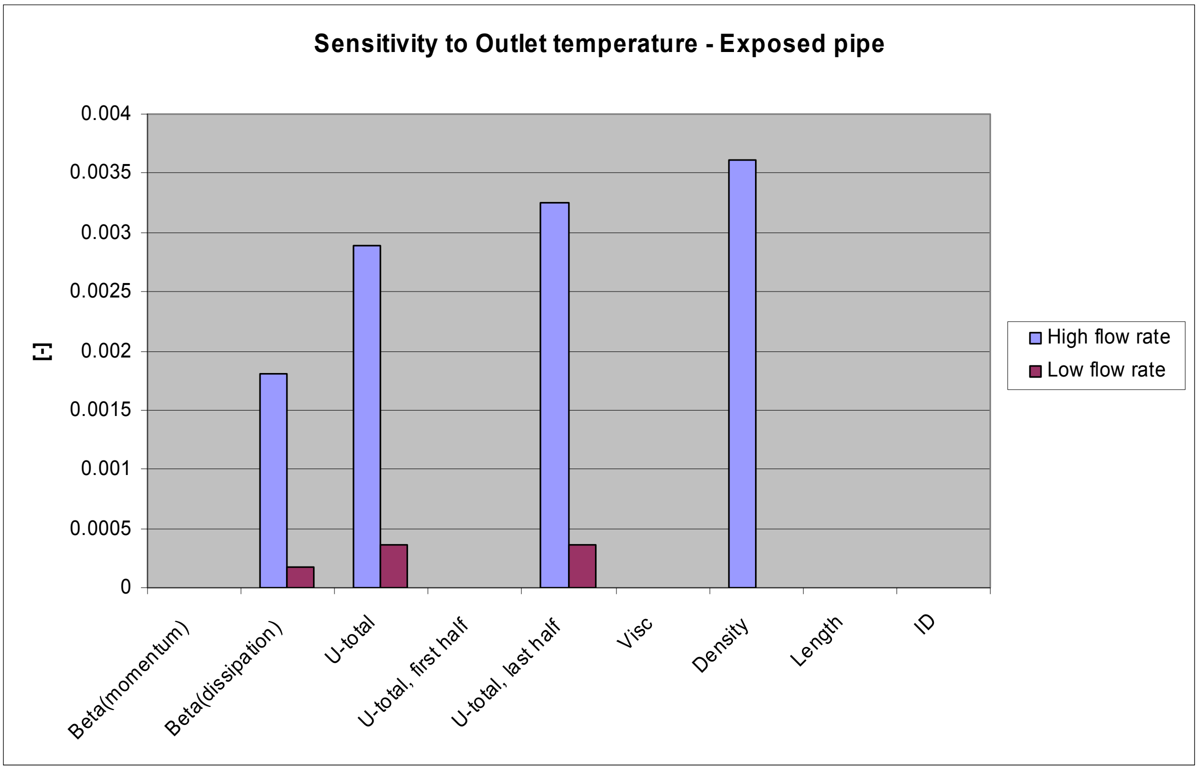

Figure 3.3 Sensitivity coefficients on outlet temperature.

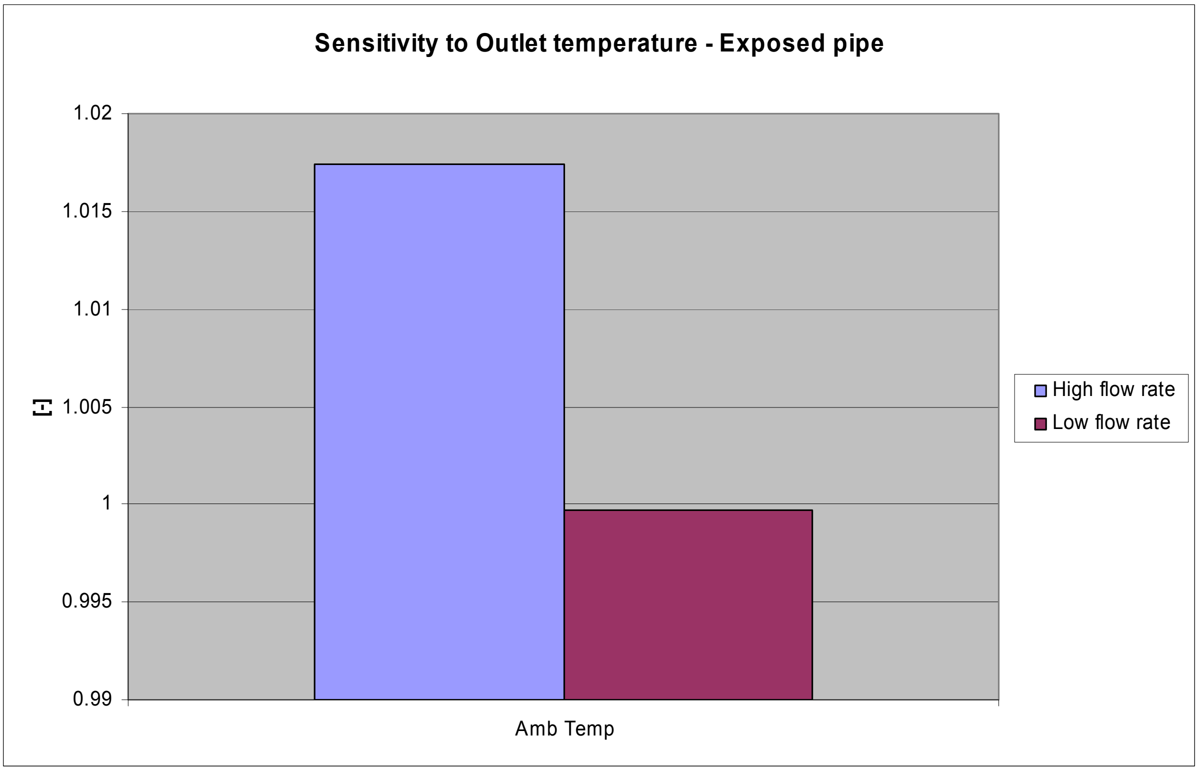

Figure 3.4 Sensitivity coefficients on outlet temperature.

The sensitivity coefficient from ambient temperature to gas outlet temperature is naturally close to 1.

3.4.2 Sensitivity coefficients, tuned roughness and ambient temperature

Figure 3.5 - Figure 3.6 show the influence from the relative change in sensitivity parameter on the tuned roughness, i.e.:

$$\frac{\Delta roughness}{\Delta parameter \big/ parameter} \qquad \textbf{Eq. 3.3}$$

which means that the plotted values have the dimension [μm].

In Figure 3.7 the influence on the tuned ambient temperature is shown, with dimension [K] along y-axis.

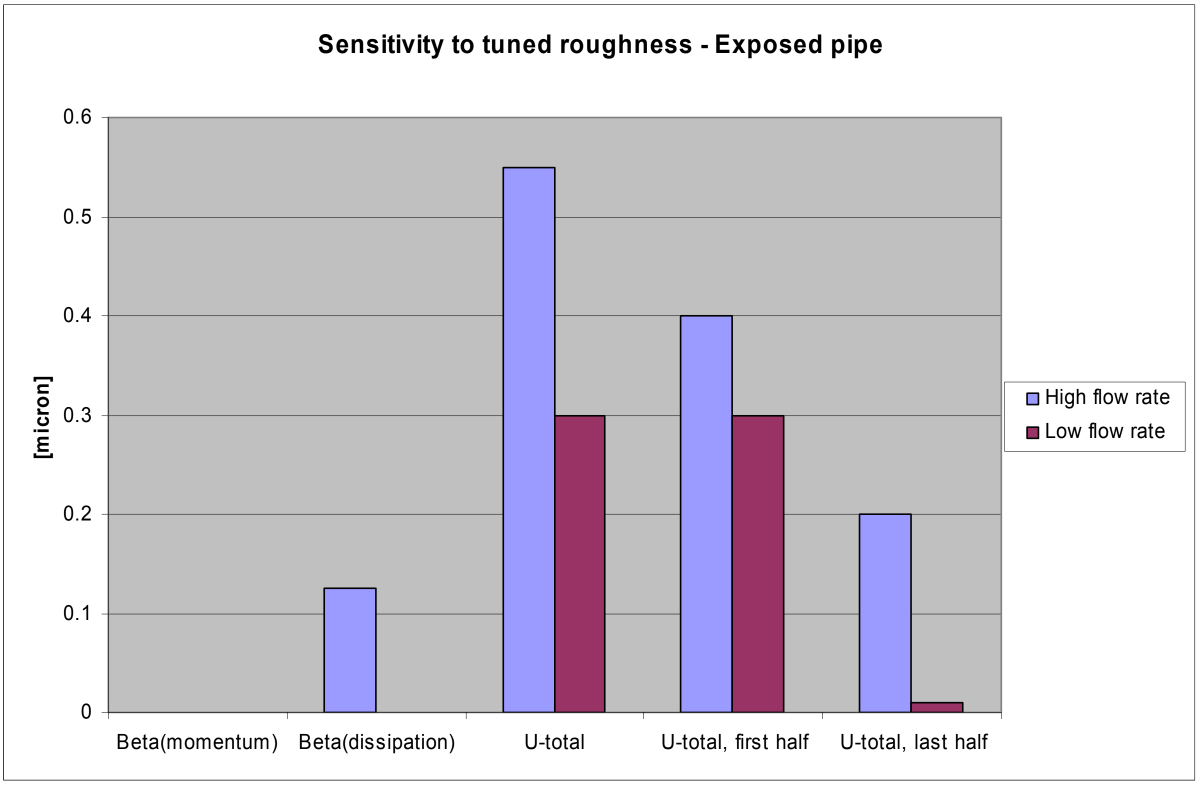

Figure 3.5 Sensitivity coefficients on tuned roughness.

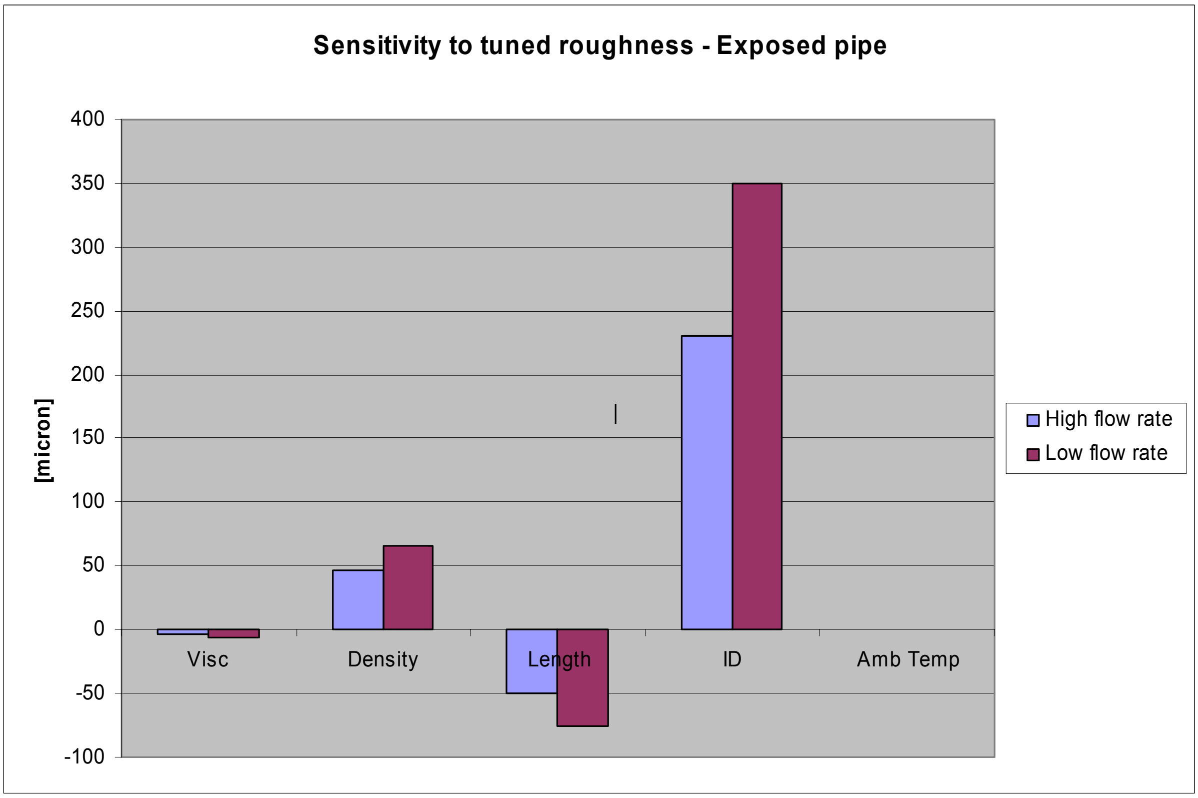

Figure 3.6 Sensitivity coefficients on tuned roughness.

The effect on tuned roughness is nonlinear, which means that a systematic error in the modeled heat transfer coefficient for example cannot be compensated by a fixed change in tuned roughness across a large Reynolds number range. For *U* and the dissipation correction factor, a larger effect is seen at high flow rates than at low flow rates. This is due to the same explanation as earlier; at low flow rates the gas temperature is closer to equilibrium with ambient sea temperature, and less sensitive to changes.

On the contrary will an increase in viscosity, density, length and inner diameter require larger roughness compensation at low flow rates than at high flow rates.

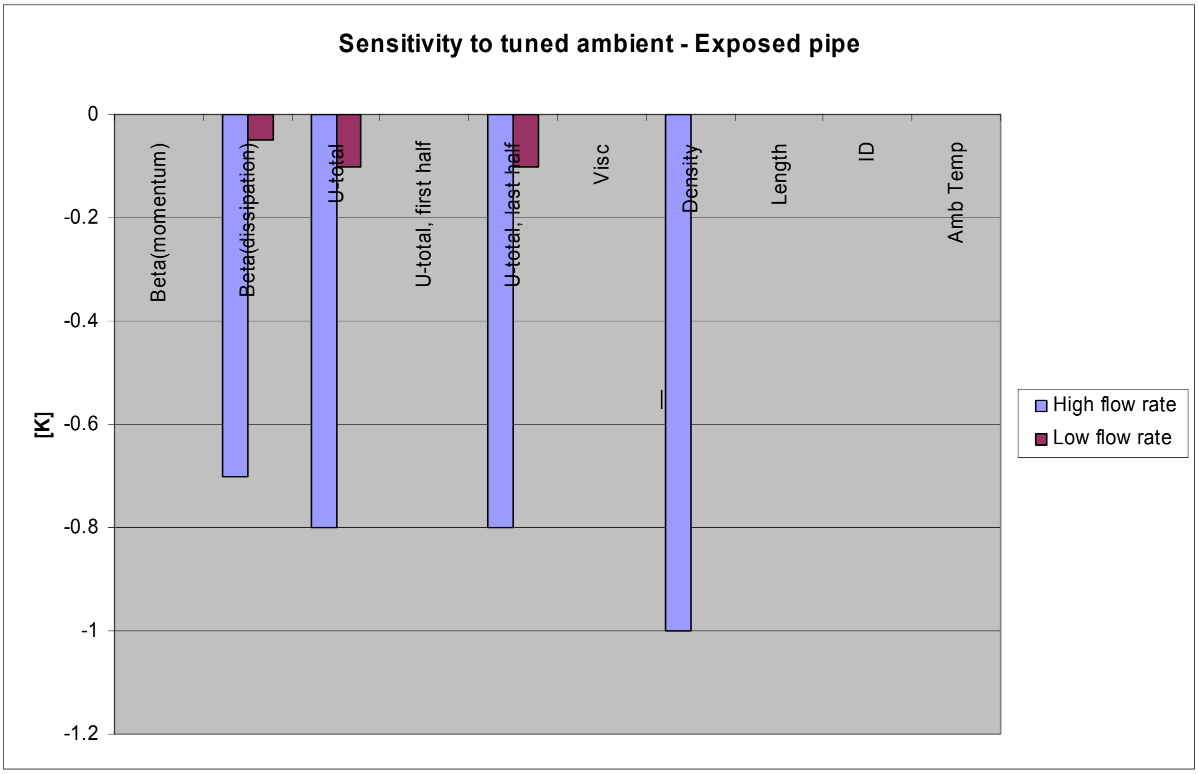

Figure 3.7 Sensitivity coefficients on tuned ambient temperature.

3.4.3 Sensitivity coefficients in heat transfer calculation

U_{total}

The total heat transfer coefficient for the pipe, U_{total}, is a combination of the inner film resistance, U_{inner}, the wall resistance, U_{wall}, and the outer film resistance, U_{outer}. This was thoroughly described in Section 2.2.2.

U_{inner}, U_{wall} and U_{outer} were multiplied by the factor 1.1 one by one to see how an error in each of these calculations would possibly affect the calculated U_{total}.

For a pipe that is exposed to sea-water, the wall with the current configuration represents the largest heat resistance (smallest heat conductivity, U). Figure 3.8 shows that a 10% change in U_{wall} gives approximately 8.5% change in U_{total}, and it does not change significantly with flow rate. A 10% change in U_{inner} or U_{outer} gives less than 1% change in U_{total}.

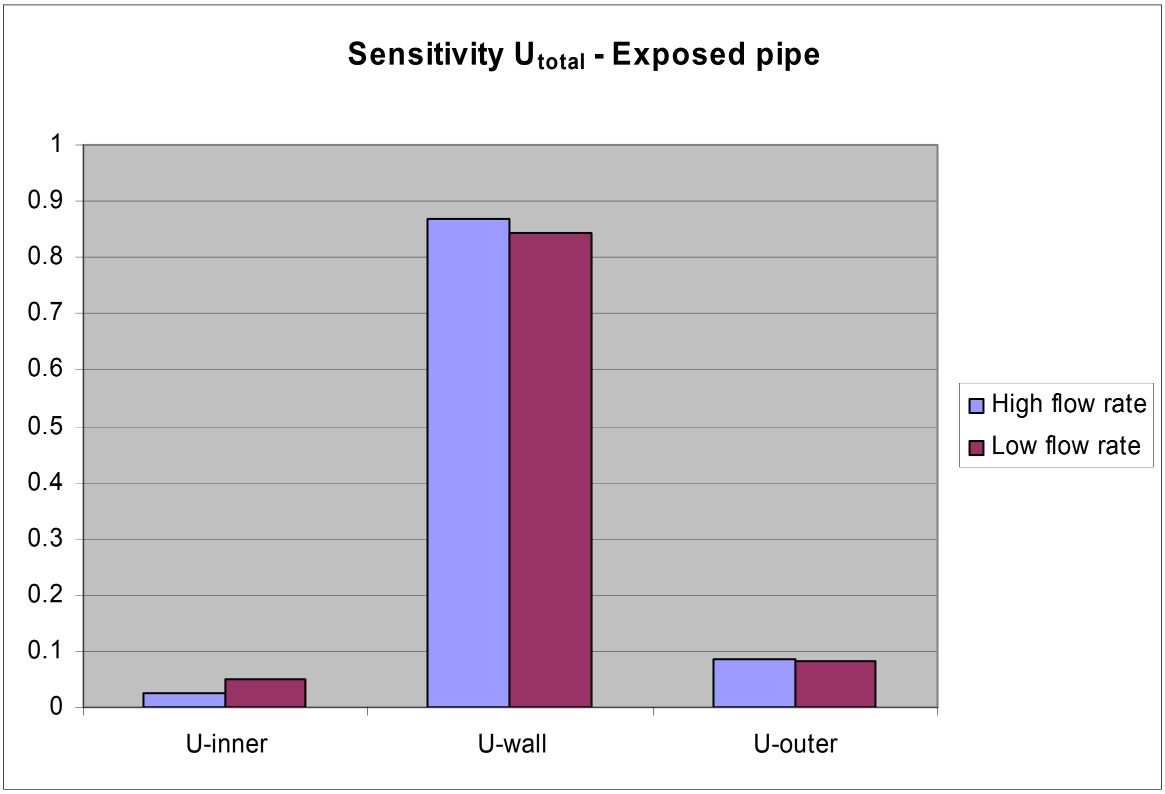

Figure 3.8 Sensitivity of U_{inner}, U_{wall} and U_{outer} on U_{total}.

U_{wall}

Figure 3.9 illustrates the relative importance of getting the material properties correct. The concrete conductivity and thickness has a sensitivity coefficient around 0.6-0.7. For steel the thermal conductivity is so large that the sensitivity coefficient is negligible.

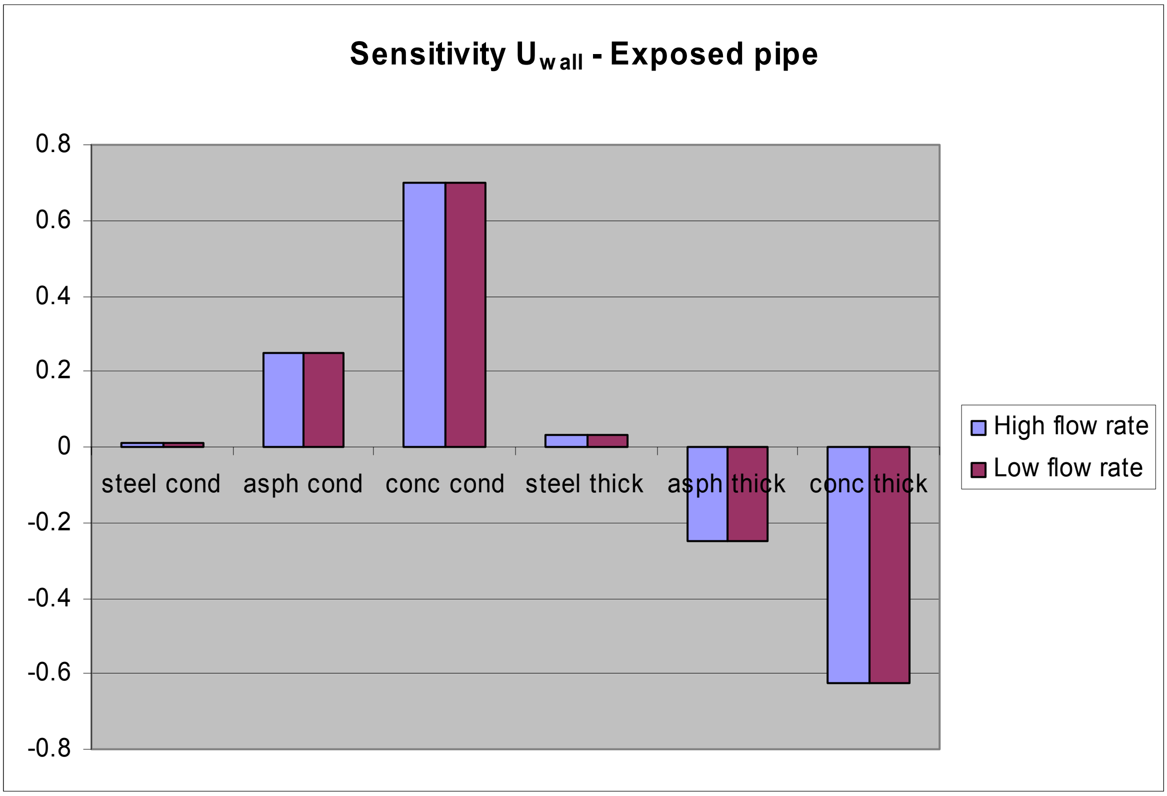

Figure 3.9 Sensitivity of material conductivies and thicknesses on U_{wall}.

U_{outer}

U_{outer} depends heavily on the sea-water velocity, as the cooled (heated) sea-water is transported away and replaced by fresh warm (cold) water with this velocity. The sea-water properties required to calculate the Nusselt number are assumed to be well known. The uncertainty connected to the actual choice of Nussel number correlation has not been looked into here, but will of course also add uncertainty to U_{outer}.

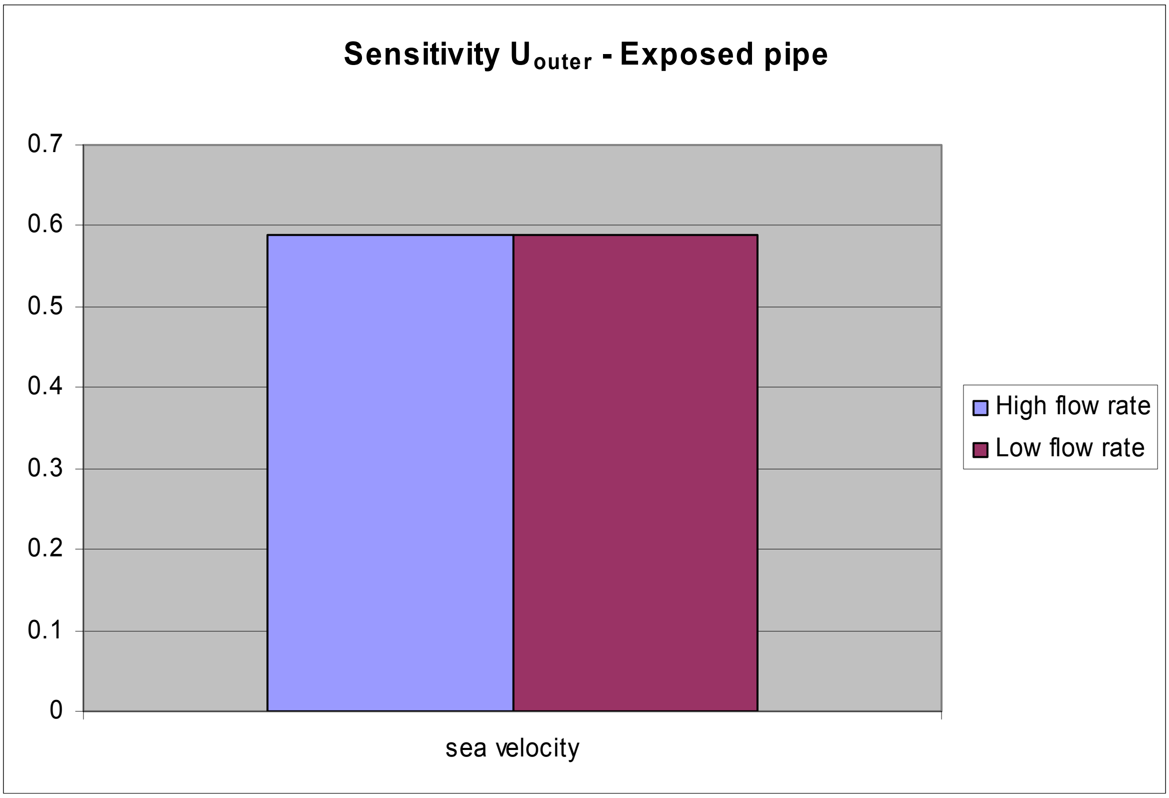

Figure 3.10 Sensitivity of sea velocity on U_{outer}.

3.5 Discussion

3.5.1 Correction-factor in the momentum balance

The acceleration term in the momentum balance was adjusted by a factor to investigate the error made by the simplified integration process as described in Appendix A. The results show that this does not have any impact at all, and the conclusion is that this error is negligible.

This is also easily seen by comparing the magnitude of the different terms in the momentum balance for typical flow conditions. In the simulated case the frictional force balances the pressure drop, and hence the acceleration term plays a minor role in the momentum balance.

The steady-state momentum balance for a horizontal pipeline reads:

$$\frac{\partial U}{\partial x} = -\frac{1}{\rho U}\frac{\partial p}{\partial x} - \frac{1}{2}U\frac{f}{D} \qquad \textbf{Eq. 3.4}$$

The gas velocity increases from about 4 m/s to 8 m/s in a 700 km long and 1 meter diameter pipeline with a flow rate of around 35-40 MSm^3/d, which are typical conditions in a Gassco-operated pipeline. This yields an acceleration term of the magnitude $5.7 \cdot 10^{-6}$. Using an average gas velocity of 6 m/s and a friction factor of 0.0075, which is an approximate value for a smooth pipeline at Reynolds number $30\text{-}40 \cdot 10^6$, this gives a friction term of around 0.02. It is seen that the acceleration term is around 10^4 less than the friction term. It may also be concluded that the pressure drop term has to balance the friction term, leaving these two terms as the important ones at these conditions.

If the velocity gradient is increased, but keeping the velocity at the same order of magnitude, the frictional term will remain the same, while the other two terms will increase. If the velocity gradient is large enough, the acceleration term and the pressure drop term will be the two dominant terms in the equations. In this situation the acceleration term correction will have a larger effect.

In conditions with a small velocity and pressure gradient, the inaccuracy introduced by the acceleration term is totally negligible.

3.5.2 Correction-factors in the energy balance

Friction term

The friction term in the energy balance accounts for the breakdown of mechanical turbulent energy to thermal energy. The term will hence always be positive.

The expected error in this term is around 10-20%, Ytrehus (2004-2007), and it was tried to increase the term by 20% by adding a factor to the term in the source code. Table 3.6 shows that the gas temperature increased and the flow rate decreased. The warmer gas yields higher resistance to the flow, and hence the flow rate goes down. It is also worthwhile noting that the effect is very unlinear, which is clearly illustrated in Figure 3.5 and Figure 3.7.

It is seen that the error performed by not using an exact value of the friction term, which is believed to be between 10 and 20% higher than what is used in the original equations, is observable, but still very small at the investigated conditions.

Heat transfer term

The heat transfer term accounts for the energy transferred to the gas from the surroundings, driven by the temperature difference, in this case between the sea-water and the gas.

The term was increased by 10% by increasing the heat transfer coefficient in the source code, which leads to a warmer gas but also a higher flow rate, which may seem as an inadequate combination. But the explanation is obvious. The higher heat transfer cools the gas faster in the beginning when the gas temperature is above ambient temperature, but it also ensures that there is a slightly warmer gas after the point where the gas is heated. The increased flow rate proves that the weighted average gas temperature in the pipe decreases, so that the total flow resistance decreases.

For an exposed pipe, the effect of a potentially inaccurate heat transfer term is small, but it cannot be considered insignificant. For a buried pipe or particularly a partly buried pipe, where the heat transfer correlations are poorer, the expected uncertainty is larger.

3.5.3 Corrected diameter

The pipeline radius will be slightly influenced by the difference between the internal and external pressure. This pressure difference can be used together with material properties such as thickness and Young's elasticity modulus to calculate an exact radius under different conditions:

$$E = \frac{FL_0}{A_0 \Delta L}$$ **Eq. 3.5**

where E is Young's modulus with the approximate value $200 \cdot 10^9$ Pa for steel.

In this analysis, the diameter was assumed to equal the chosen design diameter, 0.9664 m, at gas pressure 115 barg, which is the arithmetical mean between the inlet and outlet pressures for both cases. The diameter was then updated for the 10 sections of the pipeline, based on the pressure in each section. In this calculation a linear pressure profile was assumed. The expansion was calculated based on a steel layer only, with a thickness of 25 mm. Since pressure expansion is dominating the temperature expansion, the latter was ignored.

Table 3.8 and Table 3.9 show the modified diameters for the two base cases:

Table 3.8 Modified pipe diameters for high flow rate case.

Pipe	Presure [barg]	reference P [barg]	delta P [barg]	base D [m]	delta D [m]	modified D [m]
Pipe 1	137.5	115	22.5	0.9664	0.000207	0.966607
Pipe 2	132.5	115	17.5	0.9664	0.000161	0.966561
Pipe 3	127.5	115	12.5	0.9664	0.000115	0.966515
Pipe 4	122.5	115	7.5	0.9664	0.000069	0.966469
Pipe 5	117.5	115	2.5	0.9664	0.000023	0.966423
Pipe 6	112.5	115	-2.5	0.9664	-0.000023	0.966377
Pipe 7	107.5	115	-7.5	0.9664	-0.000069	0.966331
Pipe 8	102.5	115	-12.5	0.9664	-0.000115	0.966285
Pipe 9	97.5	115	-17.5	0.9664	-0.000161	0.966239
Pipe 10	92.5	115	-22.5	0.9664	-0.000207	0.966193

Table 3.9 Modified pipe diameters for low flow rate case.

Pipe	Presure [barg]	reference P [barg]	delta P [barg]	base D [m]	delta D [m]	modified D [m]
Pipe 1	119.5	115	4.5	0.9664	0.0000414	0.9664414
Pipe 2	118.5	115	3.5	0.9664	0.0000322	0.9664322
Pipe 3	117.5	115	2.5	0.9664	0.0000230	0.9664230
Pipe 4	116.5	115	1.5	0.9664	0.0000138	0.9664138
Pipe 5	115.5	115	0.5	0.9664	0.0000046	0.9664046
Pipe 6	114.5	115	-0.5	0.9664	-0.0000046	0.9663954
Pipe 7	113.5	115	-1.5	0.9664	-0.0000138	0.9663862
Pipe 8	112.5	115	-2.5	0.9664	-0.0000230	0.9663770
Pipe 9	111.5	115	-3.5	0.9664	-0.0000322	0.9663678
Pipe 10	110.5	115	-4.5	0.9664	-0.0000414	0.9663586

The modified diameters do not affect the simulation results at all. The same flow rates are obtained using the modified pipe diameters as was obtained in the base cases.

3.5.4 Viscosity

The dynamic viscosity of a fluid is a unique function of fluid composition, pressure and temperature.

For a given mass flow rate, the Reynolds number decreases with increasing viscosity. As long as part of the wall friction is due to frictional or viscous drag, the friction factor and pressure drop will increase accordingly.

In this sensitivity analysis, the viscosity calculated by the LGE-correlation was increased by 1% before it was used in the calculations. It is seen in Table 3.6 that the flow rate decreases by 0.016 MSm^3/d in the high flow rate case and 0.010 MSm^3/d in the low flow rate case. The temperature shows no difference. The required compensation in roughness to maintain the nominal flow rate is -0.03 μm and -0.065 μm respectively, proving that a strong unlinearity is present.

Discussion of unlinearity, viscosity on mass flow

The reason for this observed unlinearity is analyzed further:

By a straightforward manipulation of the friction factor definition, one may obtain the expression:

$$\dot{m} = \frac{\pi}{4}\sqrt{\frac{1}{2}\Delta p \rho \frac{D^5}{fL}} \qquad \textbf{Eq. 3.6}$$

which also is an approximation of Eq. 2.59, and is valid for short horizontal pipe sections under steady-state conditions.

Assuming a fixed pressure drop, the equation can be differentiated with respect to the viscosity:

$$\frac{\partial \dot{m}}{\partial \mu} = \frac{\pi}{4}\sqrt{\frac{1}{2}\Delta p \rho \frac{D^5}{L}}\frac{\partial}{\partial \mu}\left(\frac{1}{\sqrt{f}}\right) \qquad \textbf{Eq. 3.7}$$

where:

$$\frac{\partial}{\partial \mu}\left(\frac{1}{\sqrt{f}}\right) = \frac{\partial}{\partial f}\left(\frac{1}{\sqrt{f}}\right)\frac{\partial f}{\partial \mu} = -\frac{1}{2}\frac{1}{f^{3/2}}\frac{\partial f}{\partial \mu} \qquad \textbf{Eq. 3.8}$$

and

$$\frac{\partial f}{\partial \mu} = \frac{\partial f}{\partial \mathrm{Re}}\frac{\partial \mathrm{Re}}{\partial \mu} \qquad \textbf{Eq. 3.9}$$

and

$$\frac{\partial \mathrm{Re}}{\partial \mu} = -\frac{\rho U L}{\mu^2} = -\frac{\mathrm{Re}}{\mu} \qquad \textbf{Eq. 3.10}$$

which means that the sensitivity coefficient of dynamic viscosity on mass flow rate, as defined in Eq. 3.1 can be expressed as:

$$\frac{\partial \dot{m}}{\partial \mu}\frac{\mu}{\dot{m}} = \frac{\pi}{4}\sqrt{\frac{1}{2}\frac{D^5}{L}}\sqrt{\Delta p}\sqrt{\rho}\left(-\frac{1}{2}\frac{1}{f^{3/2}}\right)\left(-\frac{\mathrm{Re}}{\mu}\right)\frac{\partial f}{\partial \mathrm{Re}}\frac{\mu}{\dot{m}} \qquad \textbf{Eq. 3.11}$$

The different terms on the right hand side of this equation are quantified for the low and high flow rate cases respectively in Table 3.10. The assumption behind the approximation was that the pipe segment was short, so using this equation for the 500 km long pipe challenges its validity.

Table 3.10 Quantification of different terms in equation.

Term	Quantification		Comment
	Low flow rate	High flow rate	
$\frac{\pi}{4}\sqrt{\frac{1}{2}\frac{D^5}{L}}$	=		Does not differ
$\sqrt{\Delta p}$	$\sqrt{120-110} = 3.16$	$\sqrt{140-90} = 7.07$	
$\sqrt{\rho}$	≈		Assumed approximately the same, mean pressure does not differ much
$-\frac{1}{f^{3/2}}$	$-\frac{1}{\left(8.1\cdot 10^{-3}\right)^{3/2}}$	$-\frac{1}{\left(7.6\cdot 10^{-3}\right)^{3/2}}$	Approximate mean value from the simulations
Re	$16\cdot10^{6}$	$37\cdot10^{6}$	Average
$\frac{\partial f}{\partial \mathrm{Re}}$	$-4.8\cdot10^{-11}$	$-1.3\cdot10^{-11}$	Calculated numerically and presented in Figure 3.11
$\frac{1}{\dot{m}}$	$\frac{1}{20.6}$	$\frac{1}{47.5}$	

By combining these figures, the expected ratio between the sensitivity coefficients, as expressed in Eq. 3.11, at low and high flow rates is estimated to be 1.50. Using the simulated results from Table 3.6, the same coefficient is 1.44. Thus the approximation works well, and it is also found that the different $\frac{\partial f}{\partial \mathrm{Re}}$ at the two Reynolds numbers is the main reason why a given percentage change in viscosity results in larger relative change in flow rate at low flow rates than at higher flow rates. $\frac{\partial f}{\partial \mathrm{Re}}$ is also plotted in Figure 3.11 together with the friction factor itself.

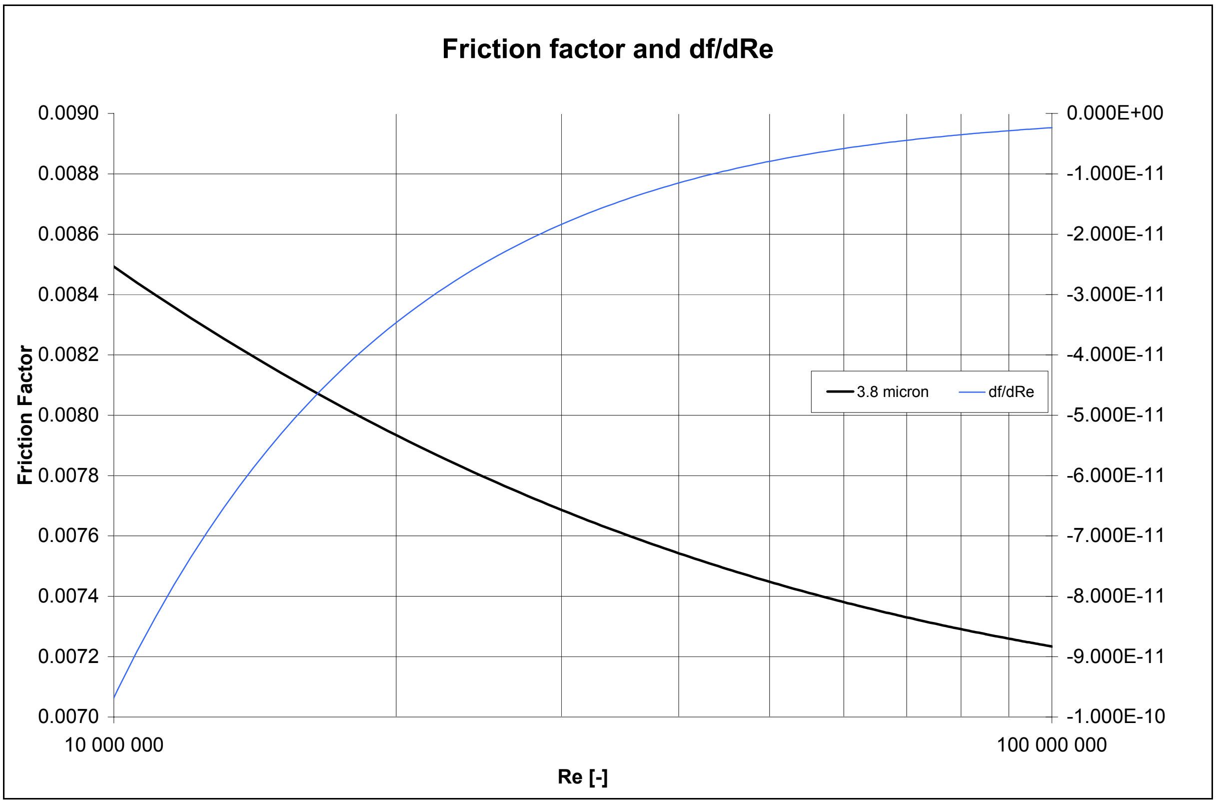

Figure 3.11 Colebrook-White friction factor for k = 3.8 micron, and the friction factor differentiated with regard to the Reynolds number holding k constant at 3.8 micron.

Discussion of unlinearity, roughness on mass flow

The same approach is taken to break down the different contributors to the partial derivative of mass flow with respect to roughness in order to analyze why the flow rate is less sensitive to roughness changes at low flow rates than at high flow rates.

Eq. 3.6 is now differentiated with respect to the roughness:

$$\frac{\partial \dot{m}}{\partial k} = \frac{\pi}{4}\sqrt{\frac{1}{2}\Delta p \rho \frac{D^5}{L}}\frac{\partial}{\partial k}\left(\frac{1}{\sqrt{f}}\right) \qquad \textbf{Eq. 3.12}$$

where:

$$\frac{\partial}{\partial k}\left(\frac{1}{\sqrt{f}}\right) = \frac{\partial}{\partial f}\left(\frac{1}{\sqrt{f}}\right)\frac{\partial f}{\partial k} = -\frac{1}{2}\frac{1}{f^{3/2}}\frac{\partial f}{\partial k} \qquad \textbf{Eq. 3.13}$$

$\dfrac{\partial \dot{m}/\dot{m}}{\partial k/k}$ can then be written:

$$\frac{k}{\dot{m}}\frac{\partial \dot{m}}{\partial k} = \frac{\pi}{4}\sqrt{\frac{1}{2}\Delta p \rho \frac{D^5}{L}}\left(-\frac{1}{2}\right)\frac{1}{f^{3/2}}\frac{\partial f}{\partial k}\frac{k}{\dot{m}} \qquad \textbf{Eq. 3.14}$$

The different terms are quantified as:

Table 3.11 Quantification of different terms in Eq. 3.14.

Term	Quantification		Comment
	Low flow rate	High flow rate	
$\frac{\pi}{4}\sqrt{\frac{1}{2}\frac{D^5}{L}}$	=		Does not differ
$\sqrt{\Delta p}$	$\sqrt{120-110}=3.16$	$\sqrt{140-90}=7.07$	
$\sqrt{\rho}$	≈		Assumed approximately the same, mean pressure does not differ much
$\frac{1}{f^{3/2}}$	$\frac{1}{\left(8.1\cdot 10^{-3}\right)^{3/2}}$	$\frac{1}{\left(7.6\cdot 10^{-3}\right)^{3/2}}$	Approximate mean value from the simulations
$\frac{\partial f}{\partial k}$	$1.18\cdot 10^{-4}$	$1.66\cdot 10^{-4}$	Calculated numerically and presented in Figure 3.12
K	=		
$\frac{1}{\dot{m}}$	$\frac{1}{20.6}$	$\frac{1}{47.5}$	

Based on these calculations, the ratio between the sensitivity coefficients at high and low flow rates is 1.50. The effect of roughness on the friction factor decreases with decreasing Reynolds numbers as shown in Figure 3.12. This is also evident from the Moody diagram where the curves get closer at lower Reynolds numbers.

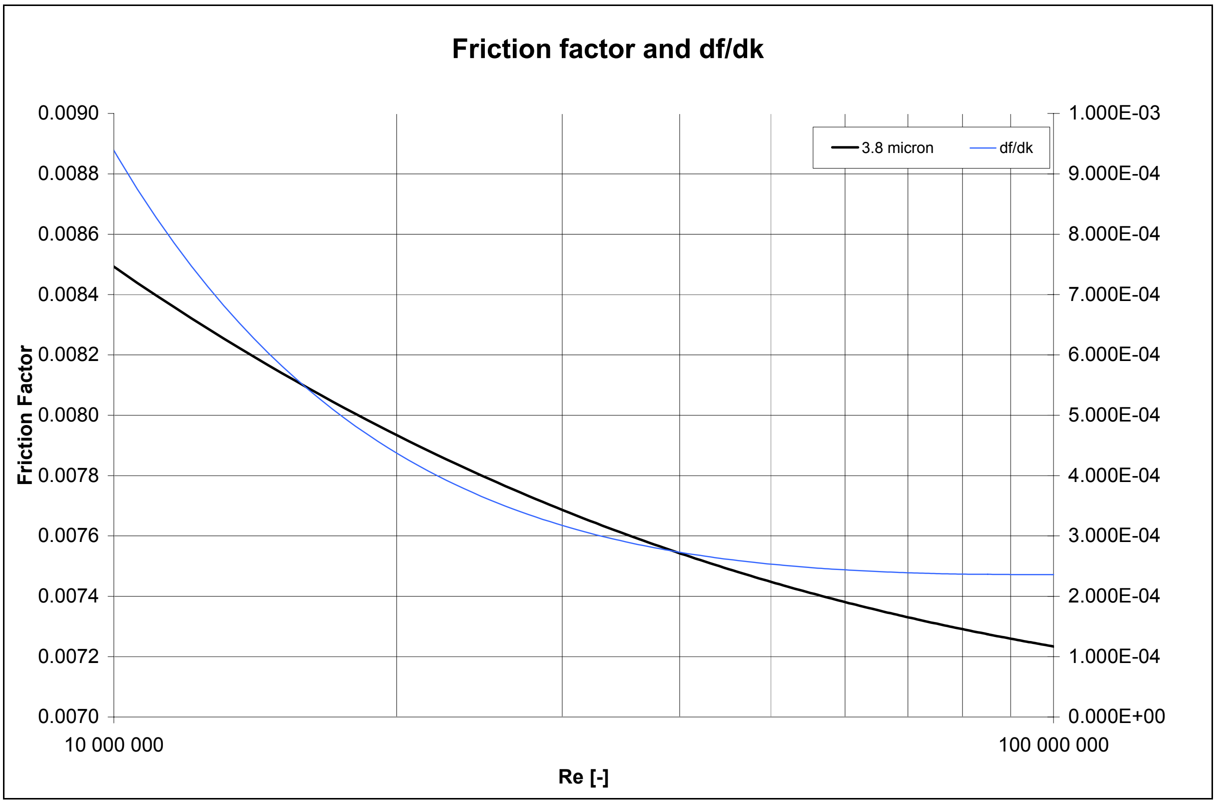

Figure 3.12 Colebrook-White friction factor for k = 3.8 micron, and the friction factor differentiated with regard to roughness.

3.5.5 Equation of state

The equation of state describes the dependence between pressure, density and temperature. No one has succeeded in establishing a theoretically founded equation of state that is valid for a broad range of conditions. The BWRS equation used by TGNet has a set of parameters that has been specifically tuned for gas compositions and pressure seen in the North Sea. The uncertainty is nevertheless still around 1%, which has been used in this sensitivity analysis.

The increased density resulted in an increased gas flow rate of 0.235 and 0.102 MSm^3/d respectively, which was the largest effect in Table 3.6 except for the change in ambient temperature.

CHAPTER 4

Experimental: Viscosity measurements

4.1 Introduction

The *viscosity* of a fluid is a measure of its resistance to being deformed by either shear stress or extensional stress. A low viscosity fluid, such as water, is usually considered a "thin" fluid, whereas a high viscosity fluid, like oil, is considered "thick". The viscosity relates the shear stress to the velocity gradient, and in a Newtonian fluid this *dynamic viscosity* factor, is constant across different conditions. Both turbulence and frictional resistance in fluid flow are due to viscous forces, which are intermolecular forces and still not very well understood.

The importance of a correct calculation of the dynamic viscosity was analyzed and discussed together with other parameters in the sensitivity chapter (CHAPTER 3). It turned out that the viscosity is an important parameter with regard to the unlinearity it represents. The sensitivity coefficient regarding the mass flow rate was found to be -0.049 for the high flow rate case (mean Re ~ $37\cdot10^6$) and -0.034 in case of low flow rate (Re ~ $15\cdot10^6$). The influence of the viscosity calculation is not very large, but the unlinearity it represents calls for further investigation.

The theory still fails to give a full description of the molecular motion and intermolecular forces, and so the predictive models need to be partly based on empirical results as well. Most efforts, both theoretical models and measurements, are focused on artificial gas compositions of only a few components. The Lee-Gonzalez-Eakin (LGE) equation was presented by Lee et al. (1966), see also Section 2.2.3. It is an empirical correlation using nine coefficients which is based on 3,000 viscosity measurements of gas hydrocarbon mixtures. Several updated parameter sets exist. SUPERTRAPP is a commercial computer program developed by the US National Institute of Standard and Technology (NIST), and calculates the thermodynamic and transport properties of pure fluids and fluid mixtures, see Huber (2007). It is based on the corresponding-states principle. The Lucas equation is an old, empirical correlation, and is described in Poling et al. (2000). Vesovic (2001) summarizes the Vesovic-Wakeham methodology which is based on rigid-sphere theory, and also used in the following comparisons.

Schley et al. (2004) measured the viscosity on pure methane and on two different real natural gas samples using a vibrating wire instrument. They covered a wide range in temperature and pressure, and used the measurements to develop a new viscosity equation. Assael et al. (2001) presented viscosity measurements on one artificially created natural gas sample covering a wide range of pressures and temperatures. Nabizadeh & Mayinger (1999) is the last one of the recent viscosity measurements performed on natural gas. Their measurements are quite limited in pressure range, in that they only reach 5 MPa (50 barg).

In this chapter new viscosity measurements of three different natural gas compositions are reported and analyzed with regard to known predictive models.

It should be noted that the gas chromatograph analysis and viscosity measurements were performed by external parties. Other persons in Gassco also contributed partly to the literature review and implementing the prediction correlations in Excel, which enabled comparison with the present measurements. The author organized and supervised the abovementioned work. The discussion, data analysis and further use of the recommended viscosity correlation are solely the work of this author.

4.2 Measurement results

Three different gas samples were taken at the Kårstø and Kollsnes gas processing plants on the west coast of Norway. Kollsnes receives wet gas from the Troll, Visund and Kvitebjørn fields, separates the lean dry gas and sends it to continental Europipe through export pipelines. Six 4-liter bottles were filled with lean dry gas at around 150 barg. Kårstø processing plant receives dry rich gas from mainly the Åsgard area and the Statpipe area through two pipelines. The heavy components are separated out and transported by ship, and the dry lean gas is transported to continental Europe through Europipe 2 or via a pipeline to the Draupner platform. Two gas samples were taken at this plant, one with unprocessed rich dry gas and one with processed lean dry gas. Six different bottles were filled at line pressure, which is around 150 barg, in both cases. Each sample consisting of six bottles was reduced to two bottles by increasing the pressure to 450-500 barg.

The three gas samples enclosed in the six bottles were then sent to Ruhrgas' laboratory in Germany for compositional analysis and to Thermophysical Properties Laboratory at Aristotle University in Greece, where Professor Marc Assael and his group measured the viscosity for the samples. He uses a vibrating-wire viscometer with a claimed uncertainty of 1%. The instrument and measurement technique is well reputed and thoroughly described in Assael et al. (2001). The apparatus was calibrated with nitrogen at different pressures before and after each measurement series to ensure its good operation throughout the series. All the results were supplied to Gassco in three different reports, and the detailed results for all measurement points, including the gas compositions, are listed in Langelandsvik et al. (2007) (see Appendix D), and also briefly summarized here.

Five nominal isotherms were covered: 263, 278, 283, 288 and 303 K. For each isotherm, the pressure ranged from 5 to 25 MPa at 2.5 MPa steps (lean dry gas samples), which yielded a total number of 45 measurement points for each of these two samples. For the rich dry gas sample, which is named Sample 2, the pressure ranged from 13 to 25 MPa at 2 MPa steps in order to avoid liquid dropout. Accordingly, 35 measurement points were covered.

The measurements were compared with predictions from the models which were mentioned in the previous section. The deviations are plotted in Figure 4.1 to Figure 4.3 for the 283 K isotherm. Deviation is defined as:

$$deviation = \frac{\mu_{measured} - \mu_{predicted}}{\mu_{measured}} \qquad \textbf{Eq. 4.1}$$

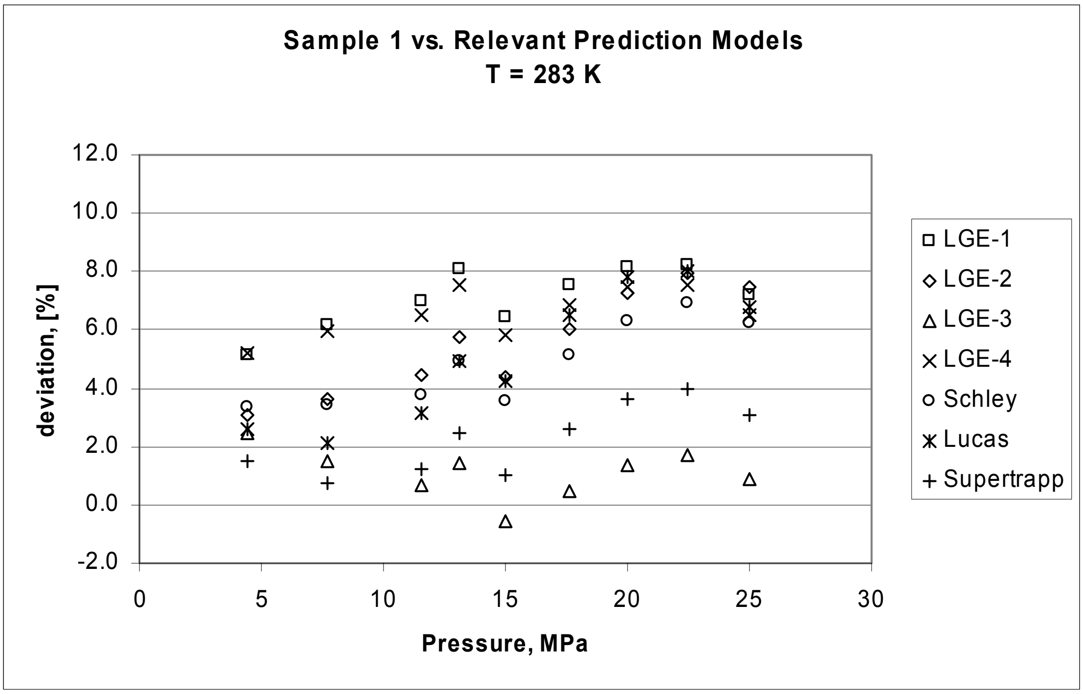

Figure 4.1 Deviation for different prediction models and Sample 1.

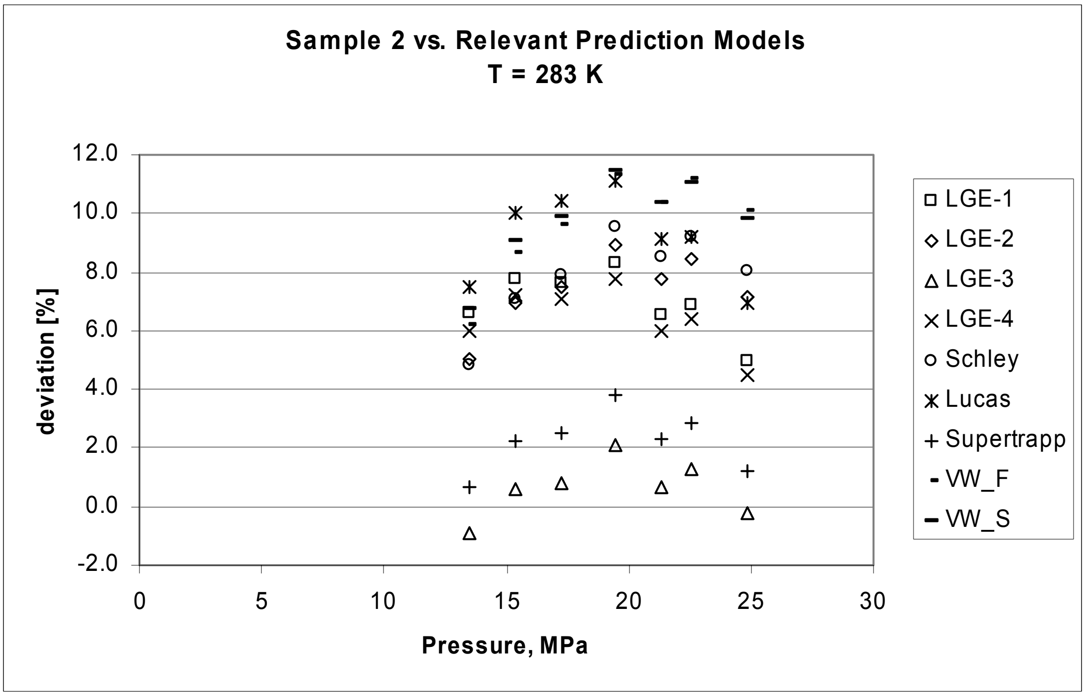

Figure 4.2 Deviation for different prediction models and Sample 2.

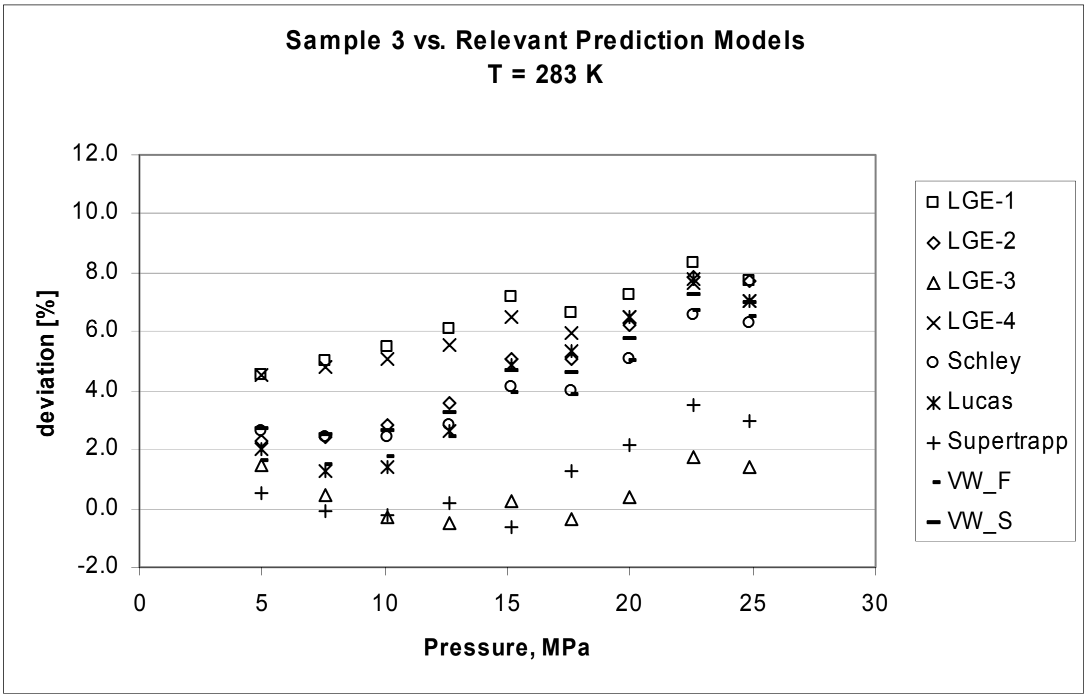

Figure 4.3 Deviation for different prediction models and Sample 3.

It is seen that most of the prediction models underpredict the viscosity. The most severe underpredictions are found for Sample 2, which is the rich dry gas with a methane content of about 80%. The Lucas correlation and the Vesovic-Wakeham scheme underpredicts by around 11% in a narrow pressure range, which is poor. The LGE-3 variant, with an extended number of decimals in the coefficients and presented by Whitson & Brule (2000), along with the SUPERTRAPP program, provide the most accurate predictions. The deviations vary between -1 and 4% which is a very good performance.

The parameter set of LGE-3 is shown in Table 4.1.

Table 4.1 LGE-3 coefficients.

k1	k2	k3	K4	k5	k6	k7	k8	k9
9.379	0.0161	209.2	19.26	3.448	986.4	0.0101	2.447	-0.2224

It is considered more challenging to predict the viscosity with high accuracy at high pressure than at low pressure, and this trend can to some extent be seen here as well. The deviations tend to be a little smaller at low pressures than at high pressures.

4.3 Discussion

It is seen that most viscosity prediction models tend to underpredict the dynamic viscosity for the real gas samples that are investigated. Most prediction models rely on artificially made gas samples with less components than that of a real natural gas sample. A natural gas sample may also contain trace components of different kinds, that possibly could affect the measurements. It is nonetheless the viscosity of real gases that are of interest in a real application, so the prediction models need to be calibrated against such gas samples. Based on the results obtained in this study, the clear recommendation is to use the LGE-3 variant instead of other prediction models and other LGE variants. The three gas samples that were taken represent three different gas compositions and sample points, and they all exhibit the same trend.

By using the new LGE coefficients named LGE-3, the experimental friction factors for Kårstø-Bokn change slightly leftwards. The slope of a possible fitted curve also decreases a little. But the effect of this change is small compared to the total uncertainty of the data, which will be fully analyzed in Section 7.2. But based on the present viscosity measurements it is nonetheless concluded that LGE-3 probably gives a better viscosity prediction for gases with the composition seen in the North Sea. It is hence recommended to use LGE-3 instead of LGE-1.

CHAPTER 5

Experimental: Roughness Measurements

5.1 Introduction

Exact characterization of the inner pipe surface is very important when trying to improve the link between the physically measured roughness and its application in flow models. Several parameters may be used in this characterization, but the two most popular ones are R_a and R_q, which are defined as the average absolute roughness and the root mean square roughness respectively. They are defined as:

$$R_a = \frac{1}{l}\int_0^l |Z(x)|dx \qquad \textbf{Eq. 5.1}$$

$$R_q = \sqrt{\frac{1}{l}\int_0^l Z^2(x)dx} \qquad \textbf{Eq. 5.2}$$

It has long been an open question how to use R_a and R_q to establish the sand grain equivalent roughness k_s, which is used in the Colebrook-White formula. It is also questioned if other parameters are needed to determine the friction factor accurately.

The research group in H.E.F. Group, an institute based in France, specializes in the roughness characterization, and is well reputed among several industries with high requirements to accurate surface characterization. It was therefore hired to measure the roughness in coated pipelines which were about to be installed in the Langeled South pipeline running from Sleipner Riser Platform in the North Sea to the receiving terminal in Easington, UK. These were the pipes available for measurement at that moment, but as will be shown, the measured roughness in these pipelines is believed to be a good representation of the roughness in any coated Norwegian pipelines.

In addition to performing the roughness measurements, the research group calculated the different roughness parameters. All the analysis is performed by this author.

5.2 Pipes and coating

The pipes used in Langeled were manufactured in Germany and shipped to Bredero Shaw in Farsund, Norway, for inside coating and application of asphalt and concrete on the outside. They were stored at the plant until shipment to the laying vessel took place. The pipe ID (inner diameter) is 1.066 m (equivalent to a nominal outer steel diameter of 44 inches), and the steel layer thickness ranges from 27.2 mm to 40.0 mm depending on the required design pressure at each specific location.

The procedure and requirements for the surface processing is specified in the Statoil governing document *Thin Film Internal Epoxy Coating for Pipelines*. The stated goal of the coating is to reduce friction and otherwise improve the flow conditions in non-corrosive gas pipelines. The coating may also offer corrosion protection during pipe storage, transport and installation. In contrast to multiphase pipelines, the dry gas pipelines do not transport oxygen or water, and are hence not exposed to corrosion during normal operation. Prior to coating the steel surface is to be shot blasted to minimum Sa 2 ½ (ISO 8501-1). The surface roughness at this stage is to be fine grade according to ISO 8503-1.

The coating is to be continuous for the full length of pipe, except for an area of 50 mm ± 10 mm next to the joint weld. The dry film thickness is specified to be between 40 and 90 μm, but most of it should be within 60 and 80 μm.

Roughness measurements were taken at five different locations in six different pipes.

5.3 Surface condition

It is clear that the surface of a pipe after one or five years in operation does not necessarily look the same as a brand new coated pipe. The dry sales gas may contain heavier components that drop out along the pipe, giving oil or condensate film on the inner surface. Contamination due to residue such as seal oil from compressor may also be present.

Figure 5.1 shows the front of a cleaning pig after a run in the 650 km long pipeline Europipe 2 in June 2007. It is obvious that such oil dirt will influence the friction along the wall compared to a clean wall. It is not known how large a portion of the pipe surface is covered by this oil/grease.

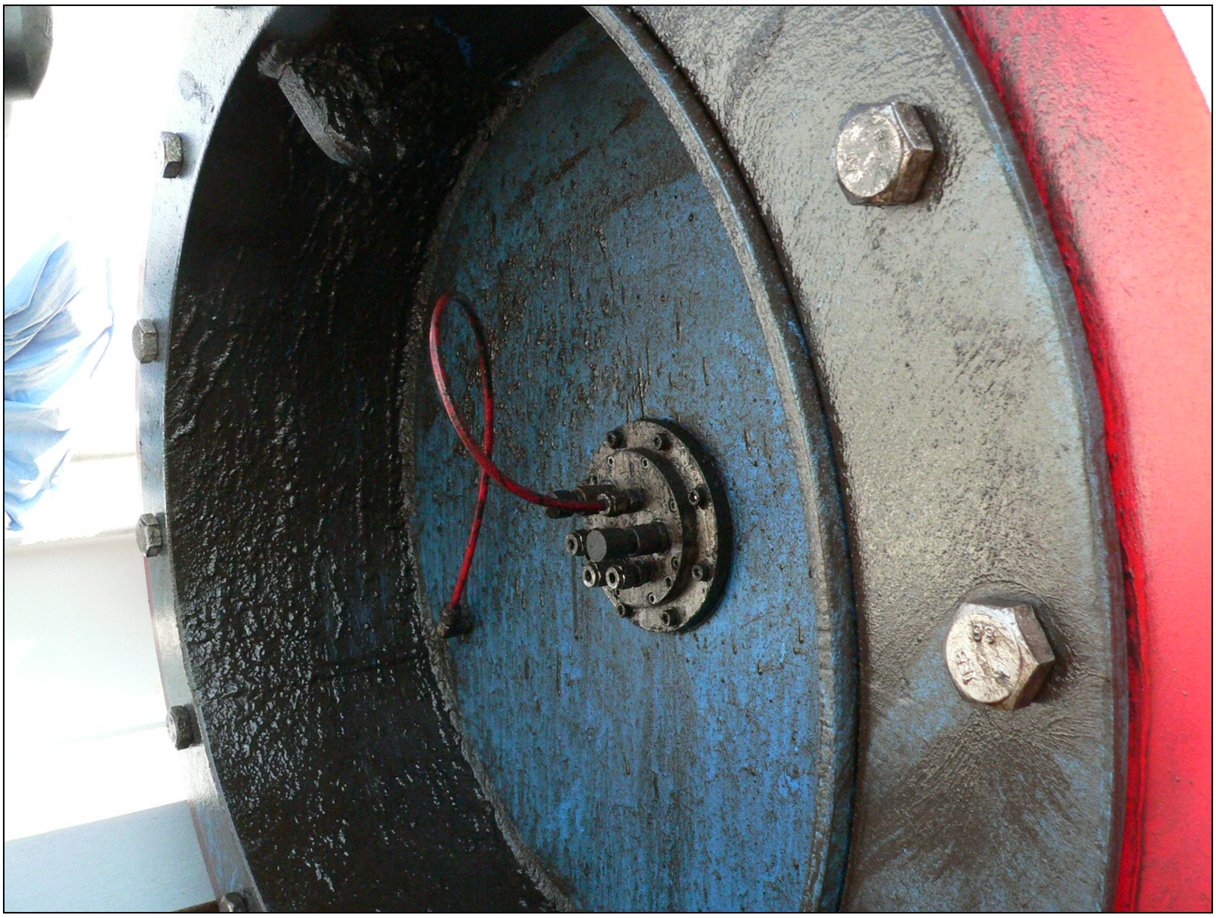

Figure 5.1 Cleaning pig in Europipe 2.

Figure 5.2 shows two pictures from cut-off pipe segments from the Norpipe pipeline, running from Draupner E to Germany. These pieces were cut off in 2007 when a new pipe was laid around the compressor platform H7. This part of Norpipe connected Ekofisk, the first platform on Norwegian sector, to continental Europipe. Hence these pipe segments have been exposed to dry natural sales gas for about 35 years.

Figure 5.2 Pipe cut-offs from Norpipe.

The internal coating is worn in some places, but the condition generally reasonable after 35 years of operation. It seems likely that the abrasion and wear will change the surface structure slightly, and hence affect the friction over time.

5.4 Methodology

HEF uses a stylus instrument which parses the surface in both x- and y-directions, giving 3D images of the surface. Bringing a high-precision roughness instrument to the site turned out to be impossible, and other alternatives were considered since one did not want to compromise the accuracy. Based on HEF's recommendations, replicas of the pipe surface were therefore made on-site with an appropriate resin (Figure 5.3). The surface parameters could then be measured indirectly in a controlled environment in HEF's laboratory in Paris.

The stylus tip was a diamond which had been machined into a cone, with a spherical shape hitting the rough surface. The tip radius was 2 μm, which enables more accurate measurements than e.g. those of Sletfjerding (1999), whose stylus tip radius was 5 μm. The size of the smallest valleys that can be accessed by the stylus is limited by this parameter.

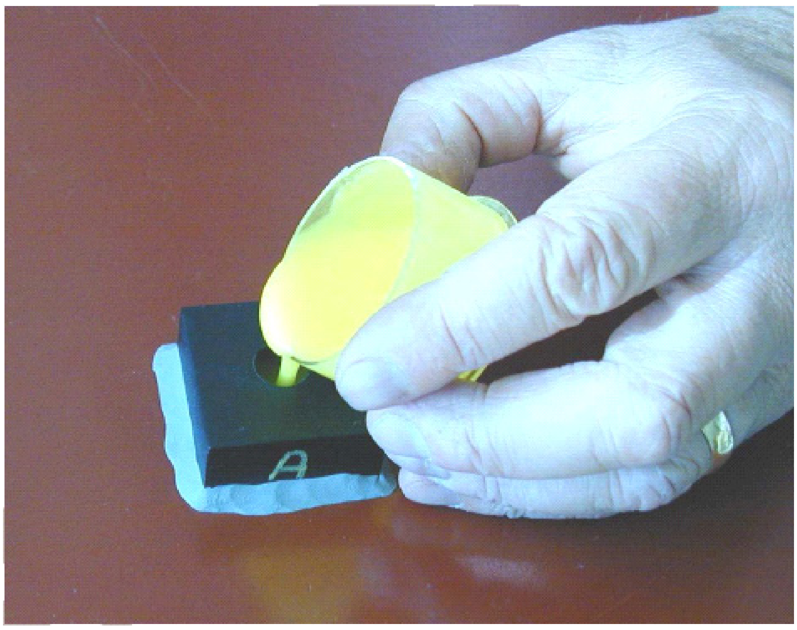

Figure 5.3 Application of resin.

Prior to the test the ability of the replica to reproduce the real surface was investigated. About 6% loss of surface patterns was seen.

The roughness was measured in six different pipes, and at five locations in each pipe: Close to the ends, in the middle and between the ends and the middle, identified as running from A to E along the pipe. An area of 2,048 x 2,048 μm was scanned for each location. The resolution in x- and y-directions is 8 μm, and the the vertical range was 100 μm. The maximum roughness wavelength that can be resolved with this sample size is 2.0 mm.

The raw data represented the primary profile. The data were also filtered in a filter with a certain cut-off wavelength, λ_c, which split the profile into one short wavelength part, the roughness profile, and one long wavelength part, the waviness profile. The selected cut off wavelength was 250 μm. This method has been described in the ISO standards 4287:1997 and 4288:1996. Unless explicitly stated otherwise, the data presented here are calculated from the primary profile.

5.5 Roughness results

The measured values for the six pipes and five different locations are shown in Figure 5.4 and Figure 5.5.

The reference plane for the roughness amplitude *Z*, as introduced in Eq. 5.1 and Eq. 5.2, is defined as the plane that minimizes the sum of the squared amplitudes across the entire plane.

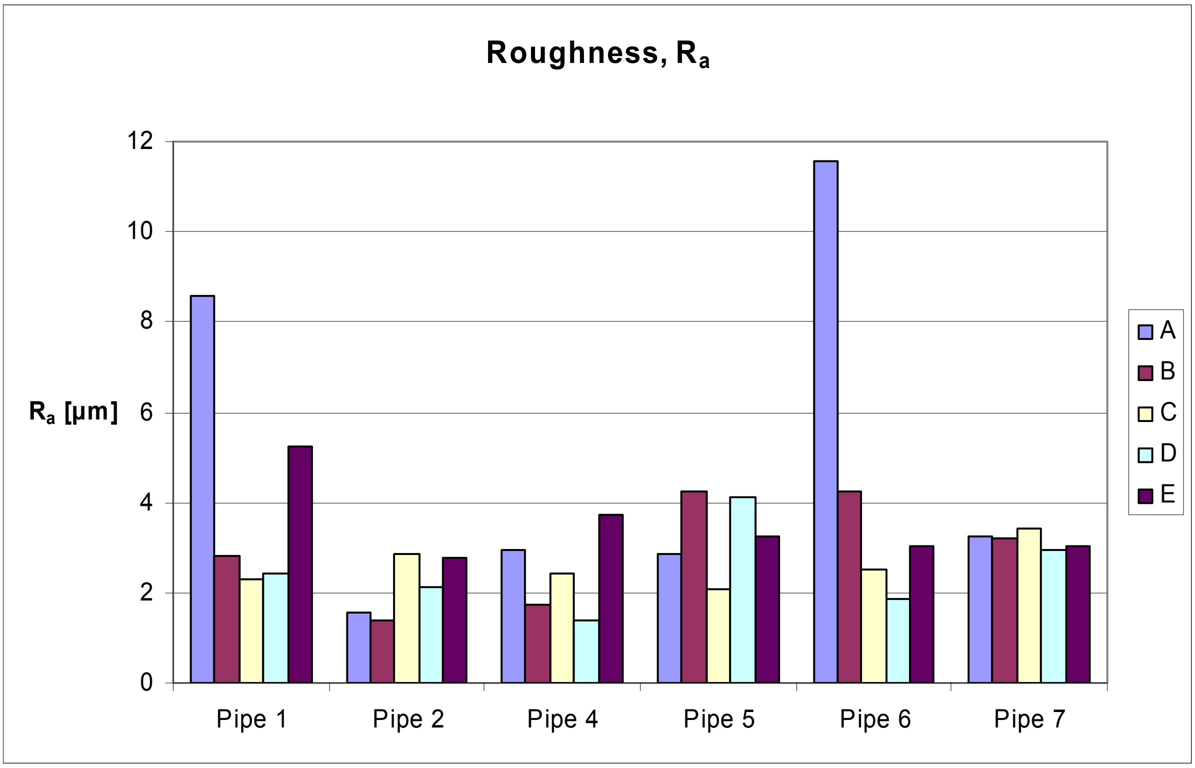

Figure 5.4 Measured R_a for the Langeled pipes.

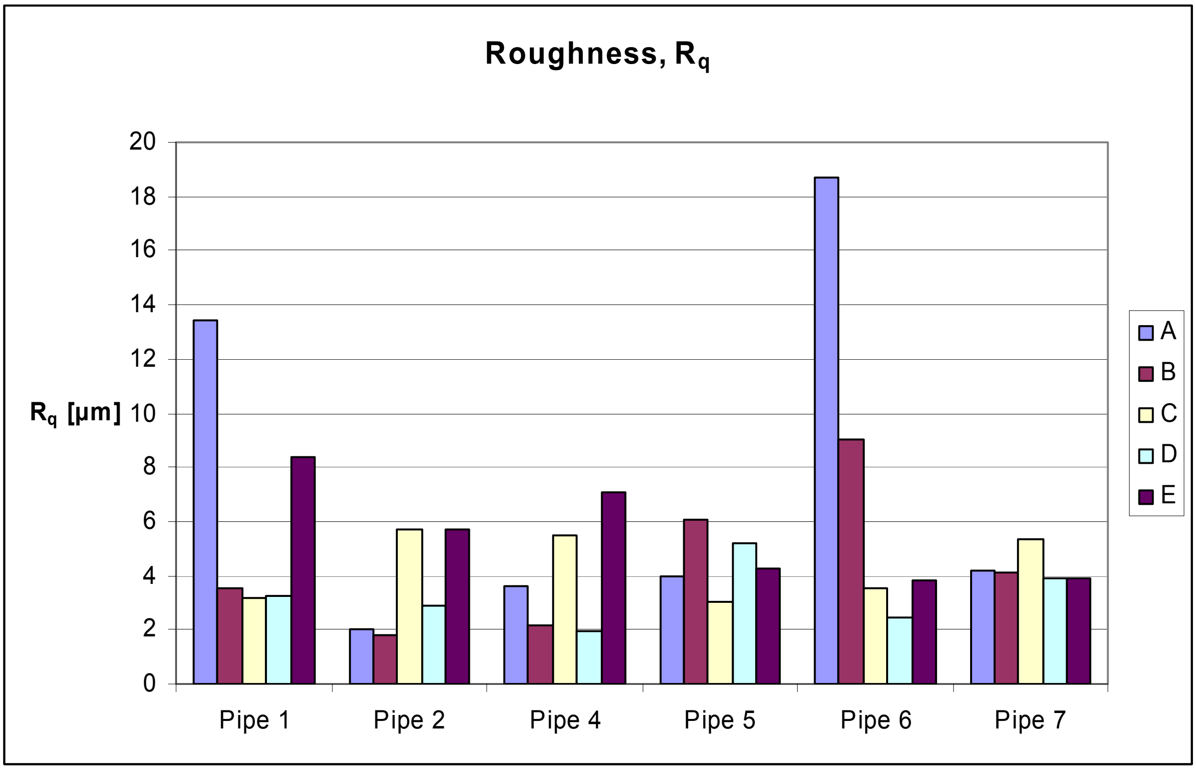

Figure 5.5 Measured R_q for the Langeled pipes.

The roughness in these pipes looks very inhomogeneous and irregular in that it varies a lot both within one certain pipe and also between the pipes. If one disregards the highest peaks, which one may treat as outliers, R_a still varies between 1.5 and 4.0 µm. The majority of the R_q values lie between 2 and 6 µm.

The inhomogeneity is obvious when one looks at the 3D images of the surfaces. Pipe1A is shown in Figure 5.6 and Pipe6A is shown in Figure 5.7. These segments have one or a few extreme summits which increases the measured roughness dramatically. The roughness does not appear to be large across the whole segment.

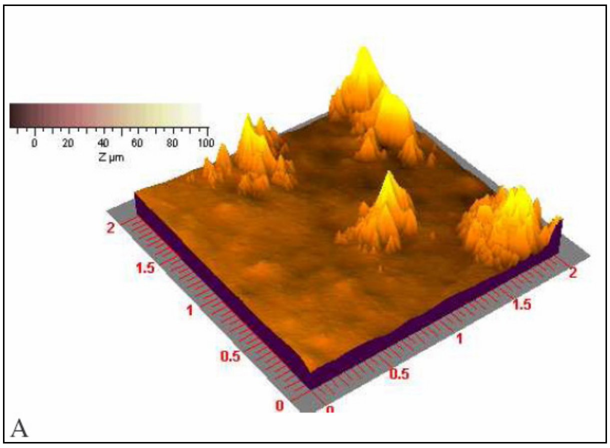

Figure 5.6 3D image, Pipe1A.

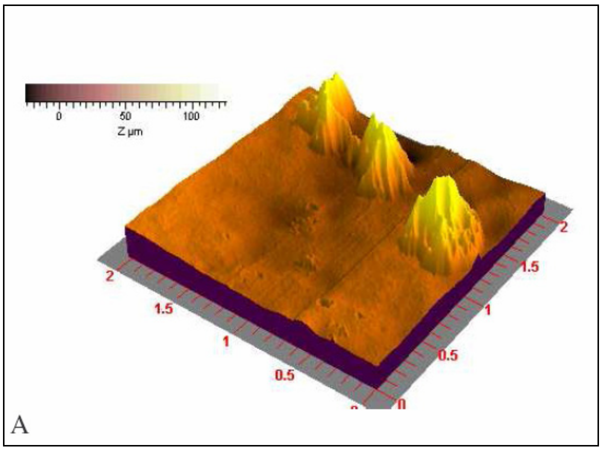

Figure 5.7 3D image, Pipe6A.

Figure 5.8 and Figure 5.9 show the roughness for another location in pipe nos. 1 and 6. There are some high peaks in pipe1C, but very little compared with pipe1A. In pipe6D there are no high peaks at all.

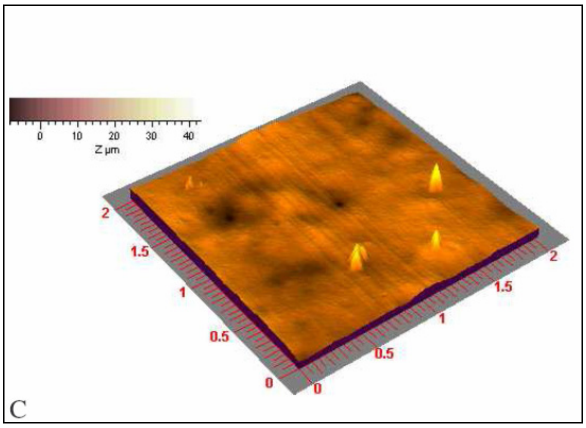

Figure 5.8 3D image, Pipe1C.

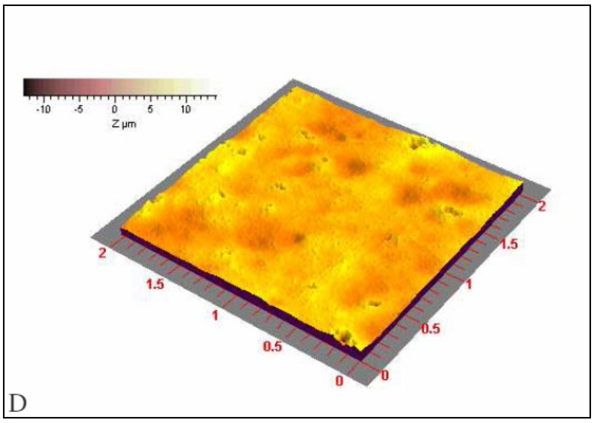

Figure 5.9 3D image, Pipe6D.

Very large portions of the surface seem to have a root mean square roughness around 2-6 µm, but at some locations the peaks reach as high as 50-80 µm above the surrounding areas. From Figure 5.6 and Figure 5.7 each high peak seems to cover a square of 0.5 mm at a maximum. It has been discussed with HEF whether these peaks are real or represent measurement errors, and they are confident this is a real part of the pipe surface. A good average rms roughness is taken as 4 µm.

These measurements may be compared with the measurements reported by Sletfjerding (1999). He measured the roughness in coated full-scale pipelines and found an R_a of 1.36 µm (standard deviation around 0.35 µm) and Rq of 1.81 µm (std 0.55 µm). This is less than found in our extensive measurements.

As originally proposed by Colebrook and White (1937) and also discussed in Langelandsvik et al. (2008), it is believed that the roughness distribution affects the transitional region. The largest roughness elements will first protrude into the turbulent region, and they will therefore determine the point of departure from the smooth curve. The statistical measure of the distribution width is the kurtosis (flatness or 4th order momentum), defined as:

$$kurtosis = \frac{\int_{-\infty}^{+\infty} (x-\mu)^4 f(x)dx}{\sigma^2} \qquad \textbf{Eq. 5.3}$$

A normal distribution has kurtosis 3. A larger kurtosis indicates a more peaked distribution with slightly fatter tails, whereas a lower kurtosis has a less pronounced peak and thinner tails.

The kurtosis from the different spots is given in Figure 5.10.

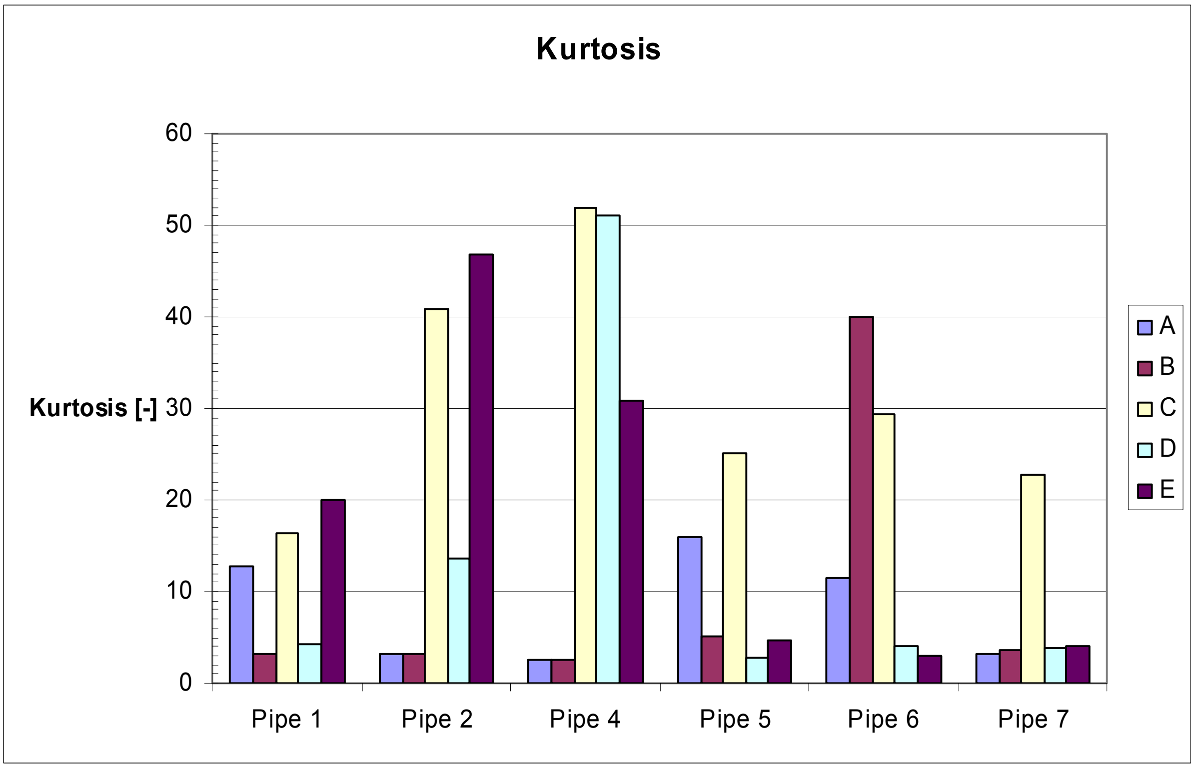

Figure 5.10 Measured roughness kurtosis in Langeled pipes.

For the vast majority of the measured spots, the kurtosis is larger than 3. For some of the spots, e.g. Pipe 4 C and D, the kurtosis reaches as high as around 50. By inspection of the surface images, the high kurtosis spots correspond to the spots which contain a few regions with very high large roughness. Because of these regions, the roughness probability function has a very long tail giving the high kurtosis. These few large roughness regions will start protruding into the turbulent region at a low Reynolds number, but since they do not cover a substantial part of the surface area, the additional drag will be modest. It might however make the friction factor depart from the smooth curve.

5.6 Determination of sand grain equivalent roughness

Establishing a model roughness, e.g. the sand grain equivalent roughness of Nikuradse, based on measurements of the surface roughness has long been a challenge. Most authors propose the sand grain equivalent roughness being a constant factor multiplied by the root mean square roughness, R_q, or the parameter expressing the maximum peak-to-valley roughness, R_z. The equivalent sand grain roughness is found by comparing the friction factor of the surface in question with Nikuradse's sand grain data in the fully rough region, independent of the particular form of the friction factor curve in the transitional rough region.

Two recent results of estimates of the sand grain equivalent roughness are the one of Shockling et al. (2006) and Sletfjerding (1999). Shockling found that k_s equals 3 times the root mean square roughness in a honed aluminium pipe. Sletfjerding measured k_s and R_q in a series of artificially roughened pipes, and found a multiplicative factor in the range 4.5 – 6.0. The measurements in a commercial steel pipe by Langelandsvik et al. (2008), see Appendix B, yielded a factor as low as 1.6. By using this range of factors, the expected k_s for the coated large-diameter pipelines will be between 6.4 and 24 μm, which is a notable large range. But as

Sletfjerding (1999) points out, k_s cannot be determined solely on the basis of R_q. More parameters are needed to characterize the surface in order to determine the fully rough friction factor. As will be shown in the next section, fully rough conditions will require an extremely large Reynolds number in these pipelines, and is currently impossible to achieve.

5.7 Application to a full-scale export pipeline

All the large diameter natural gas export pipelines in the North Sea have very similar material properties and coating. It is therefore believed that the physical surface structure and roughness in all pipelines is similar to what has been measured in the new Langeled pipes. A pipeline with an inner diameter 1.016 m, corresponding to the nominal outer diameter 42 inches, is chosen for the further analysis. This matches the diameter of for example Franpipe and Europipe 2, meaning that the specific results and figures reported here are expected to be applicable to these two pipelines.

The point where roughness effects are first seen in the friction factor, is usually determined by the roughness Reynolds number k^+, which is the roughness scaled by the viscous length. The viscous length scale is defined as ν/u_τ, and $5\,\nu/u_\tau$ is usually taken as the approximate thickness of the viscous sublayer. Many people report the first roughness effects to occur at $k_s^+ = 5$, i.e. where the sand grain equivalent roughness equals the assumed viscous sublayer thickness. It is however not well defined which roughness parameter is used in this definition. The most recent controlled experiments in a pipe, Shockling et al. (2006) and Langelandsvik et al. (2008) found the first roughness effects at $k_s^+ = 3.5$ and $k_s^+ = 1.4$ respectively. At this point the sand grain equivalent roughness is only a fraction of the viscous sublayer. But the relationships between k_s and k_{rms} (R_q) were very different in these experiments, so in terms of k_{rms}^+, the departure point was found to be 1.2 and 0.9 respectively. Meaning that the root mean square roughness is close to the viscous length scale and hence around 1/5 of the viscous sublayer thickness.

By simple manipulation, the viscous length scale can be expressed as:

$$\nu/u_\tau = \frac{D}{\mathrm{Re}\sqrt{\frac{1}{8}f}}$$

Figure 5.11 plots the calculated viscous length scale in a 1.016 inner diameter pipeline. For simplicity the friction factor has been assumed to follow the 1 μm Colebrook-White line, which is a reasonable approximation due to Figure 7.15. The roughness Reynolds number is also plotted for several different values of k_s.

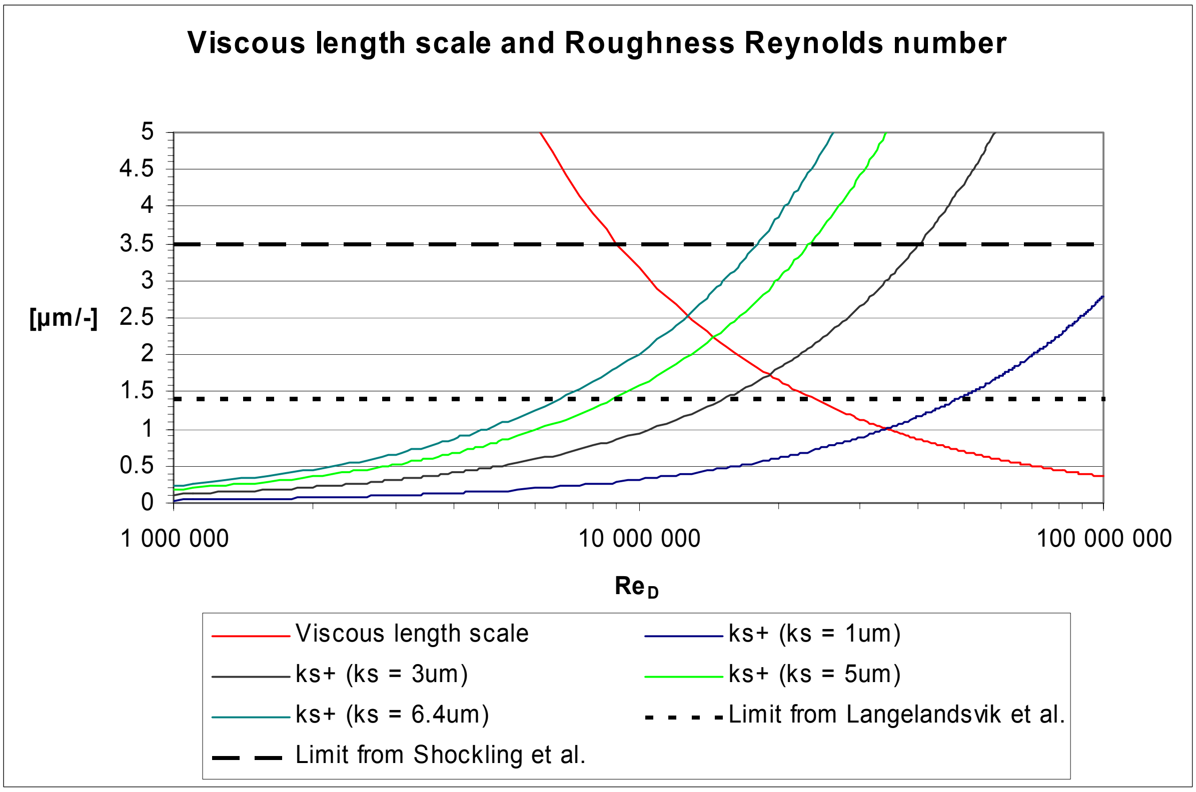

Figure 5.11 Viscous length scale and roughness Reynolds number.

By using the $k_s^+ = 1.4$ limit for the first roughness effects, it is seen that the roughness effect does not start until the Reynolds number reaches around $50 \cdot 10^6$ (k_s = 1.0 μm). For higher k_s, this limit naturally decreases. If $k_s^+ = 3.5$ is taken as the upper limit of the smooth turbulent regime, the transition point is shifted to larger Re. This is in contrast with the Colebrook-White correlation for the same roughness values. This correlation predicts a very early departure from the smooth line. From Figure 2.3 it is seen that with Colebrook-White the roughness effects are well evident at Reynolds numbers lower than $10 \cdot 10^6$.

If an average rms roughness of 4.0 μm is used, the corresponding k_s becomes 6.4 μm (Langelandsvik et al. (2008) reported k_s = 1.6 times k_{rms}), and the predicted departure from the smooth line becomes $6.5 \cdot 10^6$ accordingly. If the surface characteristic of the Langeled pipes is representative for other pipelines also with regard to the observed inhomogeneity, one may raise the question how the high peaks influence on the departure point. Even if such high peak spots are rare, they will break through the viscous sublayer at a low Reynolds number. At Re = $2.4 \cdot 10^6$, the viscous length scale has decreased to 12 μm, indicating that the viscous sublayer is 60 μm thick at this point, which is comparable in size to the highest peaks. Consequently, one may see roughness effects already as early Re = $2.4 \cdot 10^6$.

The expected point of collapse with the fully rough line can be obtained from Figure 5.12, where higher Reynolds numbers are focused on. For instance the limit found by Langelandsvik et al. (2008), k_s = 18.0, corresponds to a Reynolds number of approx. $100 \cdot 10^6$ in this pipeline, which should be good evidence of the challenges faced if one wants to cover the entire transition region in a full-scale test.

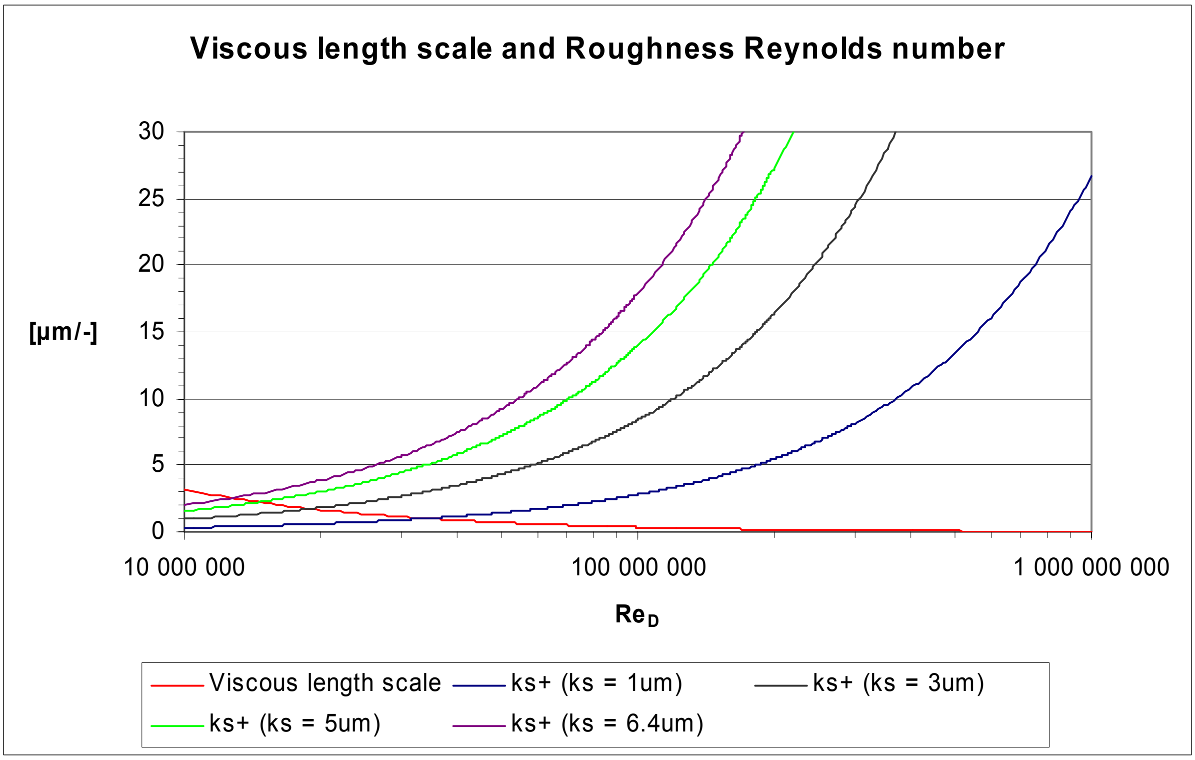

Figure 5.12 Viscous length scale and roughness Reynolds number.

5.8 Discussion

It is seen that the surface structure of the examined pipes is irregular with a large variation in both roughness and kurtosis. But the few regions with very large roughness are expected to protrude into the turbulent zone early, indicating an early departure from the smooth friction factor line. A departure point at Re ≈ $2\text{-}6\cdot10^6$ is indicated. This is earlier than the root mean square roughness indicates based on known results, but still not as early as predicted by the Colebrook-White correlation.

The link between the measured physical roughness, typically in terms of root mean square roughness, and modeled roughness, often termed sand grain equivalent Roughness inspired by Nikuradse, and how this can be used to predict the friction factor in real transport pipelines is also of great interest. Both these discussions are put off to Section 7.5.

CHAPTER 6

Experimental: Laboratory Tests of a Natural Rough Pipe

6.1 Introduction

This chapter presents friction factor and velocity profile measurements taken on a 5 inch natural rough commercial steel pipe in the Superpipe facility at Princeton University. The measurements range from Reynolds number $150 \cdot 10^3$ to $20 \cdot 10^6$, which means that they cover the smooth, transitionally rough and fully rough regimes. As far as the author is aware, this work represents the most comprehensive and detailed study of a natural rough steel pipe ever performed.

The experimental results are also presented in Langelandsvik et al. (2008), and are included as Appendix B.

6.2 Superpipe facility

The Superpipe facility was constructed in 1994-1995, in connection with the doctoral work of Mark V. Zagarola. The purpose of the facility is to enable experimental research on large Reynolds number pipe flow in different test pipes. It can be operated at pressures up to 200 barg with air velocity of 30 m/s. The corresponding maximum Reynolds number is $40 \cdot 10^6$. The first test pipe installed in the facility was a honed aluminium pipe with $k_{rms} = 0.15\ \mu m$, which resembled a perfectly smooth pipe under the given conditions. The results are presented in Zagarola (1996), and resulted in updated coefficients in the Prandtl friction factor formula for smooth pipes. A few years later, the smooth aluminium test pipe was exchanged with a rougher, but thoroughly honed, aluminium pipe. The goal was to qualitatively obtain the same roughness structure, but with larger amplitudes. The result was a test pipe with $k_{rms} = 2.5\ \mu m$. The experiments covered both the smooth, transitionally rough and rough conditions, and yielded a friction factor curve very much like that of Nikuradse with an inflectional behavior (see Shockling (2006)).

There is a continuously ongoing dispute, as to what one can call “natural roughness”. One of the comments from many scientists was that a honed aluminium pipe cannot be called “naturally rough” since it has undergone a machining process to obtain the roughness. Nevertheless, it was decided to install a third test pipe in the facility, a true natural rough steel pipe. A pipe where the surface has remained untouched by any machining process or human intervention after it was made.

Superpipe is a closed-return pressure vessel housing the actual test pipe. This eases the construction of the test pipe itself, since it does not need to hold any pressure. The pressurized air, which is the working fluid, comes from a large pressurized tank which is filled by compressors to keep the pressure at a certain level.

The flow is generated by a pump (shown down to the left in Figure 6.1), travels through a return leg, through a 180° bend before passing through a flow-conditioning section and then enters the test pipe through a contraction. The test pipe can be around 129 mm (5 inches) in diameter and 26 meters long. L/D is then larger than 200 which was proved sufficient by Zagarola to ensure fully developed flow. The primary test port is located close to the end of the test pipe. A second test port is found around 5 meters upstream of the primary test port, but this was not used in these tests.

The pump is driven by a 200 hp motor, which is controlled by a frequency controller to give the required velocity in the test section. The heat exchanger was supplied with water from a chiller, and enabled stable fluid temperature during a test.

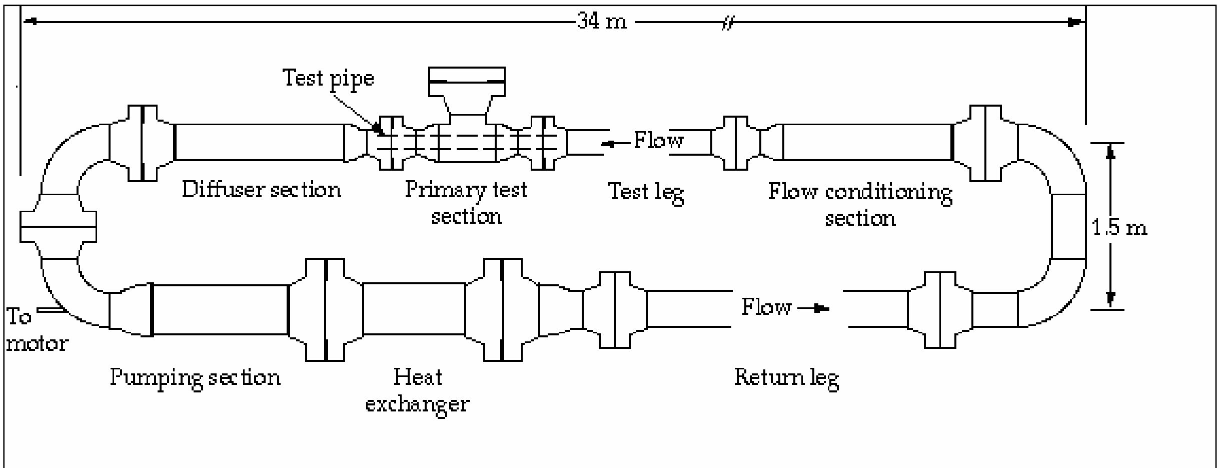

Figure 1: Diagram of the experimental facility.

Figure 6.1 Sketch of Superpipe facility.

6.3 Installation of natural rough steel pipe

The natural rough steel pipes had been shaped by bending steel plates and applying a longitudinal weld. They were supplied by Lincoln Supply in Trenton, New Jersey. The test pipe consisted of 6 segments, which were named A, B, C, D, EF and G. Section EF contained the pressure taps, and section G held the test access port. The length of section A, B, C and D was 4,723 mm (15 ft, 5-15/16 in) section EF measured 4,320 mm (14 ft, 2-1/16 in), while section G measured 1,373 mm (4 ft, 6-1/16 in). The entire test pipe was enclosed in the pressure vessel, which has been thoroughly described in Zagarola (1996).

Flanges were welded on the outside of the test pipe, a male flange at the upstream end and a female flange at the other end. Screws were then used to join the pipes together. See Figure 6.2 for details. The ends of the test pipes were made sufficiently squared to avoid a gap in the joint. This was measured in the assembling process. Shims were used in the flanges to ensure that the inside surface of the two connecting test pipe sections were flush in the joint. With a flashlight pointed down the test pipe, even a step of 25-50 μm appeared as a shiny spot or half moon to the observer. The steps in the assembled pipe are estimated to be less than about 50 µm, and they only appear in a small fraction of the circumference.

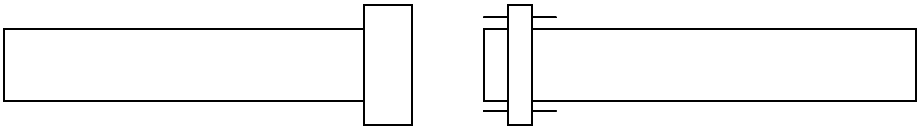

Figure 6.2 Connection of two test pipes.

For the alignment process of the new test pipe, a theodolite was used. The position and direction of the theodolite was set before the previous test pipe was disassembled. An object of almost the same diameter as the test pipe with a cross at the center was used as a target in the alignment process, and was slid up and down the pipe using a leaf blower. This ensured both that the new test pipe was straight, and that it came into the same position as the previous one, which simplified the close up of the test loop. It was ensured that all joints were aligned with the target line, within an uncertainty of +/- 0.5 mm. Furthermore, the maximum deviation from the target line at any point along the different segments was 1.5 mm. A maximum deviation of 1.5 mm at the middle of a 4,723 mm long segment, yields a radius of curvature of about 1,850 m, which gives a radius ratio (divided by inner radius) of 29,000. Ito (1959) showed that the friction factor in curved pipes equals the value in straight pipes if:

$$\Omega = \mathrm{Re}\left(\frac{r}{R}\right)^2 < 0.034 \qquad \textbf{Eq. 6.1}$$

where *Re* is the conventional Reynolds number, *r* is the inner radius of the pipe and *R* is the radius of curvature. With the numbers given above, and a Reynolds number of $20 \cdot 10^6$, Ω evaluates to 0.023. Accordingly, the pipe was considered sufficiently straight.

The EF-section facilitated the 28 pressure taps. Here, 21 were located at the top of the test pipe, and served as streamwise pressure taps. They were equally spaced, namely 165.1 mm (6.5 in), with the first one located 914 mm (36 in) from the very beginning of the section. The last streamwise pressure tap was also part of 8 radially distributed pressure taps, equally distributed around the circumference of the pipe. The diameter of the pressure taps was 0.79 mm on the interior of the pipe. The diameter on the outer side was however doubled, to simplify the connection of the tube lines. The pressure taps were drilled from the outside of the pipe using very sharp drillbits at high rpm to minimize burr. Avoiding burr completely was very difficult since one wanted to keep the surface untouched.

The longitudinal weld seam slightly affects the inside of the pipe. The width of the seam is about 7-8 mm, and it protrudes into the pipe by 0.2-0.4 mm. This means that the weld reduces the inner cross sectional area of the pipe by about 0.01-0.02%, which is deemed negligible.

Before the pipe sections were purchased, they had probably been stored in a humid environment since rusty spots were found on the interior. Since rusty spots probably are present in real steel pipelines, whether they are used for natural gas transport, water supply or any other purpose, the rusty spots were regarded as a part of the experiment. The rusty spots were circle-shaped with a diameter of around 5 mm. They were scattered around inside the pipes, but only covered a small portion of the interior, probably less than 1%.

The inner diameter of the test pipes was measured at 6 different angles and at both ends of the pipe sections from the factory. The inner diameter varied from 129.69 mm (5.106 in.) to 130.00 mm with an average of 129.84 mm (5.112 in.). It turned out that the diameter tended to vary less from pipe to pipe than it did with angle. It was hence assumed that keeping all the test pipes at the same rotational angle would minimize the steps in the joints.

6.4 Pipe surface

It is obvious that the surface geometry plays an important role in the determination of the wall friction, and the comparison of the roughness in this test pipe to the previous test pipes in Superpipe is very interesting. To make the surfaces comparable, the parameters presented here are the same as were used to describe the roughness in the smooth and the honed rough test pipes respectively.

The surface geometry was measured by using an optical technique, and it was measured at several spots in the test pipes. It was measured both on and off rust spots and also close to the seam to reveal any possible variations in the roughness throughout a pipe. A typical picture of the surface scan is shown in Figure 6.3, and the probability density function (pdf) of the roughness distribution is shown in Figure 6.4.

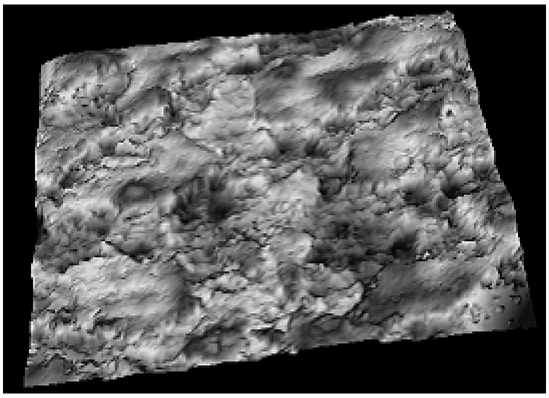

Figure 6.3 Surface scan of natural rough steel pipe.

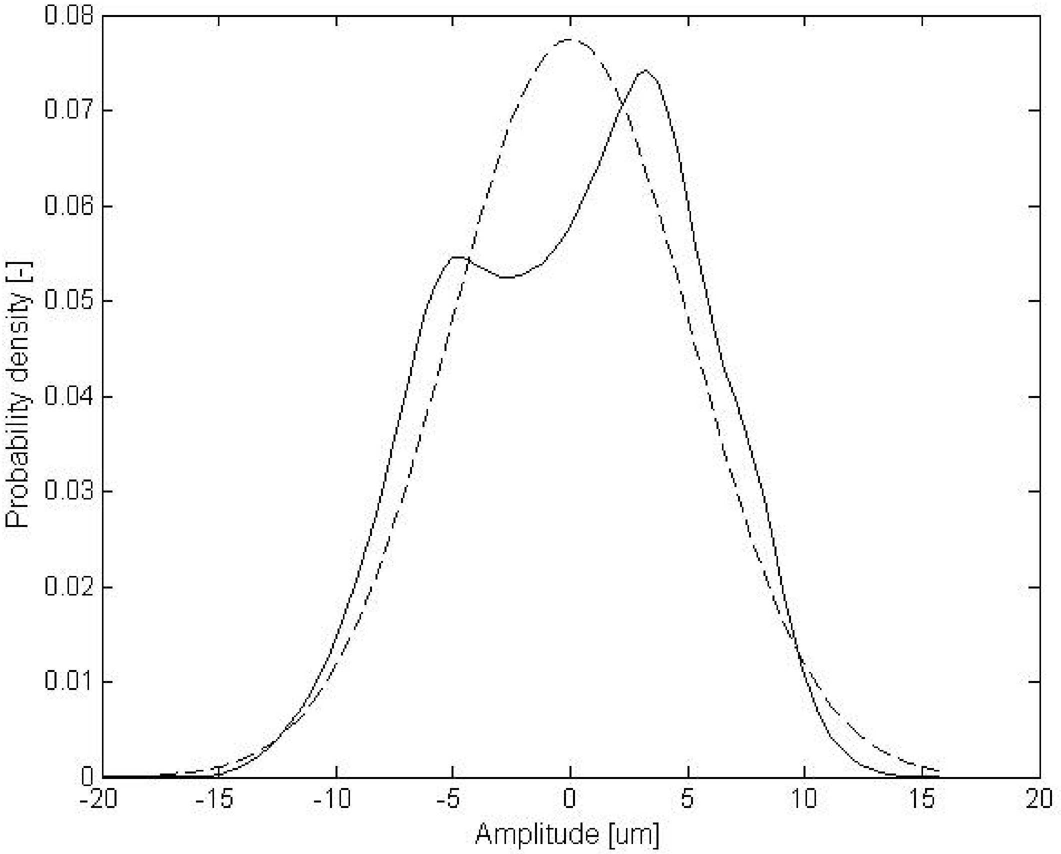

Figure 6.4 Roughness probability density function. Solid line is probability density function and dotted line is a best fit of a Gausian distribution.

For each location three different 2-D sample profiles of 1.5 mm length were taken. The root mean square roughness (R_q), the average roughness (R_a) and the flatness were calculated for each profile.

The root mean square varied between 4.5 μm and 5.5 μm with a mean of approximately 5.0 μm. This is twice the roughness that was measured in the honed pipe, which was found to be 2.5 μm. At the rust spots, the roughness increases to around 5.5-6.0 μm.

The flatness value varies a bit between the different profiles. Most values lie between 2.0 and 3.0, with a mean of around 2.5. This indicates that the probability distribution has “thinner tails” than a Gaussian distribution, which yields a flatness of 3.0, which also is evident from Figure 6.4. The previous test pipes in Superpipe, the smooth and the rough honed pipe, reported a flatness of 3.6 and 3.4 respectively. It is hence obvious that the current test pipe has a roughness distribution with “wider shoulders” and “thinner tails”. No significant difference is observed between rusty spots and non-rusty spots.

Another parameter that might be useful in describing the surface geometry is the ratio between a measure of the vertical variation and a measure of the horizontal variation. For describing the vertical variation the root mean square value, R_q is used. In horizontal direction a typical wavelength is wanted. A convenient wavelength is found by counting the number of high spots (*HSC*) exceeding R_q over a distance l, and use this to calculate $\lambda_{HSC} = l/HSC$. This quantity expresses something about the spatial distance between the large roughness elements. The steel pipe had $\lambda_{HSC} = 125\text{-}160\ \mu m$, while Shockling's honed aluminium pipe had $\lambda_{HSC} = 90\ \mu m$. λ_{HSC} can be further non-dimensionalized by dividing by R_q. The steel pipe showed a value of around 30, while this value was 36 for Shockling's honed aluminium pipe. It is seen that for the steel pipe the high spots appeared farther away from each other with regard to absolute distance, but closer when non-dimensionalized with the roughness.

Colebrook & White (1937) suggested that small roughness elements that were shielded by a few scarcely distributed large roughness elements could influence the friction behavior and lead to an early departure from the smooth friction factor curve.

6.5 Measurement technique

The mean velocity measurements were taken using a 0.40 mm pitot probe, which was mounted to a strut traversing to the pipe centerline. The strut was fitted through an oval shaped plug of the pipe, which was hand-fitted to the hole in the test port to ensure a flush interior surface. Two reference pressure taps on the plug were used to complete the dynamic pressure measurements. To find the velocity from the pitot probe measurements, several corrections were used. The integrated velocity profile yielded the bulk velocity. The traversing strut and the data acquisition were controlled by a labview program on a computer.

The pressure gradient measurements, from which the wall shear stress was calculated, was obtained by sequentially measuring the pressure difference between each of the 21 streamwise positioned pressure taps, and the reference taps used in the velocity measurements. A tube was attached to each of these taps and to a scanivalve. The scanivalve then stepped through each of these taps, and connected its line to a set of differential pressure transducers before the actual pressure was sampled for 40 seconds. Two different MKS Baratron transducers (with range 1 Torr and 10 Torr) were used in the low Reynolds number tests which were run at atmospheric conditions. In the pressurized tests, four Validyne DP transducers with diaphragms capable of a differential pressure of 0.2 psi, 1.25 psi, 5 psi and 12 psi respectively were used. Effort was taken to protect the small transducers when the differential pressure exceeded their range.

The absolute pressure in the facility was read at the beginning and at the end of each experiment, and was used to calculate the density and the viscosity for the experiment.

The working fluid temperature was continuously sampled during a test, and was kept constant to within ±0.6 K during the experiments.

For more details about the instrumentation and the measurement technique, please see Langelandsvik et al. (2008) and Shockling (2005).

6.5.1 Corrections

Pitot probes are widely used for taking velocity measurements, and their properties are pretty well known along with the corrections that need to be made. One of the most recent results was that of McKeon et al. (2002, 2003) who studied the behavior of the pitot probes comprehensively. The measurement corrections are briefly described in this section.

The presence of a probe can influence the streamline behavior, which has to be accounted for in a flowfield with a velocity gradient. McKeon et al. (2003) tested several probes across a large range of Reynolds numbers and proposed an empirical correction which has been used here. McKeon also proposed a piecewise function to correct for wall effects, which has been employed.

The pitot probe measurements also rely heavily on the measurement of the static reference pressure at the same axial position as the pitot probe. The streamlines next to the wall will deflect slightly into the pressure tap hole, and contribute to cavity vortices. This results in an overestimation of the pressure (McKeon et al. (2002)). Based on experiments McKeon also published an empirical correction function.

The probe corrections for wall proximity and the static pressure tap corrections rely on hydraulically smooth experimental data, while in our experiments roughness effects are present in most cases. But since the scaling of the corrections is based on the wall shear and the friction velocity, which are used to scale turbulent flow properties, and a comprehensive set of rough-wall corrections do not exist, it was deemed accurate to use these corrections.

6.6 Results

6.6.1 Friction factor

The friction factor measurements are shown in Figure 6.5 together with error bars, the Colebrook-White curve with $k_s = 8\ \mu m$ ($= 1.6k_{rms}$) and with $k_s = 15\ \mu m$ ($= 3.0k_{rms}$). It is clear that measured departure from the smooth line occurs at a higher Reynolds number than predicted by Colebrook-White. The transition to fully rough turbulent flow is also more abrupt, and the deviation between the measurements and the relevant Colebrook-White curve is significant in the region.

As discussed in Appendix B, the results are also best predicted by a sand grain equivalent roughness of 1.6 times the rms roughness at fully rough conditions, in contrast to the value of 3.0 to 5.0 which is commonly used.

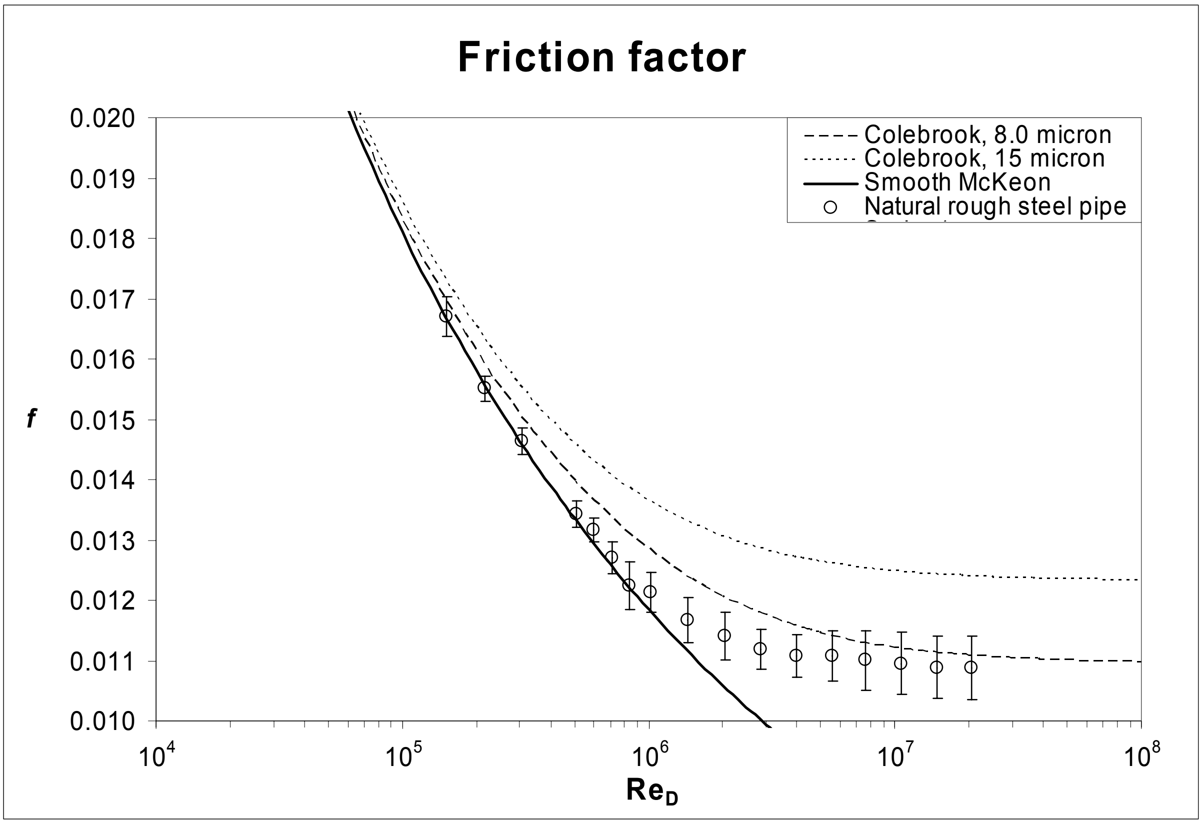

Figure 6.5 Friction factor measurements.

6.6.2 Velocity profiles

The velocity profiles in inner scaling for Re larger than $830 \cdot 10^3$ are shown in Figure 6.6. These Reynolds numbers belong to the transitionally rough and fully rough regimes. The power law and the logarithmic law using updated constants from McKeon et al. (2005) are also shown. McKeon also proposed a lower limit for the log law to be $y^+ = 600$. Above this limit, the profiles show a logarithmic behavior, though the roughness effect starts playing a role, which is seen as a downwards shift in the profiles. Eventually the maximum value of u^+ becomes constant indicating that the flow has become fully rough where only pressure drag is present.

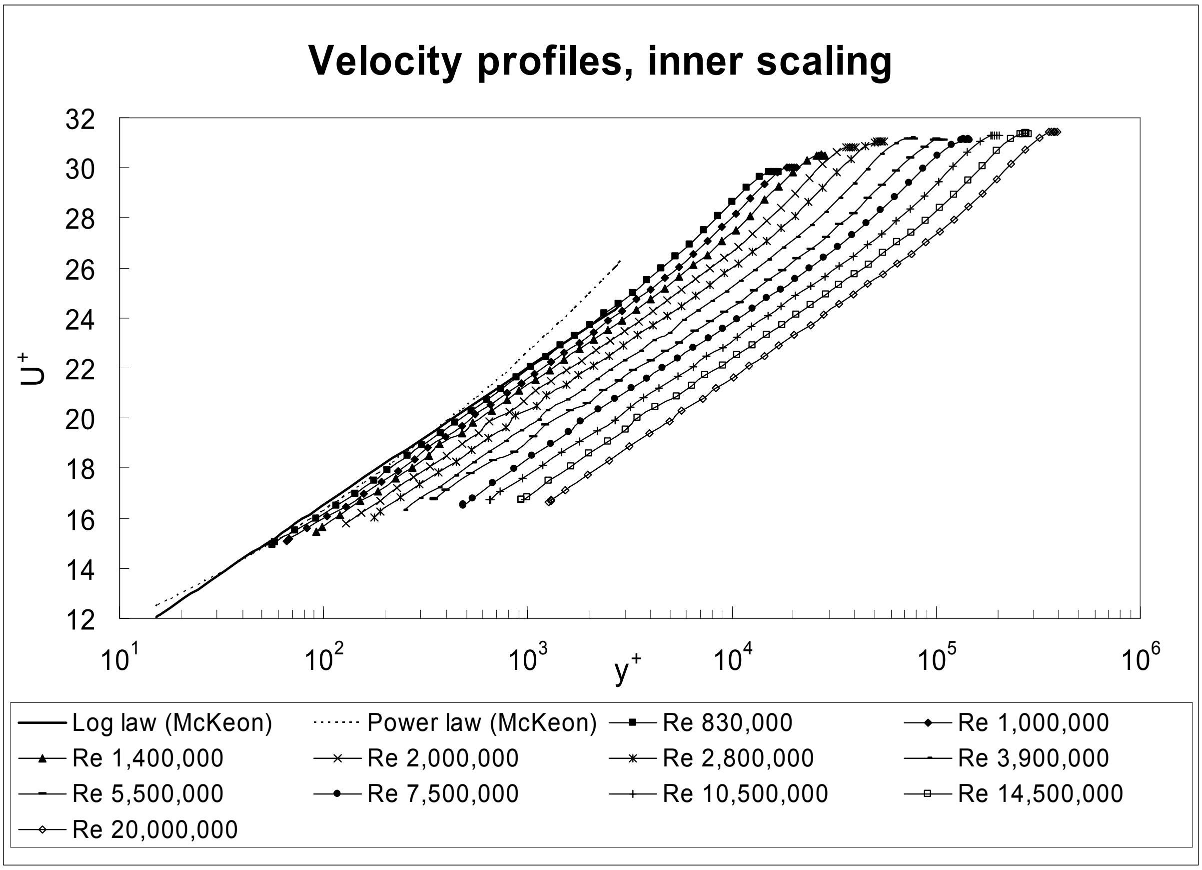

Figure 6.6 Velocity profile measurements for different Re numbers, inner scaling.

The velocity profiles are also plotted in absolute units, ie. wall distance in meters and velocity in meters per second, for two Reynolds numbers, shown in Figure 6.7.

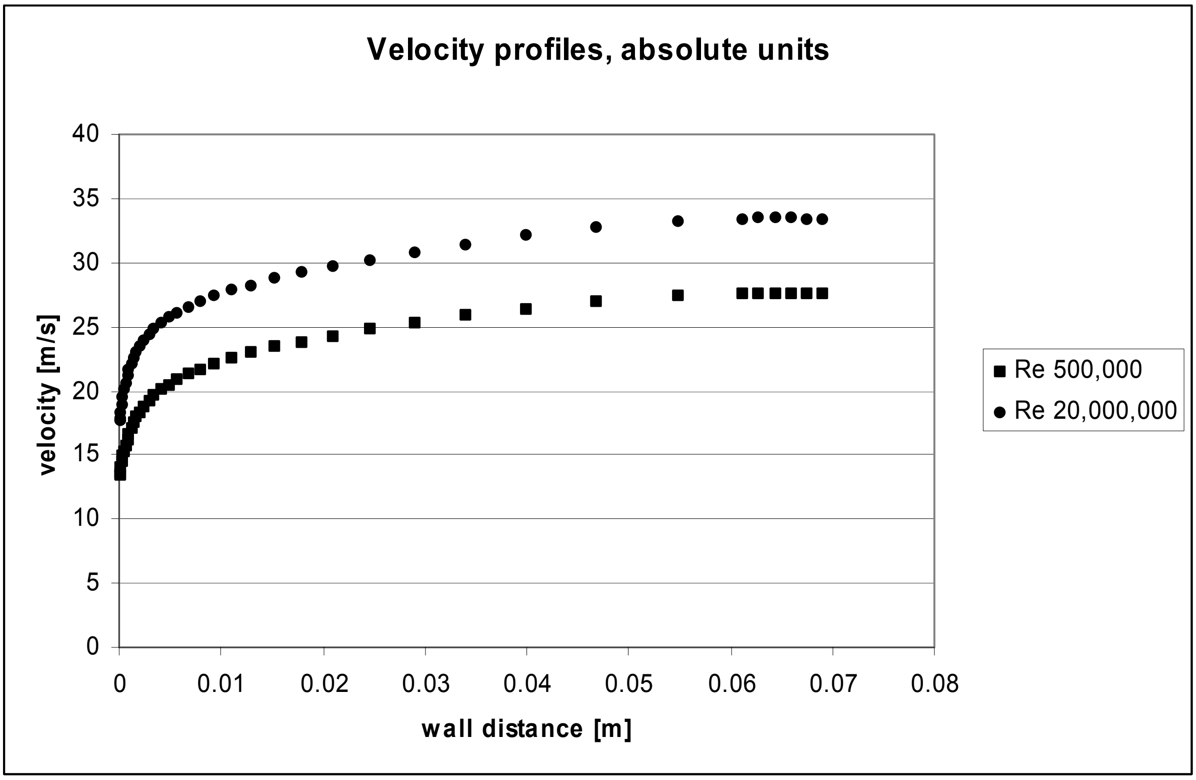

Figure 6.7 Velocity profile measurements for two different Re numbers, absolute units.

The downwards shift of the logarithmic region for different Reynolds numbers is calculated. This velocity shift is plotted in Figure 6.8, where the velocity defect is plotted versus the roughness Reynolds number, k_s^+. This gives the Hama roughness function as defined in Eq. 2.5. The first point of roughness influence, i.e. the departure from the smooth line is more easily identified in this curve and it is found to be at $k_s^+ = 1.4 \pm 0.2$. Correspondingly the collapse with the fully rough line was found to occur at $k_s^+ = 18 \pm 4.0$.

The Hama roughness function of the honed aluminium pipe is also plotted.

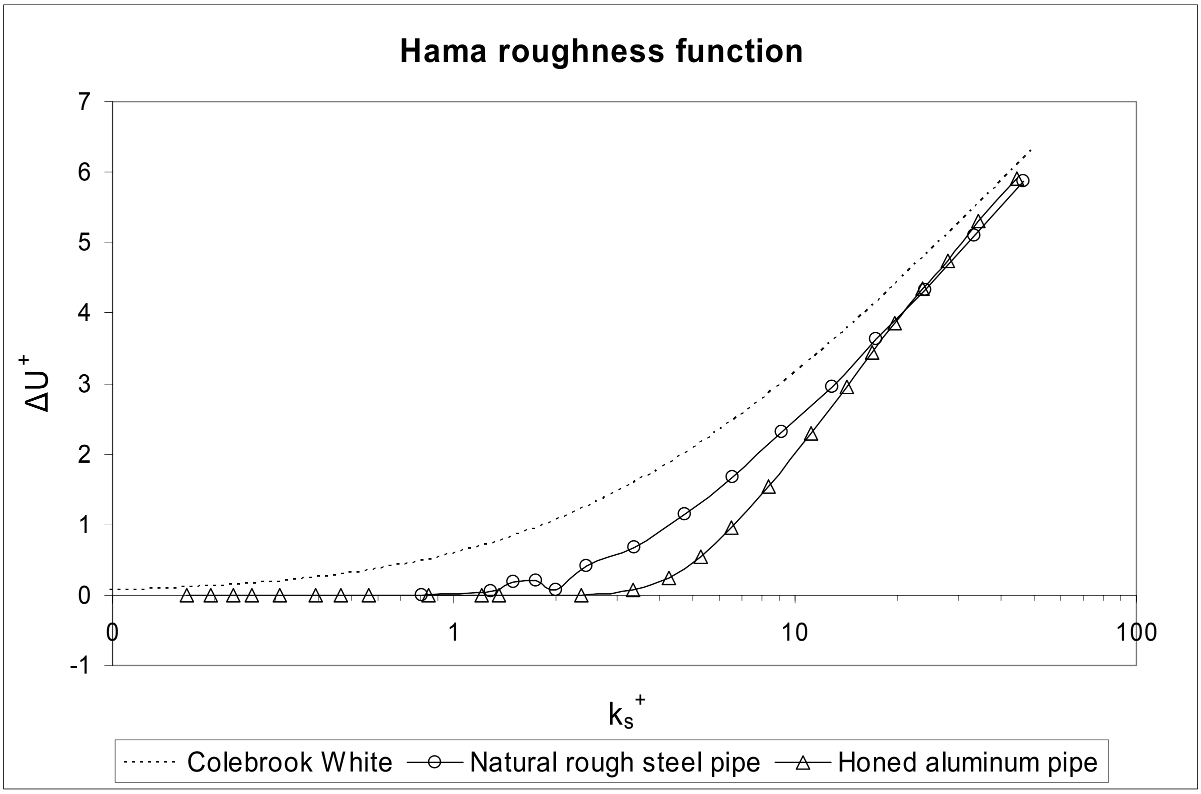

Figure 6.8 Hama roughness function.

6.6.3 Profile factors

The velocity profiles reported in Figure 6.7 were also used to calculate the profile factor in the one-dimensional momentum balance, as defined in Appendix A, Eq. A-7. The value was calculated to be 1.0155 for Re = $700 \cdot 10^3$, decreasing to 1.0126 for Re = $20 \cdot 10^6$. Gersten et al. (1999) reported 1.01 for Re = $10 \cdot 10^6$, which means that the present results are within the rounding error. The formula from Benedict (1980), which is presented in Eq. A-9 predicts 1.0124 and 1.0106 respectively, which is about 0.2-0.3% lower than the present measurements.

6.7 Uncertainty

The uncertainty in the friction factor measurement can be expressed as:

$$\frac{\Delta f}{f}=\sqrt{\left(\frac{\Delta(dp/dx)}{dp/dx}\right)^2+\left(\frac{\Delta(\frac{1}{2}\rho U^2)}{\frac{1}{2}\rho U^2}\right)^2} \qquad \textbf{Eq. 6.2}$$

assuming that the diameter does not imply any uncertainty.

In the uncertainty calculations, the one-sigma confidence interval for the pressure gradient calculation obtained from the Matlab-function is used.

To find the uncertainty in the dynamic pressure, the uncertainty in the bulk velocity calculation is first found. The uncertainty in the Validyne transducers was assumed to be 0.25% due to thorough calibration before and after each experiment, which is in contrast with the 0.5% given by the vendor. The fluid density is calculated based on the ideal gas law, and a curve fit of the compressibility factor, which is described in Zagarola (1996). The uncertainty in this process evaluates to 0.36%. This uncertainty in sample velocity at each location was evaluated using the uncertainty in differential pressure and air density. Then the uncertainty in the bulk velocity was found by integrating the contribution from the velocity at each location. This was again combined with the uncertainty in density to find the uncertainty in the dynamic pressure based on the bulk velocity.

The individual contributions and the resulting uncertainty are shown for all Reynolds numbers in the table below.

Table 6.1 Friction factor uncertainty calculations.

Re	**Pitot probe ΔP/P [%]**		**Δ(dp/dx)/ (dp/dx) [%]**	**Δ(½ρU²)/ ½ρU² [%]**	**Δ*f*/*f* [%]**
	Min (at centerline)	**Max (next to wall)**			
$150\cdot10^3$	0.97	5.88	0.76	1.76	1.92
$220\cdot10^3$	0.49	2.35	1.06	0.89	1.38
$300\cdot10^3$	0.48	2.27	1.22	0.87	1.50
$500\cdot10^3$	0.30	1.30	1.53	0.53	1.61
$600\cdot10^3$	0.26	1.03	1.45	0.48	1.53
$700\cdot10^3$	0.26	1.07	2.01	0.46	2.06
$830\cdot10^3$	0.97	3.68	2.91	1.35	3.21
$1.0\cdot10^6$	0.28	1.12	2.63	0.38	2.66
$1.4\cdot10^6$	0.28	1.08	3.18	0.37	3.20
$2.0\cdot10^6$	0.52	1.98	3.32	0.70	3.39
$2.8\cdot10^6$	0.34	1.26	2.99	0.46	3.03
$3.9\cdot10^6$	0.26	0.93	3.19	0.35	3.21
$5.5\cdot10^6$	0.63	2.16	3.60	0.84	3.69
$7.5\cdot10^6$	0.44	1.56	4.42	0.59	4.46
$10.5\cdot10^6$	0.32	1.14	4.77	0.43	4.79
$14.5\cdot10^6$	0.26	0.91	4.80	0.34	4.81
$20.5\cdot10^6$	0.33	1.20	4.82	0.45	4.84

The uncertainty in the pitot probe measurements varies a lot from experiment to experiment. This is dependent on the actual differential pressure transducer used, and how close to its maximum range it is operated. Note that the uncertainty is given as a percentage of the range. The uncertainty is larger close to the wall than at the centerline for the very same reason. It is seen that the uncertainty in dynamic pressure based on the bulk velocity is about 1.5 times the pitot probe uncertainty at the centerline.

It is also clear that the pressure gradient uncertainty is the most dominating source of uncertainty, except for the lowest Reynolds numbers. The scatter in the pressure gradient measurements increased dramatically with Reynolds number, indicating that some burr probably was present on at least some of the pressure taps. Three examples of the pressure gradient measurements are shown in Figure 6.9.

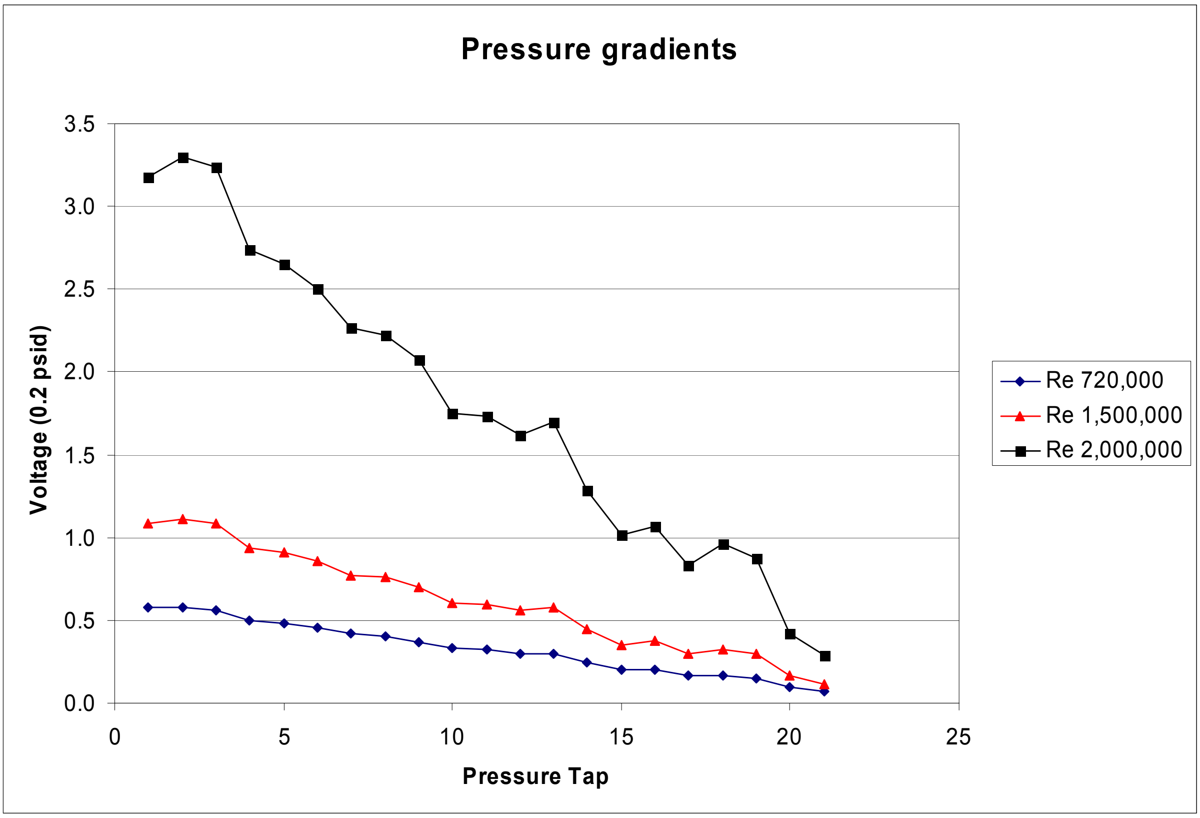

Figure 6.9 Pressure gradients.

6.8 Discussion

Two kinds of drag cause pressure drop in pipe flow. At low Reynolds numbers the flow is smooth, meaning that the roughness elements are completely covered by the viscous sublayer and the drag is unaffected by the roughness. Only frictional drag, or viscous drag is present. At high Reynolds numbers the viscous sublayer eventually vanishes, making the frictional drag zero. Instead the pressure drag causes the pressure drop. At this stage the drag is independent of viscous effects. Between these situations some of the roughness elements are in the viscous drag zone while others are in the pressure drag zone. With increasing Reynolds number, the portion of surface where only pressure drag is evident increases. The total drag will probably be an area weighted combination of frictional drag and pressure drag. And if one makes the assumption that the pressure drag per unit area is constant, the total drag can be found by weighting the two contributions by the areas they occupy.

If the departure from the smooth line occurs early, it is unlikely to see an inflectional behavior. And on the contrary if the departure from the smooth line occurs at higher Reynolds numbers, it is more likely to see an inflectional curve. In Nikuradse's famous results from 1933, the departure from the smooth line occurs at a friction factor which is lower than the fully rough friction factor of the same pipe. In this situation it is obvious that an inflectional curve will be the result. But Nikuradse's roughness type probably belongs to the most extreme case. All the roughness elements having the same height (thoroughly sieved sand) is probably the situation with lowest ratio between size of the large roughness elements and the rms roughness, which is a favorable situation for seeing an inflectional curve.

The results show a surprisingly low sand grain equivalent roughness compared with the root mean square roughness. A factor of 1.6 is significantly lower than the widely accepted value of 3.0-5.0. The explanation could probably be found by examining the shape of the roughness elements, since this factor determines the pressure drag at fully rough conditions.

The results from the commercial steel pipe also exhibit a more abrupt transition region than predicted by Colebrook-White, but not as abrupt and inflectional as in the honed aluminium pipe. The roughness distribution of the present steel pipe had slightly more rounded shoulder with corresponding thinner tails compared with the Gaussian distribution than that of Shockling et al. (2006) and the aluminium pipe. Presumably thinner tails mean fewer large and small roughness elements that can cause an early departure from the smooth line and subsequently a more abrupt and possibly an inflectional type transition. But here the effect seems to be the opposite. The explanation is probably the almost complete lack of "tails" in both distributions. The magnitude of the roughness elements is fairly restricted to 2-3 times the root mean square roughness, and perhaps the rounded shoulders of the steel pipe is the main contributor to its abrupt, but yet smoother transitional zone than the aluminium pipe.

Focusing only on k_s^+ when predicting the departure point might be misleading. k_s is relevant for the friction factor in the fully rough zone (the pressure drag), which is not the effect of interest when discussing the departure point. As found in Section 5.6, the departure point in terms of k_{rms}^+ for the present commercial steel pipe and the former rough aluminium pipe installed in Superpipe, is 0.9 and 1.2 respectively. From Figure 6.4 it can be seen that the largest roughness elements are about 14 µm, i.e. 2.8 times k_{rms}. From the probability density function in Shockling et al. (2006), the largest roughness elements are 8 µm, or 3.2 times k_{rms}. This means that in these two cases the departure point is found to be when k_{max} equals 2.5 and 3.8 times the viscous length scale respectively. This is reasonable taking into account that the common understanding is that the thickness of the viscous sublayer is around 5 times the viscous length scale. The difference in these two numbers might be attributed to experimental uncertainty and probably also to geometrical shape of the roughness elements. This means that it is not only the roughness height that determines when the first roughness effects are seen, but also its geometrical shape.

The reported point at which the flow reaches fully rough conditions is $k_s^+ = 18$ for the present measurements compared with $k_s^+ = 60$ from Shockling (estimated by Allen et al. 2005). But again the numbers get closer to each other when looking at k_{rms}^+, i.e. 11.3 and 20.0 respectively.

CHAPTER 7

Experimental: Operational Data from Full-Scale Pipelines

7.1 Introduction

A laboratory facility allows one to isolate, measure and study different effects such as friction factor, heat transfer and gas density independently of each other. The accuracy of the results is usually extremely good, which is very favorable in such tests. But laboratory tests commonly imply scaling challenges, which is also the case here. Looking at full-scale pipelines in a laboratory facility would be extremely expensive, and it would be difficult to obtain absolutely real conditions. When facing this it is clear that analysis of operational data from real natural gas pipelines is a good way to improve the knowledge about pipeline flow modeling. However, the data are usually not so accurate, but the data are real. And after all, the target is to improve the models of real pipeline flow, and not the flow in idealized conditions in a laboratory.

In a laboratory the friction factor is usually found by measuring the pressure gradient in a very limited section of the pipe. One also needs to measure the bulk velocity along with the density to get the friction factor. In a real full-scale pipeline, with a length of several to hundreds of kilometers, this approach fails. For example the density changes greatly along the pipe and the environmental conditions probably vary also, with the result that the friction is not constant along the pipe. Steady-state conditions are also harder to ensure in a pipeline where the flow rate vary continuously according to customer off-take at the exit points and operational conditions at a process plant at the entry point. For all these reasons the only way to analyze the operational data is to use a pipeline simulator.

The results in the following sections are therefore based on the application of Transient Gas Network, TGNet (version OLS 5.3, 3.12.2_GASSCOr1), from Energy Solutions International, and a configuration file for the specific pipeline. The simulator is one out of 5 to 10 well reputed simulators in the world. The whole approach is based on steady-state analysis, and operational periods with very steady operational conditions have been collected. For the full-length pipelines, Europipe 2 and Zeepipe, one such period spans 12 hours. For the Kårstø-Bokn leg, which only measures 12.5 kilometers, they span 3-6 hours. The boundary conditions at the inlet and at the outlet are averaged across this period, and used as input to the simulator. TGNet does not allow the friction factor to be manipulated directly, but requires a friction factor correlation and a roughness factor. The Colebrook-White correlation is therefore chosen as a good candidate, and the roughness is adjusted until the simulated flow coincides with the measured flow rate. When this is achieved for one steady-state period, one data point in the Moody diagram can be plotted. The whole process is illustrated in Figure 7.1, and the simulator was described in detail in CHAPTER 2.

Results from the short Kårstø-Bokn leg are presented in section 7.2, the full-length Europipe 2 in section 7.3 whereas friction factor results from Zeepipe are reported in section 7.4. Recent application of the reported results to update the calculated maximum transport capacity for these pipelines is described in section 7.5. Eventually a discussion of the full-scale operational data results is given in section 7.6.

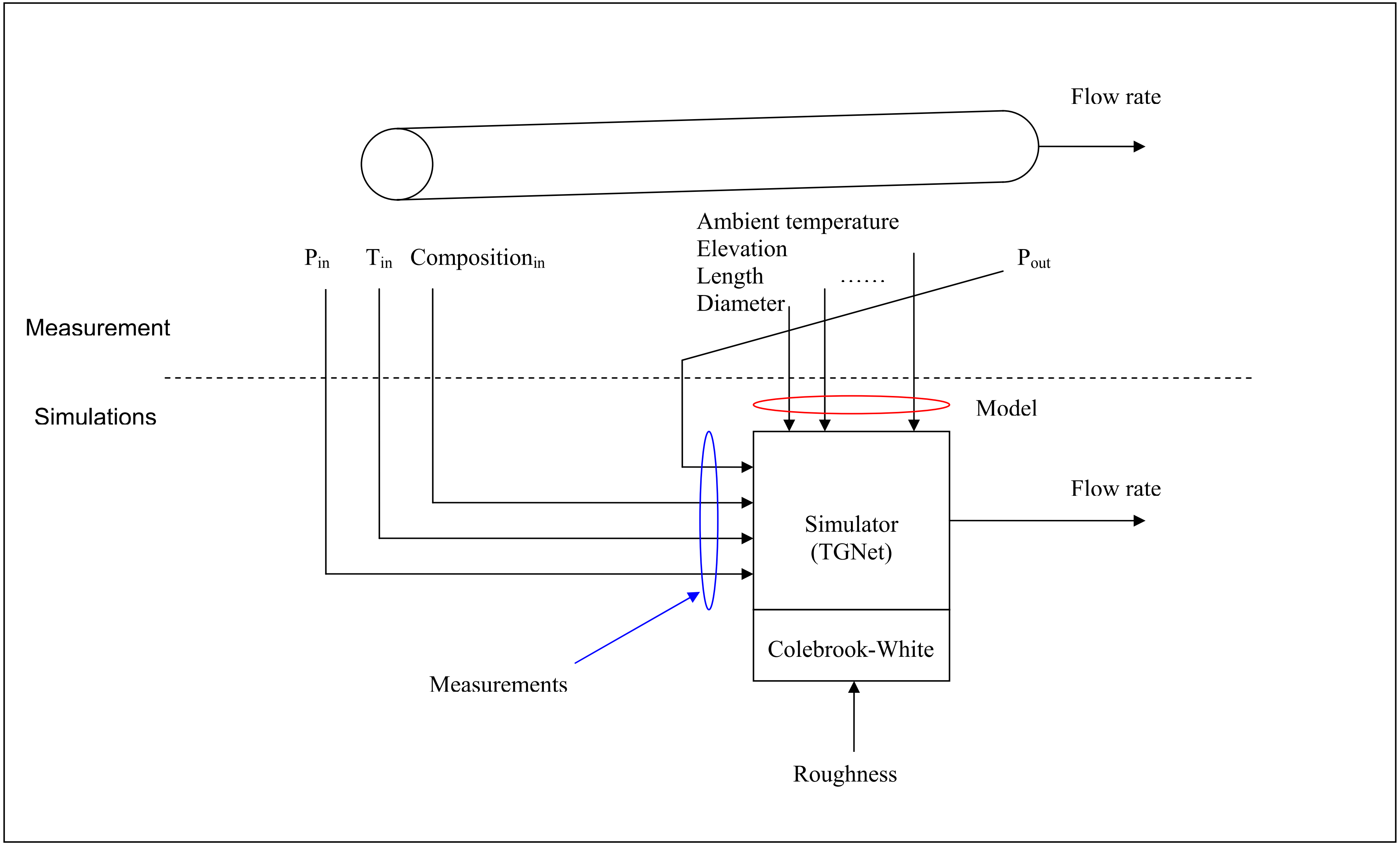

Figure 7.1 Analysis of operational data, sketch of approach.

7.2 Kårstø-Bokn pipeline leg

7.2.1 Introduction

Europipe 2 is the 658 km long natural gas export pipeline running from the gas processing plant at Kårstø, Norway to landfall in Dornum, Germany. Close to Kårstø the pipeline crosses a small island called Bokn, where additional metering equipment is installed. This section of the pipeline is equipped with accurate metering instruments, and it was assumed that the environmental conditions affecting the flow are easier controllable for this short section than the entire pipeline. This section therefore appeared very viable for further investigation of flow models in general, and the friction factor in particular.

7.2.2 Pipeline description

The test leg running from Kårstø to Bokn is 12.5 km long, and it crosses two small fjords. The detailed elevation profile is shown in Figure 7.2. The pipe has an inner diameter of 1.016 m and the walls consist of two or three layers: steel (29.8 mm or 44.0 mm), glass fiber reinforced asphalt (0.5-12.0 mm) and concrete (0-110 mm). The concrete coating is only used in the first fjord crossing, where some sections of the pipe is exposed to sea-water.

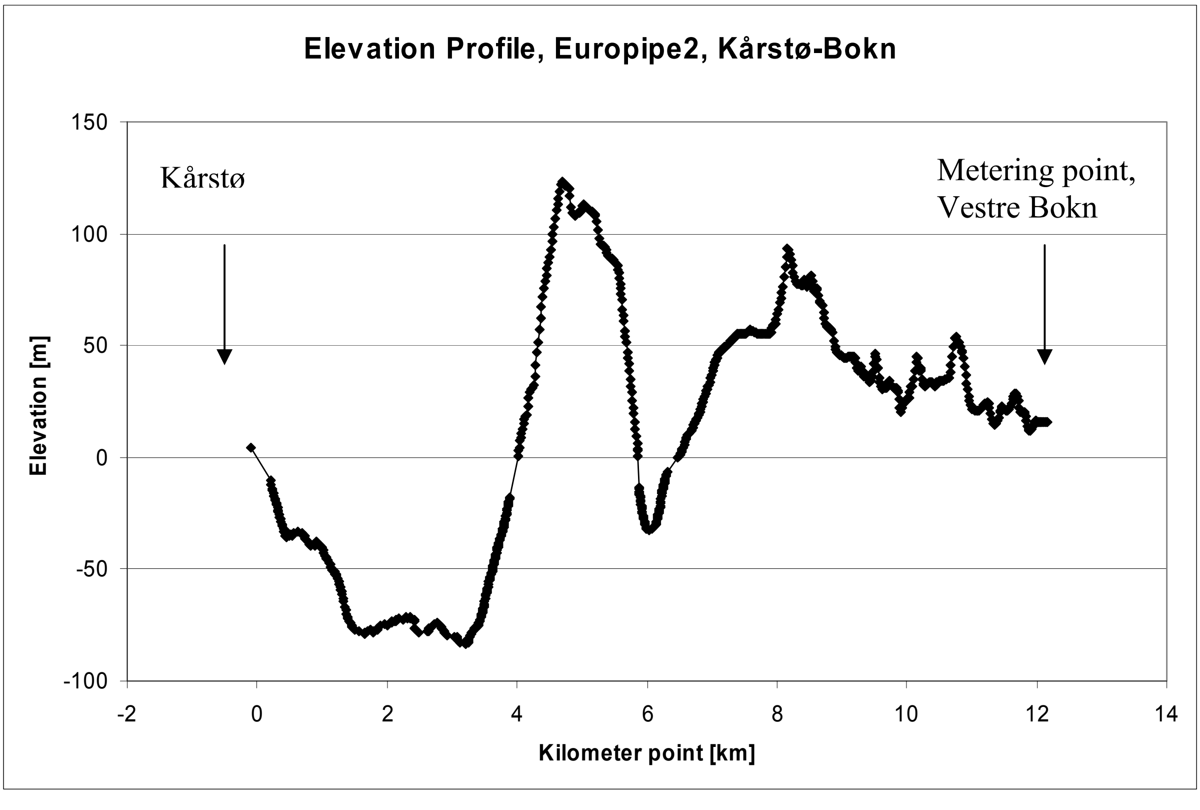

Figure 7.2 Elevation Profile, Kårstø-Bokn leg.

In the first fjord crossing, about 1/3 of the pipe is fully exposed to the sea-water, whereas 2/3 is covered by a layer of gravel. In the second fjord crossing the whole stretch is covered by gravel.

Figure 7.3 shows the Kårstø-Bokn pipeline route.

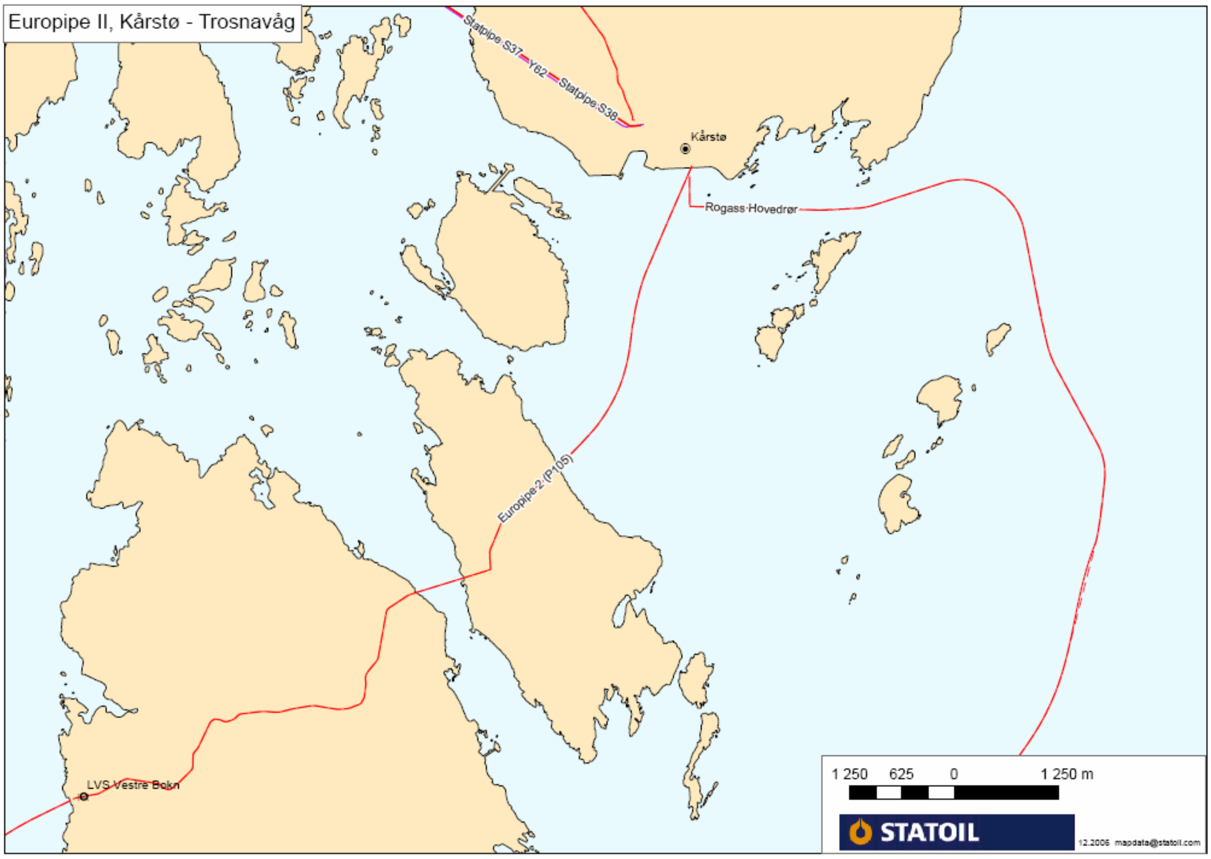

Figure 7.3 Route of Europipe2 leg from Kårstø to Bokn.

Figure 7.4 - Figure 7.6 show pictures of Europipe 2 pipes taken recently from the spare stock of pipes kept at Snurrevarden, Karmøy. Note that these spare pipes have been kept outdoors, exposed to a coastal climate since the commissioning of the pipeline system in 1999. The pipes have not been repainted during these years. For obvious reasons it is not known how well these images represent the current state of the pipeline.

Figure 7.4 Interior of a Europipe2 spare pipe.

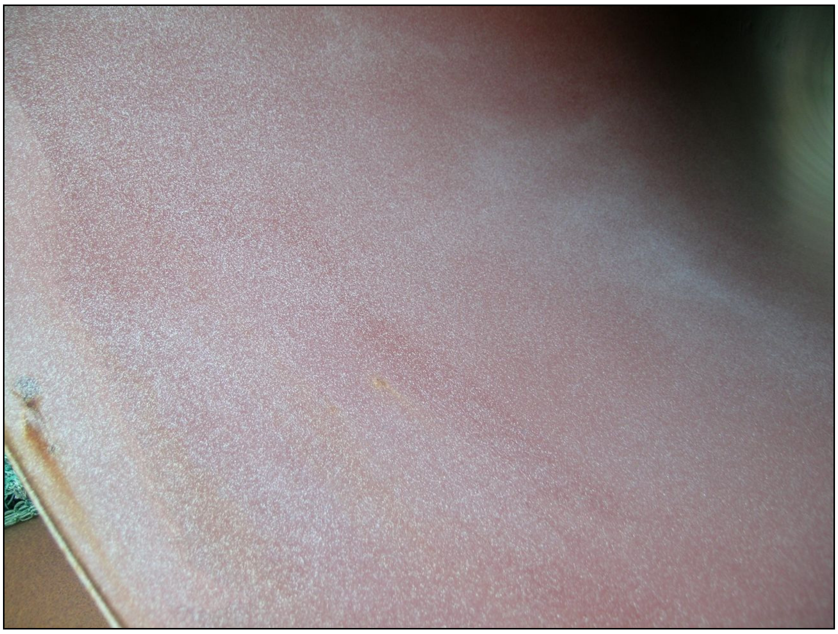

Figure 7.5 Close-up of the Europipe2 surface.

Figure 7.6 Illustrating the different pipe layers: steel, asphalt and concrete.

7.2.3 Instrumentation

Pressure readings

Both ends of the test leg are equipped with a highly accurate Paroscientific digiquartz pressure transmitter. They have a metering range of 0-3,000 psi (0-200 bar), and a given max error of 52 mbar. This means that the standard deviation is significantly less than this value. The max error is split into a systematic error or bias and a random error or repeatability.

Hysteresis is the main contributor to the repeatability. The maximum random error is 0.008% of range, i.e. 16 mbar. The maximum systematic error is then 36 mbar.

Prior to what was defined as the test period, the pressure transmitters were thoroughly calibrated together against the same reference pressure, making sure that they had the same systematic error. The error in pressure difference is then only due to the repeatability. The hysteresis effects when the pressure increases is expected to be the opposite of the hysteresis effect with a decreasing pressure. For the steady-state periods analyzed here, the standard deviation of the pressure readings is mainly in the interval 40-100 mbar, which is significantly higher than the maximum repeatability error. When the steady-state pressure is found by averaging a period of 3-6 hours, it is therefore believed that the averaged hysteresis effect is considerably less than 16 mbar. A good estimate of a 95% confidence interval, which also is supported by the transmitter vendor, is 10 mbar.

The maximum systematic error of 36 mbar only impacts the pipeline mean pressure in the simulations. 36 mbar is 0.028% of a 130 bara pressure, which leads to a maximum error in the density calculation of the same magnitude. This is far less than the general uncertainty in modern equations of state.

The transmitters are not located at the same vertical position as the centerline of the pipe. At Kårstø it is located 5.83 meters above the centerline, whereas at Bokn, its position is 2.93 above the centerline. This was measured by a local contractor, and the accuracy of the horizontal level is given as 0.08 m. The pipeline pressure is therefore slightly higher (20-100 mbar) than the sensor readings indicate. This is accounted for before the pressure is used as input to the simulator.

Flow meters

The flow metering at the processing plant consists of two independent metering stations, since two different gas processing trains supply gas to the export line. Each of the metering stations consists of two parallel metering runs. The uncertainty in mass flow and standard volume flow is 0.6% for each station. If both stations are used simultaneously and at equal flow rates, as they often are, and their errors are assumed statistically independent, the combined uncertainty is 0.4%. It is unrealistic to believe that all the parameters affecting the flow measurement in the two runs are non-correlated. Taking this into account, the combined uncertainty is probably around 0.5%. The metering stations are fiscal, and are subject to continuous supervision to keep the uncertainty at this level.

A small-diameter pipeline branch to the Norwegian distribution network Rogass is located downstream the Europipe 2 metering station. But this branch is equipped with flow meters with the same good accuracy as the main metering station, and hence does not reduce the overall accuracy.

Temperature transmitter

A temperature transmitter, with an uncertainty of 0.04% is installed at the inlet of the pipeline. A temperature transmitter is also located at Bokn, but this only measures the skin-temperature. It is not known how well this measurement represents the real gas temperature, and this temperature is hence ignored in the simulations.

Gas chromatograph

The gas composition is measured continuously by a gas chromatograph, which yields the following uncertainty for each gas component:

Table 7.1 Gas chromatograph uncertainty.

Component	Uncertainty [mole%]
C1	0.180
C2	0.080
C3	0.040
iC4	0.010
nC4	0.010
iC5	0.010
nC5	0.010
C6	0.010
C7	0.010
C8	0.010
N2	0.010
CO_2	0.005
H_2S	0.000
H_2O	0.005

The combined uncertainty in molar weight for a typical composition is 0.023 g/mole, or 0.13%.

The metering signals are transferred to an online logging unit on digital lines, without any loss of precision.

7.2.4 Signal transmission

The sensor signals from both Kårstø and Bokn are transferred to a central database at Gassco Transport Control Centre, Bygnes. The link is a high quality digital link that does not add noise or uncertainty to the signal. It was also checked whether a dead band in the PCDA-system at the Kårstø plant or in the SCADA-system/database at Gassco TCC affected the stored signal. The only potential source of extra uncertainty is that the database stores data with an interval of 20 seconds. So fluctuations in the real signal between the sampling points will not be captured. By interpolating between the sampled points and using a high number of points in the averaging procedure, it is however believed that this error will be smoothed out and can be neglected.

To double check that there is no difference between the signal from the transmitter and the signal stored in the database, a local logging unit was mounted next to the pressure transmitter at Bokn for a 2-hour period. This enabled the comparison of the locally logged pressure and the values stored in the central database. As can be seen from Figure 7.7 the two trends follow each other very closely. In Figure 7.8 a part of the signal is enlarged, and it is clear that the error is within 2 mbar, which is very good.

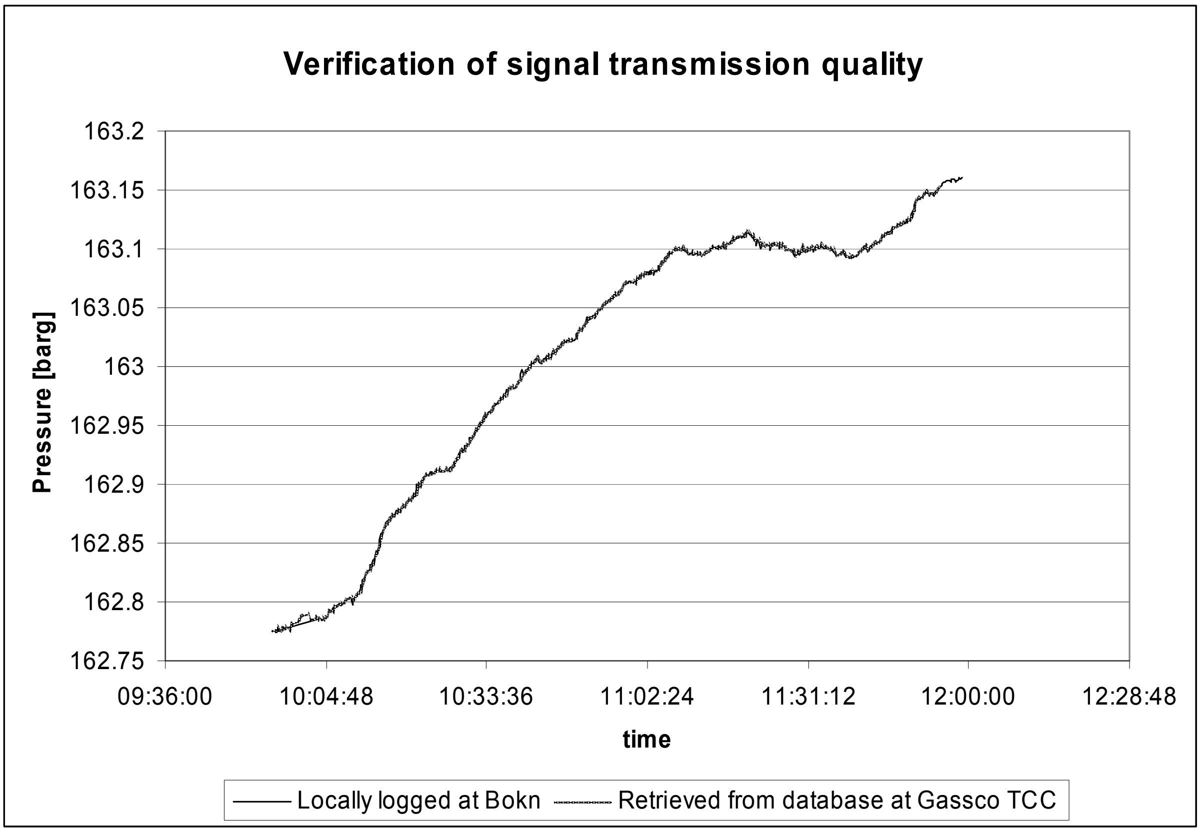

Figure 7.7 Verification of signal transmission quality.

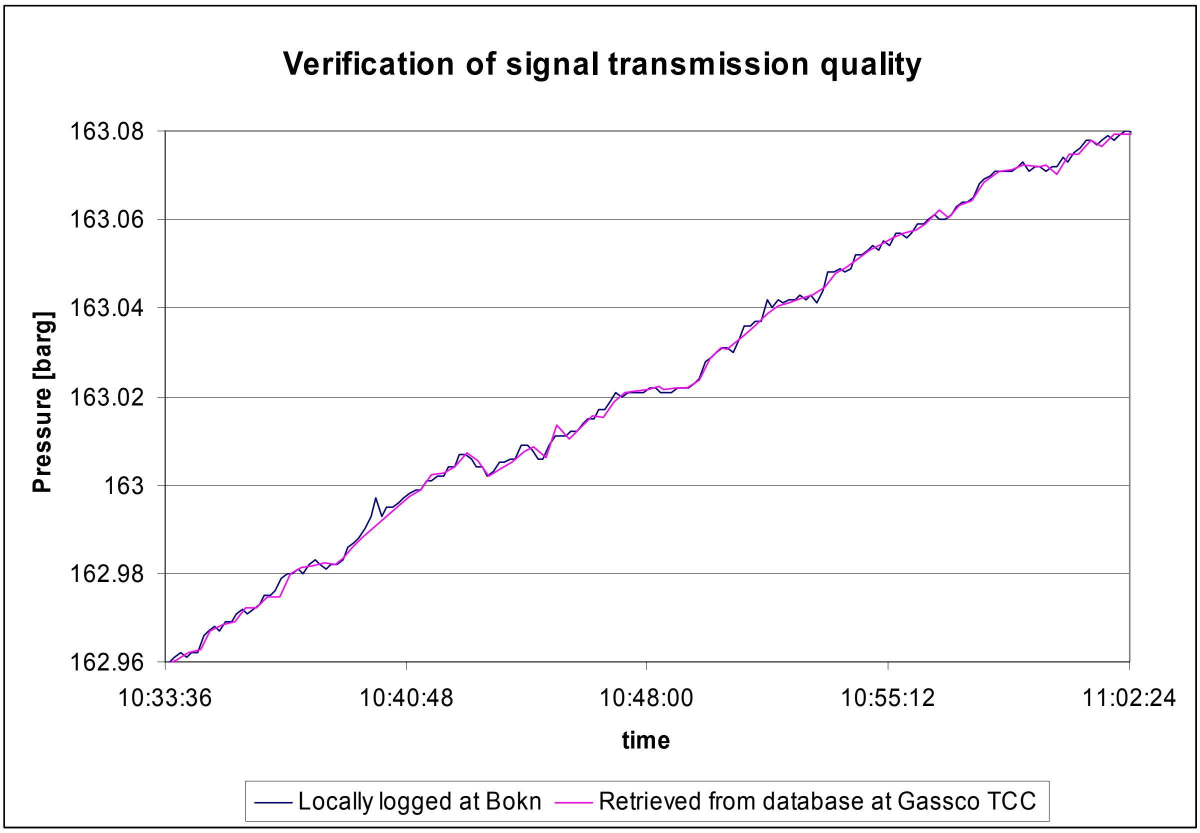

Figure 7.8 Close-up of part of the signal transmission quality.

At Kårstø some technical difficulties were encountered, which made it impossible to mount a local logging unit. Therefore some manual pressure readings made directly from the transmitter were compared to the readings at Gassco TCC. The results are found in Table 7.2 and show the same good agreement.

Table 7.2 Verification of signal transmission.

Manual reading Kårstø	Reading at Gassco TCC		Difference
[bara]	[barg]	[bara]	[bar]
166.018	165.0038	166.01705	0.00095
166.02	165.0075	166.02075	-0.00075
166.021	165.0054	166.01865	0.00235
166.027	165.0146	166.02785	-0.00085
166.034	165.021	166.03425	-0.00025

7.2.5 Steady-state operation

In the analysis of the operational data, the various metering signals are averaged for the steady-state period of interest. The whole analysis procedure is based on steady-state simulation, which means that ideally the data period should be at perfect steady-state conditions. Obviously this is not possible in a pipeline that is subject to continuous changes in operational mode and environmental conditions. It is believed that the non-steadiness in the signals contributes to the total uncertainty of steady-state simulated roughness.

In order to analyze this effect a TGNet model of the Kårstø-Bokn leg was used. Various transients in flow rate were imposed, and the resulting pressure at Kårstø and Bokn were saved. Relying on the correctness of the model, these simulations should represent real instrument signals in unsteady periods quite well. In particular, a step in the flow rate and a periodic oscillating flow rate were further analyzed. These results were averaged for different periods, and the steady-state model was tuned by using the roughness to match the averaged data. The difference between the tuned roughness and the fixed roughness that was used in the transient simulations is used as an estimation of the uncertainty that such an unsteadiness adds to the results.

A roughness of 5 μm was used in the transient simulations.

First a step in the flow rate at Kårstø was imposed on the model. As a result the pressure at both Kårstø and Bokn approaches a higher level, which is shown in Figure 7.9. After the step occurred, 6 different periods of 6 hour duration were extracted and averaged. The properties of these periods, together with the steady-state tuned roughness are shown in Table 7.3. The slope of a fitted straight line to the pressures is used as a measure of the unsteadiness.

Then a sawtooth flow signal was imposed on the model. The period of the signal was 2 hours, and the resulting pressure at Kårstø and Bokn is shown together with the Kårstø flow in Figure 7.10. Two 6 hour periods were extracted, the first starting on a flow peak and the second starting in a valley. Details about the extracted periods and the steady-state results are shown in Table 7.4.

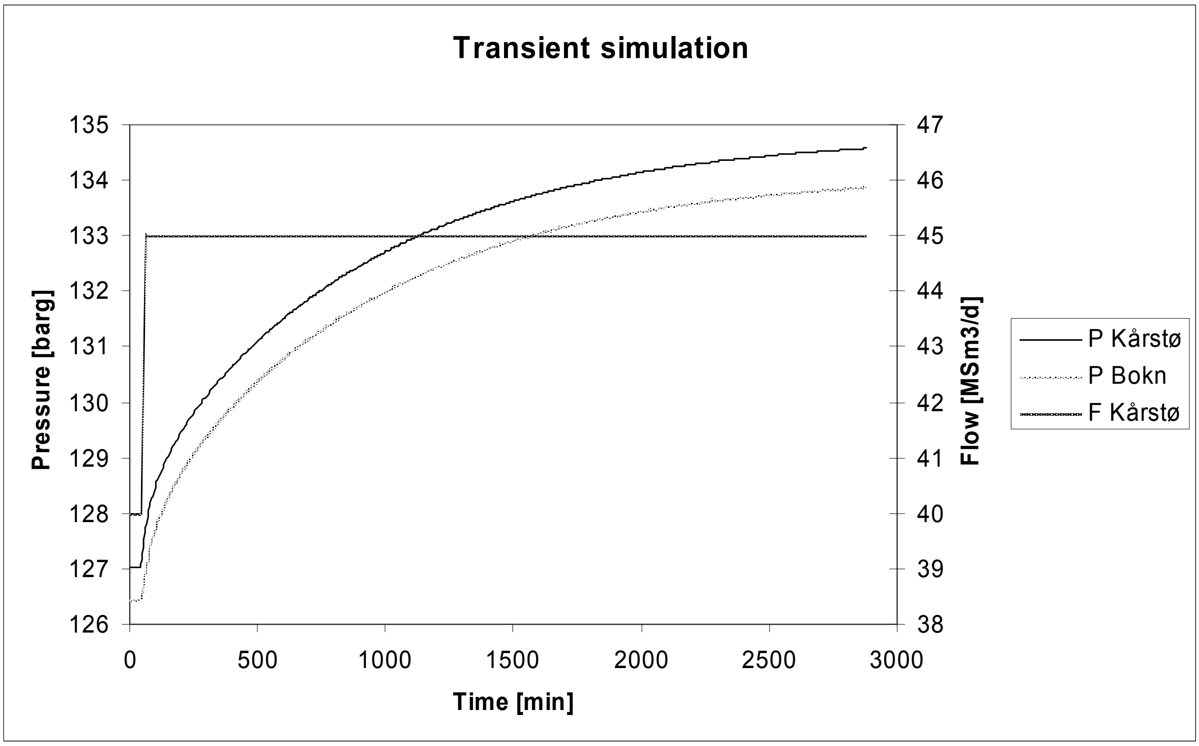

Figure 7.9 Transient signals with step in flow rate.

Table 7.3 Simulated roughness with step in flow rate.

Transient				Steady-state	
Start of period [hours after step]	**Growth rate Kårstø [barg/d]**	**Growth rate Bokn [barg/d]**	**Averaged outlet temperature [C]**	**Tuned roughness [micron]**	**Simulated outlet temperature [C]**
0	11.0	11.1	17.50	4.73	17.60
1	8.9	9.0	17.63	4.82	17.61
2	7.8	7.8	17.67	4.86	17.63
5	5.9	5.9	17.69	4.98	17.66
10	4.1	4.2	17.72	4.94	17.70
20	2.1	2.1	17.76	4.94	17.74

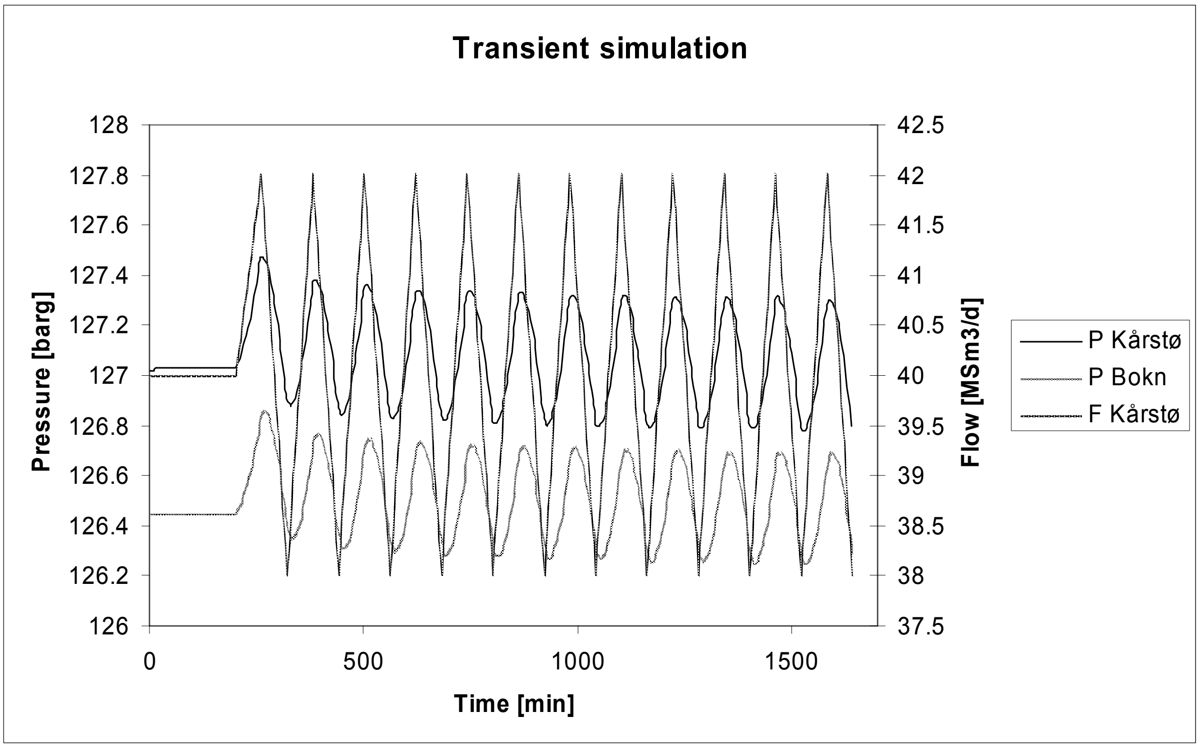

Figure 7.10 Transient signals with oscillating flow rate.

Table 7.4 Simulated roughness with oscillating flow rate.

Transient						**Steady-state**	
Start of period [min]	**Growth rate [barg/d]**		**Standard deviation [barg]**		**Averaged outlet temperature [C]**	**Tuned roughness [micron]**	**Simulated outlet temperature [C]**
	Kårstø	Bokn	Kårstø	Bokn			
500	-0.59	-0.58	0.19	0.16	16.48	4.98	16.48
560	0.40	0.36	0.18	0.16	16.48	5.03	16.48

It is seen that these disturbances affect the steady-state tuned roughness very little. The only exception are the periods extracted right after the step in flow rate has taken place, where the difference between transient and steady-state roughness is rising towards 0.25 micron (5%).

For the step the steady-state tuned roughness is lower than the transient roughness, which may partly be explained. As the pressure in the pipe increases, the inventory also increases. This means that the flow rate at Bokn is lower than the imposed flow rate at Kårstø. An improvement would be to take the average of these two flow rates from the transient simulation, and tune the roughness until the steady-state simulation matched this rate. This flow rate would be lower than the Kårstø flow rate, and hence would the tuned roughness be higher. But since there is no flow meter at Bokn and one wanted the simulations to resemble the real measurements as much as possible, this flow rate was omitted.

7.2.6 Simulation model

In the steady-state simulations for finding the friction factor for each period of steady-state operation, the simulation engine TGNet (OLS version 5.3) was used. This was described in detail in CHAPTER 2.

Detailed data for the pipeline was collected and implemented in the simulation model. Particular care was taken to make sure that all data were correctly implemented to make the results as reliable as possible. The wall layers, elevation profile, elevation of end points (pressure transmitters), burial depths etc. were all implemented in the file. Details for some aspects are further explained below.

Outer film heat transfer

The heat transfer from the surroundings to the pipe wall strongly depends on the medium surrounding the pipe. For the buried sections both onshore and offshore, the SHALLOW correlation from Section 2.2.2 was used, with ground conductivity 2.0 W/mK. In the offshore sections the pipe is covered by a thin layer of gravel and burial depth 0.1 m is used. Onshore a depth of 1.5 m is assumed. The actual ground conductivity is very uncertain, since it varies greatly with moisture and whether it is sand, soil, gravel etc. In general it increases with moisture and density.

Where the pipeline is exposed to sea-water the free stream correlation CORR1 is used with standard coefficients for sea-water. Sea-water velocity 0.1 m/s is used. This is large enough to ensure that the outer film does not add any significant resistance to the total heat transfer for these sections.

Wall

The steel layer has a density of 7,850 kg/m^3, a specific heat capacity of 0.46 kJ/kgK and the thermal conductivity is 45 W/mK. The density of the asphalt layer varies between 900 and 1,500 kg/m^3, the heat capacity is 0.92 kJ/kgK and the thermal conductivity is 0.38 W/mK. For the outer layer (concrete), the density is 3,040 kg/m^3, the heat capacity is 0.65 kJ/kgK while the thermal conductivity is 1.3 W/mK. The wall thicknesses for all parts of the pipeline were obtained and implemented.

Ambient temperature

The sea bed temperature is obtained from daily updated simulation files from UK Met Office, which has an online model of the sea bed temperature in the North Sea. This also covers the coast of Norway. The geographical coordinates of the pipe segments are given in order to pick the correct temperature from the files. This is performed automatically by TGNet.

For the onshore part of the pipe, the input ambient temperatures are based on official daily air temperature measurements at Haugesund Airport. This location is about 10-15 km away from the Kårstø-Bokn pipeline. The measurements are obtained from the Norwegian Meteorological Institute. The air temperature is however not a good representation of the soil temperature at 2 meters depth, as it takes time for a temperature change at the surface to propagate downwards in the soil. This is treated in Gersten et al. (2001), where a sinusoidal variation is assumed for the air temperature. It is then shown how the temperature at an arbitrary depth varies sinusoidally, but with a damped amplitude and a delay which depends on thermal diffusivity and burial depth. Figure 7.11 shows the air temperature measurement from December 1st 2005 to December 31st 2006. The solid line is a sinusoidal curve fit to these measurements. The period is naturally 365 days and the amplitude is 9 degrees Celsius. It is seen that this yields a fairly good approximation of the temperature. The dotted line is the modeled temperature at 2 meters depth, using a thermal diffusivity of $5 \cdot 10^{-7}$ m^2/s. The curve is shifted by 39 days and its amplitude is reduced by 4 degrees. Since the soil temperature is filtered like this, it is less sensitive to daily variations the deeper it gets.

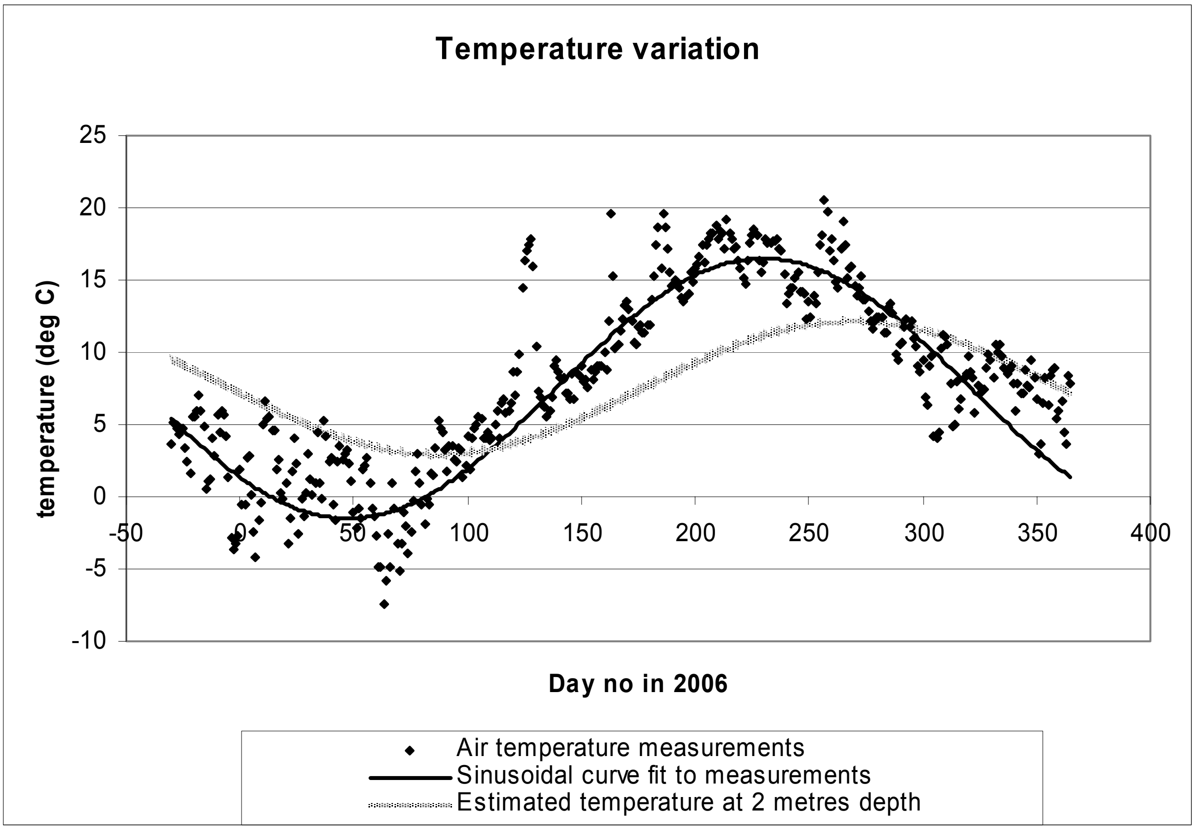

Figure 7.11 Temperature variation throughout the year.

7.2.7 Gas temperature logging

The calculated effective roughness and friction factor embraces all inaccuracies and errors in the model. So in order to get a good picture of the pure wall friction, an accurate model with respect to all parameters is needed. It is particularly important to simulate the gas temperature correctly. A too warm gas yields higher resistance to the flow, and the tuned friction factor becomes too low and vice versa. The importance of the gas temperature was clearly illustrated in the sensitivity analysis reported in CHAPTER 3.

To verify the goodness of the heat transfer model and other input parameters that determine that gas temperature, a pig with temperature sensors were sent. It was launched from Kårstø processing plant on Monday June 4, 2007 at time 21:43. It took around 57 minutes till it passed the pressure transmitter at Bokn. The pig was equipped with two logging units working in parallel, one temperature sensor at each end, one pressure transmitter at each end and two odometer wheels to keep track of its location. Everything was logged versus time at the rate 10 Hz.

Several measurements of the sea bed temperature were taken on the same day as the pig was sent. The temperature measurements were taken by a stand-by emergency group at Kårstø Processing Plant. An Aquatec Aqualogger 520T temperature transmitter was lowered down to sea bed using a fishing line, and kept at the same position for about 5 minutes until the temperature reading had stabilized.

The seabed measurements are plotted versus kilometer position (kp) together with daily updated modeled temperature data from the UK Meteorological Institute, which are usually used in the simulations. The elevation profile is also plotted, and the dependency of the temperature on sea depth is obvious.

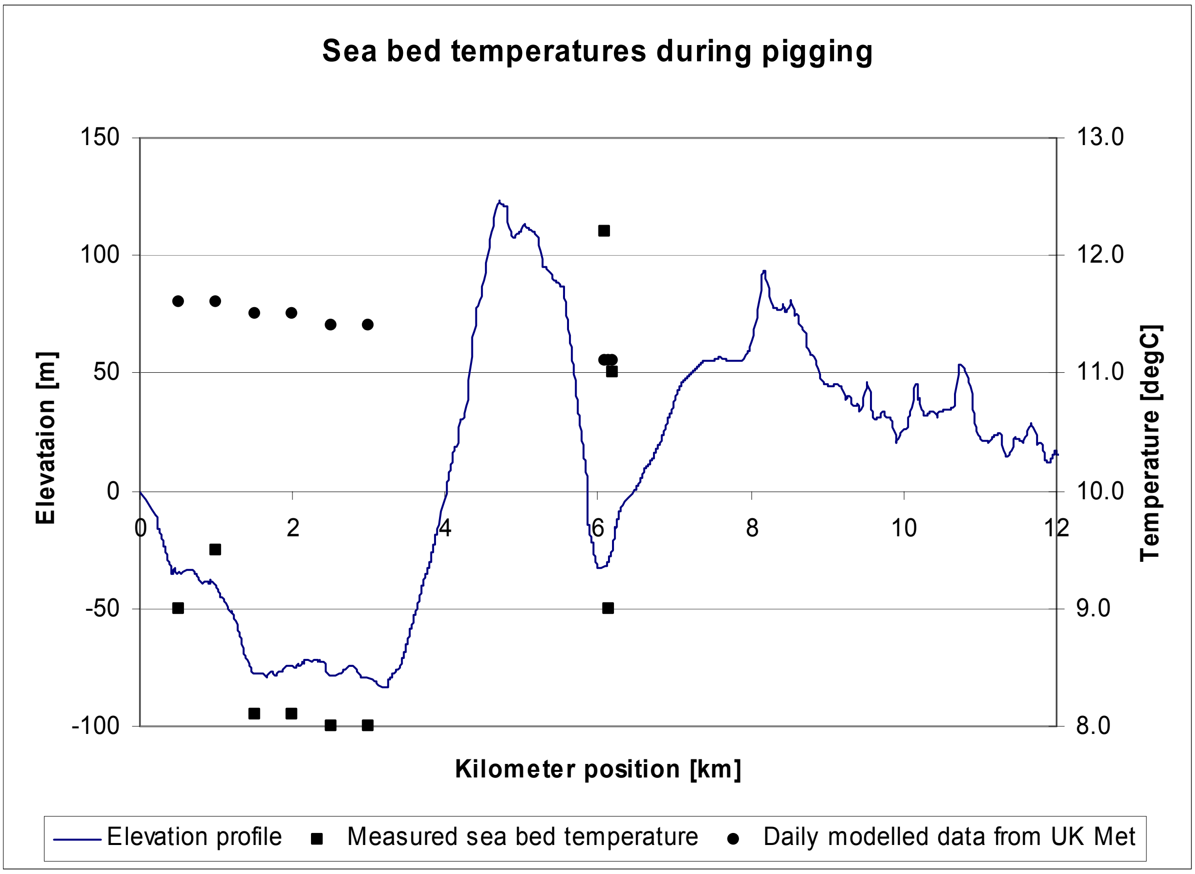

Figure 7.12 Measured and UK Met modeled sea bed temperatures during pigging.

The measured temperatures are generally lower than the predicted ones, particularly in the first fjord crossing. The deviation is 2-3.5 ˚C, which is higher than the stated model uncertainties, which typically is around 1 ˚C. It is also seen that the dependency of the measured temperatures on the sea depth is more pronounced. In the second fjord crossing, the modeled values are about the same as in the first fjord crossing, whereas the measured values vary a lot. The lowest measurement was taken in the middle of the fjord, and it corresponds well with the measured values in the first fjord at the same depth. The high measurements were taken close to shore at shallow water. They were also taken in the afternoon on a very sunny summer day, and the water may have been warmed by the sun during the day.

The overall conclusion is that the modeled temperature values are 2-3.5 ˚C higher than the measured ones. If this tendency is valid during all the simulated steady-state periods, it leads to a too warm gas in the simulations and a too low friction factor. It also indicates that an uncertainty of 3-5 ˚C should be used for the daily modeled data obtained from UK Met. The UK Met data is probably more accurate farther from the coast than in fjords along the coast.

The gas temperature was also simulated by running a transient simulation with real time data extracted from the database Imatis as input to the model. The pressure and temperature at Kårstø and pressure at Bokn were used as input, and the pipeline was simulated starting at 20:00 that very evening lasting until 23:00 hours. The data points were extracted with an interval of 2 minutes. The gas composition was held fixed at average conditions during this simulation. The effect of this simplification is minimal compared to the other uncertainties. In Figure 7.13 the gas temperature measured at the front and at the rear of the pig is plotted against actual travelled distance. Note that travelled distance is slightly different from the kilometer position, as the kilometer position is the distances projected onto the xy-plane, which means that the elevation changes are disregarded. The simulated gas temperature is also plotted. This can be compared directly with the measured temperature, as the value at a given position was extracted for the same time as the pig passed this position.

The measured temperatures reported in Figure 7.12 were used as ambient temperatures in the model.

The gas temperature at the pig position was first simulated with the model parameters proposed in the previous section. This gave a too large temperature along the whole route (green line in Figure 7.13) with a difference of approximately 1.7 degC at Bokn. It is clear that the heat transfer is too low in this model and the cooling of the gas is too slow.

It was then tried to increase the concrete conductivity from 1.3 W/mK to 2.9 W/mK. According to the data sheets for Europipe 2 this value should be 1.3, but for other Gassco operated pipelines a value more like 2.9 are used. It was therefore suspected that this conductivity value could be incorrect. From the figure it is seen that the cooling in the first fjord crossing now increases considerably, giving a good match with the measurements up to kp 4. From that point the cooling effect is still too low, giving a difference of 1 degC at Bokn.

In order to further increase the heat transfer it was tried to increase the ground conductivity from 2.0 W/mK to 4.0 W/mK. This has greatest impact in the onshore sections, where the pipe is buried 1.5 m. Gersten (2001) recommends 2-4 W/mK for the ground conductivity, so 4.0 is still within this band. It is now seen that the simulation model predicts the gas temperature during this period very well. The model predictions are between the measurements from the front and end of the pig most of the time, which is very good. It was therefore decided to use the model with these updated model parameters in the further analysis.

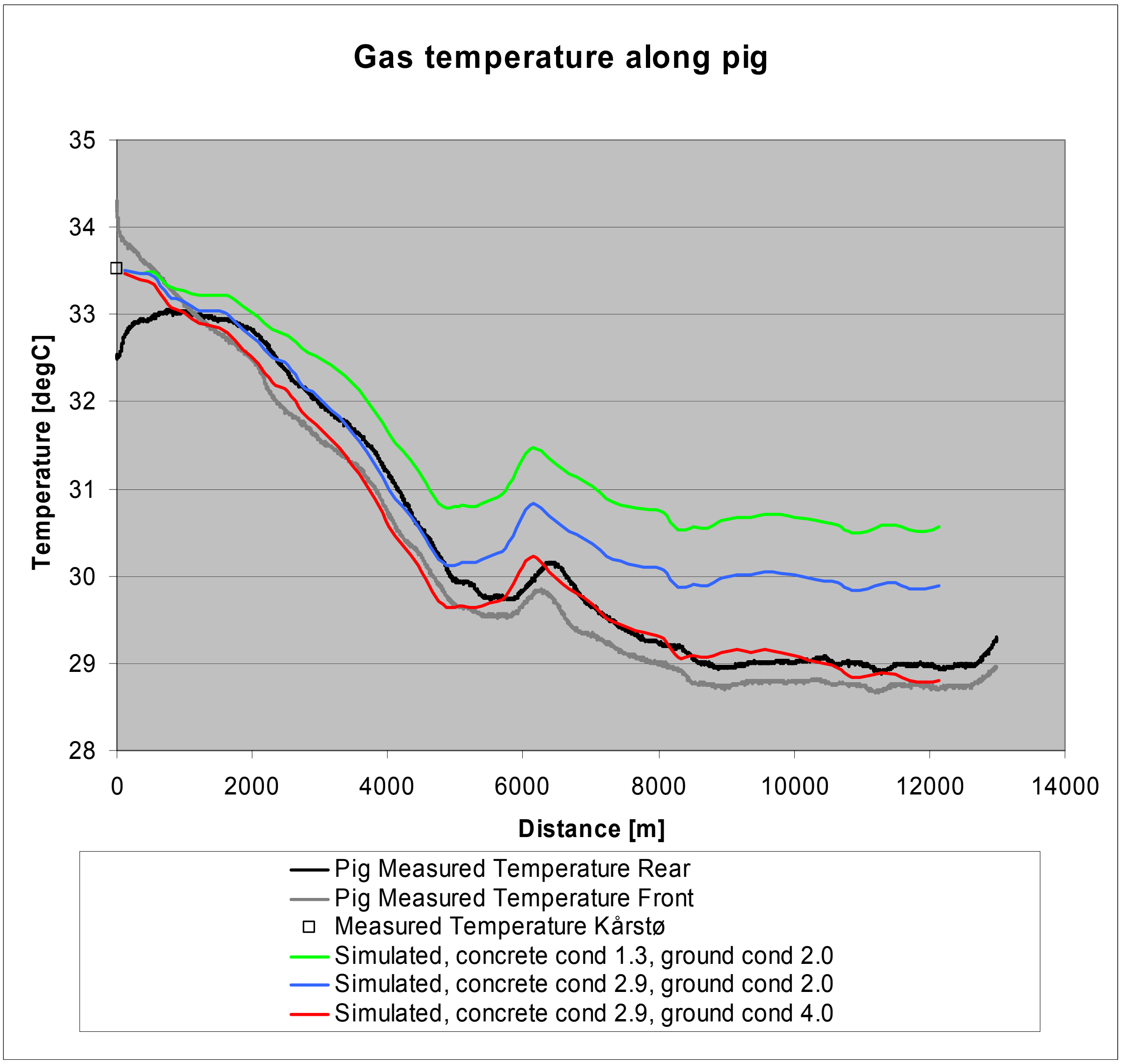

Figure 7.13 Measured and simulated gas temperature at the pig's current position.

The logged temperature has a strange shape at the beginning, which has a viable explanation. Before launch the pig is in the pig launcher, which is slowly pressurized with natural gas flowing to the back side of the pig. The temperature of the pig itself and the surrounding gas will stabilize with the surroundings etc. So when the pig trap is opened, and a sufficiently large fraction of the gas is directed behind the pig, the pig starts moving. After just a few meters it passes the t-junction where the gas is normally routed, but where the flow rate is low at this moment. It is therefore seen that the logged temperature is probably not a good representation of the gas temperature at the very beginning of the pipe. But these effects will fade away after a while, and the logged temperature becomes reliable.

The Bokn station is also equipped with a temperature sensor which measures the skin temperature of the pipe. When the pig passed the station, this showed around 18.7 degC, which is significantly lower than the pig-logged temperature. The skin temperature sensor can thus not be used to predict the gas temperature.

It is also seen that the front and back temperatures differ by around 0.3-0.5 degC, which can probably be explained by the driving pressure drop across the pig.

Figure 7.14 compares logged pressure with simulated pressure.

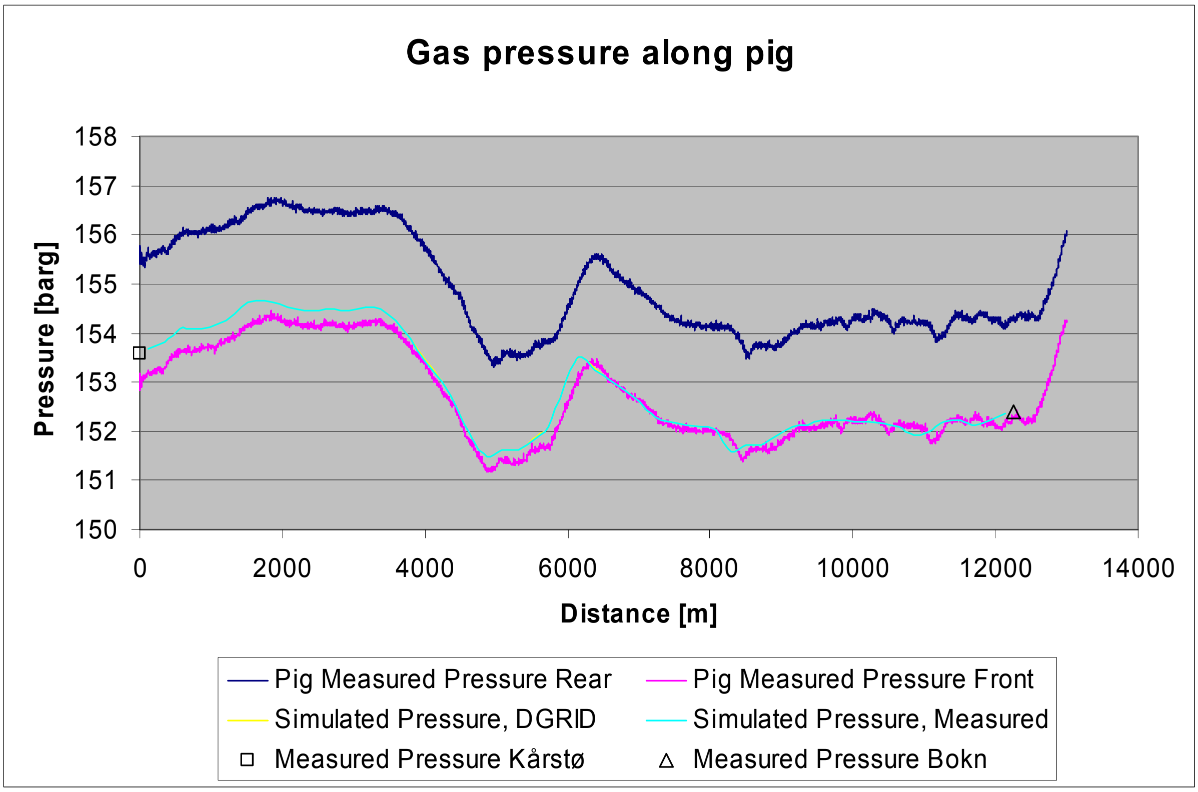

Figure 7.14 Measured and simulated gas pressure at the pig's current position.

The driving pressure drop across the pig is around 2 bar. It is seen that the simulated pressure follows the front logged pressure very closely, which may be explained by the fact that pressure needs to be built up behind the pig in order to push it. The simulated pressure does not differ with ambient sea bed temperature.

It is seen that the simulations with the present model are a very good representation of the actual measured pressure and temperature, particularly when the measured sea bed temperatures are used. This gives support to the goodness of the simulated friction factor results and the uncertainty analysis presented in the next section.

7.2.8 Results

Steady-state data from 13 periods of 6 hours duration have been extracted from the database Imatis. The periods cover the months March to September 2006. The flow rate ranges from 27.9 MSm^3/d (Re $\approx$ 19.5$\cdot$10^6) to 72.1 MSm^3/d (Re $\approx$ 41.0$\cdot$10^6). This is the largest span of steady-state flow rates found in normal operation of this pipeline. 72.1 MSm^3/d is very close to the pipeline's hydraulic capacity, while lower steady-state flow rates than 27.9 MSm^3/d are extremely rare.

The steady-state simulated friction factors for these 13 periods are presented in Figure 7.15. Error bars are included for the lowest and highest Reynolds number. It is expected that the uncertainty decreases monotonically with increasing Reynolds numbers. The uncertainty in Reynolds number is also given.

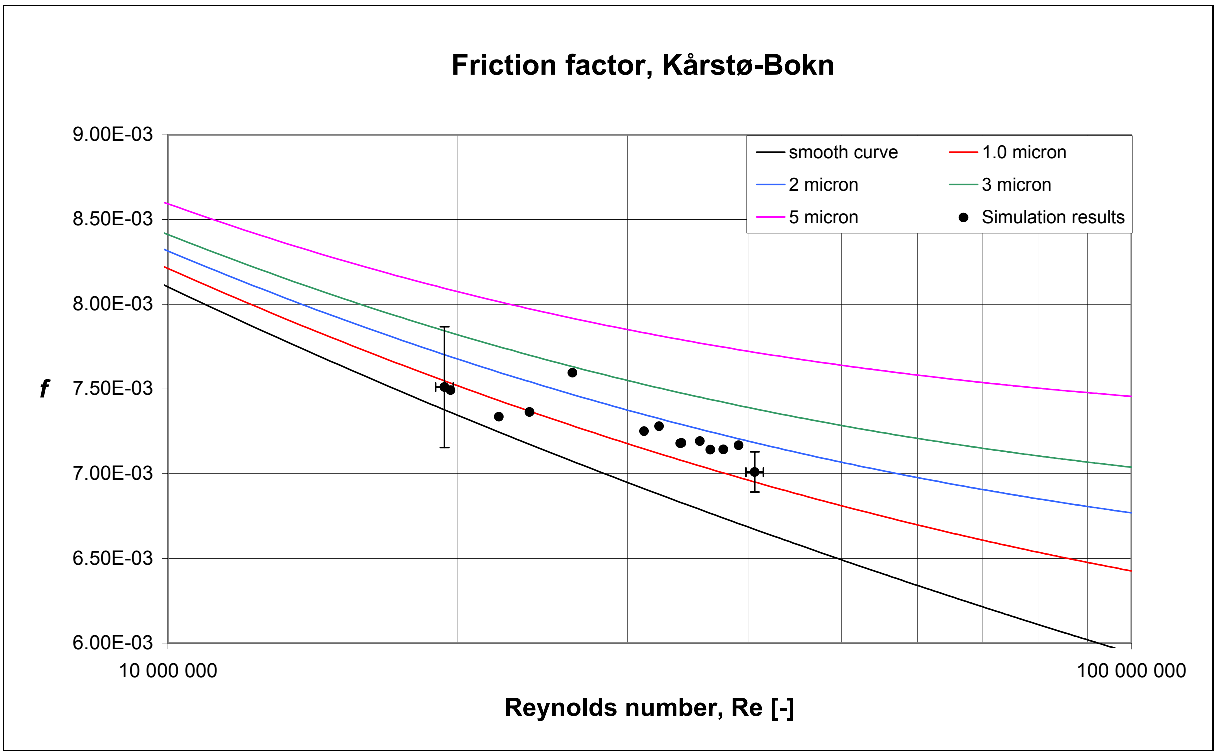

Figure 7.15 Simulation Results Kårstø-Bokn compared with CW curves.

The results collapse pretty much around a straight line with only moderate scatter. The slope is however marginally weaker than the Colebrook-White curves with similar sand grain equivalent roughness. The indicated uncertainty, which is quantified in a later chaper, also increases with decreasing Reynolds numbers.

Further details about each steady-state period are given in the table below.

Table 7.5 Details about steady-state periods, Kårstø-Bokn.

ID	Start Period	Duration [hours]	Averaged P [barg]		Averaged F [MSm^3/d]	Averaged C1 content [%]	Averaged T [deg C]	Reynolds number [-]	Tuned roughness [µm]
			Kårstø	Bokn	Kårstø		Kårstø		
Period08	03.03 04:00	6	181.741	179.980	71.70	86.39	30.06	40 656 552	1.24
Period09	08.03 23:00	6	171.505	170.073	61.82	88.69	29.79	36 555 820	1.50
Period13	26.03 03:30	6	176.742	175.123	67.46	88.70	31.08	39 124 444	1.82
Period25	23.04 00:15	6	167.984	166.709	57.28	87.91	27.41	34 124 844	1.47
Period26	01.05 22:00	6	152.923	151.706	53.42	87.91	28.73	34 020 848	1.45
Period36	15.06 01:40	6	156.332	155.260	50.11	88.02	25.64	31 204 430	1.50
Period39	26.06 02:00	6	144.493	143.801	36.49	88.06	21.34	23 734 568	1.05 (EFF = 1.001)
Period40	03.07 22:00	6	171.415	170.033	60.03	88.54	30.63	35 662 020	1.66
Period44	22.07 21:00	6	181.208	179.649	65.23	88.37	34.98	37 724 040	1.60
Period52	09.09 21:00	6	135.672	135.139	29.27	86.39	20.16	19 654 022	1.27 (EFF = 1.006)
Period56	15.09 03:00	6	127.893	127.389	27.74	89.14	22.09	19 366 072	1.58 (EFF = 1.009)
Period56b	16.09 01:00	6	131.388	130.787	32.14	89.23	19.72	22 051 348	1.00 (EFF = 1.007)
Period59	27.09 22:00	6	176.512	175.299	55.43	87.88	32.50	32 346 516	1.77
Period60	11.10 15:00	6	155.637	154.787	42.26	88.62	23.68	26 291 516	2.77

7.2.9 Viscosity

From the viscosity measurements and viscosity study that was reported in CHAPTER 4 it is clear that the LGE-3 correlation gives more accurate predictions of the viscosity than other correlations and also other variants of the Lee-Gonzales-Eakin correlation (see Lee et al. (1966)).

The effect on friction factor by using LGE-3 instead of LGE-1 is analyzed by repeating the analysis of the steady-state operational data from the Kårstø-Bokn pipeline leg which were reported in Section 7.2.8.

LGE-3 was used instead of LGE-1 when the friction factor was estimated by means of simulations for each of the steady-state periods. Figure 7.16 shows the operational data periods for the Kårstø-Bokn tests using both LGE-1 and LGE-3.

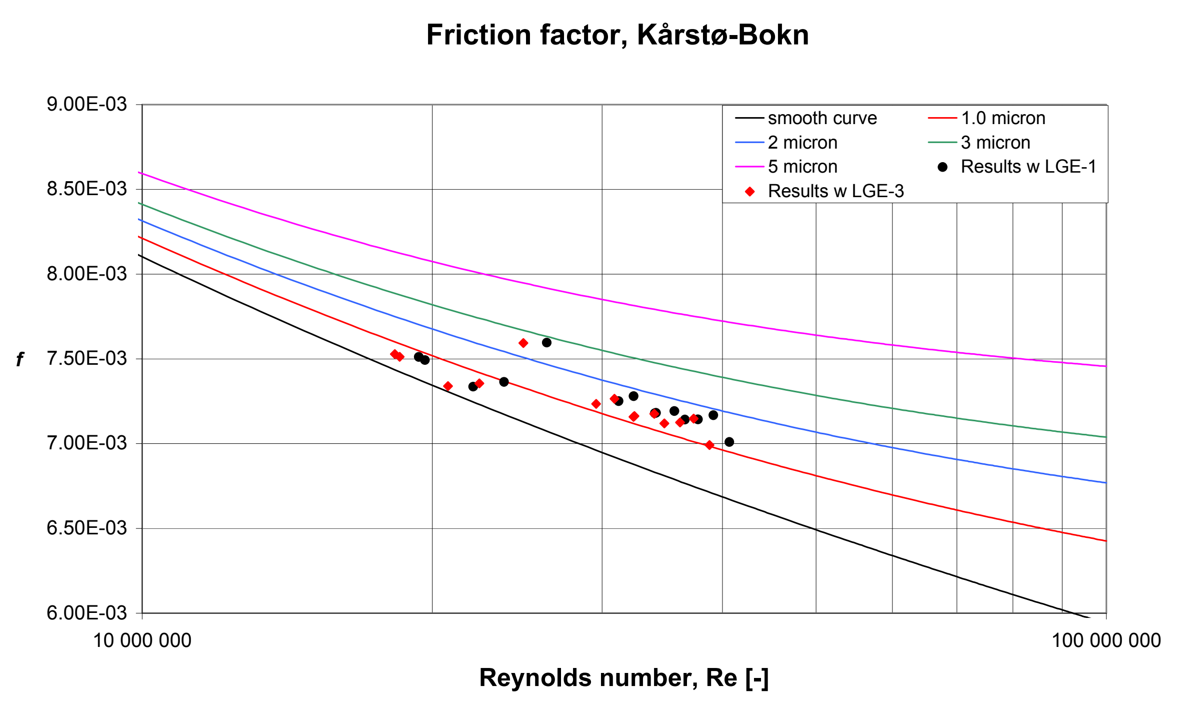

Figure 7.16 Kårstø-Bokn results, comparing LGE-1 and LGE-3.

The data points are shifted leftwards in the figure, meaning that the Reynolds numbers decrease while the friction factor remains unchanged. The Reynolds number is a function of the fluid density, bulk velocity, diameter and dynamic viscosity. The density and bulk velocity can be combined with the diameter to give the mass flow rate, which stays constant since the procedure implies the roughness being adjusted until the measured flow rate is achieved. A percentage change in viscosity will therefore propagate to an equivalent percentage change in Reynolds number for a given steady-state operational period. The friction factor has to remain unchanged since the flow rate is unchanged and independent of which viscosity prediction equation is in use.

By exchanging LGE-1 with LGE-3, the Reynolds number decreases by 4-6%. The percentage change is slightly lower for high Reynolds numbers than for low Reynolds number, which also is visible from Figure 7.16. In terms of friction factor curve slope, this means that a curve fitting of the data points is less steep. This means that the data points deviate even more from the friction factor curve predicted by Colebrook-White.

7.2.10 Curves

Additional pressure drop due to curves have been discussed in Section 2.2.5. The pipeline from Kårstø to Bokn is not perfectly straight. It possesses curves both horizontally and vertically, though the curves are much smoother than the impression one may get from Figure 7.2. In this figure the y-axis scale is much finer than the x-axis scale.

The radius of curvature changes continuously along the pipe, so the pipe has to be discretized and the piecewise radii of curvature have to be found. The elevation profile provides an exact location for the pipeline every 10-12 meters. For every data point in this profile, a local radius of curvature is calculated by fitting a circle to this point and its two neighboring points. In this way a number of overlapping circle segments are found, as is illustrated in Figure 7.17. Curvature in both the vertical and horizontal directions is included in the calculation.

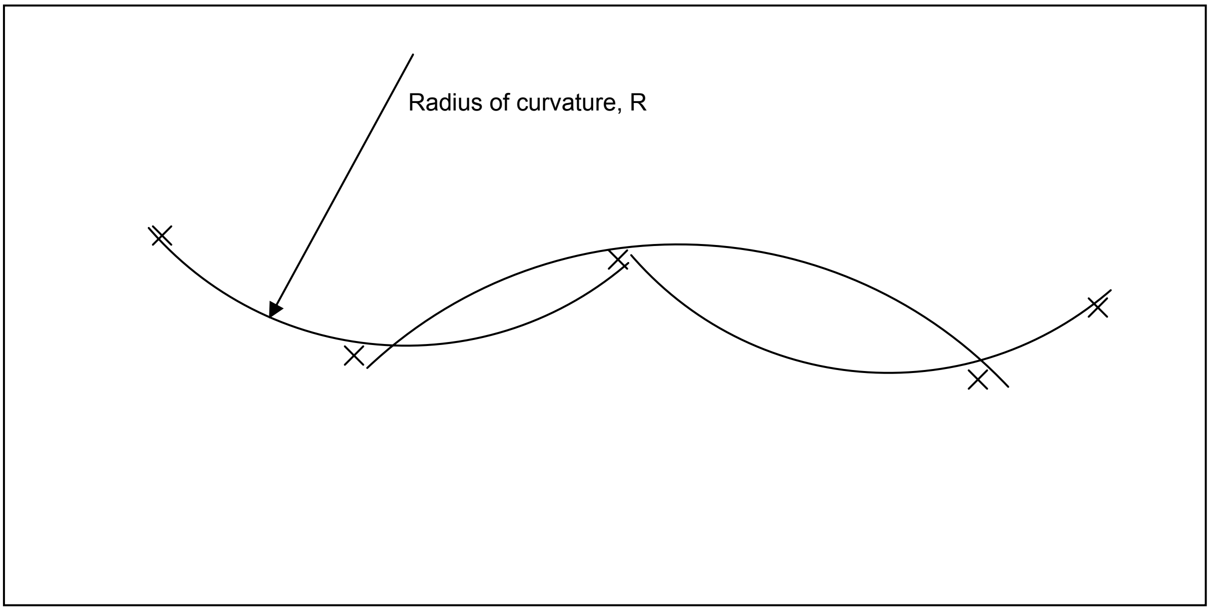

Figure 7.17 Illustration of piecewise circle segment fit to pipeline data.

Figure 7.18 shows a histogram of the curvature distribution. $\mathrm{Re}\left(r/R\right)^2$ is used as a measure of the curvature of each segment, where R is the radius of curvature and r is the inner radius of the pipe. A Reynolds number of $30\cdot10^6$ is assumed in these calculations. The length of the discretized segments varies from 5 to 50 meters, with a mean of 15 meters.

According to Ito (1959) a pipe can be considered perfectly straight if the following inequality holds:

$$\mathrm{Re}\left(r/R\right)^2 < 0.034 \qquad \textbf{Eq. 7.1}$$

In this case the curvature of the pipe is not expected to give any additional contribution in the friction factor. As is seen from Figure 7.18, only 12 segments of this pipeline can be considered straight. It is therefore clear that the curvature does represent an additional friction resistance compared to a straight pipe.

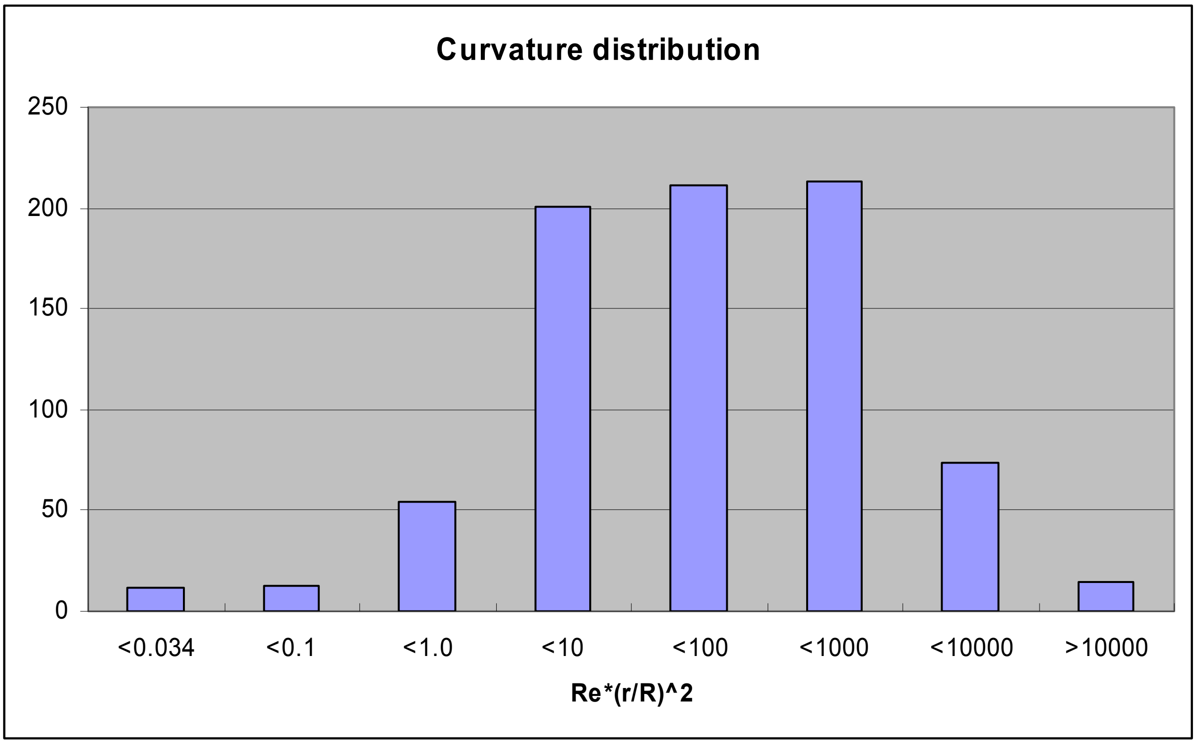

Figure 7.18 Curvature distribution.

Based on experiments using water flow in curved brass tubes, Ito (1959) found a formula for the friction factor in curved pipes. The radius ratio ranged from 16.4 to 648, whereas the majority of the pipe segments in the Kårstø-Bokn leg have a radius ratio between 100 and 1000. But the Reynolds number in Ito's experiments was significantly less, in that it was limited to about $3\cdot10^5$. Ito's formula, which is stated to be valid for $\mathrm{Re}\left(\frac{r}{R}\right)^2 \geq 6$ reads:

$$\frac{f_c}{f_s} = 1.00\left[\mathrm{Re}\left(\frac{r}{R}\right)^2\right]^{1/20} \qquad \textbf{Eq. 7.2}$$

where f_c is the curved pipe friction factor and f_s is the friction factor of a straight pipe of the same length.

The results in Figure 7.15 cover Reynolds numbers from $20\cdot10^6$ to $40\cdot10^6$. The pipeline geometry is obviously the same for all periods, so by keeping r and R fixed in Eq. 7.2 it is seen that:

$$\left.\frac{f_c}{f_s}\right|_{\mathrm{Re}=40\cdot10^6} = 2^{1/20}\left.\frac{f_c}{f_s}\right|_{\mathrm{Re}=20\cdot10^6} \qquad \textbf{Eq. 7.3}$$

which means that f_c is increased by 3.5% more above f_s at Re = $40\cdot10^6$ than at Re = $20\cdot10^6$. This is illustrated in Figure 7.19. If the thick black line represents a straight line fit to the actual results, the thick red line has the expected slope if the results were acquired in the same pipeline, but with no curves. Note that the level of the curve also has to be adjusted due to the curvature effect in order to find the true curve.

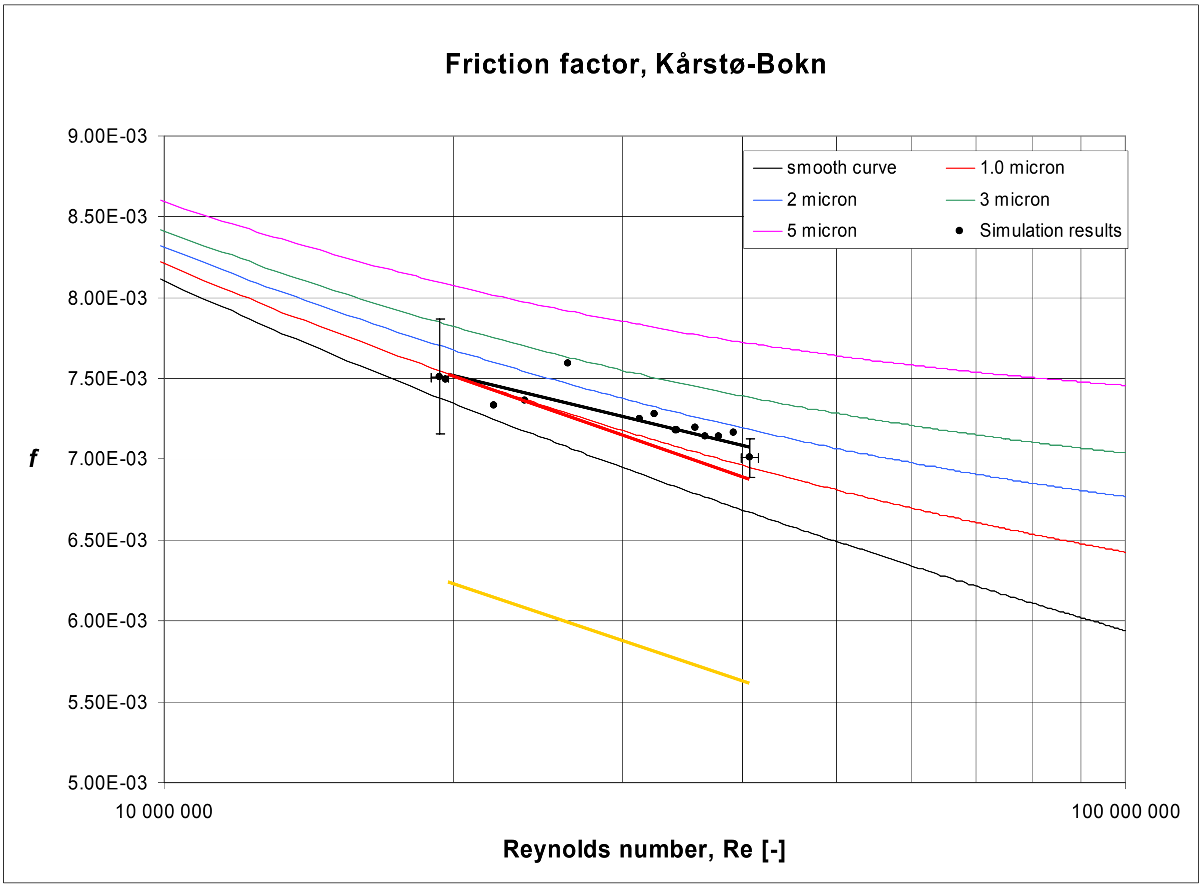

Figure 7.19 Friction factor effect due to curvature.

By keeping the Reynolds number fixed to $30\cdot10^6$ in Eq. 7.2, one can analyze the curvature effect on the curved pipe friction factor results:

Table 7.6 Curvature effect on curved pipe friction factor.

$\mathrm{Re}\left(\frac{r}{R}\right)^2$	f_c/f_s
6	1.09
60	1.23
600	1.37
6000	1.54

From Figure 7.18 it can be estimated that the average curvature, $\mathrm{Re}\left(\frac{r}{R}\right)^2$, is in the order of 50-100, which means that the simulated f_c is increased by around 25% compared to f_s. As a consequence of this analysis, the smooth pipe friction factor curve should be illustrated by the thick yellow curve in Figure 7.19. This is significantly below the Colebrook-White curve for smooth turbulent flow, which for obvious reasons cannot be true. It can therefore be concluded that the additional frictional drag calculated by Ito's formula is unrealistically large under these conditions.

7.2.11 Uncertainty in *f*

Many sources of uncertainty need to be accounted for in order to calculate a total uncertainty for each simulated friction factor. Some have a random uncertainty, i.e. it may change from period to period, while some uncertainty sources are systematic. For example if the burial depth is incorrect, it remains constant among all the periods. Others can exhibit a mixed behavior. The uncertainty sources can be categorized as follows:

Table 7.7 Friction factor uncertainty for Kårstø-Bokn results.

	Random	Systematic
Metering		
• Pressure at Kårstø	x	
• Pressure at Bokn	x	
• Flow at Kårstø	x	
• Fluid composition	x	
The data period is not at perfect steady-state	x	
Simulation model uncertainty		
• Equation of state	x	
• Viscosity correlation	x	
• Heat transfer model	x	
Ambient quantities		
• Soil conductivity		x
• Burial depth on land		x
• Burial depth on sea bed		x
• Ambient temperature	x	
• Sea-water velocity	x	
Pipeline characteristics		
• Inner diameter		x
• Imperfect roundness of the pipe		x
• Length		x
• Elevation of end points and pressure transmitters		x

The random uncertainty and errors will appear as deviations from a smooth line in the Moody diagram whereas systematic errors will influence every data point the same way, and may thus lead to an incorrect slope of the data.

The simulated friction factor depends on all these quantities, which can be expressed as:

$$f_{sim} = f_{sim}(\dot{m}, P_{in}, P_{out}, T_{in}, T_{amb}, A_1, A_2, ...) = f(x_1, x_2, \ldots, x_n) \qquad \textbf{Eq. 7.4}$$

where P_{in} and P_{out} are pressure at inlet and outlet respectively, $\dot{m}$ is flow rate, T_{in} is inlet temperature, T_{amb} is ambient temperature, and A_1, A_2,…is the gas composition.

This relationship, which in general is nonlinear, can be reduced to a linear function by employing a Taylor series expansion:

$$f_{sim} = f(x_1, x_2, ..., x_n) = f(x_1^o, \ldots, x_n^o) + \sum_{i=1}^{n} \left.\frac{\partial f}{\partial x_i}\right|_{x_j = x_j^o} (x_i - x_i^o) \; + \; O((x_i - x_i^o)^2) \qquad \textbf{Eq. 7.5}$$

Close to the working point the higher order terms can be ignored. One can then utilize the fact that the variance of a linear combination of stochastic variables, $Z = aA+bB$, is given by:

$$Var(Z) \; = \; a^2 Var(A) \; + \; b^2 Var(B) \; + \; 2abCov(A,B) \qquad \textbf{Eq. 7.6}$$

By assuming that the input variables are uncorrelated, this yields:

$$Var(f) = \sum_{i=1}^{n} \left(\left.\frac{\partial f}{\partial x_i}\right|_{x_j = x_j^o} \right)^2 Var(x_i) \qquad \textbf{Eq. 7.7}$$

or

$$Std(f) = \sqrt{Var(f)} = \sqrt{\sum_{i=1}^{n} \left(\left.\frac{\partial f}{\partial x_i}\right|_{x_j = x_j^o} \right)^2 Var(x_i)} \qquad \textbf{Eq. 7.8}$$

Since the flow rate is the output variable in the simulator, and friction factor/roughness is an input variable, an estimate of the sensitivity coefficient is found by:

1) Start with a thoroughly tuned steady-state simulation.
2) Make a small adjustment in the input variable of interest, x_i. (which results in another flow rate than the measured for that period). Gives the estimate $\partial x_i \approx \Delta x_i$.
3) Adjust the friction factor until the desired flow rate is achieved again. Gives the estimate $\partial f \approx \Delta f_i$.
4) Calculate the sensitivity coefficient $\partial f / \partial x_i \approx \Delta f_i / \Delta x_i$.
5) The variance of the input variable x_i, is found from datasheet or other available information.
6) Iterate through all input variables.

If the input variable adjustment in step 2 above is made equal to the uncertainty or standard deviation of the variable, the equation reduces to:

$$Std(f) = \sqrt{Var(f)} \approx \sqrt{\sum_{i=1}^{n} \left(\left.\frac{\Delta f_i}{stdev(x_i)}\right|_{x_j = x_j^o} \right)^2 (stdev(x_i))^2} = \sqrt{\sum_{i=1}^{n} (\Delta f_i)^2} \qquad \textbf{Eq. 7.9}$$

which is the exact formula which was used to calculate the uncertainties given in Table 7.8.

The uncertainty in f has been calculated by iterating through the steps above for all input parameters. For many of the parameters it is very difficult to obtain a scientific uncertainty. Then one has to rely on estimations. The uncertainty calculation is performed for one low Reynolds number data point, and for one large, as it is expected that the uncertainty varies with the Reynolds number.

Table 7.8 Friction factor uncertainty contributions in Kårstø-Bokn experiments.

Input variable	**Uncertainty**	**Uncertainty contribution** $\Delta f_i / f$			
		Re ~ $19.5\cdot10^6$		**Re ~ $41\cdot10^6$**	
		Systematic	**Random**	**Systematic**	**Random**
Pressure Kårstø	10 mbar		3.14%		0.69%
Pressure Bokn	10 mbar		3.14%		0.69%
Flow Kårstø	0.5%		0.97%		1.01%
Fluid composition	0.18% C1 -0.18% C2		0.15%		0.08%
density	1%	0.75%		0.89%	
viscosity	2%	0		0	
Heat transfer					
Ground conductivity	1.0 W/mK	0.12%		0.14%	
Burial depth	0.5 m	0.07%		0.07%	
Ambient temperature	3.0 K		1.18%		0.06%
Sea-water velocity	0.5 m/s		0.58%		0.01%
Inner diameter	0.001 m	0.54%		0.53%	
Roundness					
Length	25 m (0.2%)	0.15%		0.17%	
Pressure transmitter height, Kårstø	0.08 m	0.34%		0.12%	
Pressure transmitter height, Bokn	0.08 m	0.26%		0.05%	
Uncertainty in f [%]		1.04%	4.73%	1.07%	1.41%
Total uncertainty in f [%]		4.85%		1.77%	

The uncertainty contribution from each parameter is calculated with the simulation engine, except for the contribution from viscosity and density, which is calculated based on the analytical approach outlined below.

For the low Reynolds number case, the random error (repeatability) dominates the systematic error. The pressure uncertainty is the main contributor. The uncertainty calculated solely on the basis of the randomly contributors evaluates to 4.73%. For the high Reynolds number case, the flow metering, density and inner diameter also contributes by the same order of magnitude as the pressure transmitters.

Analytical approach

The uncertainty in friction factor can also be evaluated using an analytical approach. By assuming a horizontal pipeline, constant temperature and compressibility and by ignoring the kinetic energy, the momentum balance may be integrated to:

$$\dot{m} = \frac{\pi}{4}\sqrt{\frac{M_g}{zRT}\left(P_1^2 - P_2^2\right)\frac{1}{f}D^5\frac{1}{L}} \qquad \textbf{Eq. 7.10}$$

or equivalently:

$$f = \frac{\pi^2}{8\dot{m}^2}\frac{M_g}{zRT}\Delta P\overline{P}D^5\frac{1}{L} \qquad \textbf{Eq. 7.11}$$

The uncertainty in f, $\Delta f/f$ can thus be calculated as:

$$\frac{\Delta f}{f} = \sqrt{\left(\frac{\Delta(\Delta P)}{\Delta P}\right)^2 + \left(\frac{\Delta L}{L}\right)^2 + \left(2\frac{\Delta\dot{m}}{\dot{m}}\right)^2 + \left(5\frac{\Delta D}{D}\right)^2} \qquad \textbf{Eq. 7.12}$$

By ignoring the uncertainty in all other input parameters than ΔP, it is seen that an uncertainty of x% in ΔP yields an uncertainty of x% in f. This is in slight disagreement with the simulation results presented above. The uncertainty in Kårstø pressure measurement is 10 mbar. The Re ~ $19.5\cdot10^6$ case has pressure drop 468 mbar. The uncertainty in this transmitter thus represents an uncertainty of 2.1% in pressure drop. The simulated $(\Delta f_i)^2$ is however $5.28\cdot10^{-8}$, which, by ignoring the other uncertainty sources, gives $\Delta f/f = 3.14\%$. For Re ~ $41\cdot10^6$ the pressure drop is 1.71 bar, the pressure drop uncertainty reduces to 0.58%. The simulated $\Delta f/f =$ is 0.69%.

The Kårstø-Bokn leg is not a horizontal pipeline, as clearly illustrated in Figure 7.12. Also, the elevation of the end point is about 11 meters above the start point. This means that the gravity term in the momentum balance cannot be ignored. In fact, the magnitude of this term is around 1/5 of the pressure gradient term for Re ~ $19.5\cdot10^6$. The friction factor term is then around 4/5 of the pressure gradient. This assumes that the kinetic term can be ignored, which can be proved to be valid here. The gravity term does not change when the inlet pressure, and hence the pressure drop, is adjusted. Then the increased pressure gradient has to be counteracted by increased friction factor, and since the friction factor term is smaller than the pressure gradient term, the percentage increase needs to be bigger. For Re ~ $41\cdot10^6$ the magnitude of the gravity term is around 1/10 of the pressure gradient.

The uncertainty in dynamic viscosity is around 2%, but since this parameter is not a part of the momentum balance, it does not contribute to the uncertainty calculation in f.

According to Eq. 7.12, the uncertainty in density propagates to the same percentage uncertainty in friction factor. But since the Kårstø-Bokn leg is not horizontal, the gravity term cannot be neglected. The gravity term in the momentum is $\rho g \sin\alpha$, whereas the friction term can be written $-\frac{1}{2}\frac{\dot{m}^2}{\pi^2 R^4}\frac{1}{\rho}\frac{f}{D}$. If ρ increases by 1%, the gravity term decreases by 1% (*g* is negative), and the friction term increases by 1%. Since the gravity term effect works in the opposite direction than the friction term, the uncertainty in friction factor is less than 1%. When the gravity term is 1/5 of dp/dx and the friction term is 4/5 of dp/dx, the uncertainty in *f* becomes 0.75%. This is a realistic figure, as it is expected that the equation of state has an uncertainty of around 1%. For Re ~ $41\cdot 10^6$ the friction factor uncertainty due to density becomes 0.89%.

7.2.12 Uncertainty in Re

The Reynolds number is expressed as $\mathrm{Re} = \frac{\rho U D}{\mu}$ or equivalently $\mathrm{Re} = \frac{4\dot{m}}{\pi D \mu}$. Assuming that the uncertainty in mass flow is 0.5%, diameter is 0.1% and dynamic viscosity is 2%, the combined uncertainty in Reynolds number is 2.1%. The error bars are included in Figure 7.15 accordingly.

7.3 Europipe 2, full length

7.3.1 Pipeline description

Operational data from the full length Europipe 2 have also been analyzed. For a full length pipeline, the uncertainty contribution from pressure drop measurements are almost negligible, in contrast to what was seen for the much shorter Kårstø-Bokn section. But the disadvantage is that the environmental conditions can vary a lot along the pipeline, and it is harder to ensure good steady-state conditions in the data periods.

Europipe 2 is 658 kilometers long and runs from Kårstø processing plant to Germany where it comes ashore in Dornum at the Europipe Receiving Facilities terminal (ERF). The pipeline was commissioned in 1999. Nominal outer diameter of the steel is 42 inches (1.0668). Including the asphalt layer and concrete layer, which is used almost along the whole pipe, the outer diameter is around 1.2 m. The transported gas is processed dry sales gas, and is hence quite lean with a methane content around 90 mole%. The maximum operational inlet pressure is 189 barg, whereas the minimum outlet pressure is 89 barg. This yields a hydraulic capacity of 74.0 MSm^3/d.

The instrumentation at Kårstø processing plant was thoroughly described in the previous section. At ERF the pressure, temperature and standard volume flow rate is measured. The pressure transmitter is a digiquartz transmitter with 0.052 bar uncertainty. The flow meters are orifices, and they measure the flow rate into the NETRA distribution system. This is mainly Europipe 2 flow, and the uncertainty is around 0.5-0.7%. But some gas is also exchanged with Europipe 1, which also comes ashore at this terminal, meaning that some Europipe 2 gas does not go into NETRA but some Europipe 1 gas does. These crossover flows are measured by means of ultrasound meters, but due to uncertainty with regard to composition and standard density, they have higher uncertainty, typically around 2-5%. So in periods with extensive use of this crossover, the total uncertainty in flow rate is higher.

7.3.2 Simulation model

The exact length from pressure transmitter at Kårstø to pressure transmitter at ERF, which is the important length with respect to modeling work, is 658.23 km.

The burial depth has been updated to reflect the most recent information from surveys that have been run. It is plotted in Figure 7.20. Burial depth is here defined as the thickness of the soil layer covering the top of the pipeline. So a positive burial depth means that the pipe is entirely covered by soil at this position, whereas burial depth of -1.2 m (or less) means entirely exposed to sea-water. It is seen that the pipeline is partly buried along most of the length. Closer to landfall, the pipe becomes more buried and the last kilometers it is entirely buried. It comes ashore a few kilometers ahead of the terminal, where it shares a tunnel with Europipe 1.

The pipeline wall is composed of steel, asphalt and concrete. The steel layer thickness typically varies from 25 mm to 30.3 mm, the asphalt coating is mainly 6 mm thick and the concrete is mainly between 55 mm and 115 mm thick. Concrete is usually omitted in the onshore areas.

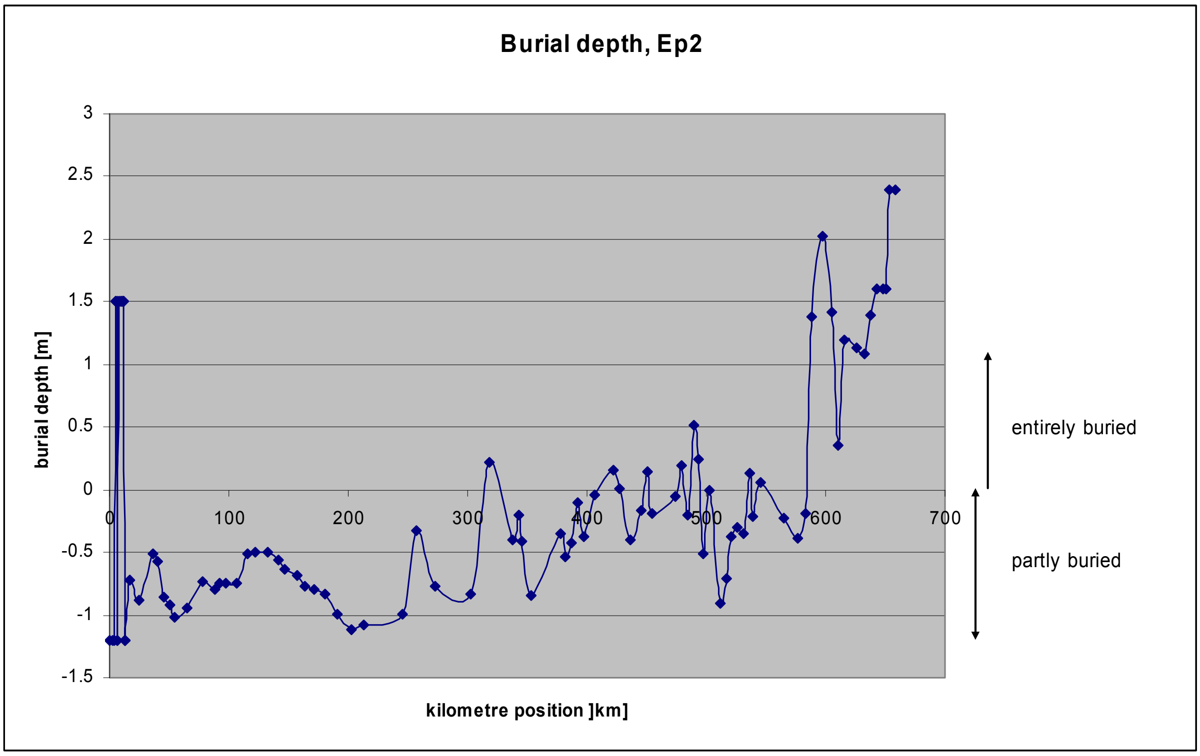

Figure 7.20 Burial depth Ep2.

Since heat transfer between a partly buried pipe and the surroundings is not well known, two different approaches were taken here. In the first configuration file all the partly buried areas were modeled as entirely exposed to sea-water, i.e. the free stream correlation from Section 2.2.2 was used to model the outer film heat transfer. In the second configuration file a total U [W/mK] was specified for all pipe segments that are partly buried. The total U was found by using an approximate expression developed by Morud and Simonsen (2007) which is proved valid for partly buried pipelines. The resulting U is close to a linear interpolation between the total heat transfer for pipes in free-stream and buried pipes. Such linear interpolation is recommended by Gersten et al. (2001). For the Kårstø-Bokn leg the two configuration files were identical since one assumes that the pipe segments in this area are either entirely exposed to sea-water or entirely covered by soil/gravel. Two versions were also made of each configuration file, one using concrete conductivity 1.3 W/mK and ground conductivity 2.0 W/mK, as originally assumed correct, and one using 2.9 W/mK and 4.0 W/mK respectively, as recommended after the Kårstø-Bokn analysis reported in Section 7.2. In the following the four versions are named:

Table 7.9 Details about the different configuration files that were tested for Europipe 2.

Name	Partly buried sections	Concrete conductivity [W/mK]	Ground conductivity [W/mK]
exposed(1.3, 2.0)	Modeled as exposed pipe	1.3	2.0
exposed(2.9, 4.0)	Modeled as exposed pipe	2.9	4.0
partly(1.3, 2.0)	Hard coded U-value based on interpolation	1.3	2.0
partly(2.9, 4.0)	Hard coded U-value based on interpolation	2.9	4.0

The two different configuration files were used to simulate the gas temperature along the pipe when the pig with the logging equipment was sent June 4 2007, as described in Section 7.2.7. Online measurement data for the period June 4 00:00 to June 7 00:00 was obtained for the Kårstø pressure, the ERF pressure and the gas temperature at Kårstø, and fed into the TGNet simulator. The pig was launched June 4 21:43 and arrived at ERF two days later at 23:03. 5 minutes sampling period was used in the simulation. Figure 7.21 and Figure 7.22 show the simulated gas temperature at the actual position of the pig during the pig run. The measurements in front and in rear of the pig are also shown, together with the ambient temperature used as input to the calculations. From kp 0 to kp 12.5 the sea-water temperature measurements as presented in Section 7.2.7 were used, while from kp 12.5 to kp 658 the daily modeled data from UK Met for this specific date was used. The onshore temperature between kp 0 and kp 12.5 was calculated by filtering the measured air temperature as described in Section 7.2.6.

Unfortunately one of the loggers stopped working after about 400 kilometers, so for the last 250 kilometers only the front temperature of the pig is available. The odometer stopped working as well, so the temperature is presented versus time after pig launch.

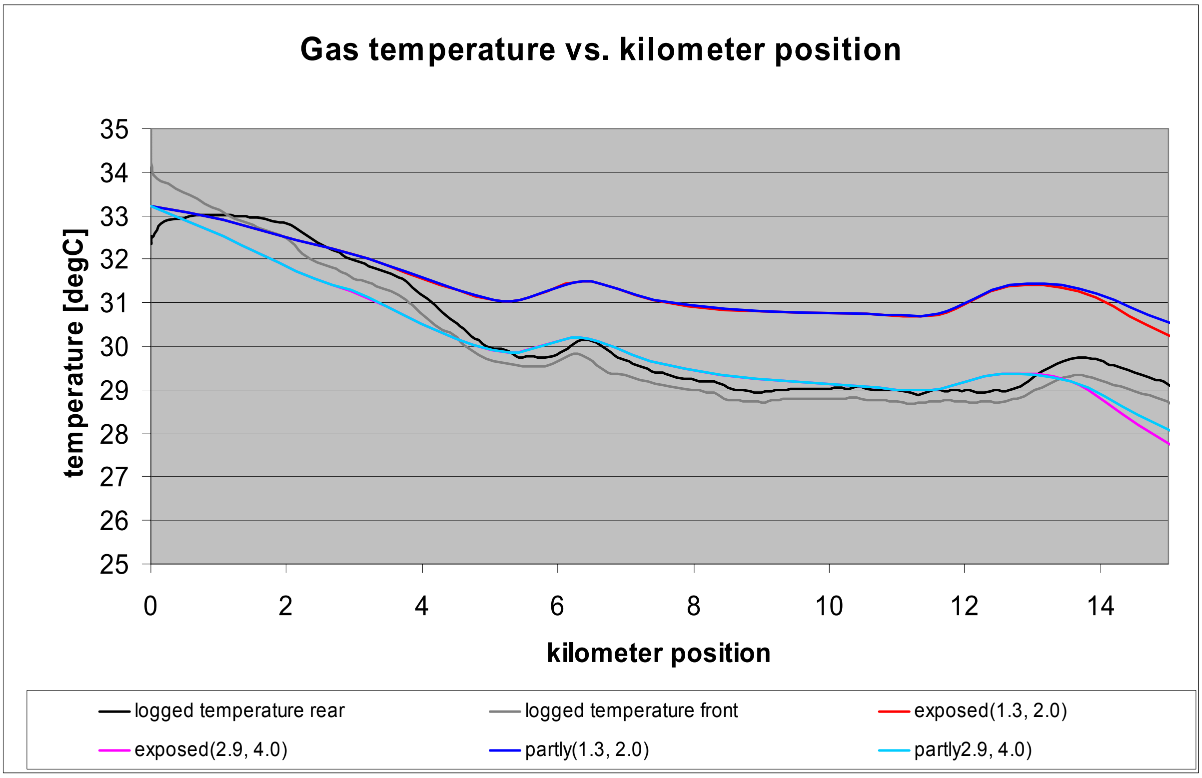

Figure 7.21 Simulated gas temperature versus kilometer position, Kårstø-Bokn.

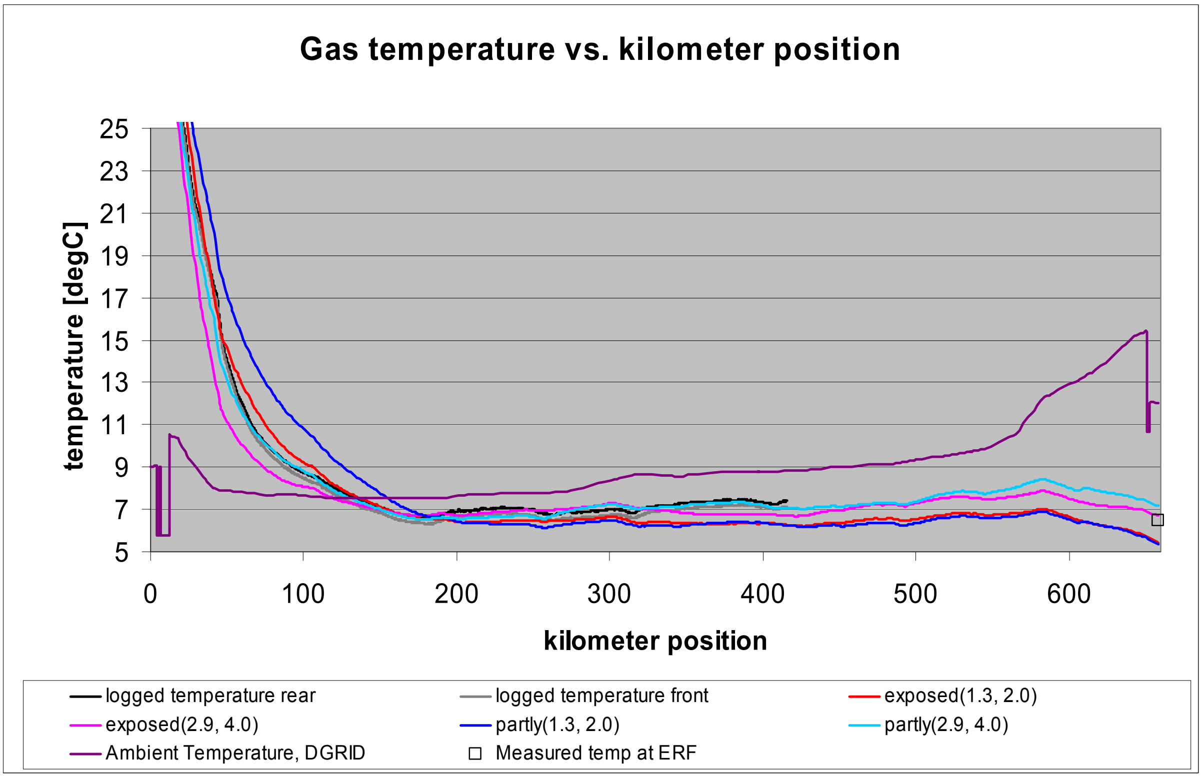

Figure 7.22 Simulated gas temperature versus kilometer position.

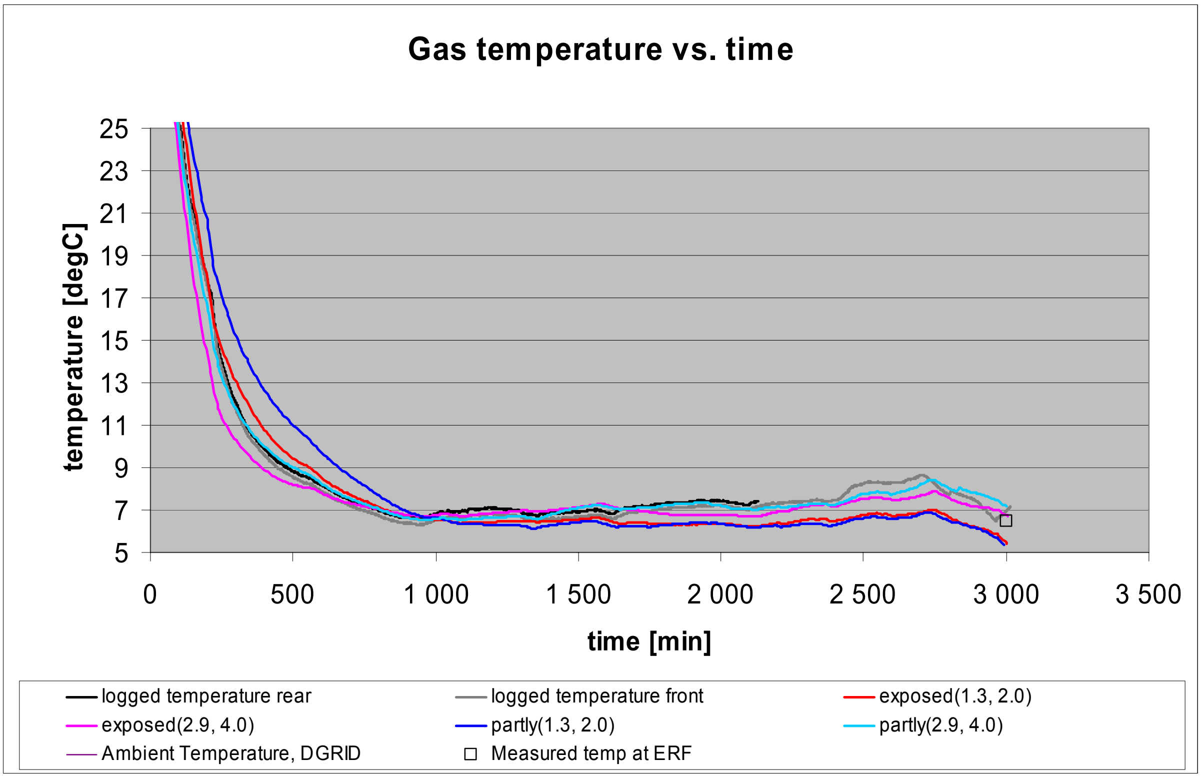

Figure 7.23 Simulated gas temperature versus time after pig launch.

For the Kårstø-Bokn leg, the two versions having concrete and ground conductivity set to 2.9 and 4.0 W/mK respectively, predict the gas temperature very well. This is the same result as reported in Section 7.2.

For the next 150 kilometers after Bokn, which is the section where the gas is cooled down to approximately ambient temperature, exposed(1.3, 2.0) and partly(2.9, 4.0), give the best results. partly(1.3, 2.0) has a too low heat transfer while exposed(2.9, 4.0) has a too high heat transfer. Looking at the remaining 500 kilometers of the pipeline, where the gas temperature more or less follows the ambient temperature, partly(2.9, 4.0) proves to be the best configuration. The other configuration files in general predict a too low gas temperature. Partly(2.9, 4.0) is therefore selected for further analysis, but exposed(1.3, 2.0) is kept as a sensitivity.

It should be noted that the DGRID ambient temperatures are assumed correct here, although they proved to fail by 2-3 degrees in the Kårstø-Bokn area. It is however believed that they are more accurate farther away from the coast where local effects are smaller. But if this assumption fails, the conductivities could have been tuned to incorrect values such that they neutralize the wrong ambient temperature. This attempt is nevertheless the best that can be achieved based on these data.

7.3.3 Steady-state data periods

A total of 27 steady-state data periods of mainly 12 hours duration were found by examining the operational data for Europipe 2 from July 2002 to December 2007. Finding periods with perfect steadiness in a real transport system is impossible, so the steadiness is slightly compromised compared with what one ideally would want to have. The following criteria were set for the periods:

Inlet and outlet pressure: Growth rate < 3 barg/d
Inlet and outlet flow rates: Growth rate < 2 MSm^3/d/d
Packing: < 0.2 MSm^3/d

Details about each period can be found in Table 7.10.

Table 7.10 Details about the steady-state periods in Europipe 2. Reported results are from exposed(1.3, 2.0).

ID	Start Period	Duration [hours]	Averaged P [barg]		Averaged F [MSm^3/d]		Averaged C1 content [%]	Averaged T [deg C]	Reynolds number [-]	Tuned roughness [µm]
			Kårstø	**Dornum**	**Kårstø**	**Dornum**		**Kårstø**		
Period 2	28.07.02 17:45	12	158.78	122.05	44.50	44.74	88.28	23.65	27,738,688	1.03
Period 5	26.11.02 12:40	12	157.92	99.89	54.10	54.34	88.07	29.44	35,292,020	1.69
Period 7	11.12.02 17:55	12	158.52	96.14	56.46	56.35	88.32	26.93	36,740,004	1.56
Period 10	12.04.03 17:00	12	154.69	103.21	51.40	51.74	88.50	26.50	33,374,860	2.02
Period 12	04.05.03 5:30	12	159.44	120.01	47.07	47.28	88.65	24.78	29,186,248	1.10
Period 15	14.05.03 20:00	12	148.42	125.29	34.63	34.78	87.53	28.60	22,007,428	1.47
Period 16	22.05.03 2:00	12	141.08	132.54	19.94	20.06	87.57	30.13	12,812,490	0.94
Period 17	31.05.03 17:20	12	157.92	136.40	34.45	34.51	87.74	30.27	20,773,308	1.02
Period 20	02.07.03 16:40	12	152.98	130.55	34.38	34.47	87.36	29.75	21,358,220	1.22
Period 22	15.07.03 1:50	12	152.49	129.91	34.08	34.26	87.74	29.80	21,267,406	1.86
Period 23	22.07.03 19:15	12	148.64	124.85	34.61	34.42	87.53	29.35	22,008,588	1.87
Period 27	30.08.03 3:55	12	153.14	133.79	31.57	31.39	87.46	28.31	19,491,602	1.87
Period 28	13.09.03	12	158.43	142.58	28.30	28.22	87.28	29.79	16,926,816	4.17

	13:40									
Period 29	19.09.03 12:57	12	144.06	135.39	20.02	19.98	90.32	22.64	12,803,503	9.38
Period 32	01.02.05 16:56	12	155.72	99.64	53.58	53.32	87.77	30.09	34,921,592	1.72
Period 34	20.03.05 0:49	12	153.47	94.36	54.50	54.74	87.53	28.42	36,064,200	1.57
Period 35	09.04.05 22:06	12	154.76	100.14	53.05	53.04	87.97	29.87	34,582,588	1.53
Period 40	15.08.05 8:14	12	156.89	100.32	53.58	53.40	88.13	27.92	34,691,196	1.34
Period 41	08.10.05 9:33	12	164.32	101.49	57.31	57.42	87.80	31.45	36,318,372	1.01
Period 43	16.04.06 12:06	12	171.63	104.93	61.59	61.70	88.44	27.84	37,493,680	1.49
Period 46	23.10.06 13:00	12	169.63	115.48	54.53	54.25	88.20	32.44	33,121,112	1.41
Period 48	10.12.06 7:00	12	173.31	98.11	63.76	63.87	89.05	29.92	39,570,128	1.44
Period 56	04.11.07 14:00	12	185.32	87.78	72.77	72.43	88.83	30.19	43,667,576	1.67
Period 61	13.12.07 15:00	12	181.52	97.18	68.84	68.41	88.47	30.10	41,125,920	1.72

7.3.4 Results

The simulated friction factors for the different test periods are plotted in Figure 7.24 to Figure 7.26 for the two different configuration files recommended in Section 7.3.2. The first two figures report exactly the same results, but the latter figure uses a larger Reynolds number range. Note that in the first configuration file the partly buried sections are modeled as fully exposed to sea-water and the conductivities for concrete and ground are set to 1.3 and 2.0 W/mK respectively. In the second configuration file the partly buried sections have had their U-value set to a fixed value by means of interpolation, whereas the concrete and ground conductivity are set to 2.9 and 4.0 W/mK.

The Reynolds number increases along the pipe, due to increasing gas velocity. The present results were taken from the middle of the pipeline length (kp 330).

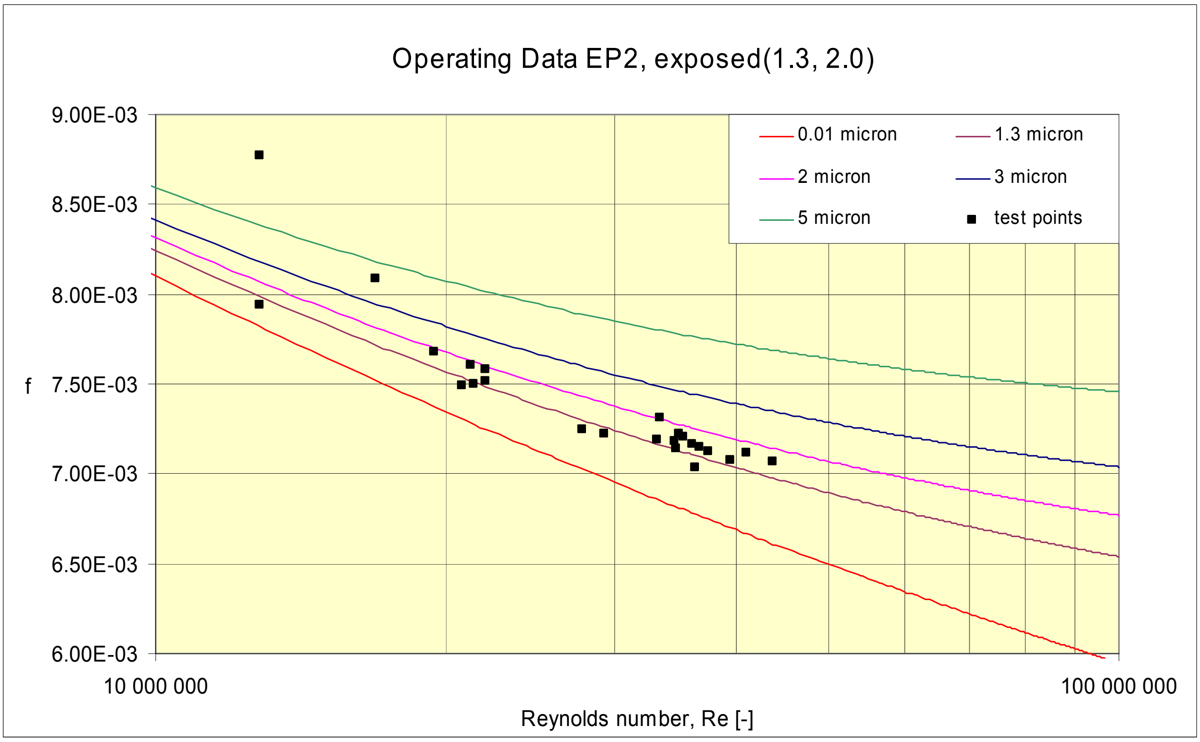

Figure 7.24 Simulated friction factors with first configuration file compared with CW.

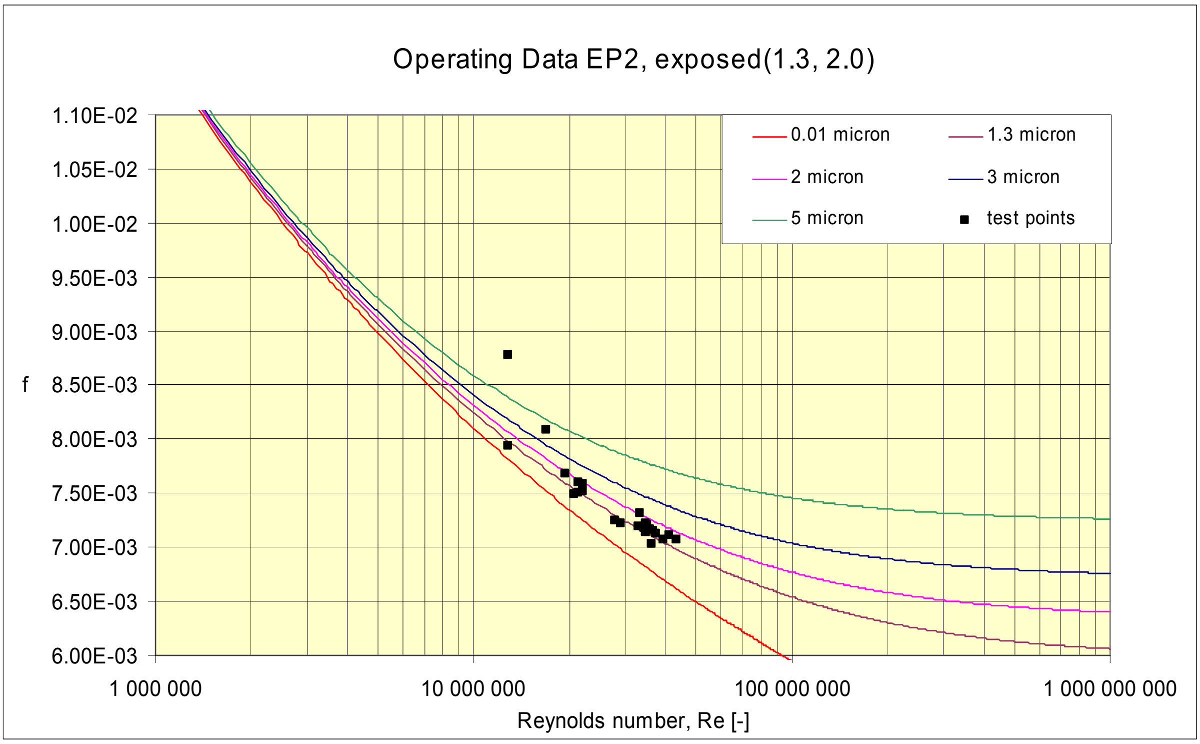

Figure 7.25 Simulated friction factors with first configuration file compared with CW curves, larger Reynolds number range.

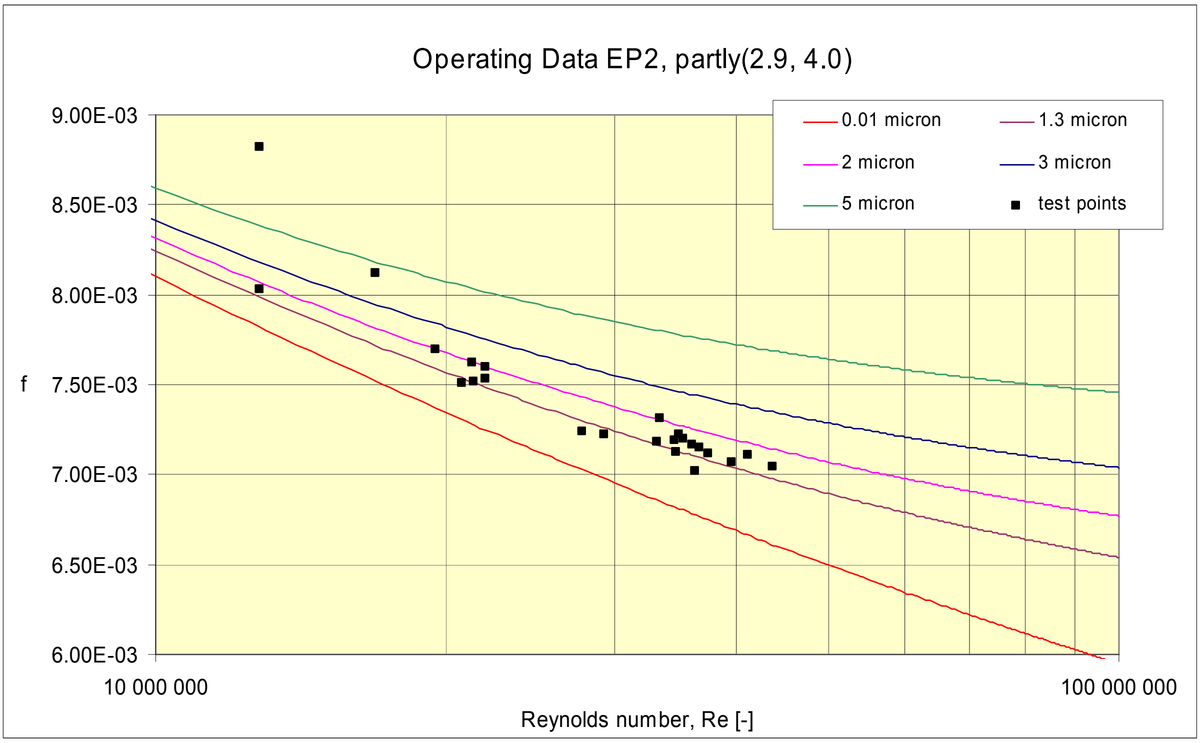

Figure 7.26 Simulated friction factors with second configuration file compared with CW.

It is seen that the friction factor results generated from the two configuration files are almost identical. In both cases they collapse around the Colebrook-White curve for sand grain roughness 1.5 µm, with a standard deviation of 0.3 µm. The only exception is the points for

Reynolds numbers below $20 \cdot 10^6$ where the results are more scattered. The trend of the data points seem to have the same slope as the Colebrook-White curves, which means that they do not support the idea that the Colebrook-White correlation predicts a wrong slope in this area. But the uncertainty of the data makes it impossible to give a firm conclusion.

It is somewhat surprising that two different configuration files generate almost identical results. But they were both found to match the logged gas temperature profile pretty well (increasing to 1 degC towards the end of the pipeline), and consequently ended up with approximately the same total heat transfer coefficient U.

The two data points with Reynolds numbers larger than $40 \cdot 10^6$ are dated 4 and 5 months after the logging pig was sent. No significant changes are hence seen after pigging. So if sending a pig changes the pressure drop due to wall friction in a pipe, the effect vanishes after less than 4 months.

The temperature deviation at ERF for all periods is plotted in Figure 7.27 and Figure 7.28. The deviation is defined as $T_{measured} - T_{simulated}$. It is again seen that the results from the two configuration files are very similar. For Reynolds numbers larger than $30 \cdot 10^6$ the deviations are distributed around zero, but the deviations for the second configuration file (partly(2.9_4.0)) are generally 0.5-1.0 degC lower than for the first configuration file. However, this seems to play a minor role since the friction factor results were the same. On average the models predict the outlet gas temperature well. For low Reynolds numbers the simulated outlet temperatures are systematically larger than the measured ones. If that trend is applicable for the entire pipeline length, it leads to too low simulated friction factors for these Reynolds numbers.

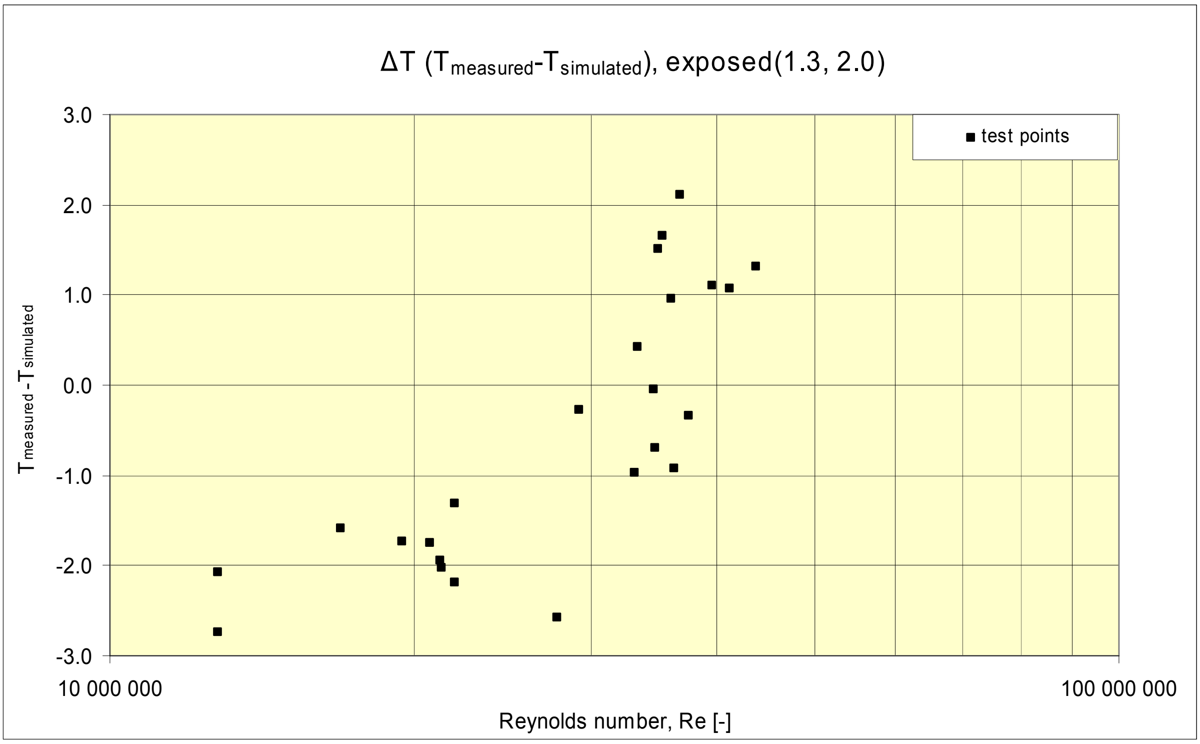

Figure 7.27 Temperature deviation for the test points exposed(1.3, 2.0), $T_{measured}$-$T_{simulated}$.

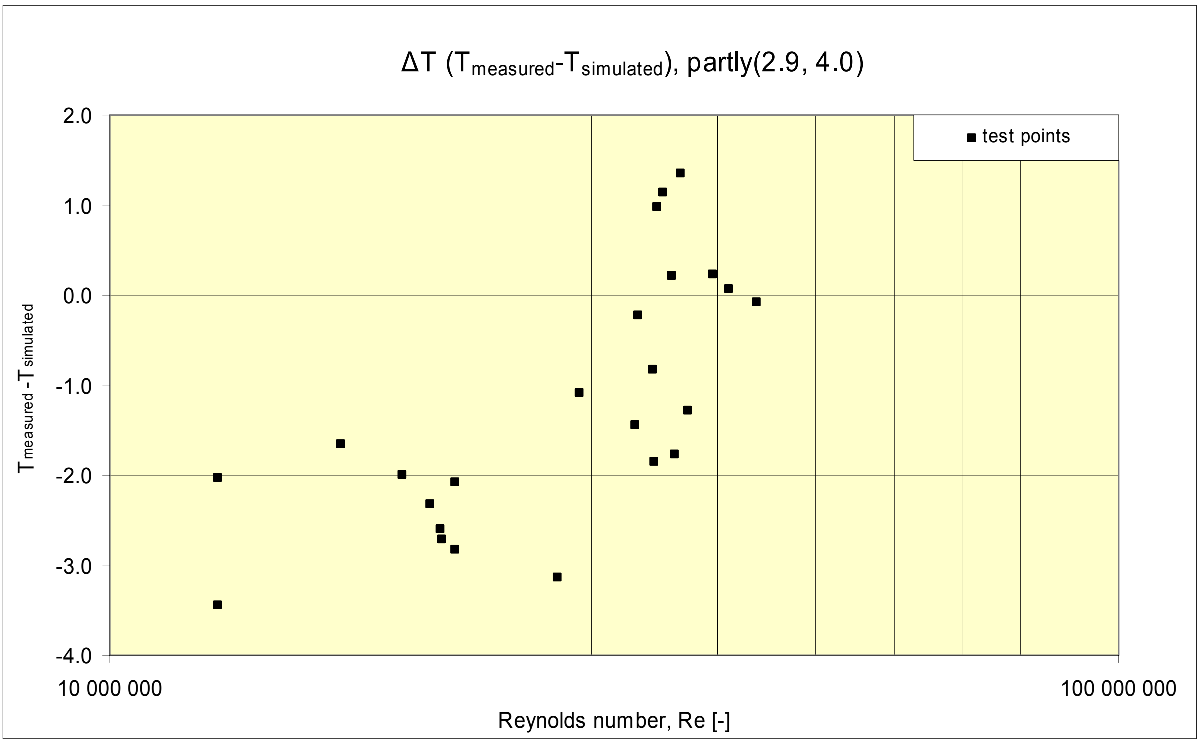

Figure 7.28 Temperature deviation for the test points partly(2.9, 4.0), $T_{measured}$-$T_{simulated}$.

7.3.5 Uncertainty in *f*

The uncertainty in the Europipe 2 friction factor results was calculated similarly to how the Kårstø-Bokn uncertainties were calculated in Section 7.2.11. The estimated uncertainty in the different input parameters are reported in Table 7.11 together with the resulting friction factor uncertainty contribution and the total uncertainties.

Table 7.11 Friction factor uncertainty for Kårstø-Bokn results.

Input variable	Uncertainty	Uncertainty contribution $\Delta f / f$			
		Re ~ $20 \cdot 10^6$		Re ~ $40 \cdot 10^6$	
		Systematic	Random	Systematic	Random
Pressure Kårstø	52 mbar		0.29%		0.09%
Pressure Dornum	52 mbar		0.26%		0.05%
Flow Kårstø	0.5%		0.50%		0.50%
Flow Dornum	1.0%		1.00%		1.00%
Fluid composition	0.18% C1 -0.18% C2		-0.02%		-0.04%
Density	1%	1.00%		1.00%	
viscosity	2%	0		0	
heat transfer					
Ground conductivity	1.0 W/mK	0.10%		-0.01%	
Burial depth	0.5 m	-0.06%		0.02%	
Ambient temperature	2.0 K		-1.27%		-1.57%
Sea-water velocity	0.5 m/s		0.00%		0.01%
Inner diameter	0.001 m	0.49%		0.50%	
Roundness					
Length	500 m (0.1%)	-0.10%		-0.09%	
Pressure transmitter height, Kårstø	0.08 m	0.00%		0.00%	
Pressure transmitter height, Dornum	5.0 m	-0.34%		-0.05%	
Uncertainty in *f* [%]		1.18%	1.74%	1.12%	1.93%
Total uncertainty in *f* [%]		2.10%		2.23%	

The major uncertainty contributions are from the flow measurements, the density calculation and the ambient temperature. Note that the contribution from the density has not been simulated, but rather calculated based on Eq. 7.12. The pressure transmitters, including the transmitter heights, are a little important for the low Reynolds numbers, but they can be neglected for higher Reynolds numbers.

The uncertainty due to heat transfer could be analyzed further by examining the conductivity of the different wall layers, the layer thicknesses etc. This was not performed, since the difference between the two investigated configurations is believed to capture this uncertainty.

Compared with the Kårstø-Bokn uncertainty analysis, it is seen that the contribution from the ambient temperature is greater here. The simulations show that increasing the ambient temperature by 2 degrees, gave a 2 degrees (approximately) warmer gas in the whole pipeline length. The ambient temperature had a direct influence on the gas temperature, whereas in the shorter Kårstø-Bokn leg, the ambient temperature had less influence on the gas temperature. The other notable difference from the Kårstø-Bokn analysis is the role of the pressure transmitters. But in Europipe 2, the pressure drop is much larger (50 – 80 bar), so the relative uncertainty in pressure drop is lower.

The total uncertainty is calculated to around 2.1-2.2%, and is quite independent of Reynolds number. The only significant uncertainty that is not quantified in this calculation is the treatment of the quasi steady-state periods as fully steady-state periods.

7.4 Zeepipe

7.4.1 Pipeline description

Zeepipe is the 813 kilometer long export pipeline running from Sleipner Riser platform to Zeebrugge in Belgium. The gas transported in the pipeline used to be a mix of Kollsnes gas (Zeepipe IIA) and Sleipner processed gas. After Langeled North came into operation in 2007, the gas however also contains Ormen Lange gas coming to Sleipner Riser through Langeled North. Depending on the fraction of the heavier Sleipner gas, the methane content can vary from around 80 mole% to 90 mole%. The maximum inlet and minimum outlet pressure are 149 and 83 barg respectively, giving the hydraulic capacity 42.4 MSm^3/d. The pipeline was commissioned in 1993.

On Sleipner Riser, the Zeepipe inlet flow rate is calculated based on the measured flow rate from Langeled North, Zeepipe IIA, Sleipner Platform and possibly also from Draupner in periods when the Sleipner-Draupner pipeline is operated in back-flow mode. Reference is made to Figure 1.1 for an overview of the pipeline network. The different flow meters are mostly non-fiscal ultrasound meters with nominal uncertainty around 0.7%. But one stream is an annubar with poorer accuracy. Around 2.0% is stated by the metering personnel. The actual uncertainty in flow rate will hence depend on the relative flow from the different sources, but will in general be around 1.0-1.5%. At the Zeebrugge terminal the flow measurement is fiscal ultrasound equipment with 0.5-0.7% uncertainty. The pressure transmitters are digiquartz transmitters of the same type as in Europipe 2, with 52 mbar uncertainty. Sleipner Riser is also equipped with Gas Chromatographs in all flow runs, allowing a detailed compositional analysis of the gas entering Zeepipe. Gas temperature into the pipeline can also be determined with sufficient accuracy.

7.4.2 Simulation model

Detailed information about the pipeline has been collected, and all physical aspects of it were thoroughly implemented in its TGNet model file. This includes information about:

- Pipeline length
- Inner diameter
- Elevation profile, including the end points
- Thickness of different wall layers, including relevant wall layer properties
- Burial depths along the route

The elevation profile and burial depth are shown in Figure 7.29 and Figure 7.30 respectively.

The pipeline is modeled as exposed to free stream sea-water at all locations where it is partly buried. It is only modeled as buried at those stretches where it is entirely covered with soil or gravel.

Environmental data such as ground conductivity and sea-water velocity are also included with the best available figures. Ground conductivity is set to 2.0 W/mK and the concrete conductivity is set to 2.9 W/mK.

Daily modeled temperature data from UK Met Office are used as ambient temperature.

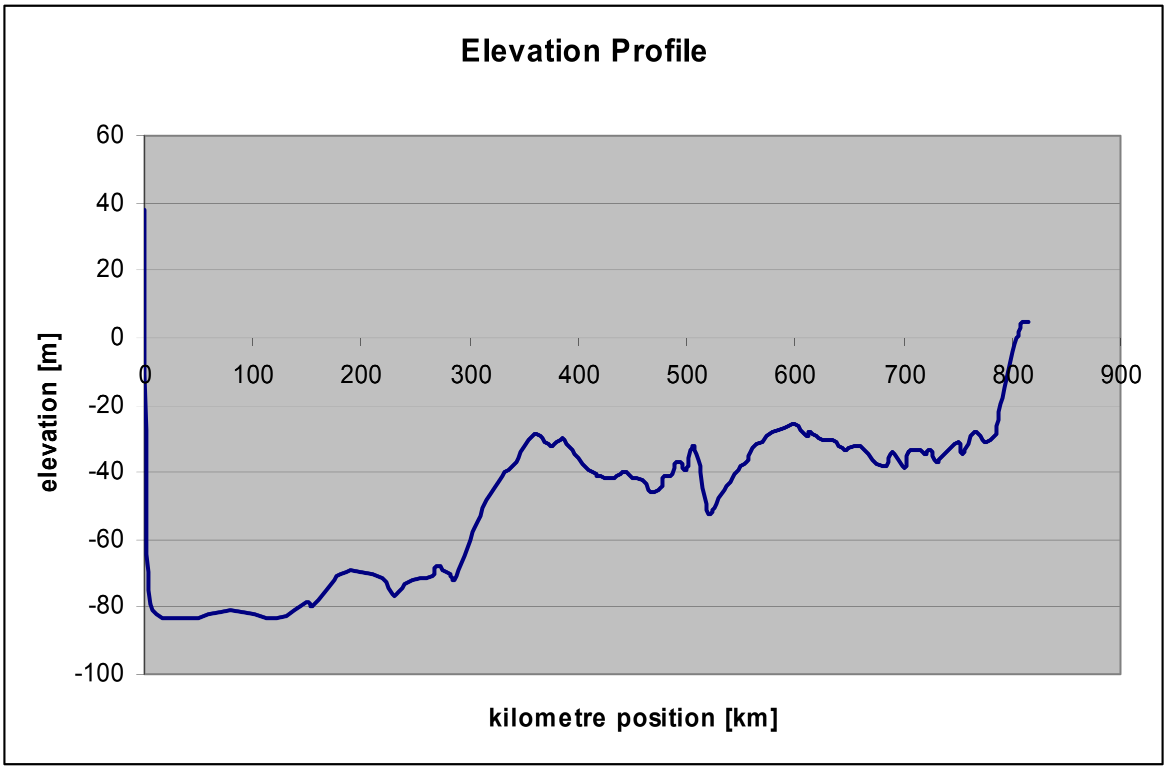

Figure 7.29 Elevation profile Zeepipe.

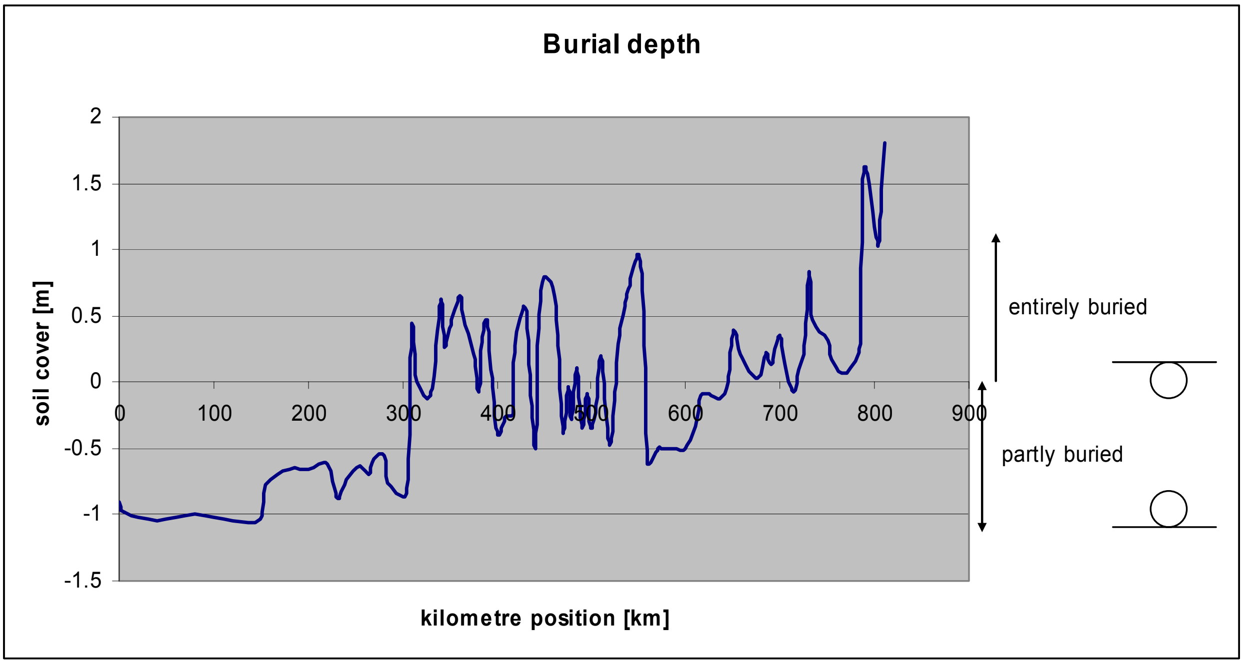

Figure 7.30 Burial depth Zeepipe.

7.4.3 Steady-state data periods

A total of 15 steady-state periods of 12 hour duration were collected for Zeepipe. The oldest period is from May 2002 and the newest is from May 2007. They all have a very good quality with regard to steadiness. The Reynolds number ranges from $11 \cdot 10^6$ to $35.5 \cdot 10^6$, but Reynolds numbers lower than $25 \cdot 10^6$ are very rare, particularly for long enough periods to ensure good steady-state conditions.

Details about the periods are reported in Table 7.12.

Table 7.12 Details about the steady-state periods in Zeepipe.

ID	Start Period	Duration [hours]	Averaged P [barg]		Averaged F [MSm^3/d]		Averaged C1 content [%]	Averaged T [deg C]	Reynolds number [-]	Tuned roughness [µm]
			Sleipner	**Zeebrugge**	**Sleipner**	**Zeebrugge**		**Sleipner**		
01	19.05.2002 16:10	12	132.59	100.04	29.80	29.68	90.89	13.84	23,615,168	2.52
02	16.06.2002 07:00	12	139.61	131.83	15.58	15.43	90.68	17.61	10,982,084	2.17
03	27.07.2002 09:15	12	143.55	87.96	38.54	38.36	84.30	45.25	32,266,936	2.27
04	25.10.2002 04:00	12	147.86	96.06	38.58	38.56	91.51	14.02	30,351,942	2.35
05	30.10.2002 09:45	12	147.68	94.66	38.67	38.87	91.25	15.77	30,671,178	2.67
06	13.01.2003 10:05	12	148.80	90.21	41.36	41.29	91.24	16.33	32,969,886	2.53
07	07.03.2004 18:30	12	149.09	82.11	43.85	43.99	92.93	5.71	35,349,076	2.32
08	12.04.2004 01:50	12	142.76	87.34	39.31	39.24	91.41	14.15	31,753,256	2.57
09	09.01.2005 16:30	12	149.32	82.84	43.27	43.41	92.11	10.90	35,001,280	2.55
10	14.06.2005 15:00	12	142.88	108.33	32.34	32.39	91.05	8.46	24,649,138	1.61
11	18.07 2005 01:30	12	146.70	83.70	41.73	41.66	89.75	18.43	34,217,036	1.63
12	08.01 2006 04:30	12	148.44	82.22	43.58	43.65	91.38	10.11	35,539,976	1.71
13	22.10.2006	12	134.10	116.76	22.46	21.90	91.74	3.64	16,617,802	2.67

	18:00									
14	17.12.2006 09:15	12	139.32	80.33	39.54	39.37	90.77	12.13	32,918,560	1.66
15	16.05.2007 18:00	12	136.40	101.40	31.39	31.22	90.88	16.36	24,603,200	2.24

7.4.4 Results

The simulated friction factor for all the steady-state periods are plotted in Figure 7.31.

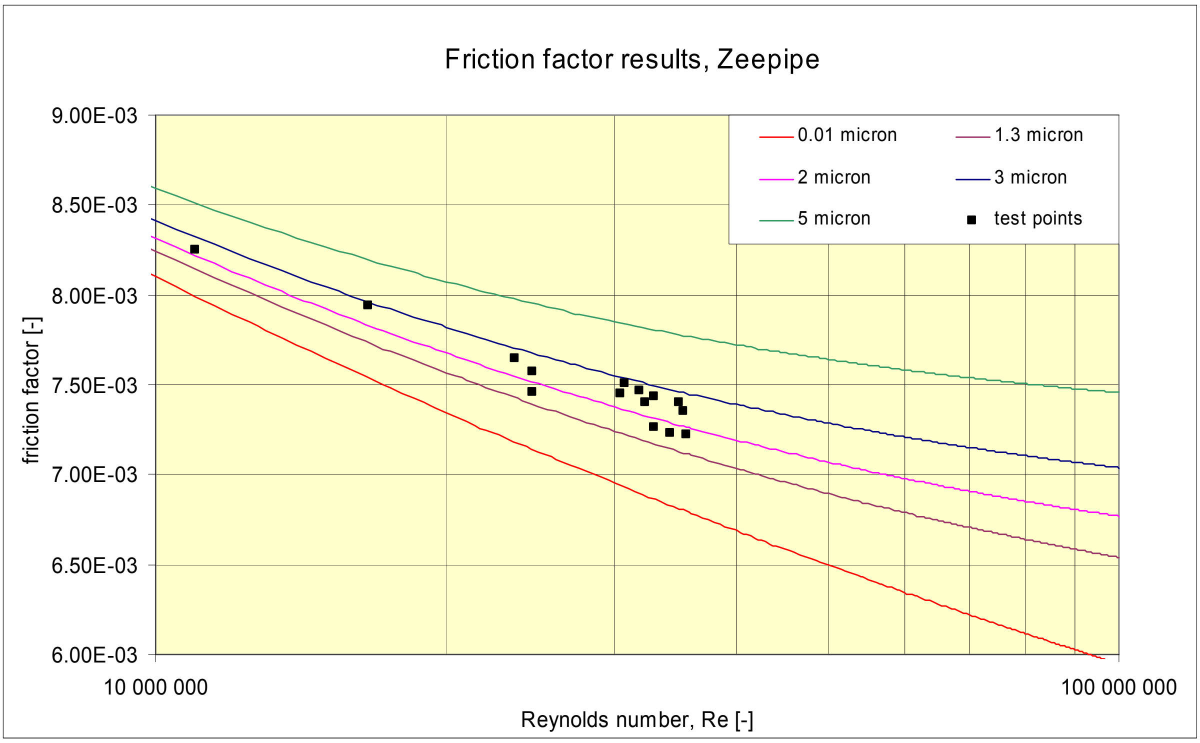

Figure 7.31 Simulated friction factors Zeepipe compared with CW curves.

As for Europipe 2, it is seen that the friction factor follows the Colebrook-White lines reasonably well, though some scatter exists. But the narrow Reynolds number range makes it difficult to obtain a curve with a different slope with great confidence. The friction is higher than in Europipe 2, and a sand grain equivalent roughness of 1.6-2.7 µm is needed to obtain the correct friction factor.

The difference between the measured and simulated outlet temperature is also examined to get a measure of how correct the simulated gas temperature is. The results are plotted in Figure 7.32.

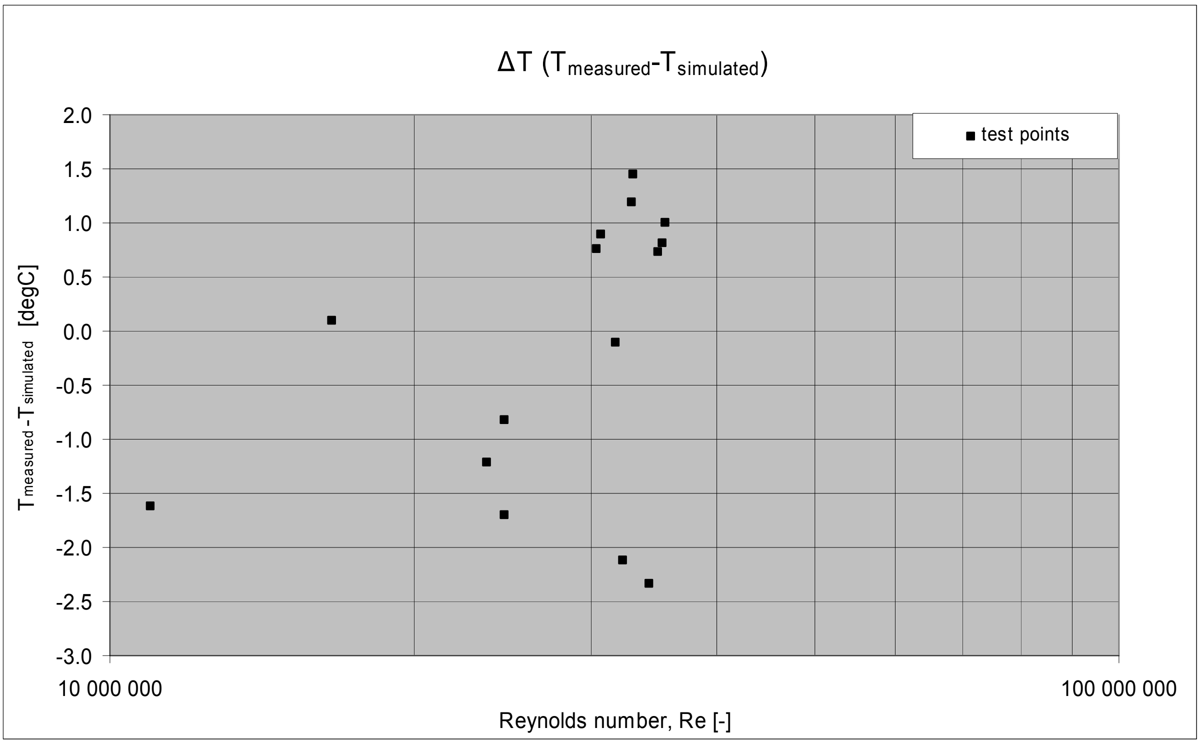

Figure 7.32 $T_{measured}$-$T_{simulated}$ in Zeepipe.

The temperature deviation is quite evenly distributed around zero, and shows that on average the model predicts correct outlet gas temperature. But a deviation of around 2 degrees at the most is large, and proves that the model can be improved. The deviation shows no dependency on Reynolds number.

In Figure 7.33 the deviation between measured and simulated gas outlet temperature is plotted versus season, i.e. instead of having Reynolds number abscissa, the abscissa is the month numbered 1 (January) to 12 (December) from which the steady-state period belongs. This shows that the simulator systematically predicts a too low gas temperature in the winter months and a too high a gas temperature in the summer months. But the deviation at the outlet cannot be taken as evidence that the whole gas temperature profile is too low or too high. In Figure 7.34 the simulated roughness is plotted with month on the abscissa. The simulated friction factors (or roughness) show no dependency on season. If the entire gas temperature profile was systematically predicted to be too cold or too warm depending on season, the friction factor would also depend on season.

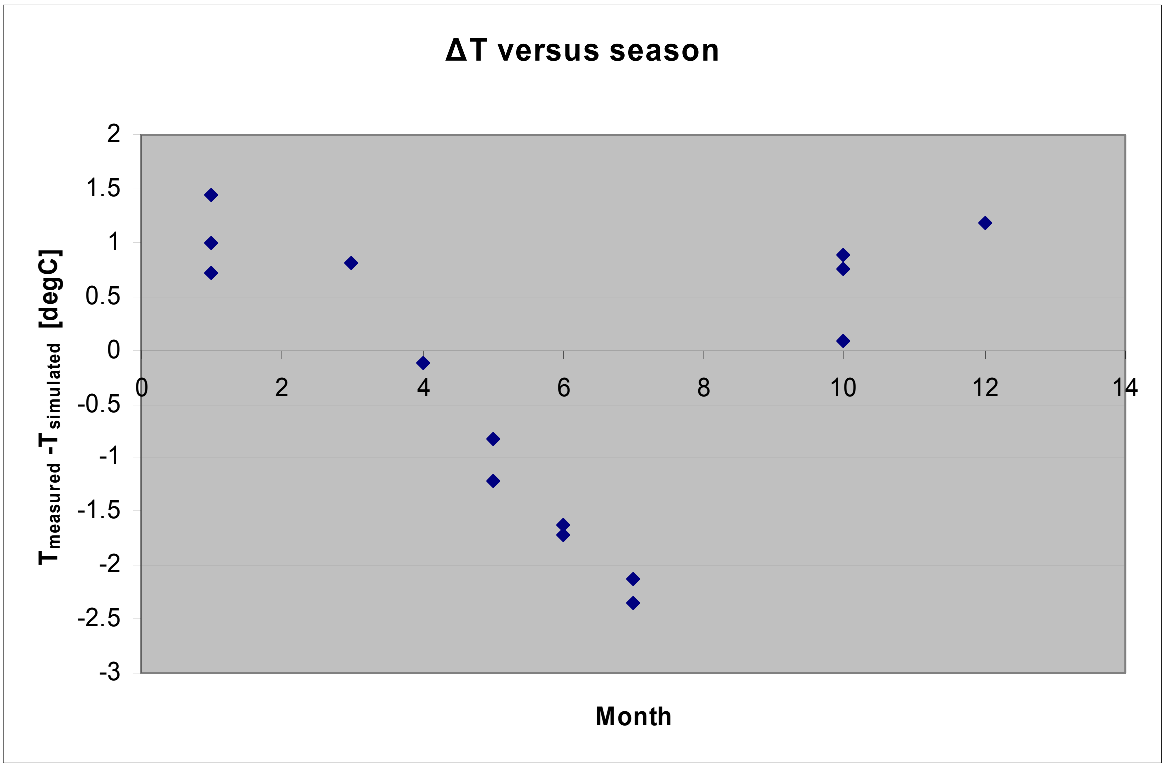

Figure 7.33 Temperature deviation versus season in Zeepipe.

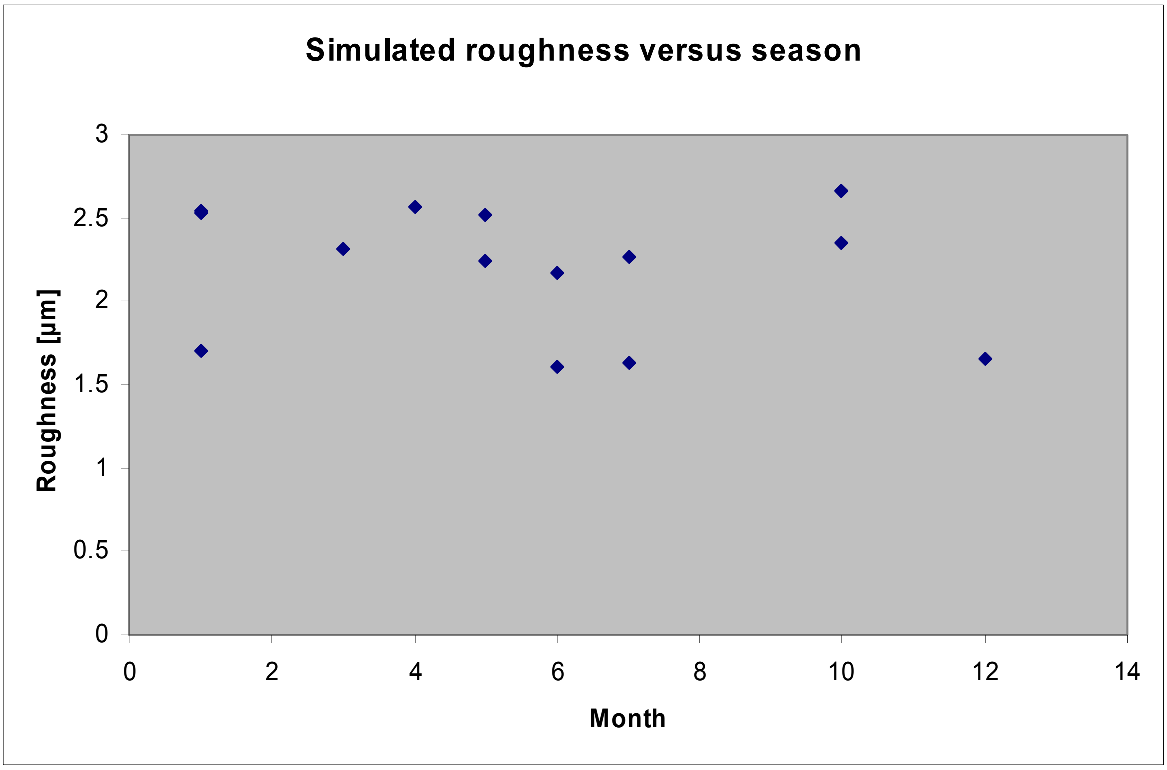

Figure 7.34 Simulated roughness versus season in Zeepipe.

7.5 Calculations of transport capacity

As briefly described in CHAPTER 1, the traditional way of calculating a long-term transport capacity for a natural gas pipeline in the North Sea is by tuning an effective roughness for a complete pipeline model in a well-controlled steady-state capacity test of the pipeline. The flow rates are often significantly lower than maximum capacity, due to insufficient gas available at the time of the test. The capacity is then found be employing this effective roughness and the hydraulic pressure limits, i.e. maximum inlet pressure and minimum outlet pressure to the pipeline model. This is performed at least once for all Gassco-operated pipelines, and often shortly after commissioning of a new pipeline.

This methodology is particularly prone to the accuracy of the effective roughness found from the single capacity test and the accuracy of the friction factor correlation used when extrapolating and finding the friction at maximum capacity. These two major uncertainty sources are reduced with an improved methodology for capacity estimation. Based on the present analysis of operational data, the transport capacity has been recalculated for both Europipe 2 and Zeepipe. The updated calculations were performed by averaging the calculated roughness for steady-state operational periods at large flow rates, typically with Reynolds numbers larger than $30 \cdot 10^6$. This corresponds to flow rates larger than around 80% of the maximum capacity. The updated calculations led to increased calculated capacity in Europipe 2 and Zeepipe of around 0.2-0.5%, which is of great benefit for the users of the system. Another pipeline, which was not chosen as a case here, showed a capacity increase of more than 1%. The friction factor at maximum transport capacity is hence lower than previously calculated for these pipelines. The results from the previous sections indicate that the extrapolation along Colebrook-White curves at these relatively narrow Reynolds number ranges work well. The main reason for the increased capacity is therefore probably due to more data points and better simulation models.

7.6 Discussion

The simulated friction factor results from the Kårstø-Bokn leg, Europipe 2 full length and Zeepipe seem to follow the Colebrook-White curves reasonably well, though some deviations are seen. The Kårstø-Bokn results decrease slower with increasing Reynolds number than predicted by Colebrook-White, but by taking the uncertainty into consideration, this is not significant. And the Europipe 2 results closely follow the Colebrook-White curve for roughness 1.3-1.4 μm, which is about the same roughness value as predicted by Kårstø-Bokn. The Zeepipe results follow a Colebrook-White curve with larger roughness than that of Europipe 2.

But the roughness measurements from CHAPTER 5 show that the root mean square roughness in a pipe of this type is around 4 μm (mean value between the sample points). The lowest sand grain equivalent roughness in the fully rough region that is suggested, is the one from Langelandsvik et al. (2008), with $k_s = 1.6 \cdot k_{rms}$. In this case this corresponds to $k_s = 6.4$ μm. The fully rough friction factor would then be $7.5 \cdot 10^{-3}$, which is about 7% larger than the lowest friction factor point reported for Europipe 2 in Figure 7.35. One viable explanation to this could be that the simulated friction factors are the first part of an inflectional curve just before the point where the curve turns upwards to its fully rough value. The curve would then exhibit a much stronger downwards dip than for example that measured by Shockling et al. (2006), where the dip was 2-3% lower than the fully rough value. Another, and probably more likely explanation, is that the physical wall roughness is smoothed by small amounts of liquid.

By looking at the pig sent in Europipe 2 after arrival in Dornum (Figure 7.36), it is clear that some oil or grease must be present in the pipe. Whether this results from drop out of heavy hydrocarbon components or is lubrication oil from e.g. compressors or valves is uncertain. But a thin liquid film in parts of the pipeline could probably smooth the physical wall roughness, and give lower friction factor than a clean surface would.

Gersten & Papenfuss (1999) discuss the effect of a very thin liquid film on the pipe surface, based on a theoretical approach and also by using available experimental flow test results particularly from Uhl et al. (1965). Their proposal is that below a critical Reynolds number the liquid is not moving, it smoothes the surface and hence reduces the wall friction. At larger Reynolds numbers the liquid becomes wavier, starts moving with the gas flow and increases friction. In total this could explain an abrupt or inflectional transition. But their model also requires that the liquid hold-up increases with the Reynolds number, which seems unlikely in a long pipeline where the liquid, if any, must reside in the pipeline for a very long time. The liquid hold up necessary to explain the proposed behavior is given as around 10^{-4}. For a 1 m diameter pipeline with the liquid film evenly smoothed out around the circumference, this corresponds to a film thickness of 25 µm. This is larger than the roughness elements in the Gassco operated pipelines, but is still in the same order of magnitude. The total amount of liquid in Europipe 2 would then be 50 m^3, which is hard to believe compared with the very limited amount of liquid cleaned out by the pig. And the strong rubber disk on the pig must have worked as an effective scraper. But at least the results by Gersten & Papenfuss support the idea that small amounts of liquid could affect the wall friction in either way.

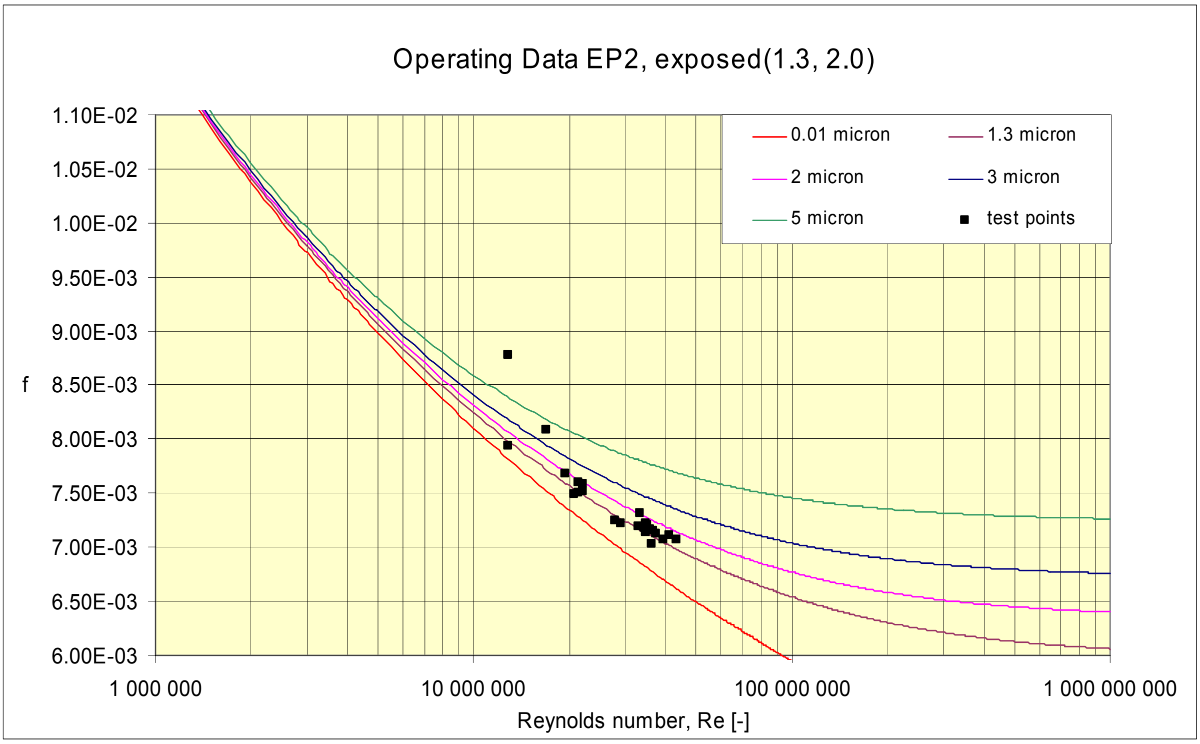

Figure 7.35 Simulated friction factor results Europipe 2 compared with CW curves.

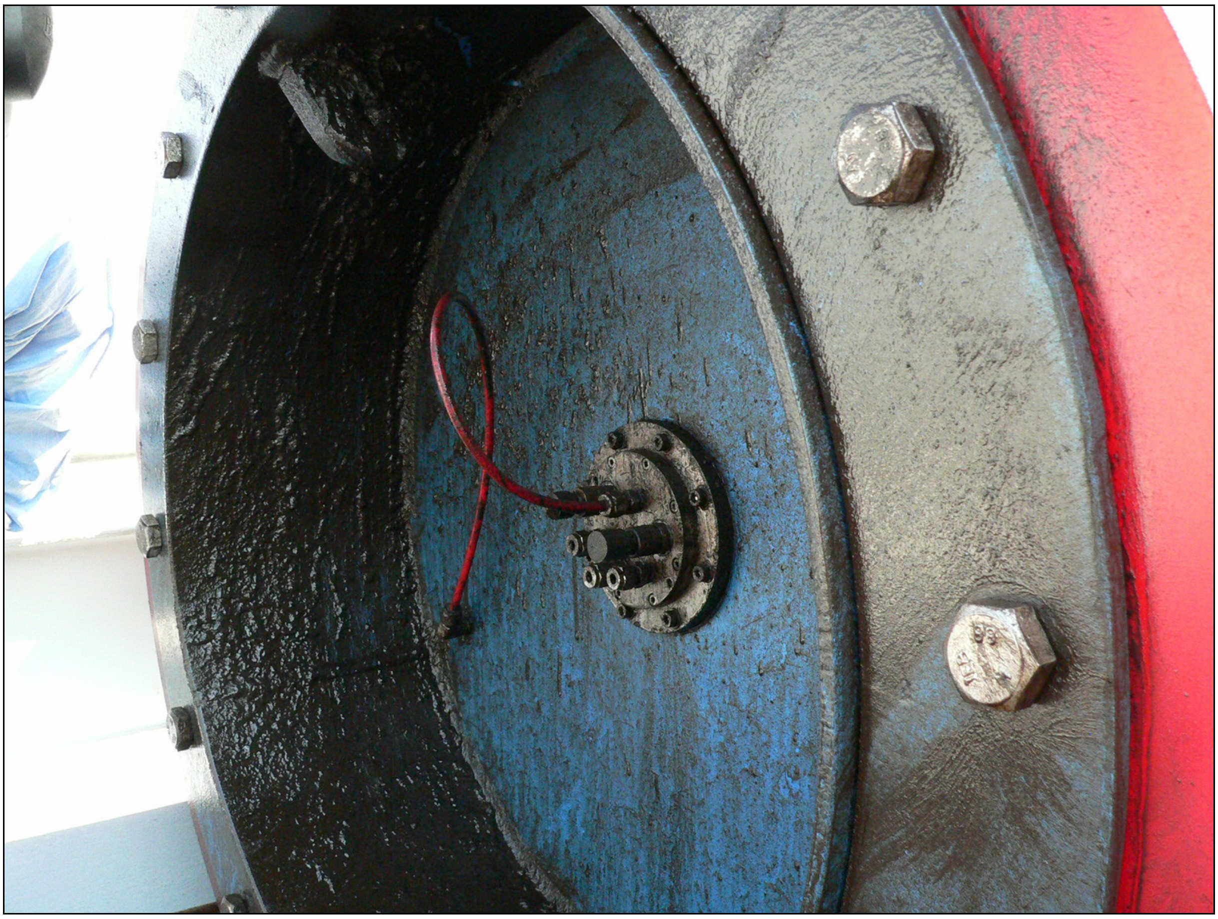

Figure 7.36 Europipe 2 pig after arrival in Dornum.

Figure 7.37 plots the Europipe 2 results together with several predictions of the collapse point with the fully rough line. It is illustrated that the fully rough friction factor predicted by Langelandsvik et al. (2008) (k_s = 1.6 k_{rms}) and using k_{rms} = 4 µm is larger than the simulated friction factor results. The corresponding Reynolds number for collapse with the fully rough line is also around $100 \cdot 10^6$. Together this would predict a sudden and unlikely change in the friction factor development. The same roughness and the factor from Shockling et al. (2006) (k_s = 3.0 k_{rms}) would predict an even more unlikely behavior, with an extremely sharp inflectional curve.

But by assuming a physical roughness of 2 µm, either that it is reduced by small liquid amounts or that the true roughness for other reasons is lower than our measurements, it is seen that k_s = 1.6 k_{rms} gives a more likely curve. In this case our points at the largest Reynolds numbers are very close to the fully rough line. But one cannot predict if a downwards dip would also be present.

It is recalled from CHAPTER 5 that the full-scale coated pipelines have a very large kurtosis, for some samples as large as 10 - 50, being explained by small areas showing a very large roughness compared with the total root mean square value of the sample. It is hard to state that the large kurtosis would make a real pipeline behave more like the aluminium pipe with inflectional transition from Shockling et al. (2006), which also had a kurtosis larger than the Gaussian value of 3, because the kurtosis is so much larger than both the discussed laboratory pipes from Superpipe (2.5 for commercial steel pipe and 3.4 for honed rough aluminium pipe). The irregular pattern with spots with extremely large roughness also makes this a different type of surface.

The black dashed line in Figure 7.37 represents one imaginary friction factor curve the Europipe 2 results might be a part of. It departs from the smooth curve at the point predicted by Langelandsvik et al. (2008) and ends up at the predicted fully rough friction factor, though at a larger Reynolds number than would be expected based on the Superpipe results.

Most results show that the real friction factor shows a more abrupt transitional region, either inflectional or monotonic, which means that the sand grain equivalent roughness at fully rough conditions is larger than that of the Colebrook-White curves which coincidentally matches the results in the relatively narrow Reynolds number range. The friction factor is therefore believed to deviate from its Colebrook-White curve at larger Reynolds numbers. Extrapolating along this curve into a larger Reynolds number is hence not recommended.

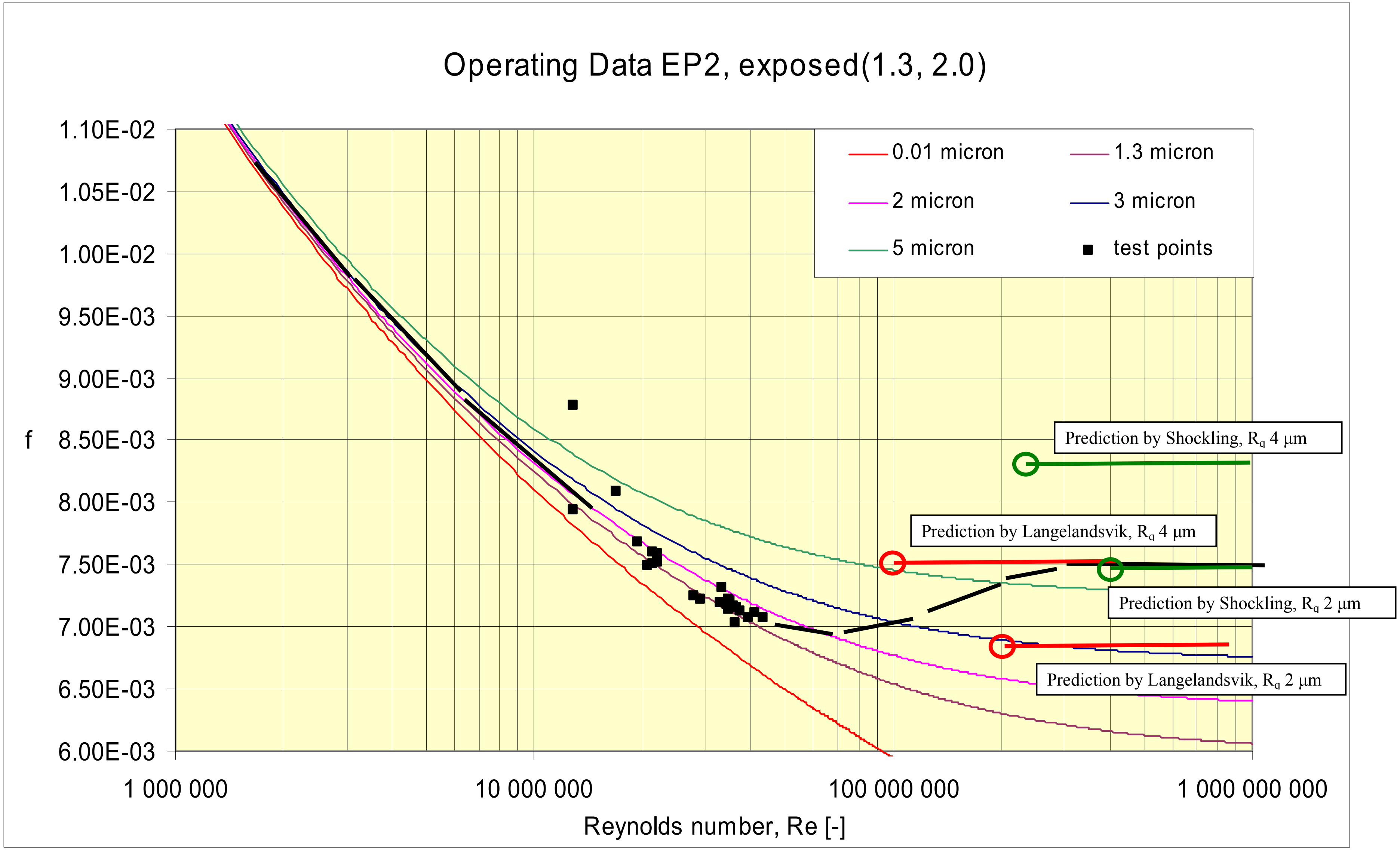

Figure 7.37 Possible points of collapse with fully rough line for Europipe 2.

In Section 5.6 it was proposed that the first roughness effects are seen for Re ≈ 2-6·10^6, which is based on an estimate of the largest roughness elements. But the roughness measurements also revealed that the kurtosis is very large, meaning that the size of the largest roughness elements is large compared to the average value (R_a or R_q), which due to traditional explanation causes a long transition region. This fits well together with the Europipe 2 and Zeepipe results.

An effect that was discussed for the Kårstø-Bokn leg, but was omitted for the full-length pipelines, is the additional pressure drop due to curves. The curvature turned out to be so strong that additional pressure drops are expected. However the available results in the literature within these operational conditions make it impossible to quantify the effect. But the effect will support the discussion above in that the measured friction factor in the pipelines seems to be low.

The GERG friction factor formula presented in Gersten et al. (2000), and also described in Section 2.1, is plotted together with the Europipe 2 and Zeepipe results in the figure below. The curves colored green and blue represent a friction factor where additional pressure drop due to curves, valves and other fittings are accounted for, i.e. where the draught factor is lower than 1. It is not obvious that either of these two curves yields a better fit of the data. But still the operational data cover a too narrow Reynolds number range to draw a firm conclusion.

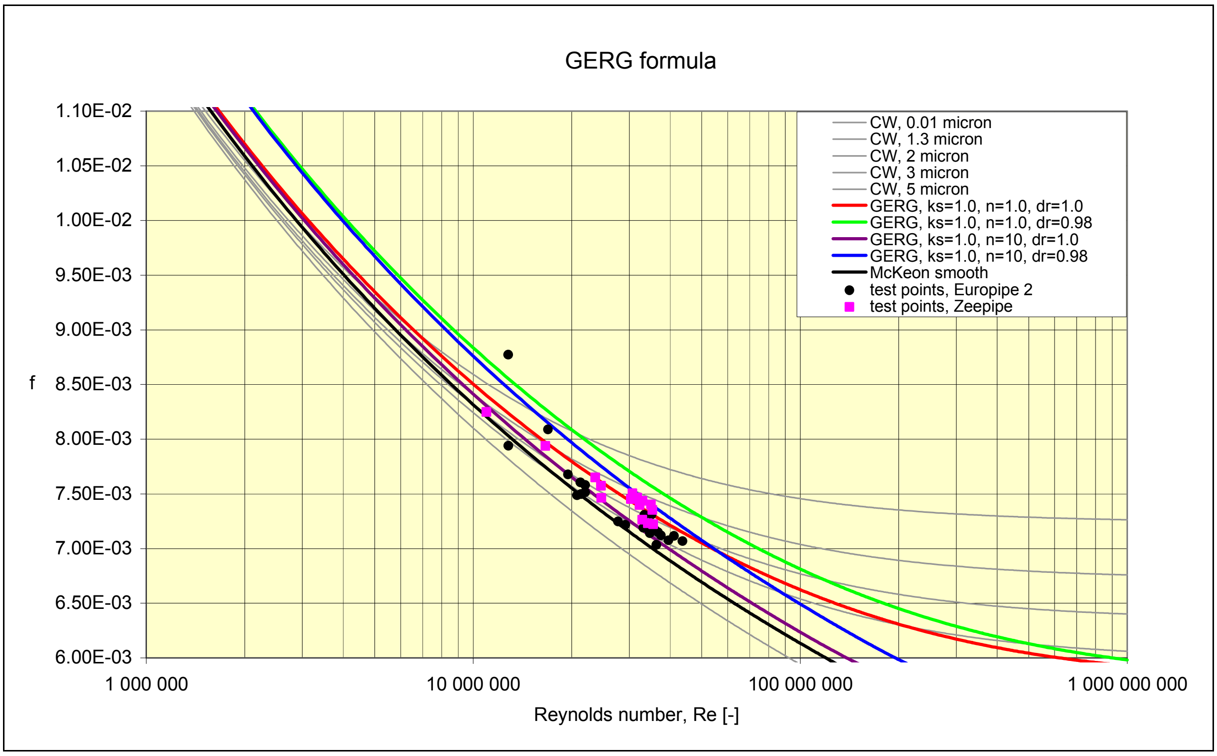

Figure 7.38 Friction factor results compared with different versions of the GERG formula.

The smooth curve of McKeon is also plotted in Figure 7.38. This curve is about 3% above the Colebrook-White smooth curve, implying that the results from particularly Europipe 2 are very close to McKeon's smooth line.

The uncertainty in the Europipe 2 experiments were slightly above 2% across the whole Reynolds number range, while for the Kårstø-Bokn leg it was less than 2% for large Reynolds numbers, but growing to 4-5% for $Re = 20 \cdot 10^6$. The only open question in these uncertainty calculations is the effect of small transients in the operational periods that are treated as completely steady-state. It will contribute to a larger uncertainty, but of unknown magnitude, though the brief investigations performed in Section 7.2.5 for Kårstø-Bokn pipeline using the dynamic part of TGNet, indicated a very little contribution.

Experimental data from the Langeled pipeline were also originally analyzed. But they turned out to exhibit an extremely strange trend which was impossible to explain. The data set was therefore deemed an anomaly and omitted from the further analysis.

CHAPTER 8

Conclusions

The analysis of full-scale operational data covering different Reynolds numbers, and particularly Reynolds number close to the maximum capacity of pipelines, has successfully lead to better calibration in terms of effective roughness for the models. Better calibration and better knowledge about the actual friction factor at large flow rates also lead to more accurate knowledge about the hydraulic capacity in the pipelines.

As a result, the capacity that Gassco makes available to the shippers of gas, has been increased by 0.2-1.0% for several pipelines. Based on new viscosity measurements, the viscosity correlation in use has also been changed. And thanks to the sensitivity analysis performed, more knowledge about the relevant importance of the different input parameters has been gained.

The quality of one-dimensional pure gas phase pipeline simulators in general, and TGNet in particular has been shown to be very good. A derivation of their different terms was carried out, and the conclusion is that they resolve the physics of bulk quantities well. The unresolved issues include:

- The friction factor of curved pipes
- Heat transfer for partially buried pipes

which are the most severe. The non-unity profile factors due the velocity profile not being flat are negligible, both because the factor is close to unity and because the terms it is applied to are very small. The numerics of TGNet were described, but not analyzed in detail.

The sensitivity analysis performed on an artificial model as well as the uncertainty analysis for the full-scale experiments both indicated which parameters are most important in the simulations:

- Gas density calculation
- Ambient temperature (affecting the gas temperature)
- Flow rate measurement
- Inner diameter of pipeline

The present work sheds some light on the link between the physically measured roughness and the model roughness (hydraulic roughness).

- Measurements in Princeton Superpipe were taken on a natural rough steel pipe and covered Reynolds numbers from $150\cdot10^3$ to $20\cdot10^6$, meaning that they reached a Reynolds number range not yet covered for natural rough pipes. They revealed a transition region which is more abrupt than predicted by the Colebrook-White equation.

- The experiments in Superpipe show a remarkably low friction for this natural rough surface, in that the sand grain equivalent roughness equals 1.6 times the root mean square roughness, in contrast to the values of 3.0-5.0 that is commonly used.
- The same measurements showed departure from the smooth line when the largest roughness elements were half the thickness of the viscous sub-layer, which generally is assumed to be five viscous length scales. A former test in Superpipe also supports an earlier departure from the smooth line than the common understanding that this happens when the large roughness elements correspond to five time the viscous length scale.

The analysis of unique full-scale operational data covering Reynolds numbers from $10\cdot10^6$ to $45\cdot10^6$ showed:

- Taking the uncertainty into account, the data points collapse reasonably well around the Colebrook-White curves for the investigated Reynolds number range.
- Roughness measurements of a coated large-scale natural gas transport pipeline showed an average root mean square roughness of 4 μm. The surface was very irregular with some very large spots.
- The friction factor results are most likely in the transition zone between smooth and fully rough turbulent conditions. The sand grain equivalent roughness of the Colebrook-White curves that (coincidentally) match the results is 1.5-3.0 μm. This is lower than the roughness measurements would predict, and probably also lower than what the sand grain equivalent roughness would be at fully rough conditions. This shows that the transitional zone the results is part of, is more abrupt than predicted by Colebrook-White.
- Extrapolation along the associated Colebrook-White beyond the investigated Reynolds number range is questioned for the reasons given above. It is therefore not recommended to rely on this line for significantly larger Reynolds numbers. At $Re \approx 60\cdot10^6$ the deviation could become significant.

CHAPTER 9

Recommendations

In order to achieve perfect flow models for natural gas in large diameter pipelines, several aspects have been pinpointed throughout this dissertation. Some of them, such as flow meter uncertainty and ambient temperature models, are normally treated as input parameters and belong to other fields of research. Nonetheless, the uncertainty has been quantified and the potential is obvious.

The density calculation was also shown to play an important role. But research on equations of state has been focused on by many research groups for many years. It is important that research community keeps focusing on this work.

Pressure loss in slightly curved pipes rather than sharp bends has not received the appropriate attention so far. The pressure drop depending on Reynolds number, curvature and possibly other parameters needs to be quantified to improve the results from the full-scale pipelines. The significance of this effect is not known, but it may be able to explain differences in friction factors between the pipelines. A combination of CFD simulations and laboratory experiments could perhaps be a useful approach.

Another major and unquantified uncertainty is the effect of the liquid that probably is present in small amounts on the pipeline walls. The amount, distribution and condition of it most probably vary from pipeline to pipeline. It has been speculated if it is possible to mount a camera on a pig and take a film of the inner surface. This idea should be pursued. One could also dig deeper into the literature to see if others have studied the effects of liquid on a surface. The phenomena could perhaps be treated as an extreme of two phase flow.

This work has focused on steady-state effects in the simulation models and has also only analyzed steady-state periods of operational data. But realizing that these data periods were never fully steady-state, but merely transient periods which resembled steady-state, this calls for analysis of the transient and dynamic effects in a natural gas pipeline. This raises these questions: Which uncertainty is added by treating the data periods as fully steady-state? Is this uncertainty random, or may some of it be systematic? An even more fundamental question is whether a steady-state friction factor correlation is sufficient to describe a dynamic system which never reaches a perfect steady-state condition. Transient operational data could be analyzed by simulation models to contribute to an answer. The dynamic behavior of the simulation model should also be analyzed.

References

Allen, J.J., Shockling, M.A., Smits, A.J. (2005). *Evaluation of universal transitional resistance diagram for pipes with honed surface*. Physics of Fluids, Vol. 17, 121702, 2005.

Assael, M.J., Dalaouti, N.K., Vesovic, V. (2001). *Viscosity of Natural-Gas Mixtures: Measurements and Prediction*. International Journal of Thermophysics, Vol. 22, No. 1, 2001.

Benedict, R.P. (1980). *Fundamentals of Pipe Flow*. John Wiley & Sons.

Berger, S.A., Talbot, L., Yao, L.-S., *Flow in curved pipes*. Ann. Rev. Fluid Mech., 1983, 15:461-512.

Borse, G.J. (1997). Numerical Methods with MATLAB – A Resource for Scientists and Engineers. PWS Publishing Company.

Charron Y., Duval, S., Melot, D., Shaw, S., Alary, V. (2005). *Designing for internally coated pipelines*. Proceedings of the 16th International Conference on Pipeline Protection, Cyprus 2005.

Churchill, S.W., Chu, H. H. S., Correlating equations for laminar and turbulent free convection from a horizontal cylinder, Int. J. Heat Mass Transfer, 18, 1975, pp. 1049-1053.

Churchill, S.W. (2002). *Heat exchanger design handbook* (chief editor: G.F. Hewitt), part 2, chapter 2.5.9: *Combined free and forced convection around immersed bodies.* Begell House, Inc., New York, 2002.

Coffields, R.D., Brooks, P.S., Hammon, R.B., *Piping elbow irrecoverable pressure loss coefficients for moderately high Reynolds numbers,* Bettis Atomic Power Laboratory, West Mifflin Pennsylvania US, 1994, DE-AC11-93PN38195.

Colebrook, C., 1939, Turbulent flow in pipes, with particular reference to the transition regime between the smooth and rough pipe laws. Institution of Civ. Eng. Journal, 11:133-156. paper no. 5204.

Colebrook, C. F. and White, C. M., *Experiments with fluid friction in roughened pipes.* Proc. Royal Soc. (A) 161, 367-378, 1937.

Crawford, N.M., Cunningham, G., Spence, S.W.T., *An experimental investigation into the pressure drop for turbulent flow in 90° elbow bends.* Proceedings of the Institution of Mechanical Engineers, Part E. J. Process Mechanical Engineering, Vol. 221, 2007, pp. 77-88.

Gersten, K., Papenfuss, H.D. (1999). *GERG Research Project 1.19 on Calculation of Flow in Gas Pipelines Downstream of a Compressor.* Report from a GERG-project (Groupe Europeen de Recherches Gazieres) conducted by Ruhr Univeristy Bochum, Germany.

Gersten, K., Papenfuss, H.D., Kurschat, T.H., Genillon, P.H., Fernandez Perez, F., Revell, N. (2000). *New transmission-factor formula proposed for gas pipelines*, Oil & Gas Journal, Feb. 14th 2000, pp. 58-62.

Gersten, K., Papenfuss, H.D., Kurschat, T.H., Genillon, P.H., Fernandez Perez, F., Revell, N. *Heat Transfer in Gas Pipelines*, OIL GAS European Magazine, 1/2001.

Gnielinski, V., (1976), *New equations for heat and mass transfer in turbulent pipe and channel flow*. International Chemical Engineering, Vol. 16, pp. 359-368.

GPSA Engineering Data Book, 12th edition, 2004.

Hama, F.R. (1954). Boundary-layer characteristics for smooth and rough surfaces. Trans SNAME, Vol. 62, pp. 333-358.

Hillel, D. *Introduction to soil physics.* Academic Press, San Diego, CA, 1982.

Holden, H. (2005). *Personal communication*. Professor Mathematics/Numerics, Norwegian University of Science and Technology (NTNU).

Huber, M.L. (2007). *NIST Standard Reference Database 4 (SUPERTRAPP)*, Stand. Ref. Data Program, Nat. Inst. Stand. Technol. (NIST), Gaithersburg, Maryland.

Idelchik, I. (1986). *Handbook of Hydraulic Resistance.* Hemisphere Publishing Corporation, New York.

Incropera, F.P., DeWitt, D.P., *Fundamentals of Heat and Mass Transfer*, 3th edition, Wiley, New York, 1990.

Ito, H. (1959). *Friction Factors for Turbulent Flow in Curved Pipes*. Journal of Basic Engineering, June 1959.

Ito, H. (1960). *Pressure losses in smooth pipe bends*. ASME Transactions, Series D, p. 131.

Ito, H. (1987). *Flow in Curved Pipes.* JSME International Journal, Vol. 30, Issue 262, 1987, pp. 543-552.

Katz, D.L., Cornell, D., Kobayashi, R., Poettmann, F.H., Vary, J.A., Elenbaas, J.R., Weinaug, C.F. *Handbook of Natural Gas Engineering*. McGraw Hill Book Company, 1959.

Keller, H.B. (1974). *Accurate Difference Methods for Nonlinear Two-point Boundary Value Problems.* SIAM Journal on Numerical Analysis, Vol. 11, No. 2, April 1974.

Kristoffersen, R. (2005). Lecture notes in PhD course “Background in advanced CFD”, the Norwegian University of Science and Technology.

Langelandsvik, L.I., Postvoll, W., Svendsen, P., Øverli, J.M., Ytrehus, T. (2005). *An evaluation of the friction factor formula based on operational data*. Proceedings of the 2005 PSIG Conference San Antonio Texas.

Langelandsvik, L.I., Solvang, S., Rousselet, M., Metaxa, I.N., Assael, M.J. (2007). *Dynamic Viscosity Measurements of Three Natural Gas Mixtures – Comparison against Prediction Models*. International Journal of Thermophysics, Vol. 28, pp. 1120-1130.

Langelandsvik, L.I., Solvang, S., Rousselet, M., Assael, M.J. (2007) b. *New Viscosity Measurements of Three Natural-gas Mixtures & An Improved Tuning of the LGE-Correlation.* Proceedings of the Asian Thermophysical Properties Conference, 2007, Fukuoka, Japan.

Langelandsvik, L.I., Kunkel, G.J. and Smits, A.J., 2008, *Flow in a commercial steel pipe*. Journal of Fluid Mechanics, Vol. 595, pp. 323-339.

Lee, A.L., Gonzalez, M.H., Eakin, B.E. (1966). *The Viscosity of Natural Gases*. Journal of Petroleum Technology, August 1966, pp. 997-1000.

Luskin, M. (1979). An Approximate Procedure for Nonsymmetric, Nonlinear Hyperbolic Systems with Integral Boundary Conditions. SIAM Journal on Numerical Analysis, Vol. 16, No. 1, February 1979.

McKeon, B.J., Smits, A.J. (2002). Static pressure correction in high Reynolds number fully developed turbulent pipe flow. Meas. Sci. Tech, Vol. 13, 2002, pp. 1608-1614.

McKeon, B.J., Li, J., Jiang, W., Morrison, J.F., Smits, A.J. (2003). *Pitot probe corrections in fully-developed turbulent pipe flow.* Meas. Sci. Tech, Vol. 14, 2003, pp. 1449-1458.

McKeon, B.J., Zagarola, M.V., Smits, A.J. (2005). *A new friction factor relationship for fully developed pipe flow*. Journal of Fluid Mechanics, Vol. 538, pp. 429-443.

Millikan, C.A. (1938). *A critical discussion of turbulent flows in channels and circular pipes*. Proceedings of the 5th International Congress of Applied Mechanics, pp. 386-392.

Mills, A.F. (1995). *Heat and Mass Transfer.* Richard D. Irvwin, Inc., 1995.

Moody, L. (1944). *Friction factors for pipe flow*. Transaction of the ASME, 66:671-684.

Morud, J.C., Simonsen, A. (2007). *Heat transfer from partially buried pipes.* Proceedings of the 16th Australasian Fluid Mechanics Conference, Crown Plaza, Gold Coast, Australia, 2007.

Nabizadeh, H., Mayinger, F. (1999). *Viscosity of binary mixtures of hydrogen and natural gas (hythane) in the gaseous phase*, High Temperatures – High Pressures, Vol. 31, 1999, pp. 601 – 612.

Nikuradse, J. (1932). *Gesetzmessigkeiten der turbulenten stromung in glatten rohren*. Forschungsheft 356, volume B, VDI Verlag Berlin. Translated in NASA TT F-10, 359, 1966.

Nikuradse, J. (1933). *Stromungsgesetze in rauhen rohren.* Forschungsheft 361, volume B, VDI Verlag Berlin. Translated in NACA Technical Memorandum nr. 1292, 1950.

Offshore Standard, DNV-OS-F101, *Submarine Pipeline Systems*, January 2000.

Piggott, J., Revell, N., Kurschat, T. (2002), *Taking the Rough with the Smooth – a new look at transmission factor formulae*. Proceedings of the 2002 PSIG Conference Portland Oregon.

Pipeline Studio User's Guide, 1999 by LICENERGY Inc. (now Energy Solutions)

Poling, B.E., Prausnitz, J.M. , O'Connell, J.P. (2000), *The Properties of Gases and Liquids*, 5th ed. McGraw Hill, New York, 2000.

Powle, Usha A. (1981). *Energy losses in smooth pipe bends*. Mechanical Engineering Bulletin, Vol 12, No. 4, 1981, pp. 104-109.

Schley, P., Jaeschke, M., Kuchenmeister, C., Vogel, E. (2004). *Viscosity Measurements and Predictions for Natural Gas*. International Journal of Thermophysics, Vol. 25, No. 6, 2004.

Shockling, M. A. (2005), *Turbulent flow in a rough pipe*, Master thesis, Princeton University, 2005.

Shockling, M. A., Allen, J. J., Smits, A. J., 2006, *Roughness effects in turbulent pipe flow*. Journal of Fluid Mechanics, Vol. 564, pp. 267-285.

Sletfjerding, E., Gudmundsson, J.S., Sjøen, K. (1998). *Flow experiments with high pressure natural gas in coated and plain pipes.* Proceedings of the 1998 PSIG Conference Denver Colorado.

Sletfjerding, E., 1999, *Friction factor in smooth and rough gas pipelines – An Experimental Study.* Dissertation for the degree of Doktor Ingeniør (PhD), Norwegian University of Science and Technology.

Smith, R., Miller, J., Ferguson, J. (1956). *Flow of natural gas through experimental pipelines and transmission lines*. Bureau of Mines, Monograph 9. American Gas Association.

Starling, K.E. (1973). *Fluid Thermodynamic Properties for Light Petroleum Systems.* Gulf Publishing Company, Houston, Texas, 1973.

Uhl, A., Bischoff, K.B., Bukacek, R.F., Burket, P.V., Ellington, R.T., Kniebes, D.V., Staats, W.R., Worcester, D.A. (1965). *Steady flow in gas pipelines*. Institute of Gas Technology Technical report no. 10. American Gas Association.

Vesovic, V. (2001). *Predicting the Viscosity of Natural Gas*. International Journal of Thermophysics, Vol. 22, No. 2, 2001.

White, F.M. (1991). *Fluid Mechanics.* McGraw-Hill, Second Edition.

Whitson, C., Brule, M. (2000). *Phase Behaviour*. Monograph Vol. 20, Society of Petroleum Engineers, 2000, p. 26.

Winterton, R.H.S., *Where did the Dittus and Boelter equation come from?* International Journal of Heat and Mass Transfer, 41, 809, 1998.

Ytrehus, T. (2004-2007). *Personal communication*. Professor Fluid Dynamics, Norwegian University of Science and Technology (NTNU).

Zagarola, M.V. (1996). *Mean-Flow Scaling for Turbulent Pipe Flow*. Thesis submitted for the degree of Doctor of Philosophy, Princeton University, 1996.

Zagarola, M.V., Smits, A.J. (1998). *Mean-flow scaling of turbulent pipe flow*. Journal of Fluid Mechanics, Vol. 373, pp. 33-79.

Zukauskas, A. and Ziugzda, J., *Heat Transfer of a cylinder in crossflow*. Hemisphere publishing corporation, 1985.

Appendix A

Model details

A.1 Momentum Balance, 3D to 1D

The one-dimensional balance equations (Eq. 2.14, Eq. 2.15 and Eq. 2.17) have been derived by integrating the Navier Stokes equations across a cross section. The variations in y- and z-directions disappear in this integration and only the velocity and changes in the x-direction are remaining.

For the momentum balance the three dimensional Reynolds averaged version is given as:

$$\rho \frac{D\overline{V}}{Dt} = \rho g - \nabla \overline{p} + \nabla \cdot \sigma_{ij}$$ **Eq. A-1**

where the stress in the gas is composed by one laminar and one turbulent part:

$$\sigma_{ij} = \mu \left(\frac{\partial \overline{u_i}}{\partial x_j} + \frac{\partial \overline{u_j}}{\partial x_i} \right) - \rho \overline{u_i' u_j'}$$ **Eq. A-2**

and the Reynolds averaging is defined as splitting the variable into its mean part and the time varying part which by definition has mean zero.

$$\begin{aligned} u_i &= \overline{u_i} + u_i' \\ p &= \overline{p} + p' \end{aligned}$$ **Eq. A-3**

Acceleration term

Looking at the balance equation in x-direction, and averaging the term on the left hand side gives us:

$$\frac{1}{A} \iint_A \rho \frac{D\overline{u}}{Dt} dA = \frac{1}{A} \iint_A \rho \left(\frac{\partial \overline{u}}{\partial t} + \overline{u} \frac{\partial \overline{u}}{\partial x} \right) dA$$ **Eq. A-4**

which can be taken to conservation form by applying the continuity equation:

$$\frac{1}{A} \iint_A \rho \left(\frac{\partial \overline{u}}{\partial t} + \overline{u} \frac{\partial \overline{u}}{\partial x} \right) dA = \frac{1}{A} \iint_A \left(\frac{\partial \rho \overline{u}}{\partial t} + \frac{\partial \rho \overline{u}^2}{\partial x} \right) dA$$ **Eq. A-5**

This can be taken one step further by introducing the cross sectional averaged and Reynolds averaged velocity U and assuming constant density across the cross section:

$$\frac{1}{A}\iint_A \left(\frac{\partial \rho \overline{u}}{\partial t} + \frac{\partial \rho \overline{u}^2}{\partial x} \right) dA = \rho \left(\frac{\partial U}{\partial t} + \beta_1 \frac{\partial U^2}{\partial x} \right)$$ **Eq. A-6**

The β-factor is the profile factor, and is defined as:

$$\beta_1 = \frac{1}{AU^2}\iint_A \overline{u}^2 dA$$ **Eq. A-7**

If one furthermore wants to account for non-constant density across the cross section, the correction factor should be modified to:

$$\beta_1 = \frac{1}{\rho U^2 A}\iint_A \rho \overline{u}^2 dA$$ **Eq. A-8**

For a uniform velocity distribution β_1 is 1. Fully developed turbulent pipe flows at high Reynolds numbers are characterized by β_1-values very close to 1. Benedict (1980) denotes it “momentum correction factor”, and derives a formula for the factor assuming a log law velocity profile:

$$\beta_{1,\log law} = 1 + 0.9765625 f$$ **Eq. A-9**

Smooth pipe flow at Re = $30 \cdot 10^6$ has $f \approx 7\ 10^{-3}$ and hence en estimated β_1-value of 1.007. According to Gersten et al. (1999) a Reynolds number of 10^7 yields a β_1-value of 1.01. For lower Reynolds numbers it increases to about 1.04.

Viscous stresses

The net force due to viscous stresses is defined in Eq. A-2.

The term involving the viscous stresses can be approached by using a volume integral. The cross sectional average is approximated by a volume integral divided by dx. The cross sectional average of x-component hence becomes:

$$\frac{1}{A}\iint_A \frac{\partial}{\partial x_j}\sigma_{xj} dA = \frac{1}{A}\frac{1}{dx}\iiint_V \frac{\partial}{\partial x_j}\sigma_{xj} dV$$ **Eq. A-10**

What is convenient with this form is that it allows the use of the divergence theorem on a tensor:

$$\iiint_V \frac{\partial}{\partial x_j}\sigma_{xj} dV = \oiint_A \sigma_{xj} n_j dA$$ **Eq. A-11**

The volume is enclosed by the cylinder circumference and the two cross sectional discs. The contribution from the cross section is the integral of the viscous stresses in x-direction. This value is significantly less than the pressure forces. This contribution is hence neglected. On the cylinder circumference, the stress equals the wall shear stress, τ_w. The volume integral may then be expressed using τ_w:

$$\oiint_A \sigma_{xj} n_j dA = 2\pi r dx \cdot \tau_w \qquad \textbf{Eq. A-12}$$

which by introducing the skin friction coefficient c_f yields:

$$\frac{1}{A}\iint_A \frac{\partial}{\partial x_j}\sigma_{xj} dA = \frac{2}{r}\tau_w = \frac{1}{2}\rho U^2 \frac{4}{D} c_f \qquad \textbf{Eq. A-13}$$

By employing the commonly used relation $f = 4 \cdot c_f$, the term in Eq. 2.15 is identified. It is however important to note that this relation is an approximation and not a definition. The definition of the skin friction coefficient relates to the wall shear stress whereas the Darcy-Weissbach friction factor is defined using the pressure drop, which makes a slight difference.

Pressure gradient

The pressure gradient term can be nicely cross sectional averaged to obtain the term used in Eq. 2.15.

A.2 Energy Balance, 3D to 1D

The energy balance in three dimensions according to the first law of thermodynamics can be written in both the internal energy form and the enthalpy form. The internal energy form reads:

$$\rho c_v \frac{DT}{Dt} = -T\left\{\frac{\partial p}{\partial T}\right\}_\rho \frac{\partial u_j}{\partial x_j} + \Phi - \frac{\partial}{\partial x_j}\left(q_j\right) \qquad \textbf{Eq. A-14}$$

where the dissipation function Φ is defined as:

$$\Phi = \sigma_{ij}\frac{\partial u_i}{\partial x_j} \qquad \textbf{Eq. A-15}$$

By splitting up the turbulent values into a time averaged term $\overline{\psi}$ plus a fluctuating term ψ' and then time averaging the whole equation, the Reynolds equation for internal energy is obtained:

$$\rho c_v \frac{D\overline{T}}{Dt} = -\overline{T}\left\{\frac{\partial \overline{p}}{\partial T}\right\}_\rho \frac{\partial \overline{u_j}}{\partial x_j} + \overline{\Phi} - \frac{\partial}{\partial x_j}\left(q_j^t\right) \qquad \textbf{Eq. A-16}$$

where the turbulent mean dissipation consists of one laminar and one turbulent term respectively (turbulence is in equilibrium is assumed):

$$\overline{\Phi} = \left(\mu \left(\frac{\partial \overline{u_i}}{\partial x_j} + \frac{\partial \overline{u_j}}{\partial x_i} \right) - \rho \overline{u_i' u_j'} \right) \frac{\partial \overline{u_i}}{\partial x_j} \qquad \textbf{Eq. A-17}$$

and the heat transfer term also embraces one laminar and one turbulent term:

$$q_j^{tot} = -k \frac{\partial \overline{T}}{\partial x_j} + \rho \overline{u_j' c_v T'} \qquad \textbf{Eq. A-18}$$

To obtain the one dimensional energy balance, the differential version is averaged across the cross section.

Temperature change

Averaging the first term on the left hand side of A-16 across the cross section yields:

$$\frac{1}{A}\iint_A \rho c_v \frac{D\overline{T}}{Dt} dA = \frac{1}{A}\iint_A \rho c_v \left(\frac{\partial \overline{T}}{\partial t} + \overline{u}\frac{\partial \overline{T}}{\partial x} + \overline{v}\frac{\partial \overline{T}}{\partial y} + \overline{w}\frac{\partial \overline{T}}{\partial z} \right) dA \qquad \textbf{Eq. A-19}$$

This can be written on conservation form:

$$\frac{1}{A}\iint_A \rho c_v \left(\frac{\partial \overline{T}}{\partial t} + \overline{u}\frac{\partial \overline{T}}{\partial x} + \overline{v}\frac{\partial \overline{T}}{\partial y} + \overline{w}\frac{\partial \overline{T}}{\partial z} \right) dA = \frac{1}{A}\iint_A \left(\frac{\partial}{\partial t}\left(\rho c_v \overline{T}\right) + \frac{\partial}{\partial x_j}\left(\rho c_v \overline{u}_j \overline{T}\right) \right) dA \qquad \textbf{Eq. A-20}$$

Since both $\overline{v}$ and $\overline{w}$, are zero, the corresponding terms in the parenthesis drop out. Assuming constant heat capacity and density over the cross section, this can be integrated as follows:

$$\frac{1}{A}\iint_A \left(\frac{\partial}{\partial t}\left(\rho c_v \overline{T}\right) + \frac{\partial}{\partial x_j}\left(\rho c_v \overline{u}_j \overline{T}\right) \right) dA = \rho c_v \left(\frac{\partial T}{\partial t} + \beta_2 U \frac{\partial T}{\partial x} \right) \qquad \textbf{Eq. A-21}$$

Now T and U denote the cross sectional averaged Reynolds averaged temperature and longitudinal velocity respectively. β_2 accounts for the fact that the average of a product does not necessarily equal the product of the averaged quantities. In this case β_2 is simply defined as:

$$\beta_2 = \frac{1}{UT}\frac{1}{A}\iint_A \overline{u}\,\overline{T} dA \qquad \textbf{Eq. A-22}$$

For Reynolds numbers in the range of 10^7, both the temperature profile and the velocity profile becomes very flat, causing the β_2-value to approach one. An exact value is not found in literature, but it is believed to be in the same range as the profile factor in the momentum balance.

Joule Thompson effect

The cross sectional average of the second term in the Reynolds averaged energy balance may be expanded as follows:

$$\frac{1}{A}\iint_A \overline{T}\left\{\frac{\partial \overline{p}}{\partial T}\right\}_\rho \frac{\partial \overline{u_j}}{\partial x_j} dA = \frac{1}{A}\iint_A \overline{T}\left\{\frac{\partial \overline{p}}{\partial T}\right\}_\rho \left(\frac{\partial \overline{u}}{\partial x} + \frac{\partial \overline{v}}{\partial y} + \frac{\partial \overline{w}}{\partial z}\right) dA \qquad \textbf{Eq. A-23}$$

Similarly to the arguments used above, the two last terms in the parenthesis drop out since both $\overline{v}$ and $\overline{w}$ are zero. Furthermore $\left(\partial \overline{p} / \partial T\right)_\rho$ can be assumed constant in the cross section, and can hence be placed outside the integral. The averaged Joule Thompson term turns out to be:

$$\frac{1}{A}\left\{\frac{\partial \overline{p}}{\partial T}\right\}_\rho \iint_A \overline{T}\frac{\partial \overline{u}}{\partial x} dA = \left\{\frac{\partial \overline{p}}{\partial T}\right\}_\rho \beta_3 T \frac{\partial U}{\partial x} \qquad \textbf{Eq. A-24}$$

where capital *T* and *U* now denote the cross sectional averaged Reynolds averaged quantities.

The β_3-factor is a profile factor similar to what was introduced for the term on the left hand side of the equation. It is not known what a realistic value for this factor should be, but it is probably close to unity, and hence negligible.

Dissipation term

The dissipation term accounts for the temperature increase due to breakdown of the turbulent eddies and the mean flow kinetic energy. Because of the non-zero viscosity, these eddies cause stresses in the gas which again leads to mechanical kinetic energy being transferred to thermal energy.

In Eq. A-17 the Reynolds averaged dissipation term is given.

For gas flow in a constant-diameter pipe, the leading time averaged velocity gradient that is present is $\partial \overline{u} / \partial y$. Consequently, the dissipation term from Eq. A-17 simplifies to:

$$\overline{\Phi} = \left(\mu \frac{\partial \overline{u}}{\partial y} - \rho \overline{u' v'}\right)\frac{\partial \overline{u}}{\partial y} \qquad \textbf{Eq. A-25}$$

Finding the cross sectional average of this term involves the use of the universal turbulent velocity profile, which depends primarily on the Reynolds number, and an estimate of the turbulent shear stress, $-\rho \overline{u' v'}$. According to Ytrehus (2004-2007) the result of this procedure may be written as:

$$\Phi = \rho \frac{f}{2D} U^3 \cdot F(\mathrm{Re}) \qquad \textbf{Eq. A-26}$$

where the factor *F(Re)* accounts for the turbulence, and has the specific form:

$$F(\mathrm{Re}) = \left(\frac{f}{8}\right)^{1/2}\left(y_0^+ + \frac{1}{\kappa}\ln\frac{R^+}{y_0^+} - \frac{3}{2}\right)$$ **Eq. A-27**

Here y_0^+ is the thickness of the viscous sublayer in standard wall units, and R^+ is the scaled radius of the pipe. The factor increases with Reynolds number and take values from 1.0 to 1.4 in the range of Re = $10^6 - 10^8$.

It can be shown that the expression used by TGNet is valid for laminar flow. In laminar flow the turbulent contribution in Eq. A-25 vanishes, and the time averaged velocity equals the instantaneous velocity. By using the fact that the laminar velocity profile in incompressible flow is given by

$$u(r) = -\frac{\Delta p / \Delta l}{4\mu}\left(R^2 - r^2\right)$$ **Eq. A-28**

(see White (1999)), the exact expression for laminar friction factor $\left(f = 64/\mathrm{Re}\right)$ and some manipulation of the formulas, the exact expression for dissipation in laminar flow turns out to be

$$\overline{\Phi} = \rho\frac{f}{2D}U^3$$ **Eq. A-29**

Generalizing this formula by simply introducing the turbulent friction factor is obviously a questionable approximation. As noted above, the formula needs to be corrected by the factor 1.0 – 1.4 for Re between 10^6 and 10^8. Eq. A-29 is therefore a reasonable approximation also for turbulent flow, in particular since this term is relatively small in Eq. 2.17, as long as the Mach number in the flow stays low.

Heat transfer

The heat transfer term accounts for the heat transfer longitudinally and radially in the gas. In turbulent flow the internal heat transfer term consists of a turbulent convection term in addition to the molecular conduction term, which gave Eq. A-18:

$$q_j^{tot} = -k\frac{\partial\overline{T}}{\partial x_j} + \rho\overline{u_j^{'}c_vT^{'}}$$ **Eq. A-30**

As for the viscous stresses term in the momentum balance, the cross sectional average is approximated by first taking a volume integral, and then divide it by *dx*. In terms of cylindrical coordinates, the angular derivatives can be ignored for obvious reasons. By assuming that the longitudinal temperature gradient is very little, one can also omit the axial derivatives. What remains is to care about the radial components.

$$\frac{1}{A}\iint_A \frac{\partial}{\partial x_j}q_j^{tot}\,dA = \frac{1}{A}\frac{1}{dx}\iiint_V \frac{\partial}{\partial x_j}q_j^{tot}\,dV$$ **Eq. A-31**

The divergence theorem gives:

$$\iiint_V \frac{\partial}{\partial x_j} q_j^{tot} \, dV = \oiint_A q_j^{tot} n_j \, dA \qquad \textbf{Eq. A-32}$$

By ignoring the axial components, only heat transfer to and from the wall remain. The cross sectional average then becomes:

$$\frac{1}{A} \iint_A \frac{\partial}{\partial x_j} q_j^{tot} \, dA = \frac{1}{A} \frac{1}{dx} q_W \, 2\pi R dx = \frac{4 q_W}{D} \qquad \textbf{Eq. A-33}$$

Appendix B

Paper, Journal of Fluid Mechanics

J. Fluid Mech. (2008), *vol.* 595, *pp.* 323–339. © 2008 Cambridge University Press
doi:10.1017/S0022112007009305 Printed in the United Kingdom

Flow in a commercial steel pipe

L. I. LANGELANDSVIK[1], G. J. KUNKEL[2] AND A. J. SMITS[2]

[1]Department of Energy and Process Engineering,
Norwegian University of Science and Technology, N-7491 Trondheim, Norway
[2]Department of Mechanical and Aerospace Engineering,
Princeton University, Princeton NJ 08540, USA

(Received 5 February 2007 and in revised form 17 September 2007)

Mean flow measurements are obtained in a commercial steel pipe with $k_{rms}/D = 1/26\,000$, where k_{rms} is the roughness height and D the pipe diameter, covering the smooth, transitionally rough, and fully rough regimes. The results indicate a transition from smooth to rough flow that is much more abrupt than the Colebrook transitional roughness function suggests. The equivalent sandgrain roughness was found to be 1.6 times the r.m.s. roughness height, in sharp contrast to the value of 3.0 to 5.0 that is commonly used. The difference amounts to a reduction in pressure drop for a given flow rate of at least 13 % in the fully rough regime. The mean velocity profiles support Townsend's similarity hypothesis for flow over rough surfaces.

1. Introduction

Here we report flow measurements in a commercial steel pipe covering the smooth, transitionally rough, and fully rough regimes. This is the second of our investigations of rough pipe flow, the first being that by Shockling, Allen & Smits (2006), who studied the flow in a pipe with a honed surface, which is typical of many engineering applications. In the study reported here, the Reynolds number was varied from 150×10^3 to 20×10^6, with $k_{rms}/D = 1/26\,000 = 38.5 \times 10^{-6}$, where k_{rms} is the r.m.s. roughness height and D is the pipe diameter. As far as the authors are aware, the only other study of flow in a commercial steel pipe was performed by Bauer & Galavics (1936) and Galavics (1939), and we will demonstrate that the surface finish of their pipes is considerably different from that seen in a modern commercial steel pipe.

Despite the importance of 'natural' roughness in engineering applications, laboratory studies have typically focused on geometric roughnesses, such as square bars and meshes, or other artificial surfaces such as sandpaper. The most complete data set on rough pipe flow behaviour is still that obtained by Nikuradse (1933) using sandgrain roughness. As a result, the roughness of other surfaces is often expressed in terms of an 'equivalent sandgrain roughness', k_s, where k_s is found by comparing the friction factor of the surface in the fully rough regime to the friction factor of the equivalent sandgrain roughened pipe. For example, the Moody diagram (Moody 1944) uses k_s to describe the friction factor curves for rough pipes, and to find the friction factor for a given surface finish the equivalent sandgrain roughness must first be specified, which at present can only be found empirically.

Many aspects of the Moody diagram are currently being re-examined. For turbulent flow in the smooth regime, it uses the Blasius (1913) and Prandtl (1935) friction factor correlations. McKeon, Zagarola & Smits (2005) recently showed that Prandtl's friction factor correlation is inaccurate at higher Reynolds numbers, and they proposed that for $Re_D \geqslant 300 \times 10^3$, a better correlation was given by

$$\frac{1}{\sqrt{\lambda}} = 1.930 \log Re_D \lambda - 0.537, \tag{1.1}$$

where Re_D is the Reynolds number based on the diameter and the bulk velocity $\overline{U}$, ρ is the fluid density and λ is the friction factor defined by

$$\lambda = \frac{-\mathrm{d}p/\mathrm{d}x}{\frac{1}{2}\rho \overline{U}^2} D \tag{1.2}$$

where $\mathrm{d}p/\mathrm{d}x$ is the streamwise pressure gradient. Equation (1.1) gives higher friction factors than the Prandtl formulation for $Re_D > 3 \times 10^6$ (up to 3.2 % higher at 10^8).

In the transitionally rough regime, the Moody diagram uses the Colebrook (1939) correlation, given by

$$\frac{1}{\sqrt{\lambda}} = -2 \ln \left(\frac{k_s}{3.71D} + \frac{2.51}{Re_D \sqrt{\lambda}} \right). \tag{1.3}$$

This correlation is based on laboratory experiments on rough pipes performed by Colebrook & White (1937), as well as a large collection of friction factor data obtained from pipes in commercial use. Its form was constructed by asymptotically matching Prandtl's friction factor curve at low Reynolds number, and Nikuradse's fully rough, Reynolds-number-independent region at high Reynolds numbers. It is clear that the correlation does not describe well many rough surfaces, including the surfaces studied by Colebrook & White (1937). In particular, the correlation fails to reproduce the inflectional characteristics of sandgrain roughness, where the friction factor departs from the smooth correlation at some low value, and then increases in value before reaching its asymptotic high-Reynolds-number level in the fully rough regime. Hama (1954) studied a wide range of roughness types, including meshes and sandpaper roughnesses, and found that instead of following the Colebrook transitional roughness function they all displayed an inflectional behaviour in the transitionally rough regime. Furthermore, the departure from the smooth curve was often abrupt, rather than slowly varying, as implied by the Colebrook correlation.

This inflectional behaviour was also seen by Shockling *et al.* (2006) in a study of honed surface roughness. These results contradict the suggestion by Bradshaw (2000) that the abrupt or inflectional behaviour is only seen in an artificially roughened surface, and that the transition will resemble the Colebrook (1939) correlation (equation (1.3)) for natural surfaces. The equivalent sandgrain roughness of the surface was found to be $k_s \simeq 3\, k_{rms}$, in agreement with the suggestions of Zagarola & Smits (1998) for a surface produced by a similar honing process. The flow showed the first symptoms of roughness when $k_s^+ \approx 3.5$, contrary to the value implied by the Moody diagram, and the departure was much more abrupt than implied by the Colebrook correlation assumed by Perry, Hafez & Chong (2001). Finally, the large-diameter natural gas transmission pipelines on the Norwegian Continental Shelf have a surface finish similar to a honed finish, and Langelandsvik *et al.* (2005) found that operational data support a variant of the abrupt behaviour, although none of the data sets cover a large enough range of Reynolds numbers to fully determine the shape of the curve in the transitionally rough regime.

The scaling of the mean velocity U in a rough pipe was discussed by Shockling *et al.* (2006), and only the principal results will be reproduced here.

For a smooth pipe in the region of overlap, we expect a logarithmic variation of the velocity at sufficiently high Reynolds numbers. In inner variables it takes the form

$$U^+ = \frac{1}{\kappa} \ln y^+ + B \tag{1.4}$$

where $y^+ = yu_\tau/\nu$, $U^+ = U/u_\tau$, y is the distance from the wall, ν is the kinematic viscosity, and $u_\tau/\overline{U} = \sqrt{\lambda/8}$. In outer layer variables we have

$$U_{CL}^+ - U^+ = -\frac{1}{\kappa} \ln \eta + B^* \tag{1.5}$$

where U_{CL} is the centreline velocity, $U_{CL}^+ = U_{CL}/u_\tau$, and $\eta = y/R$. According to McKeon *et al.* (2004), $\kappa = 0.421 \pm 0.002$, $B = 5.60 \pm 0.08$, and $B^* = 1.2 \pm 0.1$. Furthermore, as reported by McKeon *et al.* and Zagarola & Smits (1998), the separation between the inner and outer scales must exceed a certain value before the expected logarithmic law appears. Zagarola & Smits (1998) identified a log law for Re higher than 400×10^3, but McKeon *et al.* modified this limit to 300×10^3 after applying more comprehensive Pitot probe corrections. Also, the log law was found to be valid for $600 \leqslant y^+ \leqslant 0.12R^+$. Here $R^+ = Ru_\tau/\nu$, and R is the pipe radius ($= D/2$).

With increasing Reynolds number and a fixed pipe diameter, the viscous length scale ν/u_τ decreases relative to D and may become comparable to the characteristic roughness height, k. At this point, roughness will start to play a role in determining the flow characteristics. If we assume, as argued by Townsend (1976), that roughness only affects the outer layer scaling by modulating the wall stress (that is, by changing u_τ), then the outer layer formulation is independent of roughness. In the overlap region,

$$U^+ = \frac{1}{\kappa} \ln y^+ + B - \Delta U^+ \tag{1.6}$$

where ΔU^+ is Hama's (1954) roughness function which is a function only of k^+. The Hama roughness function provides a convenient description of the behaviour in the transitional roughness regime.

It seems abundantly clear that different surface finishes have different transitional roughness behaviours, prompting further studies of rough-wall pipe flow. In such studies, it is important to cover the entire transitionally rough range from smooth to fully rough. This requirement dictates a sufficiently large Reynolds number range, something that can be achieved in the Princeton Superpipe facility used by Zagarola & Smits (1998) and Shockling *et al.* (2006). Here we report an investigation of commercial steel pipe roughness in the same facility for Reynolds numbers of 150×10^3 to 20×10^6. The investigation has important practical consequences in that commercial steel pipe is perhaps the most common type of surface finish (in terms of miles of pipe used) in engineering applications. No laboratory study of this particular surface has been performed since the early work of Bauer & Galavics (1936) and Galavics (1939), who investigated a commercially rough steel pipe with $k_{rms} = 130\,\mu\text{m}$ and $k_{rms}/D = 3.8 \times 10^{-4}$. The present surface with $k_{rms} = 5$ is probably more representative of a modern steel pipe, and thus our roughness to diameter ratio is also more realistic. This is supported by Sletfjerding, Gudmundsson & Sjøen (1998) who measured the roughness of an uncoated commercial steel pipe to be 2.36 μm (R_a) and 3.65 μm (R_q or k_{rms}). The pipe had an inner diameter of 150 mm. After coating the roughness dropped to 1.02 μm (R_a) and 1.32 μm (k_{rms}). Measurements reported by

Gersten *et al.* (2000) show $R_a = 8.5\,\mu\text{m}$ for a commercial steel pipe. Diameter is not given.

2. Experiment

The pipe used in the experiments was 5 in. Schedule 40 welded steel pipe supplied by Lincoln Supply of Trenton, New Jersey. Welded steel pipe has a weld seam about 7–8 mm wide running along its entire length. Eight sections of pipe each of length 20 foot were obtained. The inner diameter of each length was measured at six different angles and at both ends. The inner diameter varied between 129.69 mm (5.106 in.) and 130.00 mm (5.118 in) with an average of 129.84 mm (5.112 in.). Near the weld, the pipe was slightly flattened so that the inside diameter decreased by a maximum amount of about 0.4 mm.

The test pipe was installed in the Princeton Superpipe facility that uses compressed air as the working fluid to generate a large Reynolds number range, in this case 150×10^3 to 20×10^6. The facility is described in more detail by Zagarola (1996) and Zagarola & Smits (1998).

The test pipe was constructed in eight separate sections, connected so that the inside surfaces were flush at each joint. The general design followed closely that used by Shockling *et al.* (2006). The steps at each joint in the assembled pipe were estimated to be less than about 50 μm, and they never occupied more than 10 % of the circumference. During assembly of the test pipe in the pressure vessel (described in detail by Zagarola 1996), a theodolite was used to align the sections along a target line. The maximum deviation from the target line at any point along the different segments was 1.5 mm, with an uncertainty of ±0.5 mm. Note that a deviation of 1.5 mm at the middle of the longest segment (4.723 m long), yields a radius of curvature of about 1850 m, which is equal to $29\,000D$. Ito (1959) showed that the friction factor in curved pipes equals the value in straight pipes when

$$\Omega = Re_D \left(\frac{R}{R_0} \right)^2 \leqslant 0.034 \tag{2.1}$$

where R_0 is the radius of curvature. At a Reynolds number of 20×10^6 (the highest value attained in this experiment), $\Omega = 0.023$. Accordingly, the pipe was considered sufficiently straight to make curvature effects negligible.

A total of 21 streamwise pressure taps were used to measure the pressure gradient. The tap diameter was 0.79 mm and the streamwise spacing was 165.1 mm. The pressure taps were drilled from the outside of the pipe using very sharp drill-bits at high r.p.m. to minimize burr. The pressure taps were positioned approximately 120° relative to the weld seam.

A number of differential pressure transducers were used to cover the range of pressures encountered in this experiment. The lowest Reynolds number experiments ($< 250 \times 10^3$) were performed at atmospheric pressure using a 10 Torr MKS Baratron transducer with an uncertainty of ±0.2 % of full scale. At higher Reynolds numbers, the vessel was pressurized, and Validyne DP-15 strain-gauge transducers were used with full-scale ranges of 0.2 p.s.i.d. (1380 Pa), 1.25 p.s.i.d. (8600 Pa), 5 p.s.i.d. (34 500 Pa) and 12 p.s.i.d. (83 000 Pa). The Validyne transducers are accurate to 0.5 % of full scale. By individually calibrating the transducers against sub-standards, the uncertainty was reduced to 0.25 % of full scale.

The atmospheric pressure was found using a mercury manometer, with an uncertainty of 35 Pa. The absolute pressure in the facility was measured with one of two sensors. For pressures lower than 100 p.s.i.g. (0.7 MPa), an Omega transducer calibrated to an accuracy of ±350 Pa was used. At higher pressures, a Heise pressure gauge was used with an uncertainty of 1 p.s.i.g. (7000 Pa). The air temperature was measured using a standard Chromel-Alumel thermocouple interfaced with an Omega DP-41-TC-AR indicator, accurate to ±0.1 % (±0.3 K at room temperature). A heat exchanger was used to keep the temperature in the pipe constant to within ±0.6 K during an experiment.

2.1. *Velocity measurements*

The velocity profiles were taken approximately $200D$ downstream of the pipe inlet. A removable oval shaped plug, cut from an identical piece of pipe, was used to support the probe traverse assembly. The plug, measuring about 100 mm long and 50 mm wide, was hand-fitted to ensure a precise fit with the inside pipe surface. The plug was positioned approximately 120° relative to the weld seam, and 120° relative to the line of pressure taps. Two 0.40 mm static pressure taps were located on the plug surface and connected together to serve as the reference for the dynamic pressure. The mean velocity profile was measured by traversing a 0.40 mm diameter Pitot probe from the wall to the centreline of the pipe. The dynamic pressure was measured at 40 different wall distances, logarithmically spaced. The sampling time at each location was 90 s with a sampling frequency of 50 Hz. An Acurite linear encoder was used to determine the probe location with a resolution of ±5 μm. It has been shown in previous experiments that the forward and reverse travel yielded repeatability within 25 μm (see Shockling *et al.* 2006).

To find the velocity from the Pitot probe measurements, we used the same corrections as those employed by Shockling *et al.* (2006), as originally proposed by Chue (1975), McKeon & Smits (2002) and McKeon *et al.* (2003). The uncertainty in the velocity ranges from 0.5 % to 2 % for the position closest to the wall, and reduces to 0.2 % to 0.5 % for the centreline velocity.

The mean velocity was found by integrating the velocity profile. For the points close to the wall a Spalding-type fit is used in the smooth regime, and a power-law fit is used when the flow is affected by wall roughness (see Shockling *et al.* 2006 for details). Since the Pitot probe corrections described above are only valid for a smooth wall, the points near the wall (for $y \leqslant 2d$ where d is Pitot tube diameter) were not included in the fit. In addition, for all the pressurized tests, that is, for $Re \geqslant 500\,000$, the points for $y^+ < 100$ are omitted in the calculation of the mean velocity to avoid the integration effects noted by Perry *et al.* (2001). In the transitionally rough regime, the difference between a Spalding fit and a power-law fit leads to differences in the friction factor that range from 0.6 % to 1.4 %. The corresponding uncertainty in Reynolds number is 0.3 % to 0.7 %.

The accurate determination of the traverse location adds very little uncertainty to the integrated profile, and is hence omitted.

2.2. *Friction factor measurements*

For incompressible fully developed pipe flow, the wall shear stress may be found from the pressure gradient according to the streamwise momentum equation, so that

$$\tau_w = -\frac{D}{4}\frac{\mathrm{d}p}{\mathrm{d}x}. \qquad (2.2)$$

However, for a compressible flow, the acceleration term in the momentum equation is non-zero. By using the ideal gas law and assuming adiabatic flow, it is easily shown

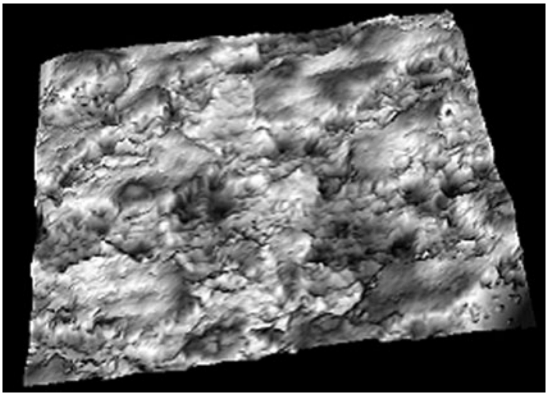

FIGURE 1. Surface scan of the pipe interior in a non-rust area. Sample size is 1.42 × 1.06 mm.

that

$$\tau_w = -\frac{D}{4}\left(1 - \frac{\rho}{\gamma p}U^2\right)\frac{\mathrm{d}p}{\mathrm{d}x}. \tag{2.3}$$

At velocities of $30\,\mathrm{m\,s^{-1}}$ the error in wall shear stress due to neglecting the acceleration term is about 0.7 %, which leads to an error of 0.35 % in the friction velocity. This inaccuracy propagates to the calculation of y^+ and u^+, but it does not affect the friction factor because the error appears in both the numerator and denominator of its definition (equation (1.2)).

The uncertainty in the friction factor originates primarily from the uncertainties in determining the pressure gradient and the dynamic pressure based on the average velocity. That is,

$$\frac{\Delta\lambda}{\lambda} = \sqrt{\left(\frac{\Delta(\mathrm{d}p/\mathrm{d}x)}{\mathrm{d}p/\mathrm{d}x}\right)^2 + \left(\frac{\Delta\left(\frac{1}{2}\rho\overline{U}^2\right)}{\frac{1}{2}\rho\overline{U}^2}\right)^2} \tag{2.4}$$

where Δ denotes the uncertainty level. The uncertainty in the pressure gradient is the main contributor. The surface roughness, and the possible imperfections in the pressure taps, introduced scatter in the wall pressure measurements which increased with Reynolds number. This is the main reason for the reported uncertainty level, which turned out to be larger than that of Shockling *et al.* (2006). The pressure gradient was found by a weighted least-squares fit to the 21 streamwise pressure measurements. The one-sigma confidence interval was used in the uncertainty calculations for the friction factor. The friction factor values agreed well with the expected values in the smooth flow regime, demonstrating that a two-sigma uncertainty interval is probably too conservative.

2.3. *Surface finish*

During the construction and installation of the test pipe, care was taken to preserve the surface finish as it was at the time of purchase, although an acetone wash was used to remove deposits of dirt and grease. Some spots of rust were found on the interior surface but they were accepted as an integral feature of a commercial steel pipe surface finish. The rust spots had a typical diameter of around 5 mm, and they covered less than about 1 % of the total surface area.

The surface geometry characteristics were measured using a Zygo non-interfering optical profiler. Typical topographical maps are shown in figure 1. The results for

	Commercial steel pipe	Honed aluminium pipe
		Shockling *et al.* (2006)
k_{rms} (μm)	5.0	2.5
k_{rms}/D	1:26000	1:52000
flatness/kurtosis	2.5	3.4
skewness	−0.19	0.31
λ_{HSC} (μm)	125–166	90
λ_{HSC}/k_{rms}	25–33	36

TABLE 1. Characteristic surface parameters.

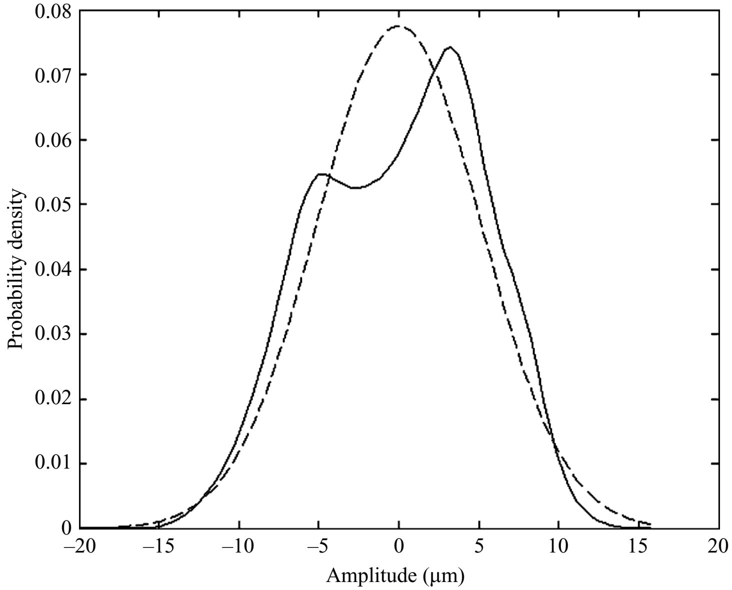

FIGURE 2. ——, Probability density function of commercial steel roughness; – – –, Gaussian distribution with the same standard deviation.

areas unaffected by rust are summarized in table 1, where a comparison with the honed surface studied by Shockling *et al.* (2006) is also given. The high spot-count wavelength, λ_{HSC}, is an estimate of the typical distance between the large roughness elements (in this case, the elements larger than k_{rms}). On the rust spots, the r.m.s. value was found to increase by approximately 0.5 to 1.0 μm, but the flatness and λ_{HSC} were unchanged.

The probability density function of the roughness height from measurements on six different samples is shown in figure 2. The distribution is clearly bimodal, indicating that two primary length scales are present. Inspection of the surface scans shows that the roughness is irregularly distributed, with relatively smooth regions separated by regions of more irregular, larger roughess elements. In contrast, the honed pipe studied by Shockling *et al.* (2006) had a unimodal PDF with a somewhat higher skewness and kurtosis (see table 1).

Re_D	λ	Re_D	λ
150×10^3	0.0167	2.0×10^6	0.0114
220×10^3	0.0155	2.8×10^6	0.0112
300×10^3	0.0146	3.9×10^6	0.0111
500×10^3	0.0134	5.5×10^6	0.0111
600×10^3	0.0132	7.5×10^6	0.0110
700×10^3	0.0127	10.5×10^6	0.0110
830×10^3	0.0122	14.8×10^6	0.0109
1.0×10^6	0.0121	20.0×10^6	0.0109
1.4×10^6	0.0117		

TABLE 2. Friction factor results.

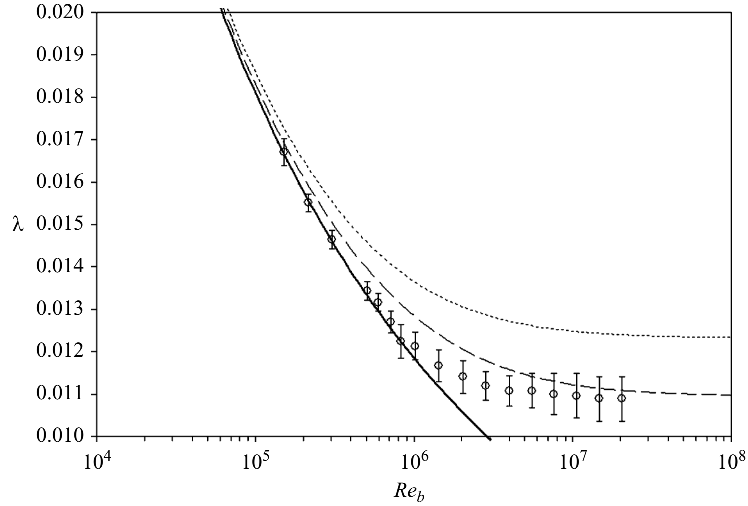

FIGURE 3. Friction factor results. ○, experiment; ——, equation (1.1); – – –, equation (1.3) with $k_s = 8\,\mu\text{m}$ ($= 1.6k_{rms}$); · · · · ·, equation (1.3) with $k_s = 15\,\mu\text{m}$ ($= 3.0k_{rms}$).

3. Results and discussion

3.1. *Friction factor*

The friction factor data listed in table 2 are shown in figure 3. The error bars indicate an uncertainty in friction factor of about ±5 % at high Reynolds number (see § 2.2). The uncertainty in Reynolds number is insignificant when presented on a logarithmic scale.

For Reynolds numbers up to about $600 \times 10^3 \pm 100 \times 10^3$ the points collapse well on McKeon *et al.*'s (2004) smooth curve given by equation (1.1). The point of departure corresponds to $k_s^+ = 1.4 \pm 0.2$, which may be compared to a value of 3.5 for the honed aluminium pipe studied by Shockling *et al.* (2006). The friction factor becomes constant at a Reynolds number of $8.0 \times 10^6 \pm 2.0 \times 10^6$, indicating that the flow is fully rough, and that the pressure drop varies quadratically with the bulk velocity. The start of the fully rough regime corresponds to $k_s^+ = 18 \pm 4.0$. This is in the same range as reported by Shockling *et al.* (2006), but considerably lower than what is typically assumed. The equivalent sandgrain roughness is $1.6 \pm 0.5k_{rms}$, significantly lower than the more commonly accepted value of $(3 - 5k_{rms})$.

The transition to fully rough turbulent flow is abrupt, and it departs significantly from the Colebrook correlation. Furthermore, it does not exhibit the inflectional behaviour characteristic of Nikuradse's sandgrain roughness and the honed surface roughness studied by Shockling *et al.* (2006).

Based on the arguments of Colebrook & White (1937), the effects of roughness are first seen at a Reynolds number where the largest roughness elements begin to protrude outside the viscous sublayer. At this point, the flow between the large roughness elements is still dominated by viscous effects and more or less unaffected by roughness. As the Reynolds number increases, a larger portion of the viscous sublayer will be affected until finally the viscous sublayer vanishes, and the flow is fully rough. In this description of the transitional roughness response, the distance between the roughness elements must be an important parameter. For example, if the distance between the largest roughness elements is very small, then the small roughness elements will not play an important role since they will be shielded by the larger elements. Consequently the behaviour suggested by Colebrook & White not only depends on the roughness distribution, but also on the characteristic wavelengths. The present results indicate that the dependence on wavelength is not simple. For example, Nikuradse's sandgrain roughness displays a notable inflectional friction factor behaviour, and we would expect λ_{HSC}/k_{rms} to be about 2. This has been estimated by approximating the sandgrains by spheres, which gives a wavelength of the same order as the diameter. k_{rms} will be approximately $D/2$, resulting in the stated λ_{HSC}. For the honed surface, the inflectional behaviour is not so pronounced, and $\lambda_{HSC}/k_{rms} = 36$ for the honed surface. However, for the commercial steel surface there is no obvious inflection point in the friction factor curve, and $\lambda_{HSC}/k_{rms} = 25$–$33$, thereby running counter to the trend established by the other two surfaces.

Colebrook & White (1937) proposed that the largest roughness elements determine the point of departure from the smooth line, while the smallest roughness elements determine the point of collapse with the rough line. It may be inferred that a narrow size distribution would exhibit an inflectional behaviour, while a broader distribution would adhere more to the behaviour described by the Colebrook correlation. The natural rough steel pipe has a flatter roughness distribution than the previous honed aluminium pipe (that is, a lower kurtosis). Given that Nikuradse's sandgrain roughness distributions were tightly controlled, it is likely that the size distributions were even narrower than for the honed surface. The data appear to follow this trend, in that the size of the inflectional dip in the friction factor curves increases with decreasing kurtosis value.

Gioia & Chakraborty (2006) have recently developed a model for the shear that a turbulent eddy imparts to a rough surface. This model produces an inflectional friction factor–Reynolds number curve in the transitionally rough regime and links friction factor behaviour to the nature of the eddy interacting with the surface. However, the model is independent of roughness structure, and will not reproduce the commercial steel pipe measurements given here. G. Gioia (private communication) has recently extended this model to surfaces described by two distinct roughness types. This model will predict a monotonic friction factor curve with an abrupt transition from smooth to fully rough for the case where the height of one roughness is much smaller than the other (typically 1/1000), and where the areas covered by these roughnesses are comparable in size.

To see if this model can be applied to our commercial steel surface, we note first that the probability distribution of the roughness heights can be closely approximated by the sum of two normal distributions, each with a standard deviation of 3.2 μm,

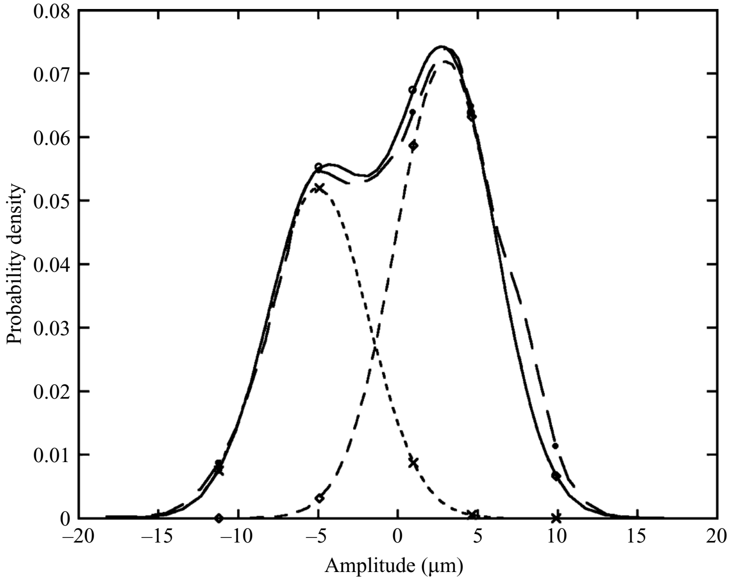

FIGURE 4. ——, Probability density function of commercial steel roughness as the sum of two Gaussian distributions with the same standard deviation. —○—, experimental distribution; - - - × - - -, $0.052\exp(-((k+5)^2/20))$; - - - ○ - - -, $0.072\exp(-((k-3)^2/20))$; – – – ● – – –, sum of exponentials.

offset by a height of about 8 μm (see figure 4). The respective areas covered by the two distributions are in the ratio of their peak values, that is 58 % for the larger roughness, and 42 % for the smaller roughness, which falls within the scope of the extended Gioia model. However, whereas Gioia requires the two roughnesses to be very different in size, we see that in this experiment they have the same r.m.s. value, offset by a relatively large distance. The total span of the roughness elements covers about 30 μm, but it would be an exaggeration to describe one roughness as being very much smaller than the other. Commercial steel roughness is perhaps more accurately described as having three distinct length scales: the two standard deviations and the offset.

Along these lines, a simple model of the growing influence of roughness with increasing Reynolds number might be based on the relative area of roughness exposed by the thinning of the viscous sublayer. First, we choose the Reynolds number where roughness initially becomes important. We could choose the point where $5\nu/u_\tau \leqslant 30\,\mu\text{m}$ (taking the origin of the roughness to be at −15 μm, as in figure 4). This Reynolds number corresponds closely to the point where the initial departure from the smooth curve is seen to occur in the experiment. Second, we assign a drag coefficient for the pressure drag of the roughness elements. Third, we assume that the total drag is given by the sum of the pressure and skin friction components, weighted by the areas they occupy (given by the running integral of the PDF of roughness heights). This model will generate an inflectional transitional roughness curve if the drag coefficient of the roughness elements is taken to be constant and equal to the friction factor in the fully rough regime (that is, about 0.0109). It will instead generate a monotonic behaviour similar to that seen in the experiment if the drag coefficient is allowed to vary from a value of about 0.013 to 0.0109 over the transitional roughness regime. This variation may be justified on the basis of low-Reynolds-number effects,

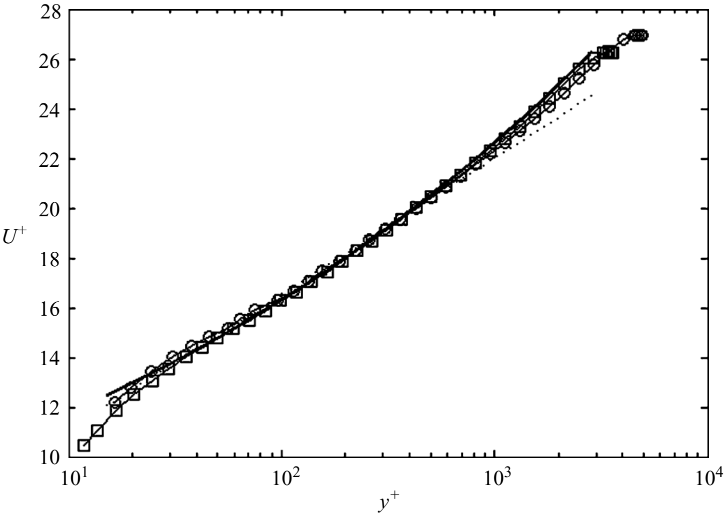

FIGURE 5. Velocity profiles, inner scaling, low Reynolds numbers. ——, equation (1.4); · · · · ·, power law from McKeon *et al.* (2004); □, Re_D 150×10^3; ○, 220×10^3.

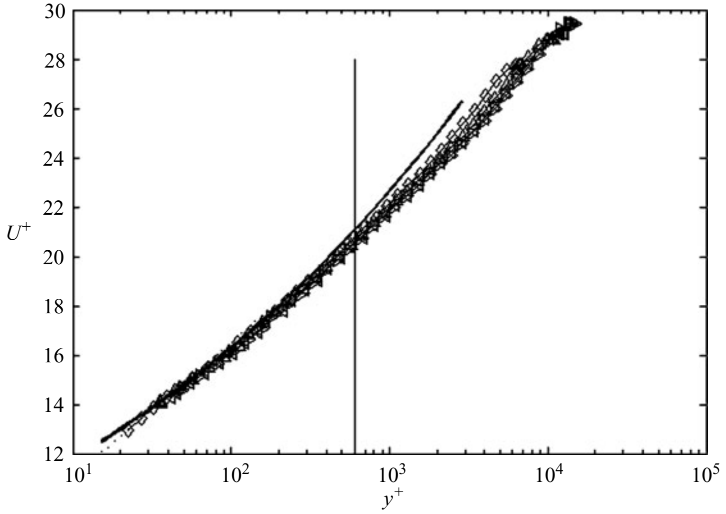

FIGURE 6. Velocity profiles, inner scaling, medium Reynolds numbers. ◇, Re_D 300×10^3; △, 500×10^3; ◁, 600×10^3; ▷, 700×10^3.

but the main point is that the drag mechanisms that govern the transitional roughness behaviour are undoubtedly subtle, and simple models are unlikely to give reliable predictive results without a good deal of additional information on the balance between friction and pressure drag in the near-wall region.

3.2. *Velocity profiles*

The velocity profiles for the two lowest Reynolds numbers are shown in figure 5. The velocity profiles collapse well with McKeon *et al.*'s (2004) power law, and at these low Reynolds numbers we do not expect to see a logarithmic region.

The velocity profiles for the other Reynolds numbers in the smooth flow regime (300×10^3–700×10^3) are shown in figure 6. The lower limit for the log law proposed

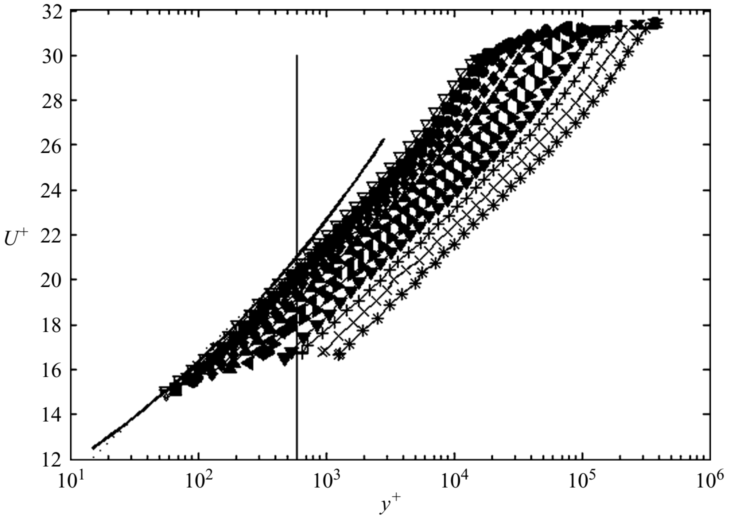

FIGURE 7. Velocity profiles, inner scaling, high Reynolds numbers. ▽, Re_D 830×10^3; ■, 1.0×10^6; ●, 1.4×10^6; ◆, 2.0×10^6; ▲, 2.8×10^6; ◀, 3.9×10^6; ▶, 5.5×10^6; ▼, 7.5×10^6; +, 10.5×10^6; ×, 14.8×10^6; ⋆, 20.0×10^6.

by McKeon *et al.* (2004) is also shown, and the logarithmic region encompasses only a few points in the velocity profile.

The velocity profiles for the transitional and fully rough regimes are shown in figure 7. The downward shift in the profiles signals the onset of roughness, and with increasing Reynolds number the maximum value of U^+ becomes constant, indicating that the flow has become fully rough. The logarithmic region is clearly present for all Reynolds numbers in this range.

Figure 8 shows the velocity defect scaled by the friction velocity ($=(U_{CL} - U)/u_\tau$). The profiles collapse well in the overlap and outer layer regions for all data (i.e. smooth, transitionally rough, and fully rough wall). This lends support to Townsend's hypothesis of Reynolds number similarity, in that the mean relative motion in the fully turbulent region depends only on the wall stresses and pipe diameter (it is independent of the roughness, except in so far as a change in roughness changes the friction velocity). This agrees with the turbulence measurements of the high-Reynolds-number atmospheric boundary layer presented by Kunkel & Marusic (2006) and the turbulence data acquired in the previous honed rough pipe presented by Kunkel, Allen & Smits (2007).

3.3. *Roughness function*

The Hama roughness function ΔU^+ for the natural rough steel pipe is shown in figure 9. The function ΔU^+, as defined by equation (1.6), was found by minimizing the least-square error between the log law and the experimental data. It was assumed that $\kappa = 0.421$, as given by McKeon *et al.* (2004). The departure from the smooth behaviour occurs at $k_s^+ = 1.4 \pm 0.2$, as indicated earlier, but it is evident that the Colebrook function for the same k_s suggests that the effects of roughness start at a Reynolds number that is at least an order of magnitude lower. Also, for a given k_s value, the roughness function is greater than was found for the honed pipe, indicating that the downward shift of the velocity profile is relatively larger. This corresponds well with the differences in friction factor behaviour shown in figure 3.

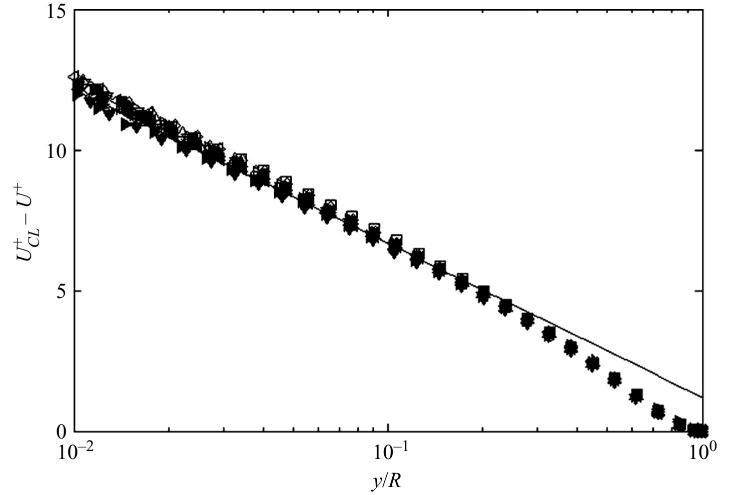

FIGURE 8. Velocity profiles, outer scaling. ——, equation (1.5); □, Re_D 150 × 10^3; ○, 220 × 10^3; ◇, Re_D 300 × 10^3; △, 500 × 10^3; ◁, 600 × 10^3; ▷, 700 × 10^3; ▽, Re_D 830 × 10^3; ■, 1.0 × 10^6; ●, 1.4 × 10^6; ◆, 2.0 × 10^6; ▲, 2.8 × 10^6; ◀, 3.9 × 10^6; ▶, 5.5 × 10^6; ▼, 7.5 × 10^6; +, 10.5 × 10^6; ×, 14.8 × 10^6; ⋆, 20.0 × 10^6.

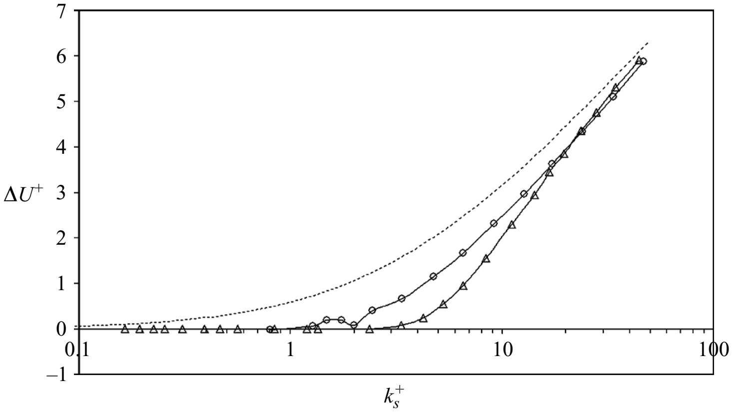

FIGURE 9. Hama roughness function. – – –, equation (1.3) with $k_s = 8\,\mu$m ($= 1.6k_{rms}$); △, honed surface (Shockling *et al.* (2006)); ○, present results.

4. Friction factor diagram for commercial steel pipes

Our results suggest that the Moody diagram as currently constituted is not accurate for commercial steel pipe. Allen, Shockling & Smits (2005) have indicated how similarity arguments may be used to construct a complete friction factor diagram for a given surface using only a single friction factor data set, as long as the data cover the smooth to fully rough regime. The method requires as input the point of departure from the smooth regime, the point at which the fully rough regime begins, the equivalent sandgrain roughness, and a curve fit of the velocity profile in the wake region. Allen *et al.* (2005) gave results for the honed surface studied by Shockling *et al.* (2006). In figure 10, we use this method to suggest a new friction factor diagram for welded commercial steel pipe. Six curves corresponding to $k_s/D = 8.0 \times 10^{-6}$, 6.2×10^{-5}, 2.4×10^{-4}, 6.4×10^{-4}, 1.4×10^{-3}, and 2.7×10^{-3} are shown (the present

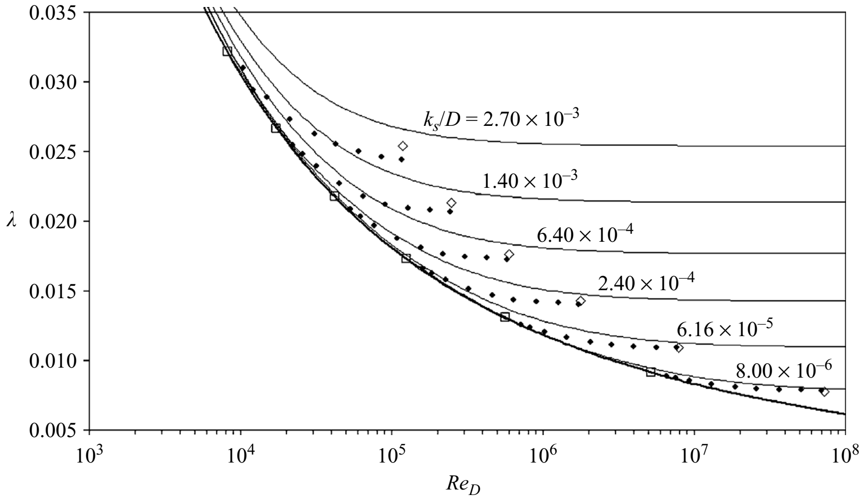

FIGURE 10. Proposed friction factor diagram for welded commercial steel pipe. ◆, Transitional roughness behaviour based on present measurements □, predicted point of departure from smooth line; ◇, predicted point of collapse with rough line; ——, Colebrook transitional roughness function (equation (1.3)).

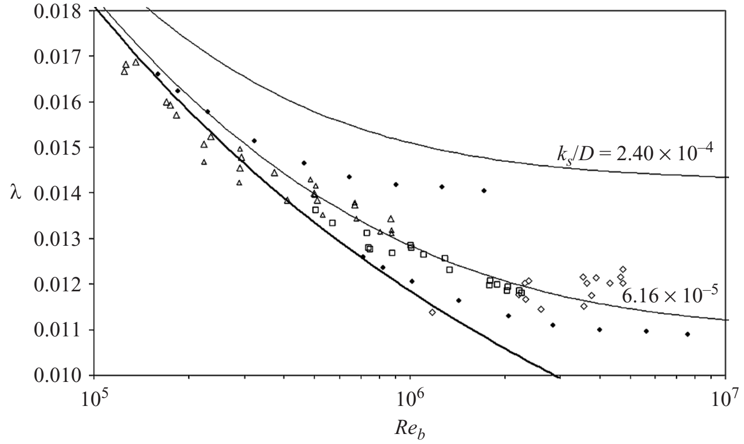

FIGURE 11. Measurements in a steel pipe by Bauer & Galavics (1936). □, $D = 450$ mm; ◇, $D = 350$ mm; △, $D = 250$ mm ◆, transitional roughness behaviour based on present measurements; ——— ; Colebrook transitional roughness function (equation (1.3)).

data had $k_s/D = 6.2 \times 10^{-5}$). As noted earlier, the transition region is considerably more abrupt than the Colebrook curve for the same equivalent sandgrain roughness would suggest. For increasing relative roughness, the end of the transition region (the rightmost ◆) deviates from the indicated point of collapse with the rough line (◇). The fitted wake function deviated slightly from the actual wake that was observed for $Re_D = 7.5 \times 10^6$, which is regarded as the last point in the transition region, and this error increases with lower Reynolds numbers.

The present results may be compared with the data obtained in steel pipes by Bauer & Galavics (1936) and Galavics (1939), as shown in figure 11. Steam at pressures ranging from about 3 to 6 bar was used as the working fluid, and the Reynolds number was varied from 25×10^3 to 2.3×10^6. Three different pipes with diameters of 250, 350, and 450 mm were used. The manufacturing processes for the different pipes are not described in detail, and neither are their roughness characteristics, except that Bauer & Galavics (1936) report that for the 450 mm pipe $k_{rms} = 40\,\mu\text{m}$, so that $k_{rms}/D = 1/11000 = 8.9 \times 10^{-5}$, which is more than two times greater than the relative roughness of the pipe studied here. None of the measurements by Galavics & Bauer cover the complete transitional roughness region, so that definitive conclusions regarding the transitional roughness behaviour cannot be made, although some general observations are of interest.

The 250 mm measurements seem to depart from the smooth curve at around 300×10^3. Using $k_s^+ = 1.4$ as the departure point, $k_{rms}/D = 6.8 \times 10^{-5}$, and $k_{rms} = 17\,\mu\text{m}$. For the 450 mm series, the departure point cannot be determined with the same accuracy but it appears to be about the same as for the 250 mm series so that $k_{rms} \approx 30\,\mu\text{m}$, which agrees reasonably well with the value reported by Bauer & Galavics (1936). It appears, therefore, that the 250 mm and 450 mm results follow a similar transitional roughness behaviour to that observed in the present measurements, although the quality of commercial steel pipes seems to have improved considerably in the intervening 68 years (k_{rms}/D has dropped by a factor of 2). In contrast to the other two pipe sizes, the 350 mm results appear to belong to an inflectional curve, since the friction factor data display a minimum in the transitional roughness regime, although this may be a spurious observation since there is considerable scatter in the data.

5. Conclusions

Friction factor and mean velocity profiles were obtained in a commercial steel pipe ($k_{rms}/D = 1/26,000$) over a large Reynolds number range from 150×10^3 to 20×10^6. To the authors' knowledge, these are the first data for this commercially important surface finish to cover the entire range from smooth to fully rough.

The transitionally rough behaviour was found to be significantly different from that suggested by the Colebrook roughness function. In particular, the departure from the smooth curve is considerably more abrupt, and the fully rough regime is attained over a relatively small interval in Reynolds number. The curve appears to be monotonic, rather than inflectional as seen for sandgrain roughness (Nikuradse 1933) and honed surface roughness (Shockling *et al.* 2006). Since the Colebrook function was devised to describe 'natural' rough surfaces, these new data cast further doubt on its universality.

The probability distribution of the roughness heights can be closely approximated by the sum of two normal distributions, each with the same standard deviation of $3\,\mu\text{m}$, offset by a height of about $8\,\mu\text{m}$ (the standard deviation of the combined distribution is $5\,\mu\text{m}$). The respective areas covered by the two distributions are about 58 % for the larger roughness, and 42 % for the smaller roughness. This observation suggests a stepped uncovering of the roughness elements as the Reynolds number increases. Two simple models discussed here help to give some insight into how this process may proceed, but fail to give predictive results.

We also note the equivalent sandgrain roughness was found to be about $1.6k_{rms}$, instead of the commonly accepted value of 3–5 k_{rms}. For the fully rough regime, and indeed for most of the transitional regime, this gives a friction factor about 13 % lower than that given by the Moody diagram using $k_s = 3.2k_{rms}$.

Finally, the mean velocity profiles support Townsend's similarity hypothesis for flow over rough surfaces. See also Flack, Schultz & Shapiro (2005) and Shockling *et al.* (2006).

Financial support was received from ONR under Grant N00014-03-1-0320 and NSF under Grant CTS-0306691. L. I. L. was supported by a graduate research fellowship from the Norwegian Research Council, and G. J. K. was supported in part by Princeton University through a Council on Science and Technology Fellowship. Special thanks are due to Bob Bogart for contributing his technical skills to the design and installation of the pipe.

REFERENCES

Allen, J. J., Shockling, M. A. & Smits, A. J. 2005 Evaluation of a universal transition resistance diagram for pipes with honed surfaces. *Phys. Fluids* **17**, 121702.

Blasius, H. 1913 Das Ahnlichkeitsgesetz bei Reibungvorgangen in Flussigkeiten. *Forschg. Arb. Ing.* **135**.

Bradshaw, P. 2000 A note on 'critical roughness height' and 'transitional roughness'. *Phys. Fluids* **12**, 1611–1614.

Bauer, B. & Galavics, F. 1936 Untersuchungen über die Rohrreibung bei Heiβwasserfernleitungen. *Archiv Waermewirtschaft* **17** (5), 125–126.

Chue, S. H. 1975 Pressue probes for fluid measurement. *Prog. Aerospace Sci.* **16** (2), 1–40.

Colebrook, C. F. 1939 Turbulent flow in pipes, with particular reference to the transitional region between smooth and rough wall laws. *J. Inst. Civil Engrs* **11**, 133–156.

Colebrook, C. F. & White, C. M. 1937 Experiments with fluid friction in roughened pipes. *Proc. R. Lond. Soc.* A **161**, 367–378.

Flack, K. A., Schultz, M. P. & Shapiro, T. A. 2005 Experimental support for Townsend's Reynolds number similarity hypothesis on rough walls. *Phys. Fluids* **17**, 035102.

Galavics, F. 1939 Die Methode der Rauhigkeitscharakteristik zur Ermittlung der Rohrreibung in geraden Stahlrohr-Fernleitungen. *Schweizer Archiv* **5** (12), 337–354.

Gersten, K., Papenfuss, H.-D., Kurschat, T., Genillon, P., Fernandez Perez, F. & Revell, N. 2000 New transmission-factor formula proposed for gas pipelines. *Oil & Gas J.* **98** (7), 58–62.

Gioia, G. & Chakraborty, P. 2006 Turbulent friction in rough pipes and the energy spectrum of the phenomenological theory. *Phys. Rev. Lett.* **96**, 044502.

Hama, F. R. 1954 Boundary-layer characteristics for smooth and rough surfaces. *Trans SNAME* **62**, 333–358.

Ito, H. 1959 Friction factors for turbulent flow in curved pipes. *Trans. ASME: J. Basic Engng* **6**, 123.

Kunkel, G. J. & Marusic, I. 2006 Study of the near-wall-turbulent region of the high-Reynolds-number boundary layer using an atmospheric flow. *J. Fluid Mech.* **548**, 375–402.

Kunkel, G. J., Allen, J. J. & Smits, A. J. 2007 Further support for Townsend's Reynolds number similarity hypothesis in high Reynolds number rough-wall pipe flow. *Phys. Fluids* **19**, 055109.

Langelandsvik, L. I., Postvoll, W., Svendsen, P., Øverli, J. M. & Ytrehus, T. 2005 An evaluation of the friction factor formula based on operational data. *Proc. 2005 PSIG Conference, San Antonio, Texas.*

McKeon, B. J. & Smits, A. J. 2002 Static pressure correction in high Reynolds number fully developed turbulent pipe flow. *Meas. Sci. Tech.* **13**, 1608–1614.

McKeon, B. J., Li, J., Jiang, W., Morrison, J. F. & Smits, A. J. 2003 Pitot probe corrections in fully-developed turbulent pipe flow. *Meas. Sci. Tech.* **14**, 1449–1458.

McKeon, B. J., Li, J., Jiang, W., Morrison, J. F. & Smits, A. J. 2004 Further observations on the mean velocity distribution in fully developed pipe flow. *J. Fluid Mech.* **501**, 135–147.

McKeon, B. J, Zagarola, M. V. & Smits, A. J. 2005 A new friction factor relationship for fully developed pipe flow. *J. Fluid Mech.* **538**, 429–443.

Moody, L. F. 1944 Friction factors for pipe flow. *Trans. ASME* **66**, 671–684.

NIKURADSE, J. 1933 Laws of flow in rough pipes. *VDI Forschungsheft* **361**. Also *NACA TM* **1292**, 1950.

PERRY, A. E., HAFEZ, S. & CHONG, M. S. 2001 A possible reinterpretation of the Princeton superpipe data. *J. Fluid Mech.* **439**, 395–401.

PRANDTL, L. 1935 The mechanics of viscous fluids. In *Aerodynamic Theory III* (ed. W. F. Durand), p. 142; also Collected Works II, pp. 819–845.

SHOCKLING, M. A., ALLEN, J. J., SMITS, A. J. 2006 Roughness effects in turbulent pipe flow. *J. Fluid Mech.* **564**, 267–285.

SLETFJERDING, E., GUDMUNDSSON, J. S. & SJØEN, K. 1998 Flow experiments with high pressure natural gas in coated and plain pipes. *Proceedings of the 1998 PSIG Conference* Denver, Colorado.

TOWNSEND, A. A. 1976 The Structure of Turbulent Shear Flow. *Cambridge University Press.*

ZAGAROLA, M. V. 1996 Mean-flow scaling of turbulent pipe flow. Doctoral Dissertation, Princeton University.

ZAGAROLA, M. V. & SMITS, A. J. 1998 Mean-flow scaling of turbulent pipe flow. *J. Fluid Mech.* **373**, 33–79.

Appendix C

Paper, Pipeline Simulation Interest Group

Appendix D

Paper, International Journal of Thermophysics

Is not included due to copyright